THE INFLUENCE OF MAGNETIC COHESION ON

THE STABILITY OF GRANULAR SLOPES

Kathryn Helen Taylor, MPhys.

Thesis submitted to the University of Nottingham for
the degree of Doctor of Philosophy

May 2009

Abstract

This thesis presents an investigation into the influence of magnetic cohesion on the stability of granular slopes. We consider magnetic cohesion that results from the interaction between dipole moments induced in grains by a uniform magnetic field.

The dipole-dipole force is highly anisotropic; dipoles attract in the direction parallel to the magnetic field, and repel in the direction perpendicular to the field. In granular ensembles, the magnetic attraction due to dipoles in one area of space can be fully or partially cancelled out by the magnetic repulsion due to other dipoles. We directly observe this cancellation effect by measuring the magnetic dipole-dipole force between magnetine beads, both singly and in a regular two-dimensional lattice.

The repose angle of spheres is known to increase much more slowly with magnetic cohesion than in experiments with liquid-bridge cohesion. To our knowledge, nowhere in the literature has anyone offered a satisfactory explanation of this discrepancy.

We carry out two-dimensional molecular dynamics simulations of granular piles to investigate in detail the role played by magnetic cohesion. Our simulations show that shear occurs deep in the pile, and the addition of a magnetic field causes the avalanche motion to shift farther down into the pile, preventing the slope angle from increasing substantially. We investigate different models of wall friction, and discover that the wall interactions have a significant influence on the rate of increase of the slope angle with magnetic cohesion.

In three-dimensional simulations the angle of repose of a granular pile initially decreases as the cohesion is increased, contrary to our expectations. As cohesion is increased further, the slope becomes steeper again. To understand this behaviour we measure the transverse magnetic force on grains close to the front and back walls of the container. The mechanism responsible for the dip in angle depends on the container width. In containers narrower than six particle diameters the grains are attracted towards the bulk of the pile and away from the walls, and this reduces

the pile stability. In wider containers, however, the transverse magnetic force has the opposite sign at low cohesion. This magnetic force causes a change in the grain distribution of the heap, with grains pulling towards the walls and leaving a lower grain density in the centre. In this region there is an increased grain velocity, which reduces the stability of the pile and causes the observed dip in the angle of repose.

In contrast, draining crater experiments reveal that the angle of repose of dia-magnetic bismuth grains increases dramatically with cohesion in a vertical magnetic field. We argue that this difference is due to the highly non-spherical shape of our bismuth grains, and investigate further the influence of particle shape by using non-magnetic 'voids' of different shapes in a paramagnetic solution. These 'voids' have induced magnetic dipole moments, which interact in the same way as magnetic particles with the same moment. We discover a strong positive correlation between the particle aspect ratio and the size of the effect of magnetic cohesion on the slope angle. This is because a non-spherical grain accumulates magnetic 'charge' on sharp edges and corners, increasing the magnetic field in its immediate vicinity and leading to stronger interactions with neighbouring grains, than would be the case for spheres. Also, in piles of grains with larger aspect ratios, avalanches occur closer to the surface, thus increasing the stability of the pile.

We measure the angle of repose of bismuth in a horizontal magnetic field, using the rotating drum method. When the magnetic field is aligned parallel to the plane of the drum, the slope angle increases as much as for a vertical field of the same magnitude. In both cases a component of the attraction in the direction of the field is directed towards the surface of the pile, increasing the stability and resulting in a higher angle of repose. However, no change in slope angle is observed when the magnetic field is perpendicular to the plane of the drum.

Acknowledgements

Contents

Chapter 1

Introduction

1.1 Introduction

This thesis investigates the influence of magnetic cohesion on the stability of granular slopes. We consider the magnetic cohesion that results from the interaction between dipole moments induced in grains by a uniform magnetic field. We have used experimental measurements and molecular dynamics simulations of the angle of repose of granular piles to determine how the angle depends on the strength of the magnetic cohesion. We also investigate how the particle shape and the field direction affect the dependence of the angle of repose on the magnetic field.

This chapter is a general introduction and literature review. We first describe dry, non-cohesive granular slopes. Then follows a description of the various different kinds of cohesion, and the concept of magnetic cohesion is introduced. We discuss the angle of repose as a measure of cohesion. The literature review covers three different areas: the influence of cohesion on slopes and their angles; the separation of binary mixtures of cohesive particles; and the influence of particle shape on the angle of repose.

1.1.1 Introduction to granular materials

Granular materials consist of a collection of solid particles or grains. They can vary in size, ranging from kilometres (eg. asteroids in an asteroid belt) to micrometres (eg. very fine powders such as flour). The individual particles or grains are

large on an atomic scale; each grain contains a large number of atoms or molecules, and the grains are not subject to thermal effects.

Granular materials are unique in that they possess some of the characteristics of all three phases of matter: solids, liquids and gases. Granular materials are incompressible like solids; they flow and take the shape of the container like liquids; and they can be dilute and highly excited like gases.

Fingerle *et al.* [1] have observed all three phases in cohesive glass particles subjected to vertical vibration. Phase transitions between solid, liquid and gas states were observed as the vibration conditions were varied.

1.2 Dense cohesionless flows

For recent reviews of dense flows in dry granular media, in the absence of cohesion, see Pouliquen and Chevoir [2] and GDR MiDi [3]. A 'dense' granular flow is one in which the volume fraction is high, between random loose packing and random close packing. The motion of the grains is constrained, and it cannot be assumed that grains experience only binary collisions.

Dense granular flows can be studied in several different configurations with both confined and open geometries. In a shear cell, granular material is sheared between parallel walls or coaxial cylinders. Steady flows exist only above a critical shear rate. Below this limit, 'stick-slip' behaviour is observed, in which shear occurs in distinct bursts rather than at a steady rate. In the steady flow regime, most of the motion is localized close to the moving surface. The volume fraction is lower in this sheared region.

Another confined geometry is the silo, in which granular material is allowed to flow under gravity between two rough walls. The velocity profile is mostly flat across the width of the silo, but there are strongly sheared regions close to the walls. As in the shear cell these shear zones are dilated, with a much lower volume fraction.

As well as confined geometries, dense granular materials can undergo free surface flows. One of these is flow down a rough inclined plane. A steady uniform flow can only develop under certain conditions; for each inclination there is a critical thickness

below which no steady flow occurs. This thickness increases for steeper inclinations. When the inclination reaches the angle of repose, the thickness diverges to infinity.

With flow on the surface of a pile, unlike the flow down a rough inclined plane, the system itself chooses the slope of the pile rather than it being dictated by geometry. Steady uniform flows exist at high flow rates. At lower flow rates, stick-slip motion is observed and the slope of the pile oscillates between two angles: the maximum angle of stability, and the angle of repose. The flow happens close to the free surface, with a velocity profile that is linear near the surface and exponential further down into the bulk. The volume fraction decreases close to the surface, in the region with the linear velocity profile.

1.3   Different types of cohesion

Cohesion may be due to liquid bridges: these are small volumes of liquid which form a bridge between neighbouring grains and help them to stick together and to support their own weight against the force of gravity. Dry grains can be made cohesive by adding small quantities of interstitial liquid. The quantity of liquid added is very small in comparison to the volume of the grains. Alternatively, humidity from the air can condense onto the grains.

Cohesion in snow avalanches is an important research area in geophysics. At temperatures above -3°C, snow is wet and cohesive [4]. At the microstructure level, wet snow can be modelled as a cohesive granular material.

In very fine powders (diameter $\sim 10\mu$m), van der Waals cohesion can be a significant factor in determining the avalanche dynamics. The van der Waals forces can be orders of magnitude greater than the particle weight. The force between grains results from the interaction between the dipole fields of neighbouring molecules, and is isotropic and attractive.

Electrostatic cohesion results from the interaction of electrically charged particles. For fine particles in particular, electrostatic cohesion can be a problem in granular dynamics experiments.

Magnetic cohesion is caused by the interaction between magnetic dipoles. When

weakly magnetic particles are placed in a magnetic field, dipole moments are induced in each particle. These magnetic dipole moments interact, creating a cohesive force between the grains. Magnetic interactions are more dramatic for ferromagnetic particles because they have a large susceptibility, but in strong enough magnetic fields cohesion can be induced between diamagnetic or paramagnetic particles. The cohesive forces are absent in zero magnetic field and increase with field strength.

It should be noted that liquid-bridge cohesion differs from magnetic cohesion in a fundamental way. The force due to a liquid bridge between two particles is always attractive. In contrast, the force due to the magnetic dipole-dipole interaction between two particles can be either attractive or repulsive, depending on the relative positions of the particles and the orientation of the magnetic field.

1.4   Angle of repose as a measure of cohesion

When poured gently onto a surface, granular materials will form a pile with a surface angle characteristic of the substance used. For example, dry sand will form an angle of around 20-30° with the horizontal, whereas wet sand can support angles of up to 90°. The reason for this dramatic difference is that wet sand grains are cohesive.

Cohesion in general may be due to liquid bridges, van der Waals interactions, magnetic or electrostatic forces, or some combination. As the particles become more cohesive, we expect the angle of a granular slope to increase. Thus the angle of repose can be used to quantify the effects of cohesion.

There are several different ways of measuring of the angle of repose. The slope angle of a static pile can be measured, formed either by pouring grains onto a flat surface or into a container, or by allowing grains to drain out through a small hole. A static pile can be tilted, or more material can be added to the top, until the slope angle increases above a critical value and an avalanche occurs. The slope angle just before an avalanche is the maximum angle of stability; the angle just after an avalanche is the angle of repose. At faster rates of rotation or adding mass to the pile, the surface flows continously and the slope angle is called the dynamic angle
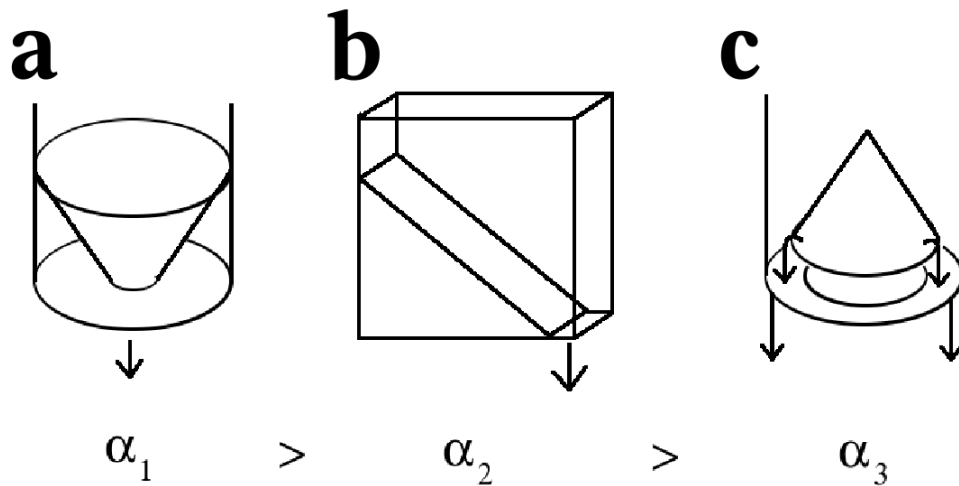
Figure 1.1: *Three different geometries are shown for the draining crater method:* **a** *conical cavity;* **b** *rectangular container; and* **c** *conical heap. The differences in geometry lead to slight differences in the angle of repose.*

of repose.

1.4.1 Draining crater

In a draining-crater experiment, granular matter is placed in the upper chamber of a container and allowed to drain into a lower chamber through a small hole. When motion stops, a measurement of the angle can be taken of the angle of repose.

There are several different experimental configurations for draining crater experiments [5, 6]. A granular bed in a cylindrical container can be allowed to drain through a circular hole in the base (see Figure 1.1**a**). This produces a conical cavity, whose slope angle can be measured. Another configuration is a narrow rectangular cell (Figure 1.1**b**) with an aperture at one edge, across the whole width of the cell. Material drains through the aperture, leaving a pile with a plane surface and enabling the repose angle to be measured. In a third configuration (Figure 1.1**c**), a granular bed is supported on a circular platform and surrounded by a cylindrical support. When the support is lowered, the material slowly drains from the edges of the platform, leaving a conical pile.

The experimental geometry has been found to have an effect on the slope angle.

In the conical cavity formation, each particle on the surface is, on average, positioned slightly behind its neighbours. This geometry increases stability, and leads to a higher repose angle. In a rectangular cell, particles are, on average, level with their neighbours, so the pile is a little less stable and the repose angle is slightly lower. In a conical pile, each surface particle is, on average, slightly in front of its neighbours. This configuration reduces the pile stability further, and results in a lower repose angle. The repose angle in a rotating drum geometry is closest to the angle of repose in a rectangular cell. In both of these geometries, the surface is planar rather than curved.

1.4.2 Rotating drum

The rotating drum experiment is a dynamic process; a circular drum is partially-filled with granular material, rotated, and observed from the side. The slope angle increases as the surface rotates with the drum until a critical angle is reached (the maximum angle of stability α_m), at which point an avalanche occurs and the system reaches equilibrium at a lower angle (the angle of repose α_r). The drum is constantly rotating at a fixed speed, so the post-avalanche slope increases in steepness until a second avalanche occurs. This process is repeated so that measurements can be taken of the slope angle both before and after each of a series of sequential avalanches. At high rotation rates there are no discrete avalanches and the surface is continuously flowing.

1.4.3 Hele-Shaw cell

The Hele-Shaw cell is similar to the draining crater experiment in that granular matter is dropped from the top of the cell and forms a slope, but, like the rotating drum method, it is a continuous process. Grains are released from a feeder slope and the slope of the sandpile formed underneath grows and becomes steeper until a critical angle is reached, at which point an avalanche occurs. In large cells many sequential avalanches can be measured.

1.5 Literature review

1.5.1 Effect of cohesion on slopes

Lian and Shima [7] report the results of a two-dimensional molecular dynamics simulation, incorporating electrostatic cohesive forces. They measured the angle of repose of a pile of particles poured onto a flat surface, and also in a rotating drum. The angle of repose was found to increase with cohesion, and also with the coefficient of friction.

Valverde *et al.* [8] investigated the effect of van der Waals cohesion in fine powders. They tilted beds of xerographic toner particles (mean diameter 8.5 μm) and measured the angle just before an avalanche occurred, and the depth of the avalanche. They found that avalanches took place at a depth of several millimetres, which is much greater than the particle size. Quintanilla *et al.* [9] made larger beads (~ 100 μm diameter) cohesive by coating them with toner particles. They studied the avalanching of these cohesive beads in a rotating drum, and observed that failure occurred deep within the bulk of the material, rather than in a surface layer as is the case for non-cohesive grains.

Peters and Lemaire [10] investigated the effect of magnetic field anisotropy on repose angles of steel spheres, both using the draining-crater method and also by rotating the cell until an avalanche occurred. They measured both the maximum angle of stability and angle of repose. The magnetic field was produced by two pairs of Helmholtz coils, and could be vertical or horizontal, or any angle in the plane of the cell. The authors also investigated the effect of a time-averaged cohesive force, in which anisotropy is eliminated by using a rotating magnetic field. They found that both the maximum angle of stability and the angle of repose were greatest when the magnetic field was applied parallel to the surface of the slope.

Forsyth *et al.* [11] carried out a series of experiments investigating the influence of magnetic cohesion on repose angle. They poured steel ball-bearings into a Hele-Shaw cell to measure the angle of repose α_r in a uniform vertical magnetic field. The authors also measured the dynamic angle of repose in a rotating drum. The slope angle was found to increase slowly and linearly with the interparticle cohesive

force. The angle of repose α_r increased by tens of degrees when the inter-particle cohesive forces were tens of times greater than the particles' weight.

This effect is smaller than expected. When the interparticle cohesive force is of the same magnitude as the gravitational force, we expect the magnetic dipole-dipole force to be strong enough so that one particle can be suspended from another. At this point it would be reasonable to expect angles of repose approaching 90°. This result is not in accordance with the findings of Forsyth *et al.*

The angle of repose of dry spheres is generally measured as about 23° (see [12] and references therein). The value of 31° obtained by Forsyth *et al.* is rather high, and this can be attributed to the narrowness of the container (width 5 particle diameters). Forsyth *et al.* found that the repose angle decreased when they used a wider container. A detailed experimental investigation of the influence of side walls on the repose angle has been carried out by Nowak *et al.* [13].

In contrast with magnetic systems, liquid bridge experiments on granular materials show a dramatic increase in angle of repose when a small quantity of liquid is added [12, 14, 15]. Liquid bridges have been observed to form between particles in contact, providing a cohesive force. It is, however, difficult to directly relate the quantity of liquid to the interparticle force. Albert *et al.* [12, 14] measured the angle of repose of spherical glass particles with varying amounts of oil added. They fitted their data using a model based on the stability of a particle on the surface of a pile, treating the volume of the liquid bridges as an unknown parameter. They found that the slope angle approached 90° when the interparticle cohesive force was comparable to the weight of a particle.

Samadani *et al.* [13, 16] investigated the influence of cohesion on the angle of repose by injecting a small volume of interstitial liquid into granular matter. Liquid bridges were formed between neighbouring particles, providing a cohesive force. In both draining crater and rotating drum experiments, the angle of repose was found to increase with the volume fraction of the liquid and then saturate. Increasing the viscosity of the interstitial liquid also increased the angle of repose. The angle was observed to decrease with increased particle size.

In a second series of experiments, the grains were fully immersed in a liquid.

The repose angle was found to be the same in the liquid as in air. The viscosity of the liquid had no systematic effect on the angle of repose. Samadani and Kudrolli observed that, instead of landing directly on the surface of the slope, particles were more likely to be deflected down the slope in a viscous fluid. They postulated the existence of a boundary layer around each particle, with a size proportional to $\sqrt{(\eta d/\rho V)}$, where η is the liquid viscosity, d is particle size, ρ is density and V is particle volume. At high viscosities this boundary layer was thicker, so a particle falling towards the surface was more likely to be deflected down the slope.

Forsyth *et al.* [11] conducted a similar experiment to that of Samadani and Kudrolli with an inclined rotating drum at various different humidities. They observed two distinct kinds of motion: continuous flow at low humidities, and stick-slip at higher humidities. There was a critical humidity at which the phase transition between these two regimes occurs, and this critical humidity was found to increase with particle size. This result can be explained as follows. The larger the particles, the greater the attraction to the surface of the slope that is required to oppose the force of gravity to such an extent that the particle sticks to the surface for a short time before sliding down the slope, therefore the greater the cohesive force needed to instigate stick-slip motion. The cohesive force increased with humidity (greater number and size of liquid bridges), so the greater the particle size, the greater the critical humidity.

This transition between different phases of motion was also observed by Tegzes *et al.* [17]. They conducted a rotating drum experiment with various volume fractions of interstitial fluid, and observed three kinds of behaviour, depending on the quantity of fluid. At low volume fractions the system was similar to the case where no interstitial fluid is present, with a hysteretic transition between continuous flow and stick-slip motion. At medium volume fractions the transition occurred at a higher rotation rate, and the hysteresis vanished. At higher volume fractions, a regime of viscoplastic flow was observed, in which contacts between particles were lasting, and the transition hysteresis returned. Avalanches occurred through a series of small local rearrangements followed by a large avalanche over the whole surface [18].

1.5.2   Effect of cohesion on the separation of binary mixtures

The principles of diamagnetic levitation are described in Appendix A. One interesting application of diamagnetic levitation is in the field of mineral separation. Different materials may have different values of the ratio of magnetic susceptibility to density, χ/ρ. When a mixture of two such materials is placed in a large inhomogeneous magnetic field, different magnetization forces are experienced, leading to different values of effective gravity $\tilde{g}$.

Vibration can cause the materials to separate. Consider a granular bed, consisting of a mixture of two kinds of particle with different susceptibility to density ratios χ/ρ. The granular bed is placed upon a platform, which oscillates in the vertical direction with an angular frequency ω. The strength Γ of the vibration is quantified using the ratio between the maximum acceleration of the platform and gravity: $\Gamma = A\omega^2/g$, where A is the amplitude of vibration of the platform. The particles with a larger χ/ρ ratio will experience a lower effective gravity. They will therefore be thrown higher than particles that have a higher $\tilde{g}$ and thus will be likely to land on top. After many cycles of vibration, the two species of particle will separate.

Catherall *et al.* [19] successfully separated fine grains of bismuth and bronze, which had similar densities but different susceptibilities. They found that the quality of separation increased with the magnetic field. Figure 1.2, taken from reference [19], shows how the separation of two particular species of particles, bronze and bismuth, varied with Γ and $B\mathrm{d}B/\mathrm{d}z$.

In the regime where the bed was not colliding with the top of the container (below the dashed line in Figure 1.2), the quality of separation increased with increasing magnitude of $B\mathrm{d}B/\mathrm{d}z$. This is to be expected because the two species of particle were experiencing a greater difference in effective gravity. The quality of separation decreased with vibration amplitude. A possible reason for this is that at high vibration amplitudes the grains were thrown so high that they do not have time to settle before the next cycle starts.

Magnetic cohesion exists on the phase diagram for high $B\mathrm{d}B/\mathrm{d}z$ and low Γ. Magnetic dipole-dipole interactions between the diamagnetic bismuth grains caused them to aggregate into clusters, trapping bronze grains within the bismuth and thus
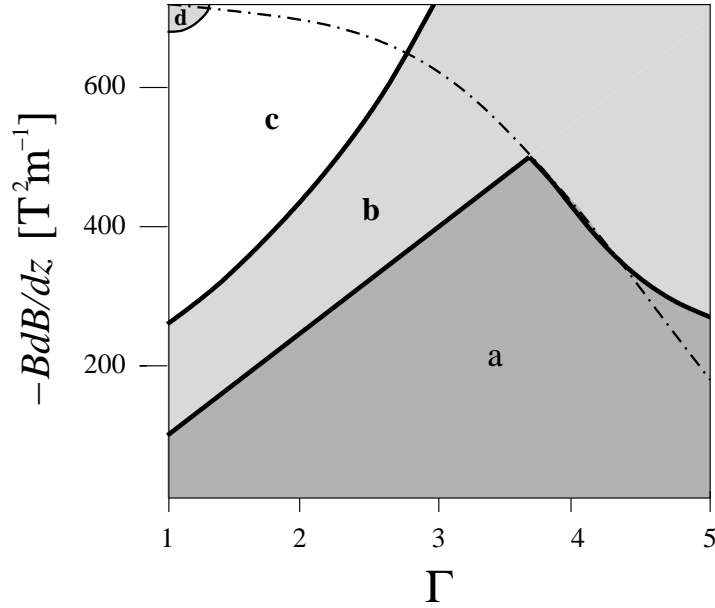
Figure 1.2: *Schematic diagram showing the separation behaviour of 75-90 μm bronze and bismuth grains in vacuum as a function of Γ and BdB/dz at $f = 10$ Hz. The labelled areas represent regions of:* **a** *poor separation;* **b** *good separation;* **c** *excellent separation;* **d** *magnetic cohesion. The dashed line indicates the onset of collisions of the bed with the roof of the container. Diagram taken from Catherall et al. [19].*

decreasing the quality of separation. For smaller particles, the region of the phase diagram in which magnetic cohesion is important was increased in size.

The extraction of minerals often requires the crushing of rock into fine powders to facilitate separation of the desired component. Cohesion can inhibit the separation process, hence the effect of cohesion on the dynamics of fine particles is of particular interest.

Hutton *et al.* [20] report an investigation of the effect of magnetic cohesion on the mixing and segregation of binary mixtures consisting of iron spheres and various non-magnetic materials. In the absence of interparticle cohesive forces, a bidisperse binary mixture poured into a Hele-Shaw cell will segregate with small grains on top and large grains on the bottom. A pair of Helmholtz coils was placed around the cell, and as the field strength was increased the segregation was first eliminated and then reversed, so that the smaller iron particles were found at the top of the pile.

A possible explanation of this is that the cohesive forces caused the iron particles to cluster together, thus increasing the effective particle size to greater than that of the non-magnetic particles.

If the two components of the mixture have differing angles of repose as well as different sizes, stratification can occur with layers parallel to the surface of the slope. In the absence of a magnetic field, the mixture was stratified with layers of the non-magnetic grains over the smaller iron particles. As the magnetic field was increased the two components became well mixed, and then stratification returned but with reversed direction.

Samadani *et al.* [21, 22] investigated the influence of cohesion on the segregation of bidisperse particles by injecting a small amount of interstitial liquid into granular matter. Liquid bridges were formed between neighbouring particles, providing a cohesive force. The presence of a small amount of liquid was sufficient to drastically reduce the size segregation observed for dry particles.

Li and McCarthy investigated the mixing and segregation of binary mixtures of cohesive particles [23]. The particles were glass and acrylic spheres, and the cohesion was due to a small quantity of water added to the grains. The ratios of size, density, and wetting angle of the two species of particles were varied, and phase diagrams of the particle behaviour were produced. The particles exhibited either mixing or segregation, depending on the particle properties.

1.5.3   Effect of particle shape on slope angles and flow

Robinson and Friedman [24] report a series of measurements of the angle of repose of a granular pile. They used various differently shaped particles: spherical glass beads, quartz grains, and tuff grains. The angle of repose was measured in a Hele-Shaw cell for grains in different size ranges. Both the maximum angle of stability and the angle of repose were found to increase with non-sphericity of the particles. Particle size had no effect on the slope angle.

Shourbagy *et al.* [25] report an investigation into the influence of particle shape and friction on the repose angle in two-dimensional simulations. Particles were discharged from a hopper, and the angle of repose of the resulting pile was measured.

Convex polygons were inscribed into circles and ellipses of varying length. Two different measures were used to quantify the particle shape: elongation (the ratio between the long and short axes of the ellipse); and roughness (the number of corners).

The angle of repose of non-elongated five-cornered polygons was measured as a function of the friction coefficient. The slope angle increased linearly with friction, then saturated at a value of $\mu = 0.4$. Particles could move by either rolling or sliding, but at higher friction coefficients (greater than the critical value of $\mu = 0.4$) the sliding was suppressed and rolling motion dominated. Rolling was not significantly affected by the friction coefficient, so the repose angle saturated and was no longer dependent on μ. The pile was built up by avalanches on the surface.

The number of corners of the grains had a significant effect on the angle of repose. The angle was about $27°$ for pentagons (non-elongated) at $\mu = 0.6$, and decreased linearly to $17°$ for particles with eight corners. The greater the number of corners, the more closely the particle resembled a circle, making it more likely to move by rolling rather than sliding. Increasing the number of corners beyond eight made no further difference to the repose angle, because the particles were rolling rather than sliding.

For particles inscribed in an ellipse with an elongation of 1.2, the angle of repose decreased with the number of corners. For larger elongations (1.4 and above), the angle did not depend significantly on the number of corners. This is because particle rolling was already suppressed as a result of the elongated shape, so the particle roughness was not important.

In a similar study, Matuttis *et al.* [26] modelled irregular two-dimensional particles by inscribing convex polygons inside ellipses. The shape was characterised by two variables: the number of edges; and the eccentricity. The stress distribution under a granular heap was calculated, and the results for spherical and non-spherical particles compared. When the polygons were almost spherical (with 12 edges), the stress in the heap was found to be similar to that of a heap of spherical particles. The contact network was regular and periodic. However, when the polygons had fewer edges and a greater polydispersity, the contact network became disordered.

The method of construction of the heap had a significant effect on the stress distribution. If the heap was constructed by releasing irregular polydisperse particles from an outlet or point source a fixed distance above the base, a dip in the vertical stress under the peak of the heap was observed. This was due to granular arching. However, when the heap was constructed slowly in a layered sequence (by dropping particles from a small distance above existing layers), the stress was more homogeneously distributed and no pressure dip was observed. The angle of repose was higher for piles constructed layer-wise than for piles constructed by particles flowing from an outlet.

Cleary [27] reports an investigation into the effect of particle shape on shear flows, using a two-dimensional molecular dynamics simulation. The shear cell was a square with the top and bottom walls moving in opposite directions, and periodic boundary conditions in the streamwise direction. The velocity, volume fraction, granular temperature, and stress distributions across the cell were measured.

The particles used were super-quadrics, with the general form

$$x^n + (ay)^n = s^n, \tag{1.1}$$

where n determines the 'blockiness' of the particle and a is the aspect ratio. When $n = 2$ and $a = 1$, particles are circular. As n tends to infinity, the corners become sharper, and the shape tends towards a square. This model captured two important elements of real particle shapes: sharp corners and elongated shapes.

As n was increased and the particles became more sharp-cornered, changes were observed in the flow behaviour. The strength of the material increased substantially. The particles were better able to grip the container walls, resulting in a higher volume fraction near the walls and a higher granular temperature in the centre of the flow.

For circular particles with aspect ratios in the range $1 < a < 1.67$, increasing the aspect ratio caused changes in the flow behaviour very similar to those observed for increasing n, but the effect was stronger. In both cases, the ability of particles to interlock (due to the presence of sharp corners, broad flat sides, and higher numbers of contacts with other particles) significantly increased the ensemble's resistance to shear.
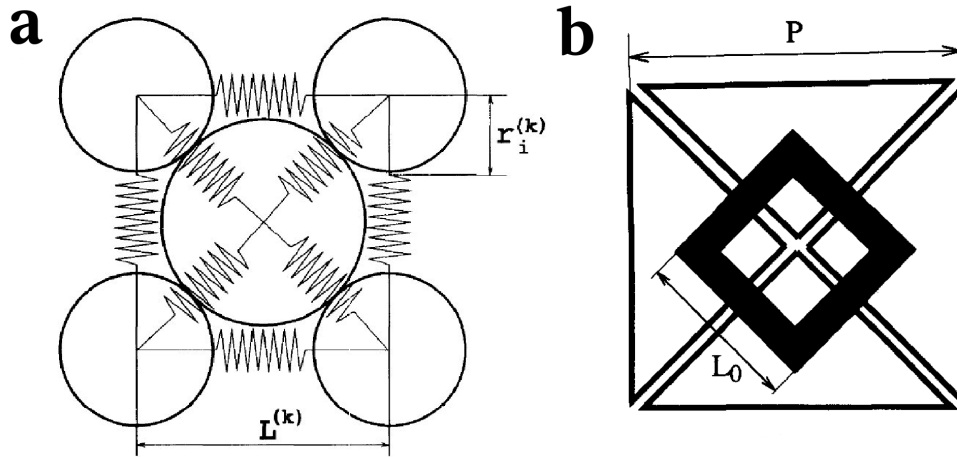
Figure 1.3: a *Composite particle consisting of five circles joined together with springs. Picture taken from Poschel and Buchholtz [29].* **b** *Composite particle consisting of four triangles connected by springs. Picture taken from Buchholtz et al. [30].*

For larger aspect ratios ($1.67 < a < 2.0$), however, the flow behaviour entered a different regime. There was almost no slip between the particles and the walls, and the volume fraction and granular temperature were almost constant across the width of the channel. The reason for this change in behaviour was that the increased aspect ratio caused a change in boundary conditions near the wall. At lower aspect ratios ($a < 1.67$), Campbell Type A boundary conditions were applicable [28]. At the point of collision, there was zero surface contact velocity. The collision therefore caused the particle to spin when leaving the wall. This high spin meant that collisions with other particles resulted in a high variation of velocities, and therefore a high granular temperature near the walls. At higher aspect ratios ($a > 1.67$), Campbell Type B boundary conditions were applicable. The centre-of-mass velocity of the particle was matched to the velocity of the wall. Particles rebounded from the walls with no spin. The granular temperature was lower near the walls. Collisions between elongated particles in the bulk flow could generate spin, and thus a high granular temperature.

The flow of a mixture of particles with a range of different shapes was found to behave in the same way as the flow of particles with a single shape in the middle of the shape range.

Poschel *et al.* [31] [29] modelled irregularly shaped particles in simulations by

constructing composite particles from simple shapes connected with springs. For example, in their two-dimensional simulations of particles in a rotating cylinder, the particles consisted of five spheres connected with springs (see Figure 1.3a). The authors demonstrated that simulations with non-spherical particles could achieve better agreement with experiments than simulations with spherical particles and a static friction term. Poschel *et al.* found that the non-spherical particles had a significantly higher angle of repose than spheres, and at slow rotation speeds, the grains moved with a stick-slip motion. Spherical particles, in contrast, did not produce avalanches.

In a second simulation, a granular pile was formed by continuously dropping particles. For non-spherical particles, avalanches were observed. It was found that the size distribution of the avalanches could be described by the self-organized criticality model; plotting frequency against change in slope angle yields a power law with a critical exponent of -1.4. For spherical particles, no avalanches were found.

The shape of the non-spherical grains could be varied by adjusting the ratio between the size of the grain and the radius of the spheres at the corners. The angle of repose was found to increase as the radius of the corner spheres was increased, reaching a maximum of 23.1° (close to the experimental value for dry spheres [12]) when the shape of the grain most closely resembled a square. It is interesting to note that, although the slope angle was independent of the number of particles for non-spherical objects, when using spheres the angle decreased as more particles were added, as the heap is less able to support itself against gravity.

Composite particles comprised of circles or spheres cannot model the sharp corners of 'real' granular materials. To overcome this problem Buchholtz *et al.* [30], in two-dimensional molecular dynamics simulations of the angle of repose in a rotating drum, used particles consisting of four triangles joined together with elastic beams (see Figure 1.3b). The beams were subject to normal and shear forces and torques, and dissipated energy by deformation. At low rotation rates the particles exhibited stick-slip motion, and at higher rotation rates the flow was continuous. The angle of repose was within the range of experiments with non-spherical grains, higher than usually measured in simulations with circular or spherical particles, or composite

particles comprised of circles or spheres.

Langston *et al.* [32] undertook three-dimensional molecular dynamics simulations using sphero-cylinders. These are non-spherical particles constructed by attaching two hemispheres to the ends of a cylinder. Particles were discharged from a rectangular silo, and the fraction of particles discharged was measured as a function of time. The simulations were run with different values of the aspect ratio of the cylinder. It was found, surprisingly, that the particle aspect ratio did not affect the discharge rate.

In two dimensions, however, the particle shape had a more dramatic effect. Non-circular particles were constructed from two overlapping circle segments. Discs with an aspect ratio of 5 were compared with circular particles. The particles were again discharged from a rectangular hopper, and the fraction discharged measured as a function of time. The discharge rate for the discs was significantly higher than for circular particles. The discs tended to form clusters, within which the particles were aligned in the same direction. The aligned discs could slide past each other more easily, thus increasing the discharge rate by 40%.

Binary mixtures of circles and discs in two dimensions, and of spheres and sphero-discs in three dimensions, revealed that similar shaped particles tend to cluster together. This demonstrates that particle shape can be an important factor in segregation.

Lia *et al.* [33] have extended this two-dimensional disc shape into three dimensions, constructing non-spherical particles from the intersection of two segments of spheres. The discharge of sphero-discs from a rectangular hopper was studied, both in simulation and in experiments (using Nestle Giant Smarties). There was good agreement between experiments and simulations in the flow behaviour and hopper discharge rates.

The authors compared the behaviour of the sphero-discs with that of spherical particles of the same volume, both in simulation and in experiment. The sphero-discs were found to discharge faster than the spheres. The shape of the discs enabled them to slide past each other more easily than spheres.

Sphero-cylinders are a simple example of a Minkowski sum. A Minkowski sum

of two sets is defined as the set resulting from adding each member of one set to each member of the other. Geometrically, this is equivalent to moving one shape around the other. A sphero-cylinder is the Minkowski sum of a line and a sphere.

Alonso-Marroquin [34] developed a new method to simulate more complex shapes using a Minkowski sum of a polygon and a disc. Geometrically, this was equivalent to sweeping the disc around the edge of the polygon. This method can be used to generate complex and non-convex shapes. One such particle used in a two-dimensional molecular dynamics simulation was the Minkowski cow, consisting of a circle swept around a 62-sided non-convex polygon in the shape of a cow. Making this shape as a composite of smaller objects (circles or convex polygons) would be a lot more computationally intensive. The number of vertices in the polygon was generally lower than the number of discs needed to create the same shape as a composite object. The Minkowski sum method was much more efficient, and also had the advantage that the surface is smooth.

The author investigated the effect of particle shape on granular flow by allowing 400 Minkowski cows to flow through a hopper of variable width. When the hopper width was below a critical value, jamming occurred. Granular arches formed across the hopper opening, supporting the weight of the particles above. With Minkowski cows, arches could be over 20 particle diameters in length. In contrast, circular particles flowed smoothly for all aperture sizes. A similar investigation with convex polygonal particles [35] concluded that arches were 4-6 particle diameters in length. This result demonstrates the importance of particle shape. Non-convex particles jammed more easily, as might be expected.

Chapter 2

Simulation Techniques

2.1 Introduction

Simulations are a useful tool to aid physicists' understanding of phenomena in granular dynamics. The advantage of simulations over experiment is that simulations yield more data: individual particles' positions and velocities can be tracked; forces acting on particles can be calculated directly; and many system parameters can be varied more easily than in experiments. The purpose of our simulations is to gain a deeper understanding of the influence of magnetic forces on the stability of granular slopes, rather than to directly model angle-of-repose experiments.

In this chapter we introduce the concept of molecular dynamics simulations and review the literature. The contact models used and our simulation methods are described in detail.

2.2 Principles of the molecular dynamics technique

The molecular dynamics technique (also called the distinct element method), was developed by Cundall and Strack [36]. A collection of spherical particles in a container is modelled. The particles are subject to collisions with other particles and with container walls, as well as external forces such as gravity. It should be

noted that despite the name 'molecular dynamics' the particles modelled are large compared to the atomic/molecular scale.

The sum of all of the forces on each particle is calculated. For a short period of time (the 'timestep'), these forces are assumed to be constant. Newton's second law (force = mass x acceleration) is then used to calculate the particles' acceleration. From this it is possible to calculate the distance that each particle will move during the timestep. The system is advanced by one timestep and all particles are moved simultaneously. The forces are then re-calculated and the process repeated.

A realistic model of the deformation of spherical particles during collisions would be very complicated and computationally intensive. To simplify the model, a penetration depth is defined as the length of overlap between between two particles (or a particle and a wall), and this is assumed to be the important parameter in determining the repulsive contact force. Molecular dynamics simulations can deal with many simultaneous collisions. This is important in quasi-static situations where each particle has multiple and long-lasting contacts with other particles.

For an overview of granular dynamics simulations, see Herrmann and Luding [37]. For a recent review of discrete element simulations and applications, see Zhu *et al.* [38].

2.3 Description of different simulation models

This section will describe a number of different contact, damping and friction models that can be used in molecular dynamics simulations.

In our two dimensional simulations, we used a Hertzian contact model with nonlinear damping and viscous friction. This enabled a close comparison of our results with those of Fazekas *et al.* [39], who also used a Hertzian model. We compared the angles of repose measured using this model to those obtained using a linear contact model with linear damping. We found that the Hertzian model consistently produced angles about 2° higher than the linear model, but there was no significant difference in the dependence of the slope angle on the cohesion strength R. We also compared viscous and static friction models, and found no significant difference in

results (see Section 4.2.5 in Chapter 4).

In our three-dimensional simulations we used a linear spring model with linear damping and viscous friction. This reduced the computational time needed to run the simulations.

2.3.1 Linear spring contact model

When two particles collide, they are treated as overlapping (occupying the same space at the same time). The separation r_{12} of their centres is smaller than the sum of their radii $r_1 + r_2$. The surfaces overlap by a small distance $\delta = r_1 + r_2 - r_{12}$. There is a repulsive contact force $\mathbf{F_n}$ proportional to the overlap distance δ. We can think of the two particles as being connected by an elastic spring of natural length $r_1 + r_2$. The spring makes the two particles repel when they are in contact, but when the contact is broken the spring ceases to exist and the particles do not interact. When the particles collide the spring is compressed to a distance δ shorter than its natural length. The spring obeys Hooke's law, and exerts a force F_n proportional to δ, opposing the spring's compression and pushing the particles apart.

The normal contact force is given by

$$\mathbf{F_n} = -k\delta\hat{\mathbf{n}}, \tag{2.1}$$

where k is the spring constant and $\hat{\mathbf{n}}$ is the normal unit vector in the direction of the line connecting the particles' centres. The spring constant k is a characteristic property of the material. Collisions between particles and walls are treated in a similar way to collisions between particles and particles. A collision occurs when the shortest distance r_w between the particle centre and the wall is less than the particle radius r. The particle overlaps with the wall by a distance $\delta = r - r_w$.

The characteristic time for one oscillation of a spring is $T = 2\pi\sqrt{m/k}$. We require that the simulation timestep be significantly shorter than this characteristic time in order to ensure numerical stability. Therefore a large spring constant requires a small simulation timestep, with a corresponding increase in the necessary computing power. For this reason, it is usual to set k to a lower value than for real physical materials.

2.3.2 Linear viscous damping model

So far we have described elastic collisions, in which there is no energy dissipation. In a real system, there will be some energy loss during collisions. The simplest damping model involves applying a linear viscous damping force $\mathbf{F_d}$. The damping force is proportional to the relative normal velocity $\mathbf{v_n}$ at the contact point of the two particles, but in the opposite direction:

$$\mathbf{F_d} = -\gamma \mathbf{v_n}, \tag{2.2}$$

where γ is the viscous damping coefficient.

2.3.3 Hertzian contact model

In the Hertzian spring model, the dependence of the normal repulsive force of two colliding particles on the overlap distance δ is non-linear. The normal force is given by

$$\mathbf{F_n} = -\frac{4}{3} E^* r^{*\frac{1}{2}} \delta^{\frac{3}{2}} \hat{\mathbf{n}}, \tag{2.3}$$

where E^* is the equivalent Young's modulus and r^* is the equivalent radius, defined as

$$E^* = \left(\frac{1 - \nu_1^2}{E_1} + \frac{1 - \nu_2^2}{E_2} \right)^{-1} \tag{2.4}$$

and

$$r^* = \left(\frac{1}{r_1} + \frac{1}{r_2} \right)^{-1}. \tag{2.5}$$

E_1, E_2 are the Young's moduli, and ν_1, ν_2 the Poisson's ratios, and r_1, r_2 the radii of the two particles. If both particles are of the same radius and material, and have a Poisson's ratio of $\nu = 1/4$, the equivalent Young's modulus reduces to $E^* = 16E/30$ and the equivalent radius reduces to $r^* = r/2$.

2.3.4 Non-linear viscous damping model

As in the case of linear damping, the viscous damping force $\mathbf{F_d}$ is proportional to the relative normal velocity $\mathbf{v_n}$ of the two particles, but in the opposite direction.

However, there is also a non-linear dependence on the overlap distance δ. The force is given by

$$\mathbf{F_d} = -c(6M^*E^*\sqrt{r^*\delta})^{-\frac{1}{2}}\mathbf{v_n}, \tag{2.6}$$

where c is a damping coefficient, M^* is the reduced mass, E^* and r^* are the reduced Young's modulus and radius respectively.

2.3.5 Tangential contact force models

We now describe two different models of the tangential interaction between particles during a collision. The models differentiate between particles adhering to one another, and sliding past one another. The viscous and static friction models treat 'sticking' contacts differently, but both curtail the frictional force in 'slipping' contacts to the Coulomb limit.

2.3.6 Viscous friction model

One simple model to describe the tangential forces is a viscous friction model. Particles moving with a low relative tangential velocity v_t experience a viscous friction force proportional to v_t, in the opposite direction. At higher values of relative tangential velocity the tangential friction force $\mathbf{F_t}$ is curtailed to the Coulomb limit $\mu|\mathbf{F_n}|\hat{\mathbf{t}}$. This can be expressed as

$$\mathbf{F_t} = \min\{\mu|\mathbf{F_n}|, \lambda v_t\}\hat{\mathbf{t}}, \tag{2.7}$$

where λ is a proportionality constant and $\hat{\mathbf{t}}$ is the unit vector in the tangential direction, in the opposite sense to the particles' relative tangential velocity.

2.3.7 Static friction model

The above viscous friction model is simplistic, and fails to accurately describe the tangential forces when the particles are sticking rather than sliding, so we also used a more sophisticated static friction model. The physical basis for static (stick-slip) friction is the surface irregularities on the particles. A 'virtual spring' is created

between two particles when they first come into contact, and its length and orientation are stored for the duration of the contact. When the particles are 'sticking', the tangential friction force is proportional to the relative tangential displacement of the particles (the tangential component of the length of the spring) since the beginning of the contact. The normal and tangential contact forces when particles are 'sticking' are given by

$$\mathbf{F_n} = k\xi_\mathbf{n}, \quad \mathbf{F_t} = k\xi_\mathbf{t}, \tag{2.8}$$

where ξ_n, ξ_t are the normal and tangential components of the spring's extension respectively. The tangential extension ξ_n is equal to the particle overlap δ, so the normal contact forces are the same as in the linear spring model.

If the value of $k\xi_t$ exceeds the Coulomb limit $\mu|\mathbf{F_n}|$, we curtail the tangential force. We consider that the particles are 'slipping' rather than 'sticking'. The tangential force can therefore be expressed as

$$\mathbf{F_t} = \min\{\mu|\mathbf{F_n}|, k\xi_t\}\hat{\mathbf{t}}. \tag{2.9}$$

We use dynamic memory allocation to store the details of each contact, deleting the information when the contact is broken. Hence the processing time required to run the simulations is reduced.

2.3.8 Rotation in simulations

The tangential friction forces during collisions cause the particles to rotate. The torque $\mathbf{T}$ imparted to a particle by a collision with another particle or wall is given by

$$\mathbf{T} = \mathbf{r} \times \mathbf{F_t}, \tag{2.10}$$

where $\mathbf{F_t}$ is the tangential force at the contact point, and $\mathbf{r}$ is the vector from the particle centre to the contact point. The torque is applied in a direction perpendicular to $\mathbf{r}$ and $\mathbf{F_t}$. In two dimensions, this is perpendicular to the plane of the simulations.

The torque is related to the particle's angle ϕ by

$$\mathbf{T} = I\frac{d^2\phi}{dt^2}, \tag{2.11}$$

where I is the particle's moment of inertia. After every timestep the torque is integrated twice, in the same way as translational forces, and the angle of the particle is updated.

2.4   Literature review of simulation models

A study by Zhang and Whiten [40] considered a collision between two particles. Different contact and damping models were compared: a linear spring with linear damping; and a non-linear Hertzian spring with non-linear damping.

The authors pointed out that the linear damping model is unphysical: the force on impact was non-zero. They carried out experiments using the Hopkinson bar equipment, colliding a disc with a steel bar (the method is described in reference [41]). By using strain gauges to measure the impact force as a function of time, they found that the force increased from zero on impact, reaching a maximum and then decreasing again as the particles separated.

Unlike the linear model, in which the damping term was a function only of the relative velocity $\mathbf{v_n}$, the nonlinear damping term depended on both velocity and the overlap δ. When the particles first came into contact, the overlap δ was zero, so the force was zero. There was good agreement between the experimental data and the non-linear model.

Mishra and Murty [42] modelled the contact behaviour of steel balls using linear and non-linear contact models. They used an equivalent linearization technique to transform their non-linear model into an equivalent linear model that accurately described the contact forces. Tracking a large number of particles (for example, 100 000 particles in a ball-mill) can be very computationally intensive. For this reason, linear contact models are often used instead of more realistic non-linear models. Linear models often have a spring constant k set to a lower value than is typical for real physical materials. The period $T = 2\pi\sqrt{m/k}$ for one oscillation of a spring is larger for low values of k, thus reducing the required computing time. Although a linear model with a low k is useful for many applications, it is not suitable for modelling a ball mill. The 'soft' contact vastly underestimates the peak force at

maximum particle overlap, and does not accurately predict abrasion and breakage of the balls. The equivalent linear model had the advantage of 'hard' contacts like non-linear models, but without requiring as much processing time.

The non-linear model had the equation of motion

$$m\frac{d^2x}{dt^2} + qx^s\frac{dx}{dt} + kx^r = 0, \tag{2.12}$$

where x was the particle's displacement, m the mass, k the spring constant, and q the damping coefficient. The parameters s and r were unknowns. The model was optimized by fitting it to experimental force-time and force-deformation data obtained in a series of drop ball tests, in which steel balls of different masses were dropped onto a flat steel rod attached to a strain gauge. The discrepancy between the non-linear model and experiments was minimized to find the values of s and r.

The equivalent linear model was developed by comparing the non-linear model with a linear model with spring constant k' and damping coefficient q'. The difference between the two models was calculated and minimized with respect to k' and q'. The spring constant k' of the equivalent linear model was found to be 100 times smaller than that of the non-linear model.

Three-dimensional molecular dynamics simulations of the energy dissipation as a function of the speed of a ball mill showed that all three models (linear, non-linear, and equivalent linear) agreed quite well with the experimental data of Liddell and Moys [43]. The equivalent linear model was a good compromise between speed and accuracy: it was faster to run than the non-linear model, and it calculated the contact forces more accurately than the linear model.

Yuu *et al.* [44] used a distinct element method to simulate the discharge of spherical particles from a rectangular hopper. Simulations were run using different values of the spring constant, and corresponding values of the timestep. The timestep is calculated on the basis of the oscillation of a single particle of mass m connected to a spring of stiffness k, with period $\tau = 2\pi\sqrt{m/k}$. Because the timestep decreases with k, setting k to the value of a real material would result in unfeasibly large processing power requirements. Most simulations use a smaller value of k, corresponding to a more practical timestep.

Ji and Shen [45] simulated binary collisions and bulk shear flow of spherical particles with two different models. They compared a linear contact model with linear viscous damping to a Hertzian (non-linear) contact model with non-linear damping. During the binary collision the particle overlap, force and relative velocity were measured as a function of time. The two models gave the same results for elastic collisions. For dissipative collisions, however, the results differed depending on the choice of model. In the linear model, initially (when there is no particle overlap) the contact force is non-zero. This unphysical result, previously reported by Zhang and Whiten [40], is due to the linear damping model. The initial contact force deviates further from zero as the damping coefficient is increased. The non-linear model does not have this problem, and predicts initial contact forces of zero when the particles collide.

In bulk shear flow the stress-strain relation, coordination number and contact times for collisions were measured. Results obtained using the two models had slight quantitative differences (well within an order of magnitude), but qualitatively the behaviour was the same. Bulk behaviour was not very sensitive to the choice of model, and the linear model was sufficient to describe the system.

Walton and Braun [46] carried out two-dimensional molecular dynamics simulations of circular particles subject to shear in a rectangular cell with periodic boundary conditions. They used a partially-latching spring model, in which normal collisions had a different value of the spring constant depending on whether loading or unloading was taking place. This led to a position-dependent hysteresis, resulting in dissipation during collisions. In the tangential direction, the hysteretic Mindlin-Dereisewicz model was used [47], in which loading, unloading and reloading are treated differently.

The effective viscosity of the grains was found to increase with the shear rate. The viscosity increases for high and low particle number density, and is lowest for intermediate number density.

Kuwabara and Kono [48] used elastic theory to develop a theoretical model, considering a normal collision between two spheres and deriving the coefficient of restitution e as a function of the impact velocity and elastic constants of the two

spheres. The authors considered dissipation due to the visco-elastic properties of the spheres. They compared their model with the results of experiments colliding two spheres, and obtained quantitative agreement for e close to 1. At lower values of e the model predicted the correct velocity dependence, but agreement with experiment was qualitative.

Stevens and Hrenya [49] investigated the collision of two spherical particles, comparing several soft-sphere simulation models to experimental results. The following models were compared: the Hertzian contact model for perfectly elastic particles; the linear spring model with linear damping; the model of Kuwabara and Kono [48] with a Hertzian repulsive force; the model of Walton and Braun [46] with a linear normal force and the damping either constant or a function of the impact velocity; the model of Thornton [50]; and the model of Lee and Herrmann [51] with a Hertzian repulsive force, and damping proportional to the relative velocity.

The authors conducted experiments to measure the coefficient of restitution and the duration of a normal collision between two cohesionless steel spheres, at a range of impact velocities, and compared these to the predictions of the models. The experiments revealed that the coefficient of restitution and the collision duration both decrease with impact velocity. Not all models reflected this behaviour in their predictions. The Hertzian and linear models, and also the model of Walton and Braun with constant damping, predicted that the coefficient of restitution would remain constant rather than change with impact velocity. The model of Lee and Herrmann predicted that the restitution coefficient would increase with particle impact velocity, rather than decrease as observed in experiment.

The time duration of a collision was found to decrease with particle impact velocity in experiment. Most of the model predictions agreed with this result, with the exception of the linear spring model, and the model of Walton and Braun, both of which predicted that the collision duration was independent of the particle impact velocity.

The normal force was expected to be repulsive towards the end of a collision, when the particle overlap was small, decreasing to zero when the overlap was zero and the particles lost contact. However, the linear spring model, the model of Lee

symbol	parameter	value	unit
d	mean particle diameter	0.8	mm
L	container length	40	mm
k	spring constant in linear model	9425	Nm^{-1}
E	Young's modulus	0.015	GPa
ρ	density	7500	kgm^{-3}
g	acceleration due to gravity	9.81	ms^{-1}
e	coefficient of restitution	0.95	
ν	Poisson's ratio	0.25	
μ	particle-particle coefficient of friction	0.5	
μ_w	particle-wall coefficient of friction	0.5	
λ	viscous friction coefficient	10	kgs^{-1}
Δt	integration time step	5	μs

Table 2.1: *Table of parameters used in two-dimensional simulations*

and Herrmann, and the model of Kuwabara and Kono, all predicted an attractive force at small overlap. The former two models both predicted a non-zero value of the force as the particle overlap tends to zero.

2.5   Details of two-dimensional simulations

Our two-dimensional molecular dynamics model followed the scheme of Cundall and Strack [36]. The particles were modelled as spheres with an approximately Gaussian distribution of diameters, with a mean value of $d = 0.8$ mm and a standard deviation of $\sigma = 0.03$ mm. The distribution was curtailed at 3.35σ, so that all diameters lay in the range $0.7 - 0.9$ mm. The particles had magnetic dipole moments that were induced by a uniform external magnetic field. The induced magnetic dipole moments were always aligned with the external field, though the particles themselves could rotate in the plane of the container. The simulation parameters are listed in Table 2.1.

We used a Hertzian contact model, as described in Section 2.3.3. There was a

non-linear damping force in the normal direction to model the dissipation of energy in collisions. The dissipation of energy during collisions happened via a viscous damping model. The values of the Coulomb friction coefficient μ and the viscous friction coefficient λ are given in Table 2.1. We varied the effective coefficient of restitution e between 0.1 and 0.95, and found that the value of e had no significant effect on our results. See Figure 4.8 in Chapter 4.

2.5.1 Efficiency

To reduce processing time, we defined a neighbour list for particle-particle interactions. The area of the container was divided into cells, and each particle was considered to be in the cell containing its centre. The condition for collision was tested only for particles with centres in the same or neighbouring cells. This substantially reduced the number of potentially colliding particle pairs that must be tested, so the required computational time was much shorter. Each cell had eight neighbouring cells. Four of these cells (above and left; above; above and right; right) were checked for colliding particles. This avoided duplicating each contact. See Figure 2.1.

We defined a separate neighbour list for magnetic interactions. Although the magnetic interactions exist over a long range, they decayed as $1/r^4$, so interactions between particles close together dominated, and interactions between particles farther away were negligible in comparison. The size of the cells was greater than that for collisions. We defined a cut-off distance of 12.5 particle diameters such that magnetic interactions were calculated only for particles separated by less than this distance [52].

2.5.2 Timestep

The timestep was chosen to be 5 μs, significantly shorter than the typical duration of a collision. Using the Hertzian contact model, we measured the duration of a binary collision at various different particle impact velocities. The collision time decreased with velocity, and also decreased slightly with the coefficient of restitution.
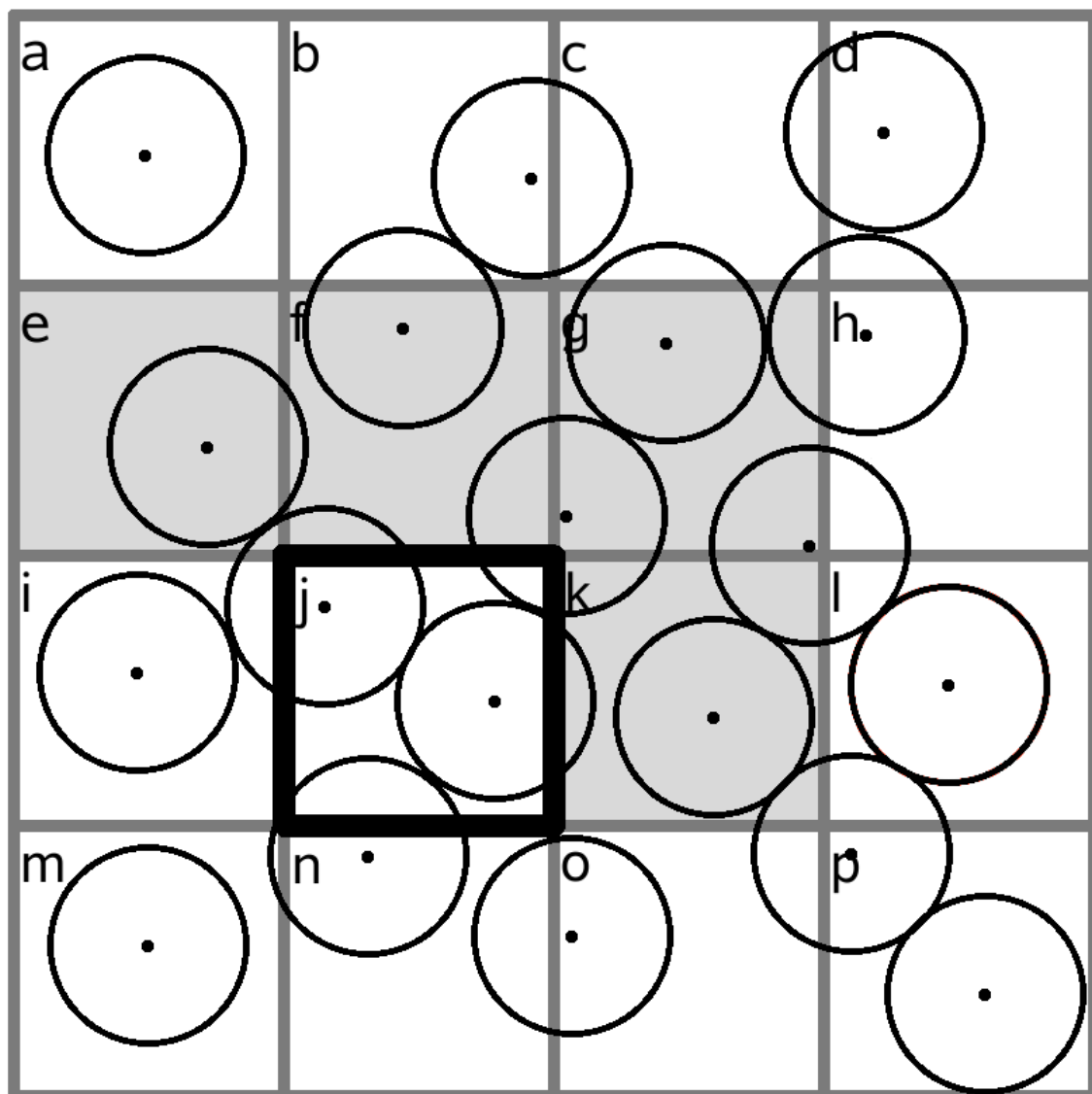
Figure 2.1: *Cell j has eight neighbouring cells: e, f, g, i, k, m, n, and o. The condition for collision is tested firstly for pairs of particles within cell j. Then, particles in cells e, f, g and i in turn are tested for collisions with particles in cell j.*

The collision time was measured as 6×10^{-4} seconds at a low velocity of 0.1 mm/s, and 1.55×10^{-4} seconds at a high velocity of 100 mm/s. Our chosen timestep was a fraction (1/30) of our lowest measurement for collision duration [53].

Another constraint on the timestep was the Rayleigh time. This is the time taken for a Rayleigh wave to travel across an elastic particle; for reasons of numerical stability, the simulation timestep should not exceed this. The Rayleigh time T_R is given by

$$T_R = \frac{\pi d}{0.16\nu + 0.88}\sqrt{\frac{\rho}{G}}, \tag{2.13}$$

where d is the particle diameter, ν is the Poisson's ratio, ρ is density and G is the shear modulus [45, 54]. Using the values given in Table 2.1, we obtained $T_R = 4.84 \times 10^{-5}$ seconds. This was almost ten times larger than our timestep, so the timestep should be sufficiently small to ensure numerical stability of the simulations.

Our linear contact model simulations had contact times much longer than for the Hertzian model (for example, at a velocity of 100 mm/s, the contact duration was 4.48×10^{-3} seconds). However, we used the more conservative value of $\Delta t = 5 \times 10^{-6}$ for the linear model also. We tested our simulations for numerical stability at a range of values for the timestep; these results are reported in Chapter 4, Section 4.2.5.

2.5.3   Magnetic interactions

The particles in our simulations were spherical and weakly magnetic, with moments induced by and parallel to a uniform vertical magnetic field **B**. It is well known that the magnetic field due to a homogeneous sphere with total magnetic moment **m** in a uniform field is equal to that of a point dipole with magnetic moment **m**, located at the sphere's centre (see Section 3.3.3 in the next chapter). In the low susceptibility limit ($\chi \ll 1$), the magnetic moment induced in each particle is too small to affect the uniformity of the field experienced by other particles. We therefore treated our spheres as point dipoles.

The interaction energy E between two point dipoles of magnetic moment **m** separated by **r** is

$$E = \frac{\mu_0 |\mathbf{m}|^2}{4\pi |\mathbf{r}|^3}(1 - 3\cos^2\theta), \tag{2.14}$$

where θ is the angle between the direction of the magnetic field and the vector $\mathbf{r}$ [55]. The magnetic dipole-dipole force between two spheres has been measured [56], and found to be in good agreement with Equation (2.14). The magnetic force is highly anisotropic; its sign changes depending on the orientation of the particles in the magnetic field.

Consider the interaction between two equal particles in contact, with diameter d, volume V and magnetic dipole moment $\mathbf{m} = \chi V \mathbf{B}/\mu_0$. When $\mathbf{r}$ is parallel to $\mathbf{B}$, the particles attract with a maximum cohesive force of magnitude $F_v = \pi \chi^2 B^2 d^2/24\mu_0$. When $\mathbf{r}$ is perpendicular to the field, the particles repel with a force of half the magnitude, $F_h = F_v/2 = \pi \chi^2 B^2 d^2/48\mu_0$.

We defined a cohesion strength R [11] [39] as the ratio of the maximum cohesive force F_v between two particles in contact, and the particle weight:

$$R = \frac{F_v}{mg} = \frac{\chi^2 B^2}{4\mu_0 \rho d g}. \tag{2.15}$$

For non-cohesive particles $R = 0$. When $R > 1$, the cohesive force is greater than the particle's weight and one particle can be suspended from another.

2.5.4 Simulation geometry

In our two-dimensional simulations, the particles were confined to move in the x-y plane, with a horizontal position x and height y. A granular slope was constructed in an L-shaped container consisting of an adhesive base at $y = 0$ of length 40 mm (50 particle diameters), and a vertical wall on the left side at $x = 0$. We describe the x-dimension as 'length'; the y dimension as 'height'; and the vertical distance of a particle below the pile surface as 'depth' (see Figure 2.5.4 for an illustation).

In our three dimensional simulations we also consider a z-dimension 'width', and we add front and back walls to the container (parallel to the x-y plane and perpendicular to z).

To simulate the formation of a granular pile, particles were introduced into the system, one every 3000 time steps (0.015 seconds). Each new particle was released with zero velocity on the left side of the container, at a height just greater than that of the highest existing particle in the pile. Hence newly-introduced particles
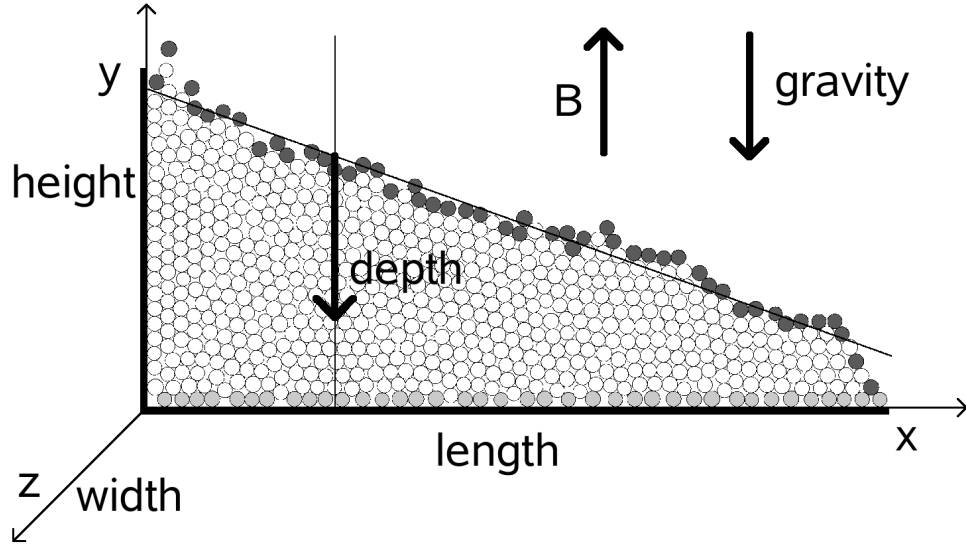
Figure 2.2: *A granular slope in two dimensions, in the absence of a magnetic field. The diagonal line is a fit to the surface particles (darkly shaded). The lightly shaded particles adhered to the base of the container. In two dimensions the particles are confined to move in the x-y plane. In our three-dimensional simulations we added a third dimension z.*

had zero momentum, and the low momentum obtained by falling from the starting position to the top of the pile did not cause any significant disturbance upon impact. Particles colliding with the base of the container became stuck, forming an uneven surface upon which the pile was constructed. Particles reaching the right side (at $x = 40$ mm) fell out of the container and were removed from the system. The magnetic field was applied in the vertical direction.

To determine the angle of repose of the pile, the length of the container was divided into bins, and the highest particle in each bin identified. A least-squares straight line fit was applied to these particles.

2.5.5   Container walls

As a first step towards three-dimensional simulations, we used different methods to model the effects of adding front and back walls of the two-dimensional container in our simulations. Firstly we compared our results to those of Fazekas *et al.* [39] in the absence of front and back container walls.

Secondly, we directed a small percentage, p, of each normal contact force F_n on

symbol	parameter	value	unit
d	mean particle diameter	0.8	mm
L	container length	20	mm
W	container width	2.4-8.0	mm
k	spring constant in linear model	9425	Nm^{-1}
ρ	density	7500	kgm^{-3}
g	acceleration due to gravity	9.81	ms^{-1}
e	coefficient of restitution	0.95	
μ	particle-particle coefficient of friction	0.5	
μ_w	particle-wall coefficient of friction	0.5	
λ	viscous friction coefficient	10	kgs^{-1}
Δt	integration time step	5	μs

Table 2.2: *Table of parameters used in three-dimensional simulations*

each particle outwards (in the z-direction), as if the particles were exerting a force pF_n on the front and back walls. Particles experienced friction $\mu_w pF_n$, where the particle-wall friction coefficient μ_w was set to 0.5. The percentage of force directed outwards was a parameter of the simulations.

Thirdly, we simulated the effect of front and back walls by treating the particles as sliding against the walls. The particles experienced a constant drag force βmg, which was proportional to the particle weight and opposed the direction of motion. Rotational drag was neglected. We treated the drag constant β as a variable parameter.

2.6 Three-dimensional simulation method

We extended our simulations into three dimensions to investigate further the effect of interactions with side walls on the angle of repose and stability of granular piles. Table 2.2 lists the parameters used in our three-dimensional simulations.

The particles were modelled as spheres with an approximately Gaussian distribution of diameters, with a mean value of $d = 0.8$ mm and a standard deviation of

$\sigma = 0.03$ mm. The distribution was curtailed at 3.35σ, so that all diameters lay in the range $0.7 - 0.9$ mm. The induced magnetic dipole moments were always aligned with the external field, though the particles themselves could rotate in the plane of the container.

Three-dimensional simulations are computationally more intensive than two-dimensional simulations, because there are more degrees of freedom and more particles are required. We therefore used a container of length 25 particle diameters (20 mm) rather than the 50 particle diameters used in our two-dimensional simulations. In addition to the base and left wall, we introduced front and back walls, forming an open container with a width of between three and ten particle diameters. There were between 1000 and 2500 particles at a time, depending on the width of the container and the value of R. The two-dimensional simulations, for comparison, used between 700 and 1000 particles at a time. We used a linear contact model rather than Hertzian, after having demonstrated that the choice of contact model has little effect on the repose angle.

We used a neighbour list for collisions, in a similar way to in our two-dimensional simulations. The volume of the container was divided into cubic cells, and each particle was deemed to occupy the cell in which its centre was located. Each cell had 26 neighbouring cells, of which 13 were checked for colliding particles.

Chapter 3

Magnetic dipole interactions and cancellation

3.1 Introduction

In this chapter the different kinds of magnetism (ferromagnetism, paramagnetism and diamagnetism) and their origins are discussed. We calculated the magnetic field due to a point dipole, and the magnetic force between two dipoles. We also demonstrated that a homogeneous sphere in a uniform magnetic field acts as a point dipole. It should be noted that 'point' magnetic charges do not exist in reality; they are a useful idealization valid for solutions of Laplace's equation.

The magnetic dipole-dipole interaction is anisotropic, so the force between two particles depends on their position in the magnetic field. Particles attract along the direction of the field and repel in the direction perpendicular to the field. A particle in a granular bed will interact magnetically with its neighbouring particles, and these attractive and repulsive forces can partially cancel each other out. The net magnetic force on a particle in a granular bed is, in general, smaller than the force between a pair of particles in isolation.

The idea of magnetic cancellation was investigated by calculating magnetic forces on point dipoles in various geometrical configurations. We calculated analytically the force between a dipole and various spaces filled with magnetic material: a thin infinite sheet; an infinitely long rod; and an infinite half-space.

We extended our analysis to the case of discrete particles rather than continuous regions of magnetic material. We numerically calculated the force on a point dipole due to a layer of point dipoles arranged in a regular lattice (square or hexagonal), as a function of the size of the layer, and separation of the point dipole from the layer.

We then measured the dipole-dipole force experimentally, using magnetine beads in a vertical magnetic field. In addition to measuring the force between two beads as a function of their separation, we measured the force on a beads suspended above a layer of beads arranged in a regular hexagonal lattice. This enabled us to quantify the effect of magnetic cancellation. The experimental measurements could then be compared to calculations of the magnetic forces, assuming that every bead acted as a point dipole.

3.2 Types of magnetism

3.2.1 Ferromagnetism

Ferromagnetism occurs in iron, cobalt and nickel, and also in some alloys of these metals. These materials exhibit very large magnetic effects. The magnetic moments due to the conduction electrons are aligned parallel to one another within macroscopic areas known as domains. If a ferromagnetic material is unmagnetized, these domains are aligned randomly. If an external magnetic field is applied, the domains tend to align along the direction of the field.

3.2.2 Diamagnetism

Diamagnetic materials respond to external magnetic fields with induced magnetic dipole moments in a direction opposed to the applied field. The susceptibility χ is small, negative, and independent of temperature. Purely diamagnetic materials have no permanent dipole moments, so magnetic properties are entirely due to these induced moments. All materials exhibit diamagnetism, but in most situations the diamagnetic effects are very weak in comparison to other magnetic effects.

3.2.3 Paramagnetism

In contrast to diamagnetic materials, paramagnetic materials have permanent magnetic dipole moments. These are due to the orbital angular momentum of unpaired electrons in the outer shell. (In diamagnetic atoms the sum of orbital angular momenta of the electrons in the atom is zero.) When subject to an external magnetic field, the dipole moments of the atoms have a tendency to align with the field. However, thermal effects tend to make the dipole moments align in random directions. The susceptibility of a paramagnetic material is positive and inversely proportional to temperature.

	substance	magnetic susceptibility
diamagnetic	bismuth	-1.65×10^{-4}
	graphite	$-1.6 \ \times 10^{-5}$
	water	$-9.0 \ \times 10^{-6}$
	sodium chloride	-1.38×10^{-5}
paramagnetic	4.75 M manganese chloride solution	$+8.37 \times 10^{-4}$
	oxygen gas (at atmospheric pressure)	$+1.92 \times 10^{-6}$
	aluminium	$+2.3 \ \times 10^{-5}$
	iron oxide (FeO)	$+7.2 \ \times 10^{-3}$
ferromagnetic	iron	~ 100

Table 3.1: *Susceptibilities of various diamagnetic, paramagnetic and ferromagnetic materials*

Table 3.1 lists the susceptibilities of various diamagnetic, paramagnetic and ferromagnetic materials. The table includes some of the materials used in our experiments, along with other materials for comparison.

3.3 Magnetic dipole interactions

This section is a review of magnetic dipole interactions. For more details, see references [55,57–61]. In this section we first derive the magnetic field due to a point

dipole. We then define the magnetic scalar potential, and solved Laplace's equation in spherical co-ordinates. The magnetic field boundary conditions are applied to the magnetic scalar potential for the case of a homogeneous sphere in a uniform magnetic field. This enables us to calculate the magnetic field due to a homogeneous sphere, and demonstrate that it is the same as the field due to a dipole in the low susceptibility limit. We calculate the magnetic force between two point dipoles, and use the maximum value of this dipole-dipole force to define the cohesion strength R.

3.3.1 Field due to a point dipole

The magnetic field $\mathbf{H}$ at a point P due to a 'magnetic monopole' of strength p is given by

$$\mathbf{H} = \frac{p\widehat{\mathbf{r}}}{4\pi r^2} = \frac{p\mathbf{r}}{4\pi r^3}, \tag{3.1}$$

where $\mathbf{r}$ is the vector between the 'pole' and point P, and $\widehat{\mathbf{r}} = \mathbf{r}/r$ is a unit vector in the direction of $\mathbf{r}$ [55, 59].

Now consider a dipole with North and South 'poles' separated by a distance d (see Figure 3.3.1). The vectors between point P and the North and South 'poles' are $\mathbf{r}_N$ and $\mathbf{r}_S$ respectively, where $\mathbf{r}_N = \mathbf{r} - \mathbf{d}/2$ and $\mathbf{r}_S = \mathbf{r} + \mathbf{d}/2$. The pole strengths of the North and South 'poles' are $+p$ and $-p$ respectively. The magnetic field at P is the sum of the fields from the two 'poles', given by

$$\mathbf{H} = \frac{p}{4\pi} \left(\frac{\mathbf{r}_N}{r_N^3} - \frac{\mathbf{r}_S}{r_S^3} \right). \tag{3.2}$$

Now we make the assumption that the two magnetic 'poles' are close together compared with the distance from the dipole to point P ($d \ll r$). Thus the vectors $\mathbf{r}_N$, $\mathbf{r}_S$ and $\mathbf{r}$ are almost parallel, and their angles to the vertical approach each other ($\theta_N \approx \theta_S \approx \theta$). To a good approximation, the magnitudes of $\mathbf{r}_N$ and $\mathbf{r}_S$ are given by

$$r_N \approx r - \frac{d}{2}\cos\theta; \quad r_S \approx r + \frac{d}{2}\cos\theta. \tag{3.3}$$

We can expand $1/r_N^3$ using the binomial theorem, and including only first-order
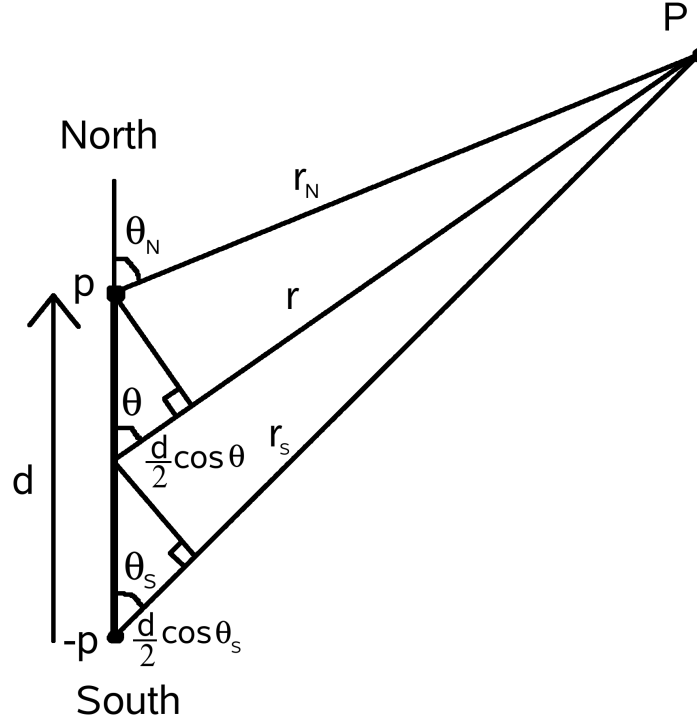
Figure 3.1: *The field due to a magnetic dipole is calculated at point P.*

terms:

$$r_N^{-3} = (r - \frac{d}{2}\cos\theta)^{-3} = r^{-3}(1 - \frac{d}{2r}\cos\theta)^{-3} \approx r^{-3}(1 + \frac{3d}{2r}\cos\theta). \quad (3.4)$$

Similarly for r_S we obtain

$$r_S^{-3} = (r + \frac{d}{2}\cos\theta)^{-3} = r^{-3}(1 + \frac{d}{2r}\cos\theta)^{-3} \approx r^{-3}(1 - \frac{3d}{2r}\cos\theta). \quad (3.5)$$

By substituting $\mathbf{r}_N = \mathbf{r} - \mathbf{d}/2$ and $\mathbf{r}_S = \mathbf{r} + \mathbf{d}/2$ into Equation 3.2, along with Equations 3.4 and 3.5, we obtain

$$\mathbf{H} = \frac{p}{4\pi r^3}\left[(\mathbf{r} - \frac{\mathbf{d}}{2})(1 + \frac{3d}{2r}\cos\theta) - (\mathbf{r} + \frac{\mathbf{d}}{2})(1 - \frac{3d}{2r}\cos\theta)\right], \quad (3.6)$$

and by cancelling the common terms, the above equation reduces to

$$\mathbf{H} = \frac{p}{4\pi r^3}\left(\frac{3d}{r}\cos\theta\,\mathbf{r} - \mathbf{d}\right). \quad (3.7)$$

The magnetic moment $\mathbf{m}$ is given by $p\mathbf{d}$, so the magnetic field produced by a dipole can be expressed as

$$\mathbf{H} = -\frac{|\mathbf{m}|}{4\pi r^3}\left(\widehat{\mathbf{d}} - 3\cos\theta\,\widehat{\mathbf{r}}\right). \quad (3.8)$$

Note that the dipole field decays as $1/r^3$; it is a shorter range than the $1/r^2$ magnetic field for a point 'pole' or the electric field due to a point electrical charge. The magnetic field has a strong angular dependence, with the field strength at the 'poles' being double that at the equator.

3.3.2 Magnetic scalar potential

We begin with Maxwell's equation $\nabla \times \mathbf{H} = \mathbf{J} + \partial \mathbf{D}/\partial t$. In the absence of currents and time-dependent fields this reduces to $\nabla \times \mathbf{H} = 0$. Since $\nabla \times (\nabla u) = 0$ for any scalar u, we can express $\mathbf{H}$ as $-\nabla \psi_m$, where ψ_m is the magnetic scalar potential.

We now solve Laplace's equation $\nabla^2 \psi_m = 0$ for ψ_m in spherical polar coordinates. $\nabla^2 \psi_m$ in spherical polars is given by

$$\nabla^2 \psi_m = \frac{1}{r^2}\frac{\partial}{\partial r}\left(r^2\frac{\partial \psi_m}{\partial r}\right) + \frac{1}{r^2 \sin\theta}\frac{\partial}{\partial \theta}\left(\sin\theta\frac{\partial \psi_m}{\partial \theta}\right) + \frac{1}{r^2 \sin^2\theta}\frac{\partial^2 \psi_m}{\partial \phi^2} = 0. \quad (3.9)$$

We can solve the above equation by separation of variables (see, for example, [58]). Let us assume that $\psi_m(r, \theta, \phi)$ is the product of three functions $R(r)$, $\Theta(\theta)$, and $\Phi(\phi)$, which are functions only of r, θ, and ϕ respectively. By substituting $\psi_m = R\Theta\Phi$ into Equation 3.9 and dividing by $R\Theta\Phi$, we obtain

$$\frac{\nabla^2 \psi_m}{\psi_m} = \frac{1}{R}\frac{1}{r^2}\frac{d}{dr}\left(r^2\frac{dR}{dr}\right) + \frac{1}{\Theta}\frac{1}{r^2 \sin\theta}\frac{d}{d\theta}\left(\sin\theta\frac{d\Theta}{d\theta}\right) + \frac{1}{\Phi}\frac{1}{r^2 \sin^2\theta}\frac{d^2 P}{d\phi^2} = 0. \quad (3.10)$$

To make the final term in the equation a function only of ϕ, we multiply by $r^2 \sin^2 \theta$:

$$\frac{1}{R}\sin^2\theta\frac{d}{dr}\left(r^2\frac{dR}{dr}\right) + \frac{1}{\Theta}\sin\theta\frac{d}{d\theta}\left(\sin\theta\frac{d\Theta}{d\theta}\right) + \frac{1}{\Phi}\frac{d^2 P}{d\phi^2} = 0. \quad (3.11)$$

The final term is a function only of ϕ, and ϕ does not appear anywhere else in the equation. Thus we can use the technique of separating the variables and set the final term to be equal to a constant. Φ must be a periodic function with a period of 2π, because adding 2π radians to an angle will result in the same point in space, and a potential must have a single value at that point. We therefore set the separation constant to be m^2 where m is an integer. Solving the equation

$$\frac{1}{\Phi}\frac{d^2 P}{d\phi^2} = -m^2 \quad (3.12)$$

gives the periodic function $\Phi = \sin(m\phi)$ or $\Phi = \cos(m\phi)$.

Substituting the constant $-m^2$ and dividing by $\sin^2\theta$, Equation 3.11 can be expressed as

$$\frac{1}{R}\frac{d}{dr}\left(r^2\frac{dR}{dr}\right) + \frac{1}{\Theta}\frac{1}{\sin\theta}\frac{d}{d\theta}\left(\sin\theta\frac{d\Theta}{d\theta}\right) - \frac{m^2}{\sin^2\theta} = 0. \tag{3.13}$$

The first term is now a function only of r, and the second two terms together are functions only of θ and ϕ. We therefore set the first term equal to a constant k and the second two terms equal to $-k$.

The first term in Equation 3.13 yields the equation

$$\frac{1}{R}\frac{d}{dr}\left(r^2\frac{dR}{dr}\right) = k. \tag{3.14}$$

By introducing the constant l, defined by $k = l(l+1)$, we can solve the above equation to find the solutions $R = r^l$ and $R = r^{-l-1}$.

The second two terms in Equation 3.13 yield the following equation:

$$\frac{1}{\sin\theta}\frac{d}{d\theta}\left(\sin\theta\frac{d\Theta}{d\theta}\right) - \frac{m^2}{\sin^2\theta}\Theta + k\Theta = 0. \tag{3.15}$$

The solutions for Θ are the associated Legendre functions

$$\Theta(\theta) = P_l^m(\cos\theta), \tag{3.16}$$

with $k = l(l+1)$, where l is an integer. The functions $P_l^m(\cos\theta)\sin m\phi$ and $P_l^m(\cos\theta)\cos m\phi$ are the spherical harmonics.

In the next section, we will consider a geometry with azimuthal symmetry. This symmetry imposes another constraint on ψ_m: there is no dependence of the potential on ϕ. The only terms which satisfy this condition are those with $m = 0$ and $\cos m\phi = 1$. The associated Legendre functions with $m = 0$ are the Legendre polynomials $P_l(\cos\theta)$. The first few terms are $P_0(\cos\theta) = 1$, $P_1(\cos\theta) = \cos\theta$, and $P_2(\cos\theta) = \frac{1}{2}(3\cos^2\theta - 1)$.

The solutions for magnetic scalar potential ψ_m are therefore given by

$$\psi_m = P_l(\cos\theta)\left\{\begin{array}{c} r^l \\ r^{-l-1} \end{array}\right\}. \tag{3.17}$$

The general solution will be given by a sum of potentials with all possible values of l:

$$\psi_m = \sum_{l=0}^{\infty} A_l r^l P_l(\cos\theta) + \sum_{l=0}^{\infty} B_l r^{-l-1} P_l(\cos\theta), \qquad (3.18)$$

where A_l and B_l are constant coefficients of the terms with different values of l.

3.3.3 Equivalence of sphere and dipole

Now we demonstrate that the magnetic field due to a homogeneously magnetized sphere in a uniform magnetic field is exactly equivalent to the field due to a point dipole of the same magnetic moment, located at the sphere's centre. Consider a sphere of radius a and relative magnetic permeability μ_{in} in a medium of relative magnetic permeability μ_{out}, subject to a vertical magnetic field of magnitude H_0. The general solution for the magnetic scalar potential ψ_m is given by Equation 3.18.

The potential ψ_{in} inside the sphere must have all B_l, the coefficients of r^{-l-1}, equal to zero, otherwise the potential would be infinite at $r = 0$. We choose to define the potential ψ_m to be zero at the centre of the sphere. This sets A_0, the coefficient of the r^l term with $l = 0$, to be zero inside the sphere. The only term with a non-zero coefficient is r^l with $l = 1$ [58, 60].

The potential ψ_{out} outside the sphere must have all A_l (coefficients of r^l) equal to zero for $l > 1$, otherwise the potential would diverge as r approaches infinity. Far away from the sphere, the magnetic field due to the sphere is negligible compared to the uniform applied field H_0. The potential must therefore be $\psi_{\text{out}} = -H_0 r \cos\theta$. This corresponds to the r^l term with $l = 1$, with a coefficient of $A_1 = -H_0$. The only other term with a non-zero coefficient is r^{-l-1} with $l = 1$.

The solutions to the Laplace equation for magnetic scalar potential ψ_m are therefore given by

$$\psi_{\text{in}} = A_1 r \cos\theta; \qquad \psi_{\text{out}} = -H_0 r \cos\theta + \frac{A_2 \cos\theta}{r^2}, \qquad (3.19)$$

where A_1 and A_2 are constants.

To calculate the values of the constants A_1 and A_2, we must apply the boundary conditions for magnetic fields at the interface between two different media. **H** parallel to and **B** perpendicular to the sphere's surface must be continuous [55]. The

magnetic field $\mathbf{H}$ is given by

$$\mathbf{H} = -\nabla \psi_m = -\frac{\partial \psi_m}{\partial r} \, \widehat{\mathbf{r}} - \frac{1}{r} \frac{\partial \psi_m}{\partial \theta} \, \widehat{\boldsymbol{\theta}} \tag{3.20}$$

(the $\widehat{\boldsymbol{\phi}}$ term is zero due to azimuthal symmetry). The field $\mathbf{H}_\parallel$ parallel to the boundary is $-(1/r) \; \partial \psi_m / \partial \theta \; \widehat{\boldsymbol{\theta}}$. Since all terms in ψ_{in} and ψ_{out} have the same dependence on $\cos \theta$, this condition is equivalent to requiring that ψ_m be continuous across the boundary. The condition perpendicular to the boundary is $\mathbf{B}_\perp = \mu \mathbf{H}_\perp = -\mu \, \partial \psi_m / \partial r \, \widehat{\mathbf{r}}$, assuming that both media are magnetically linear.

Setting $\psi_{\text{in}} = \psi_{\text{out}}$ at the boundary, where $r = a$, we obtain

$$A_1 a \cos \theta = -H_0 a \cos \theta + \frac{A_2 \cos \theta}{a^2}, \tag{3.21}$$

which simplifies to

$$A_1 a^3 = -H_0 a^3 + A_2. \tag{3.22}$$

The second condition requires that, at $r = a$,

$$\mu_{\text{in}} \frac{\partial \psi_{\text{in}}}{\partial r} = \mu_{\text{out}} \frac{\partial \psi_{\text{out}}}{\partial r}. \tag{3.23}$$

Setting $r = a$ we obtain

$$\mu_{\text{in}} A_1 \cos \theta = -\mu_{\text{out}} H_0 \cos \theta - \mu_{\text{out}} \frac{2A_2 \cos \theta}{a^3}. \tag{3.24}$$

This simplifies to

$$\mu_{\text{in}} a^3 A_1 = -\mu_{\text{out}} a^3 H_0 - 2\mu_{\text{out}} A_2. \tag{3.25}$$

We now have two simultaneous equations to enable us to find the values of A_1 and A_2. From Equations 3.22 and 3.25 we obtain

$$A_1 = \frac{-3\mu_{\text{out}} H_0}{2\mu_{\text{out}} + \mu_{\text{in}}} \tag{3.26}$$

and

$$A_2 = -H_0 a^3 \frac{\mu_{\text{out}} - \mu_{\text{in}}}{2\mu_{\text{out}} + \mu_{\text{in}}}. \tag{3.27}$$

Substituting the two constants A_1 and A_2 into the equations for ψ_{in} and ψ_{out} (Equation 3.19) and rearranging, we obtain the following:

$$\psi_{\text{in}} = \frac{-3\mu_{\text{out}} H_0}{2\mu_{\text{out}} + \mu_{\text{in}}} r \cos \theta; \tag{3.28}$$

$$\psi_{\text{out}} = -H_0 r \cos\theta + \frac{-H_0 a^3 (\mu_{\text{out}} - \mu_{\text{in}})}{2\mu_{\text{out}} + \mu_{\text{in}}} \frac{\cos\theta}{r^2}. \tag{3.29}$$

The potential ψ_{in} reveals that the magnetic field inside the sphere is uniform and vertical. The potential ψ_{out} outside the sphere consists of two terms, one due to the external magnetic field $\mathbf{H}_0$ and one due to the sphere's magnetic moment. We can say $\psi_{\text{out}} = \psi_H + \psi_S$, where $\psi_H = -H_0 r \cos\theta$ from the external field $\mathbf{H}_0$, and ψ_S is given by

$$\psi_S = \frac{-H_0 a^3 (\mu_{\text{out}} - \mu_{\text{in}})}{2\mu_{\text{out}} + \mu_{\text{in}}} \frac{\cos\theta}{r^2}. \tag{3.30}$$

Let the materials inside and outside the sphere have magnetic permeabilities of $\mu_{\text{in}} = \mu_0(1 + \chi_{\text{in}})$ and $\mu_{\text{out}} = \mu_0(1 + \chi_{\text{out}})$, where μ_0 is the permeability of free space and χ is the magnetic susceptibility. Substituting μ_{in} and μ_{out} into the above equation and rearranging, we obtain

$$\psi_S = \frac{-H_0 a^3 (\chi_{\text{out}} - \chi_{\text{in}})}{(3 + 2\chi_{\text{out}} + \chi_{\text{in}})} \frac{\cos\theta}{r^2}. \tag{3.31}$$

For small magnetic susceptibilities ($\chi \ll 1$), we can make the approximation $(3 + 2\chi_{\text{out}} + \chi_{\text{in}}) \approx 3$. The above equation reduces to

$$\psi_S = \frac{-H_0 a^3}{3}(\chi_{\text{out}} - \chi_{\text{in}}) \frac{\cos\theta}{r^2}. \tag{3.32}$$

We now calculate the magnetic field $\mathbf{H}_S$ due to the sphere, using $\mathbf{H}_S = -\nabla\psi_S$:

$$\mathbf{H}_S = -\frac{\partial\psi_S}{\partial r}\widehat{\mathbf{r}} - \frac{1}{r}\frac{\partial\psi_S}{\partial\theta}\widehat{\boldsymbol{\theta}}; \tag{3.33}$$

$$\mathbf{H}_S = -\frac{H_0 a^3 (\chi_{\text{out}} - \chi_{\text{in}})}{3r^3}(2\cos\theta\,\widehat{\mathbf{r}} + \sin\theta\,\widehat{\boldsymbol{\theta}}). \tag{3.34}$$

Substituting $\widehat{\mathbf{d}} = \widehat{\mathbf{r}}\cos\theta - \widehat{\boldsymbol{\theta}}\sin\theta$ and $V = (4/3)\pi a^3$, the above equation can be expressed as

$$\mathbf{H}_S = -\frac{H_0 V}{4\pi r^3}(\chi_{\text{out}} - \chi_{\text{in}})(3\cos\theta\,\widehat{\mathbf{r}} - \widehat{\mathbf{d}}). \tag{3.35}$$

Let us assume that the sphere has a magnetic susceptibility $\chi_{\text{in}} = \chi$, and that the medium surrounding the sphere is non-magnetic ($\chi_{\text{out}} = 0$). The magnetic moment of the sphere is therefore given by $\mathbf{m} = \chi V \mathbf{H}_0$. The magnetic field due to the sphere is therefore

$$\mathbf{H}_S = -\frac{|\mathbf{m}|}{4\pi r^3}\left(\widehat{\mathbf{d}} - 3\cos\theta\,\widehat{\mathbf{r}}\right), \tag{3.36}$$
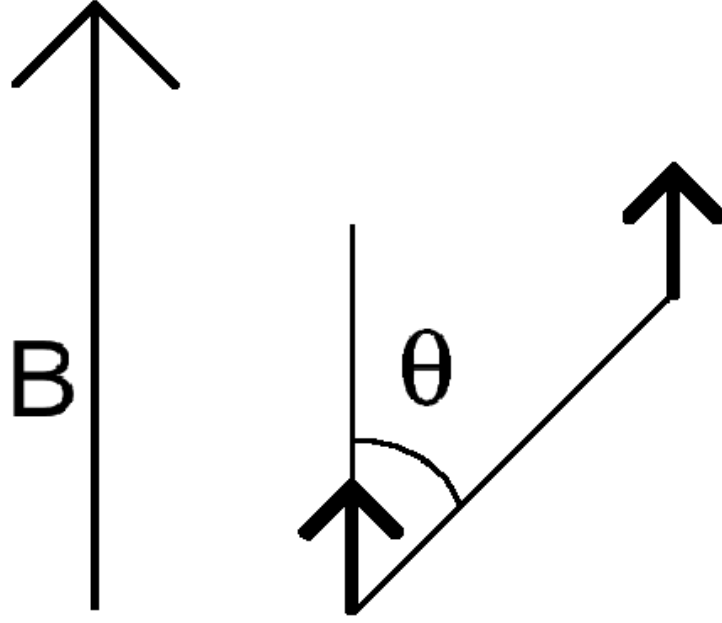
Figure 3.2: *Interaction between two point dipoles*

which is the same as Equation 3.8. This proves that the magnetic field due to a homogeneous sphere is equivalent to that of a point dipole with the same magnetic moment located at the centre of the sphere. The field $\mathbf{H}_S$ derived from the solution of the Laplace equation is exact; the only assumptions made in the analysis are that the sphere is uniformly magnetized, and has a small susceptibility ($|\chi| \ll 1$). The assumption that a dipole has the field described by Equation 3.8, however, is only valid at distances large compared to the size of the dipole.

3.3.4 Interaction of two point dipoles

Now we consider the interaction between two point dipoles. Let one dipole be at the origin, and the other at position $\mathbf{r}$ (see Figure 3.2). Both dipoles are induced by and aligned parallel to a uniform magnetic field $\mathbf{B}$. The angle between the field and $\mathbf{r}$ is θ. The interaction energy is $E = -\mathbf{m} \cdot \mathbf{B}$. The magnetic field $\mathbf{H}_S$ due to the first dipole is given by Equation 3.36. Substituting this into $E = -\mathbf{m} \cdot \mathbf{B}$ and using $\mathbf{B} = \mu_0 \mathbf{H}_S$, we obtain

$$E = -\mathbf{m} \cdot \mathbf{B} = \frac{\mu_0 |\mathbf{m}_1||\mathbf{m}_2|}{4\pi r^3} \left(\widehat{\mathbf{d}}_1 \cdot \widehat{\mathbf{d}}_2 - 3\cos\theta\, \widehat{\mathbf{r}} \cdot \widehat{\mathbf{d}}_2 \right), \tag{3.37}$$

where $|\mathbf{m}_1|$ and $|\mathbf{m}_2|$ are the magnitudes of the magnetic moments of the two dipoles.

Let us assume that the magnetic field is vertical, and the two dipoles have equal magnetic moments $\mathbf{m}_1 = \mathbf{m}_2 = \mathbf{m}$ induced by and aligned with the field. Thus $\widehat{\mathbf{d}}_1 = \widehat{\mathbf{d}}_2 = \widehat{\mathbf{z}}$, a unit vector in the vertical direction, and $\widehat{\mathbf{r}} \cdot \widehat{\mathbf{z}} = \cos\theta$. Substituting these into the above equation, we obtain

$$E = \frac{\mu_0 |\mathbf{m}|^2}{4\pi r^3} \left(1 - 3\cos^2\theta\right). \tag{3.38}$$

The inter-particle force $\mathbf{F}(\theta, r)$ can be found by taking the gradient of the interaction energy E:

$$\mathbf{F} = -\nabla E = -\frac{\partial E}{\partial r}\,\widehat{\mathbf{r}} - \frac{1}{r}\frac{\partial E}{\partial \theta}\,\widehat{\boldsymbol{\theta}}. \tag{3.39}$$

We can therefore calculate the radial and angular components of the interparticle force:

$$F_r = -\frac{\partial E}{\partial r} = \frac{3\mu_0 |\mathbf{m}|^2}{4\pi r^4}(1 - 3\cos^2\theta); \tag{3.40}$$

$$F_\theta = -\frac{1}{r}\frac{\partial E}{\partial \theta} = -\frac{3\mu_0 |\mathbf{m}|^2}{2\pi r^4}\cos\theta\sin\theta. \tag{3.41}$$

By transforming into Cartesian coordinates we obtain the force $\mathbf{F}_{\parallel}$ in the direction of the field $\mathbf{B}$, and the force $\mathbf{F}_{\perp}$ perpendicular to $\mathbf{B}$:

$$F_{\parallel} = \frac{3\mu_0 |\mathbf{m}|^2}{4\pi r^4}\cos\theta(3 - 5\cos^2\theta); \tag{3.42}$$

$$F_{\perp} = \frac{3\mu_0 |\mathbf{m}|^2}{4\pi r^4}\sin\theta(1 - 5\cos^2\theta). \tag{3.43}$$

Now consider two perfect homogeneous spheres with radius a, of a material with magnetic susceptibility $\chi \ll 1$. The magnetic moment is given by $|\mathbf{m}| = \chi V B/\mu_0$, where the volume is $V = (4/3)\pi a^3$. In a uniform field, a sphere will be uniformly magnetized and act as if there were a point dipole at its centre.

Let the two spheres be in contact ($r = 2a$), in a vertical magnetic field. When one particle is vertically above the other ($\theta = 0$), the cohesive force reaches its maximum value of

$$F_v = -\frac{3\mu_0 |\mathbf{m}|^2}{2\pi a^4} = -\frac{\pi\chi^2 B^2 a^2}{6\mu_0}, \tag{3.44}$$

and the particles are attracted to each other. When the particles are in contact and aligned horizontally ($\theta = 90^0$), they repel with the force

$$F_h = \frac{3\mu_0 |\mathbf{m}|^2}{4\pi a^4} = \frac{\pi\chi^2 B^2 a^2}{12\mu_0}. \tag{3.45}$$
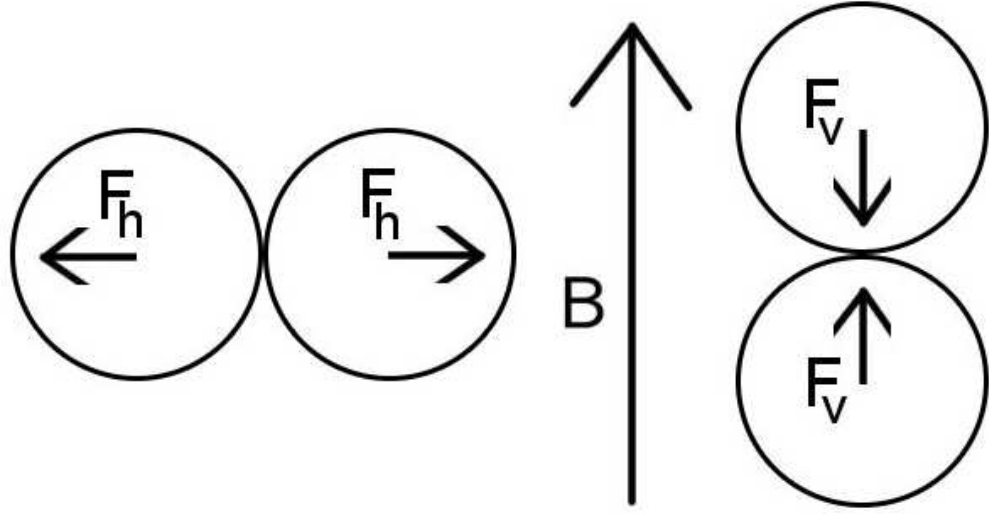
Figure 3.3: *The magnetic dipole-dipole force is anisotropic.*

This is half the magnitude and the opposite sign to F_v. See Figure 3.3 for an illustration.

3.3.5 Definition of the cohesion parameter R

We quantify the strength of magnetic interactions by introducing a cohesion parameter R, defined as the ratio of the maximum cohesive force F_v to the particle weight. For non-cohesive particles, $R = 0$. When $R = 1$, the cohesive force on a particle is equal to its weight. Thus when $R > 1$, a particle can be magnetically suspended from another.

Dividing F_v (equation 3.44) by the particle weight $\rho V g$ (where ρ is density), the ratio of inter-particle force to weight can be expressed as

$$R = \frac{F_v}{\rho V g} = \frac{\chi^2 B^2}{4\mu_0 d\rho g},$$
(3.46)

where $d = 2a$ is the particle diameter.

It is interesting to note the dependence of R on $1/d$, suggesting that fine particles are more susceptible to magnetic cohesion.

3.4   Analytical calculations

In this section we describe analytical and numerical calculations of the forces between magnetic dipoles in order to gain a deeper understanding of the magnetic cancellation effect. Various geometries are considered, in both two and three dimensions.

We calculate the force acting on a point dipole due to an infinite horizontal sheet of magnetizable material. Dipole moments are assumed to be induced parallel to an applied magnetic field in the vertical direction, perpendicular to the sheet. The dipole experiences an attractive force due to material in the plane underneath it, and a repulsive force due to material farther away. The attractive and repulsive forces counteract each other, resulting in a net force of zero. This interesting result demonstrates perfect magnetic cancellation; there is no magnetic interaction between a particle and an infinite plane in an external magnetic field.

We then carry out numerical calculations of the force acting on a point dipole positioned above a single horizontal layer of point dipoles arranged in a regular lattice. Again, a uniform magnetic field is applied in the vertical direction, and all point dipoles are assumed to be induced by and aligned with the applied magnetic field. The attraction of the point dipole to particles directly underneath is partially cancelled by the repulsion due to particles further away. Though there are more of the latter, they are farther away and thus have less of an influence. Although the cancellation effect is still present in a discrete lattice of point dipoles, only partial cancellation is achieved rather than the complete cancellation exhibited by a continuous plane. Still, the net force experienced by a dipole due to a layer of point dipoles is significantly smaller than the force between two particles in isolation.

The force on a particle in a granular bed has a sensitive dependence on the arrangement of its nearest neighbours, but is less sensitive to the positions of more distant particles. The magnetic dipole-dipole force is dominated by nearest-neighbour interactions, as the magnitude of the force decays as $1/r^4$.
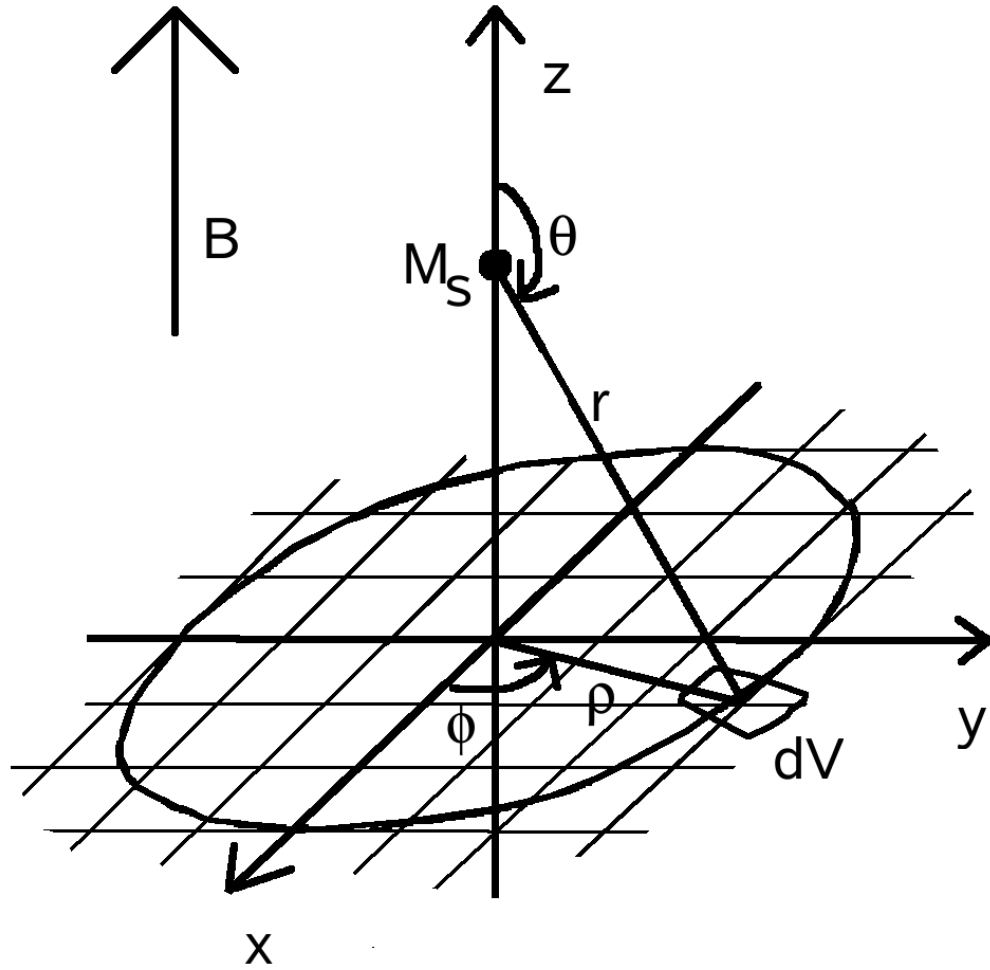
Figure 3.4: *Diagram showing a dipole and an infinite sheet of thickness h in a uniform external field*

3.4.1 Force between dipole and horizontal sheet

Consider a sphere positioned at a vertical distance z above a thin horizontal infinite sheet of thickness h. Both sheet and sphere are made of the same magnetizable material. An external magnetic field B is applied in the vertical direction (along the z-axis), perpendicular to the plane of the thin sheet. We treat the sphere as a point dipole, with a magnetic dipole moment induced by and parallel to the external magnetic field. See Section 3.3.3 for a proof that a homogeneous magnetic sphere in a uniform magnetic field acts as a point dipole. The total force on the sphere due to the sheet can be calculated by dividing the sheet into infinitesimally small volume

elements. We treat each of these volume elements as a point dipole, and sum the force on the sphere due to all of these elements. See Figure 3.4.

The horizontal force is zero due to symmetry about the z-axis, so we calculate only the component of the force in the vertical direction.

Recall the equation for $F_\parallel$ (Equation 3.42), the component of the magnetic force between two point dipoles in the direction of a uniform magnetic field:

$$F_\parallel = \frac{3\mu_0|\mathbf{m}|^2}{4\pi r^4}\cos\theta\,(3 - 5\cos^2\theta). \tag{3.47}$$

We assume that the magnetic field $\mathbf{B}$ is applied in the vertical direction (along the z-axis). θ is the angle between the vertical and the separation $\mathbf{r}$ of the two point dipoles. This equation demonstrates the highly anisotropic nature of the magnetic dipole-dipole force: when the factor $\cos\theta(3-5\cos^2\theta)$ is positive the vertical component of the force between two dipoles is positive (repulsive); when $\cos\theta\,(3 - 5\cos^2\theta)$ is negative the vertical component of the force is negative (attractive). The critical angle θ_c at which the vertical force is equal to zero is $\theta_c = \cos^{-1}(-\sqrt{3/5}) = 140.8°$.

We calculate the magnetic force on the dipole due to the thin sheet by summing the contributions from infinitesimally small volume elements. Each element has volume $dV = h\rho d\rho d\phi$, where ρ is the distance between the volume element and the point on the plane directly below the dipole, and ϕ is the azimuthal angle in the plane perpendicular to $\mathbf{B}$. Thus the vertical force on the point dipole due to one volume element at distance r and angle θ is given by

$$dF_z(r) = \frac{3\mu_0 m_s dm}{4\pi r^4}\cos\theta(3 - 5\cos^2\theta), \tag{3.48}$$

where the magnetic moment of the point dipole is m_s. The magnetic moment dm of a volume element is given by

$$dm = \frac{\chi B dV}{\mu_0} = \frac{\chi B h\rho d\rho d\phi}{\mu_0}. \tag{3.49}$$

We integrate to obtain the total vertical force on the particle due to the thin sheet:

$$F_z = \frac{3\chi B m_s h}{4\pi}\int_0^{2\pi}\int_{\rho=0}^{\infty}\left[\frac{\cos\theta(3 - 5\cos^2\theta)\rho d\rho d\phi}{r^4}\right]. \tag{3.50}$$

Integrating over ϕ gives a factor of 2π. By substituting $\cos\theta = -z/r$ and $r^2 = z^2 + \rho^2$, we obtain the vertical force

$$F_z = \frac{3\chi B m_s h}{2} \int_{\rho=0}^{\infty} -3z\rho(z^2 + \rho^2)^{-\frac{5}{2}} + 5z^3\rho(z^2 + \rho^2)^{-\frac{7}{2}} d\rho. \qquad (3.51)$$

Evaluating the integral gives

$$F_z = \frac{3}{2}\chi B m_s h \left[z(z^2 + \rho^2)^{-\frac{3}{2}} - z^3(z^2 + \rho^2)^{-\frac{5}{2}} \right]_{\rho=0}^{\rho=\infty} = 0. \qquad (3.52)$$

This interesting result demonstrates that there is no interaction between a particle and an infinite thin sheet in an external magnetic field. The contributions to the vertical force from volume elements add up to zero. The attraction of the point dipole in the vertical direction to material directly underneath (with $\theta > 140.8°$) is exactly balanced by the repulsion due to material further away (with $\theta < 140.8°$). Although there is more of the latter, it is farther away and thus has less of an influence.

Now imagine taking an infinite number of infinitely thin sheets of magnetizable material, and stacking them vertically. The resulting shape is a semi-infinite half-space. In the presence of a uniform vertical magnetic field, a point dipole above the half-space will experience zero net force.

3.4.2 Interaction of two spheres

The perfect cancellation of the magnetic force on a dipole due to an infinite half-space can be understood by considering two uniformly magnetizable spheres of radii r_1 and r_2. The first is at the origin, and the second sphere's centre is at $z = h + r_2$. The closest surfaces of the two spheres are separated by a distance $h - r_1$. In the presence of a uniform magnetic field B in the z-direction, the force between the spheres is given by

$$F_v = -\frac{3\chi^2 B^2 V_1 V_2}{2\pi\mu_0 r^4}. \qquad (3.53)$$

Substituting the distance $r = h + r_2$ and volumes $V_1 = (4/3)\pi r_1^3$ and $V_2 = (4/3)\pi r_2^3$ in this equation gives

$$F_v = \frac{8\pi\chi^2 B^2}{3\mu_0} \frac{r_1^3 r_2^3}{(h + r_2)^4}. \qquad (3.54)$$

Now imagine increasing the radius r_2 of the upper sphere, while keeping its lower surface at the position $z = h$. As the radius of curvature increases, the sphere's upper surface becomes flatter until in the limit $r_2 \to \infty$, the surface is perfectly horizontal. We now have a sphere separated from a uniformly magnetizable half-space. As r_2 increases, we can make the approximation $h + r_2 \approx r_2$:

$$F_v = \frac{8\pi\chi^2 B^2}{3\mu_0} \frac{r_1^3}{r_2}. \tag{3.55}$$

In the limit $r_2 \to \infty$, the vertical force F_v is zero, as previously demonstrated by integration.

Similarly, we can calculate the horizontal magnetic force between a point dipole and a half-space filled with magnetizable material in a vertical magnetic field. Consider a sphere of radius r_1 at the origin, and another sphere of radius r_2 centred on the x-axis at the position $x = h + r_2$. The magnetic force on the first sphere is

$$F_h = \frac{3\chi^2 B^2 V_1 V_2}{4\pi\mu_0 r^4}. \tag{3.56}$$

The separation of the two spheres is $r = h + r_2$. Substituting this, and the volumes $V_1 = (4/3)\pi r_1^3$ and $V_2 = (4/3)\pi r_2^3$ into the above equation gives

$$F_h = \frac{4\pi\chi^2 B^2}{3\mu_0} \frac{r_1^3 r_2^3}{(h + r_2)^4}. \tag{3.57}$$

Again, we allow the second sphere's radius to increase, keeping its surface crossing the x-axis at $x = h$. As r_2 tends to infinity, the surface becomes flatter and the sphere tends to the half-space with $x > h$. We can make the approximation $h + r_2 \approx r_2$, and F_h tends to zero.

3.4.3   Force between a dipole and an infinite rod

Now we shall consider a similar situation, but in two dimensions rather than three. Consider a magnetizable sphere situated a vertical distance h above an infinitely long horizontal rod (see Figure 3.5). In the presence of a vertical uniform magnetic field the sphere can be treated as a point dipole, magnetized in the direction of the field. The rod has a cross-sectional area A and is made of the same magnetizable material as the sphere.
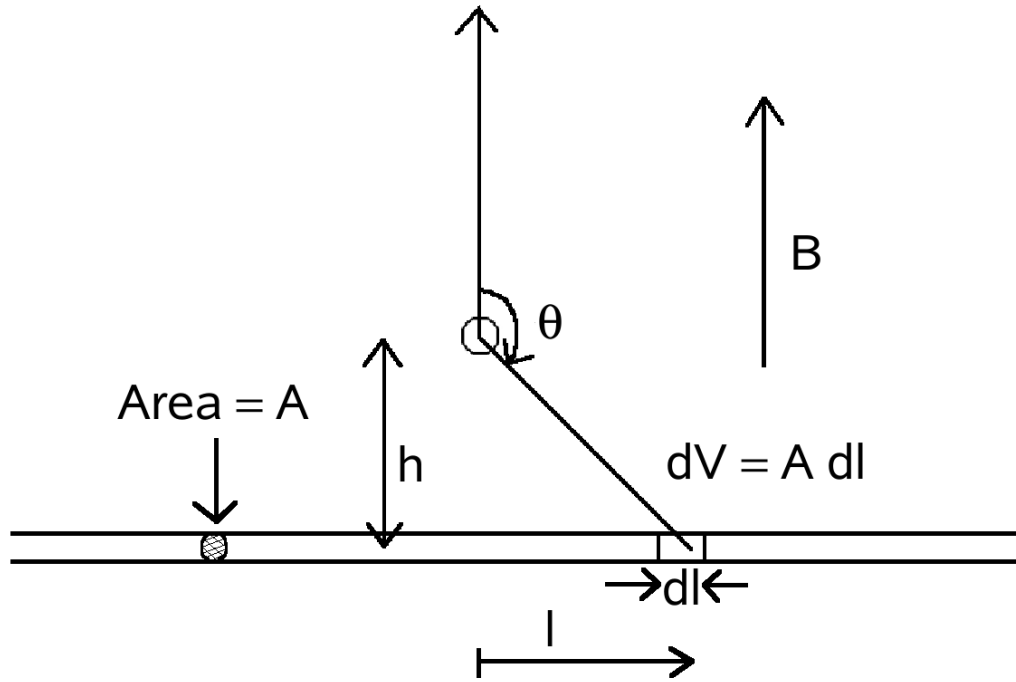
Figure 3.5: *Diagram showing a dipole and an infinitely long rod in a uniform external field*

As in the case of a dipole above an infinite horizontal sheet, we calculate the total force on the point dipole due to the rod by dividing its length into infinitesimally small volume elements. We treat each volume element as a point dipole, and sum the force on the sphere due to all of these elements. Again, horizontal forces will be zero due to symmetry, so we calculate only the component of the force in the vertical direction.

The vertical force between two point dipoles of moments m_1 and m_2 separated by a distance r is given by

$$F_v = \frac{3\mu_0 m_1 m_2}{4\pi r^4} \cos\theta (3 - 5\cos^2\theta). \tag{3.58}$$

Each element of the rod has volume $dV = Adl$, where dl is the length of the element. The point dipole has magnetic moment m_s, and the magnetic moment of a volume element is $dm = \chi B dV/\mu_0$. The force on the point dipole due to a volume element at position (r, θ) is given by

$$dF_z(l) = \frac{3\mu_0 m_s \chi B \cos\theta\, (3 - 5\cos^2\theta) Adl}{4\pi\mu_0 r^4}. \tag{3.59}$$

We define l as the distance between the volume element and the point on the rod directly below the sphere. Since $l = -h\tan\theta$, the length element is $dl = -h\sec^2\theta d\theta$. Substituting this and $r = -z/\cos\theta$, we obtain

$$dF_z(\theta) = -\frac{3m_s\chi B}{4\pi} \cdot \frac{\cos^4\theta\,(3 - 5\cos^2\theta)}{h^4} \cdot Ah\sec^2\theta d\theta. \tag{3.60}$$

Using the identity $\cos^2\theta = (1/2)(1 + \cos 2\theta)$ and rearranging gives

$$dF_z(\theta) = -\frac{3m_s\chi BA}{4\pi h^3}\left(-\frac{3}{8} - \cos 2\theta - \frac{5}{8}\cos 4\theta\right)d\theta. \tag{3.61}$$

After integrating over θ in the range $\pi/2 < \theta < 3\pi/2$ and evaluating the integral, we obtain the vertical component of the force on the point dipole

$$F_z = -\frac{9m_s\chi BA}{32h^3}. \tag{3.62}$$

The vertical force on the dipole is not zero; there is a net attraction between the dipole and the line. This clearly demonstrates that cases of an infinite rod and an infinite sheet are very different. In the case of the rod, there is less material further away from the dipole with θ smaller than the critical angle of 140.8°. The resulting repulsion is not sufficient to counteract the attraction of the dipole to material directly underneath with $\theta > \theta_c$, so the net force is attractive.

3.4.4 Horizontal force between a dipole and an infinite half-space

Consider a point dipole at the origin, subject to a uniform magnetic field B in the z direction. The dipole is at the centre of a sphere of radius a. The infinite half-space with $y > 0$ outside the sphere is filled with a homogeneous magnetic material of density ρ and susceptibility χ. We calculate the magnetic force acting on the dipole by summing the contributions from each volume element, assuming that each volume element acts as a point dipole aligned with the magnetic field. The volume of each element is $dV = r^2\sin\theta dr d\theta d\phi$, where r is the distance between the volume element and the dipole, θ is the angle between $\mathbf{r}$ and the z-axis, and ϕ is the azimuthal angle. The domain occupied by magnetic material can therefore be expressed as $\{a \leq r < \infty; 0 \leq \theta < \pi; 0 \leq \phi < \pi\}$.

The total magnetic force acting on the dipole will be in the y direction; x and z components cancel due to symmetry.

Recall the equation for F_h, the horizontal component of the magnetic force between two dipoles in a uniform vertical magnetic field:

$$F_h = \frac{3\mu_0 |\mathbf{m}|^2}{4\pi r^4} \sin\theta \, (1 - 5\cos^2\theta). \tag{3.63}$$

When the factor $\sin\theta \, (1 - 5\cos^2\theta)$ is positive, the horizontal component of the force between two dipoles is positive (repulsive), and when $\sin\theta \, (1 - 5\cos^2\theta)$ is negative, the horizontal component of the force is negative (attractive). The critical angle θ_c at which the horizontal force is equal to zero is $\theta_c = \cos^{-1}(\pm\sqrt{1/5})$, i.e. $54.2°$ or $125.8°$. This is different from the critical angle of $140.8°$ at which the vertical force is zero.

The force in the y direction on the point dipole due to one volume element at position (r,θ,ϕ) is given by

$$dF_y(r) = \frac{3\mu_0 m_s dm}{4\pi r^4} \sin\theta \, (1 - 5\cos^2\theta) \sin\phi, \tag{3.64}$$

where the magnetic moment of the point dipole is m_s. The factor $\sin\phi$ ensures that only the y component of the horizontal force is calculated. The magnetic moment dm of a volume element is given by

$$dm = \frac{\chi B dV}{\mu_0} = \frac{\chi B r^2 \sin\theta dr d\theta d\phi}{\mu_0}. \tag{3.65}$$

We integrate to obtain the total force F_y on the dipole in the y direction:

$$F_y = \frac{3\chi B m_s}{4\pi} \int_{\phi=0}^{\pi} \int_{\theta=0}^{\pi} \int_{r=a}^{\infty} \frac{\sin^2\theta \, (1 - 5\cos^2\theta)}{r^4} \sin\phi \, r^2 dr d\theta d\phi. \tag{3.66}$$

This integral is separable into ϕ, θ and r integrals that can be treated separately and evaluated:

$$\int_{\phi=0}^{\pi} \sin\phi \, d\phi = 2; \tag{3.67}$$

$$\int_{\theta=0}^{\pi} \sin^2\theta \, (1 - 5\cos^2\theta) d\theta = -\frac{1}{8}\pi; \tag{3.68}$$

$$\int_{r=a}^{\infty} -\frac{dr}{r^2} = \frac{1}{a}. \tag{3.69}$$

Substituting these results, we obtain

$$F_y = -\frac{3\chi B m_s}{16a}. \tag{3.70}$$

Recall that the maximum cohesive force between two particles of radius a, when in contact and aligned with the magnetic field, is $F_v = \pi \chi^2 B^2 a^2 / 6\mu_0$. We can now express F_y in terms of F_v. Substituting the dipole's magnetic moment $m_s = \chi V B / \mu_0$ and the volume $V = (4/3)\pi a^3$, we obtain

$$F_y = -1.5 F_v. \tag{3.71}$$

Note that this force is negative, indicating that the dipole is attracted towards the magnetic material. This seems counter-intuitive because dipoles are repelled in the direction perpendicular to the field. We demonstrated in Section 3.4.1 that the horizontal magnetic force between a point dipole and an infinite half-space is zero. The domain $y > 0$ is an infinite half-space, therefore the horizontal magnetic force must be due to the domain $\{0 < y < a; r > a\}$. There is a lot of material with θ less than the critical angle of $54.2°$ (or greater than $125.8°$), and the attraction of the dipole to this material is greater than the repulsion to material with $54.2° < \theta < 125.8°$.

3.5 Direct measurements of magnetic dipole-dipole forces

In this section we describe a series of experiments with magnetine beads (of mean diameter 3.16 mm), in which we directly measured the magnetic dipole-dipole forces between individual beads. We first describe the 16.5T superconducting magnet used in the experiments, and then describe our experimental techniques. We observed the magnetic cancellation effect by measuring the force between a bead and a layer of beads arranged in a regular pattern. We calculated the forces using Equation 3.42, and compared the calculations to our experimental results.
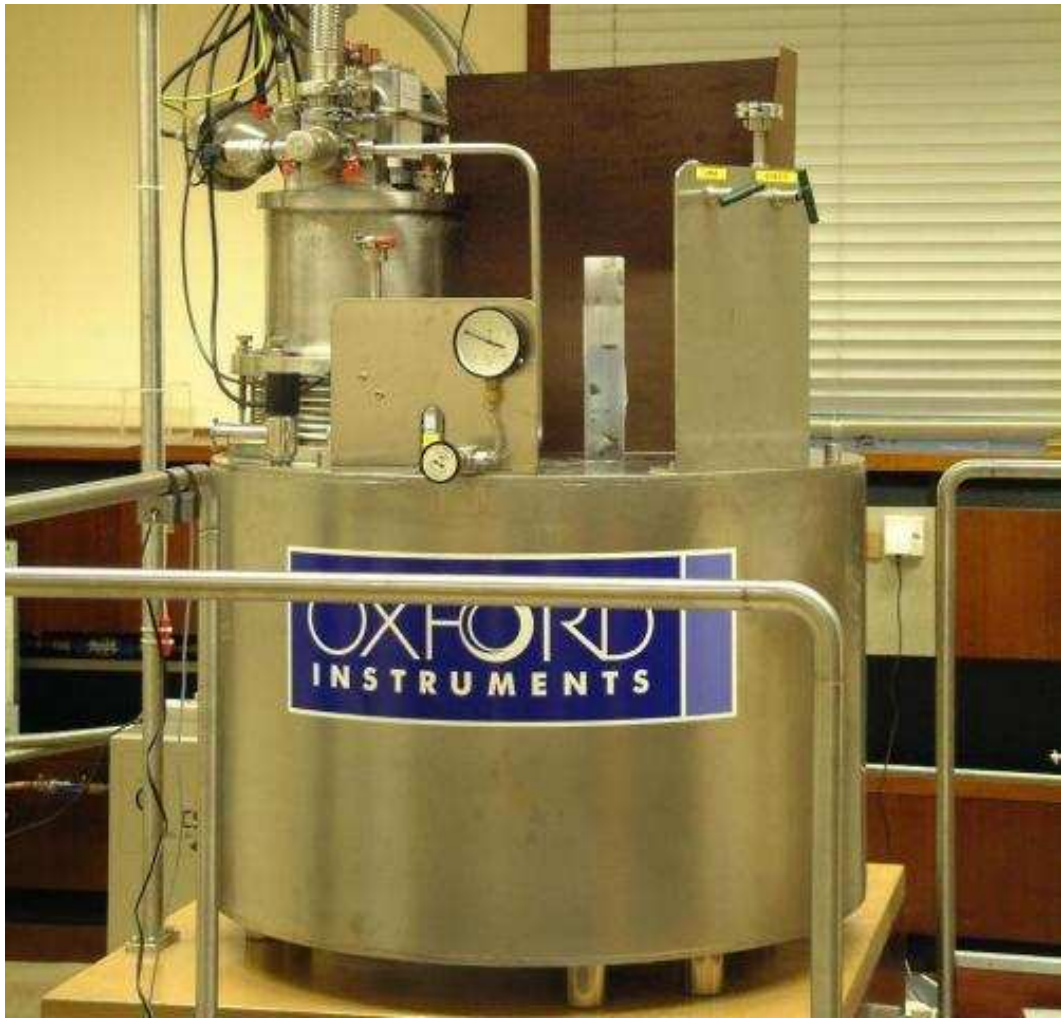
Figure 3.6: *16.5T superconducting magnet*

3.5.1   16.5T superconducting magnet

We carried out our experiments using a 16.5T helium-cooled superconducting levitation magnet, designed by Oxford Instruments (see Figure 3.6). The magnetic field was produced by a large solenoid. The coil was superconducting, allowing the current to persist for long periods of time while the magnet was not connected to an external power supply. Cooling was provided by closed-cycle cryogenics, avoiding the necessity of refilling the liquid helium. The coil was surrounded by a vacuum chamber to insulate it from the surroundings, and keep the temperature low.

When the magnet was in persistent mode, the coil was a closed circuit through which a persistent current flowed. The external power supply could be switched off,

and the magnetic field remained at the same strength.

To ramp the field strength up or down, the external power supply must be connected to the coil. The switch was a heater that made a small section of the coil resistive rather than superconducting. This caused the current to flow through the power leads, which had a lower resistance than the segment of the coil affected by the heater. The current in the power supply must be the same as the current in the coil before the heater could be switched on. When the magnet coil was connected to the power supply, the current could be ramped up or down to change the magnetic field.

Figure 3.7 shows the field profile of the magnet. The field was strongest at the centre, but quickly dropped to a few Tesla at the top of the magnet bore. Figure 3.8 shows the field-field gradient product $|BdB/dz|$ plotted as a function of the vertical distance z from the centre of the magnet, at a central field strength of $B = 16.5$ Tesla. Note that $|BdB/dz|$ is negative for $z > 0$. The maximum value of $|BdB/dz|$ at 16.5 Tesla was 1385 $T^2 m^{-1}$; this is sufficient to levitate water. See Appendix A for a brief review of diamagnetic levitation.

3.5.2   Experimental details

For these experiments, we used paramagnetic magnetine beads containing iron oxide (Fe_2O_3). The beads were approximately spherical, but with slight variations in shape and size, and a small hole through the centre. To see whether these factors were significant, we compared a sample of ten beads. The beads had a mean diameter of 3.16 mm, with a standard deviation of 0.05 mm (1.6% of the mean).

Figure 3.9 is a diagram of the experimental apparatus. We suspended one bead on a light inextensible string (a fishing line) attached to a plastic frame. The frame rested on a sensitive balance on a bracket attached to the ceiling. We attached a (non-magnetic) lead weight to the the string, to ensure that it hung vertically. The bead was positioned above the bore of the superconducting magnet, on the vertical axis. The magnetic field on the axis was vertical, increasing in strength closer to the magnet. The central field strrength was set to 16.5 Tesla. Paramagnetic objects are attracted to regions of high field strength, so the suspended bead centred itself

Figure 3.7: *Axial magnetic field B as a function of vertical position z from the centre of the magnet, at a central field strength of $B = 16.5$ Tesla. The first vertical line at $z = 7.3$ cm is the position of maximum $|BdB/dz|$, and the second vertical line at $z = 18.8$ cm is the top of the magnet bore.*
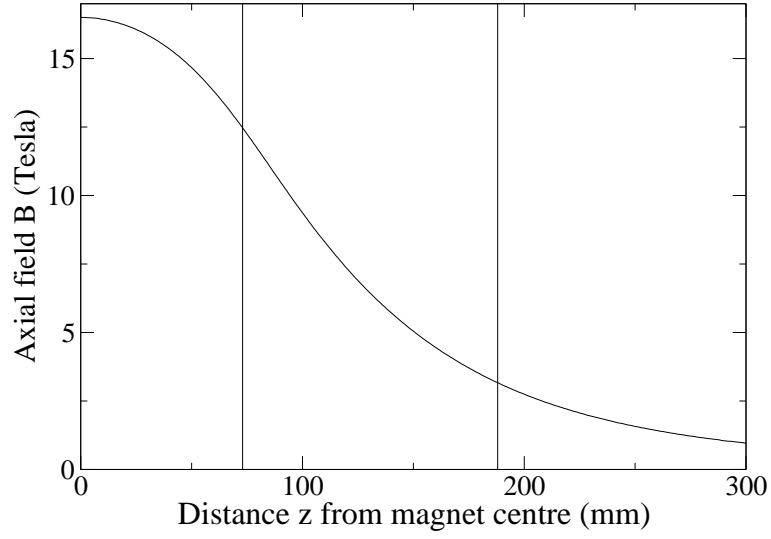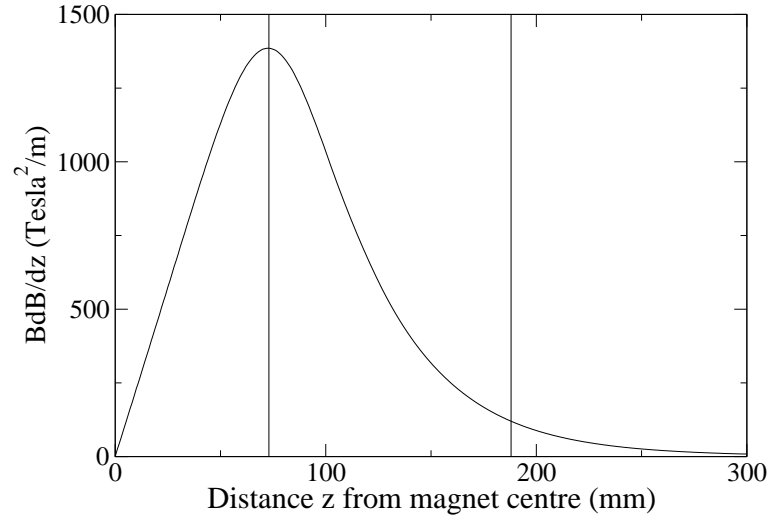

Figure 3.8: *Field-field gradient product $|BdB/dz|$ as a function of vertical position z from the centre of the magnet, for a central field strength of $B = 16.5$ Tesla. The first vertical line at $z = 7.3$ cm is the position of maximum $|BdB/dz|$, and the second vertical line at $z = 18.8$ cm is the top of the magnet bore.*
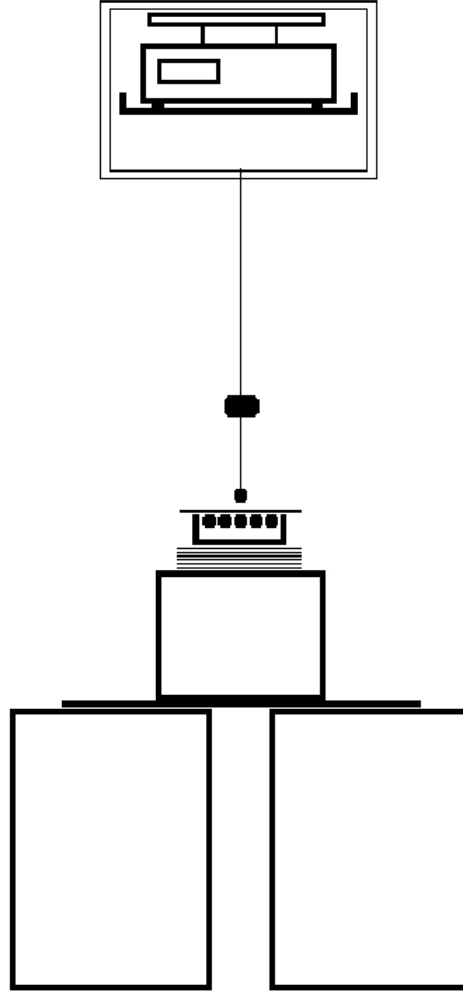
Figure 3.9: *Diagram of the experimental set-up for measurements of dipole-dipole forces between paramagnetic magnetine beads*

on the axis.

There was a magnetization force on the beads due to the field gradient, as well as the magnetic dipole-dipole interactions. The paramagnetic beads were attracted down into the bore of the magnet where the field was stronger. We suspended one bead at a height of 10 cm above the top of the magnet bore (28.8 cm above the maximum field position). We tared the balance to read zero in the absence of other beads, and kept the suspended bead at the same height. The reading on the balance was therefore entirely due to the additional magnetic dipole-dipole force.

A second bead, or layer of beads, was attached to the underside of a thin glass microscope slide with double-sided adhesive tape. The slide was supported at the
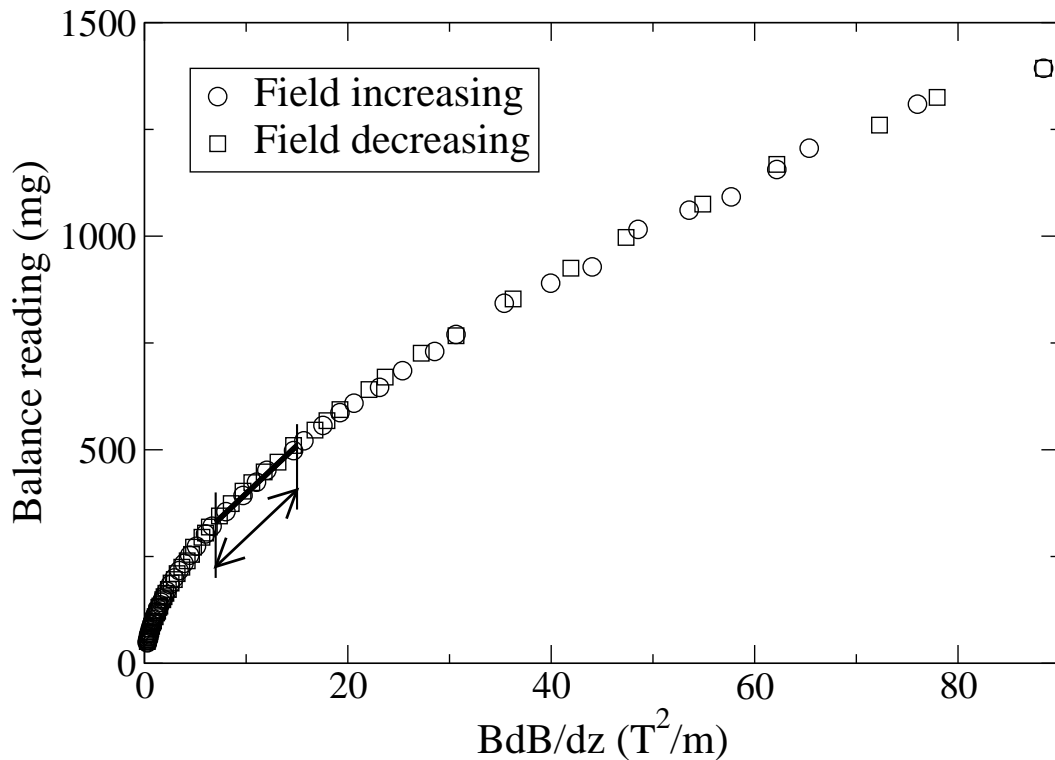
Figure 3.10: *Calibration graph to calculate the magnetic moment of magnetine beads. The solid line is a straight line fit to the curve in the region $z = 28.8$ cm.*

edges by two other slides on top of a petri dish. The height of the dish (and therefore the separation between the beads) could be varied by using more slides (of width 0.15 mm) as spacers underneath the dish.

3.5.3   Measurement of bead magnetic moment

The beads are not magnetically linear, so it was necessary to calculate the magnetic moment as a function of field strength. We measured the magnetization force on a suspended bead as a function of its height z above the centre of the magnet, from the top of the magnet up to 30 cm above the magnet bore. The balance was tared to read zero when the bead was far away from the magnet (suspended on a very short string). We lengthened the string slowly, and as the bead approached the magnet the field B and the magnetization force increased.

Figure 3.10 shows the magnetization force plotted as a function of the product BdB/dz of the magnetic field and field gradient. We took the measurements with

z increasing and decreasing, to determine whether there were any hysteresis effects due to the bead retaining magnetization. No such effects were found; the direction made no difference to the readings of the magnetization force. The graph shows that the magnetic moment of the bead was starting to saturate. For a magnetically linear material with a constant susceptibility χ, the graph would be a straight line. Over a small range of height z centred around the position of the bead at $z = 28.8$ cm, we can approximate the graph as linear. The magnetization force is described by a linear fit (marked on Figure 3.10 as a solid line):

$$F_m = a_0 + a_1 B \frac{dB}{dz} \tag{3.72}$$

near $z = 28.8$ cm, where a_0 and a_1 are constants to be determined graphically.

The magnetization force F_m is given by the gradient of the magnetic energy $E = -\mathbf{m} \cdot \mathbf{B}$. We consider only the force in the z-direction; on axis the radial forces are zero. Assuming that the magnetic moment is constant over a small range of height z (over 3 mm, the magnetic field changes by 2.8%), we can take $\mathbf{m}$ outside the differential:

$$F_m = -\frac{dE}{dz} = \mathbf{m} \cdot \frac{d\mathbf{B}}{dz}. \tag{3.73}$$

The magnetic moment $\mathbf{m}$ and the field $\mathbf{B}$ are both in the vertical direction. Equating Equations 3.72 and 3.73 and rearranging, we obtain

$$|\mathbf{m}| = \frac{a_0}{dB/dz} + a_1 B. \tag{3.74}$$

Thus we can calculate the magnetic moment of the bead using the constants a_0 and a_1 from the graph. The values obtained were $a_0 = 0.00147$ and $a_1 = 0.000204$.

We measured the magnetic moment of ten beads using the technique described above. The mean magnetic moment was $3.62 \times 10^{-4} \mathrm{JT}^{-1}$, and the standard deviation 1.28×10^{-5} JT^{-1} (3.6% of the mean). At $z = 28.8$ cm and a central field of 16.5 Tesla, this moment corresponds to a susceptibility of $\chi = 0.026$. We also measured the magnetic moment of one bead in two orientations: with the hole vertical (parallel to the magnetic field); and with the hole horizontal (perpendicular to the magnetic field). The two measurements of magnetic moment varied by only 0.1%, demonstrating that the presence of a hole in the bead made negligible difference to the magnetic forces acting on it.
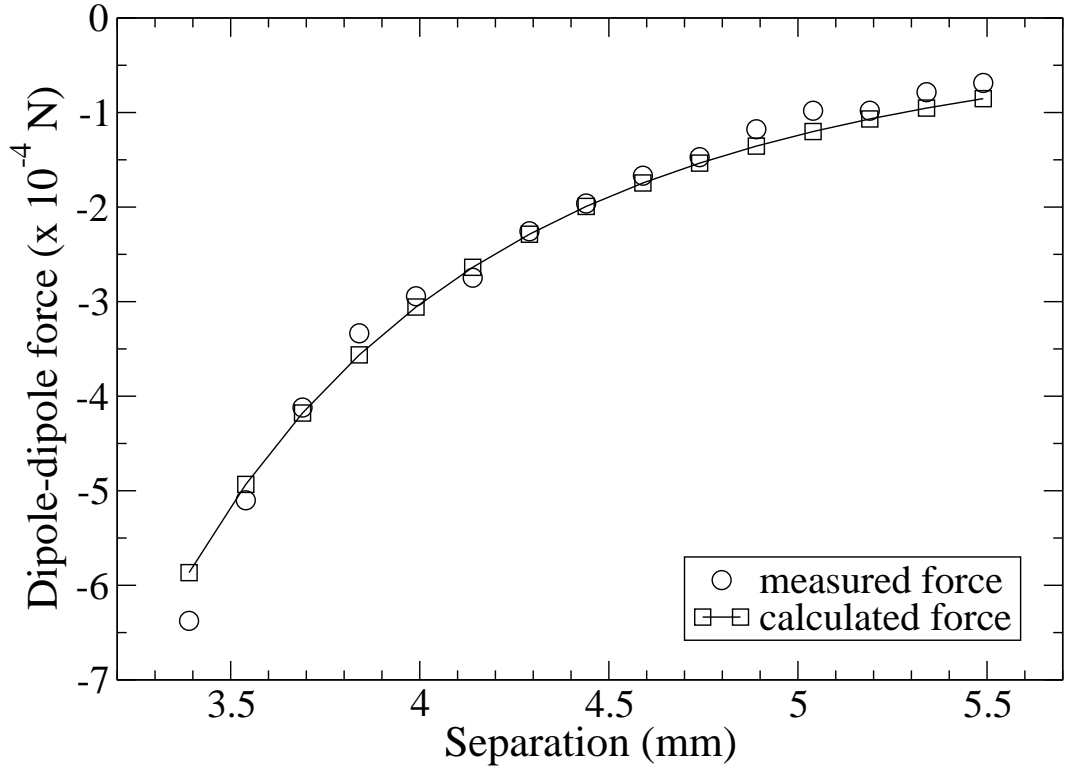
Figure 3.11: *Magnetic dipole-dipole force between two magnetine beads as a function of their separation. Bead diameter = 3.16 mm.*

3.5.4 Measurements of the force between two beads

To measure the magnetic dipole-dipole force between two beads, we suspended one bead at a position of 10 cm above the magnet bore ($z = 28.8$ cm), and tared the balance to read zero. We then placed another bead underneath and recorded the reading on the balance as a function of the separation of the two beads.

Figure 3.11 shows the magnetic dipole-dipole force between two beads plotted as a function of separation. As well as the experimental measurements of the force, we calculated the force assuming that the two beads were point dipoles. Equation 3.42 describes the interaction of two point dipoles. In a vertical magnetic field, with two vertically-aligned particles ($\theta=0$), the force is

$$F = -\frac{3\mu_0 m_1 m_2}{2\pi r^4}, \tag{3.75}$$

where m_1 and m_2 are the magnitudes of the magnetic moments of the beads, and r is their separation. We compared these calculations to our experimental measurements, and found very good agreement. This result confirms that the beads are
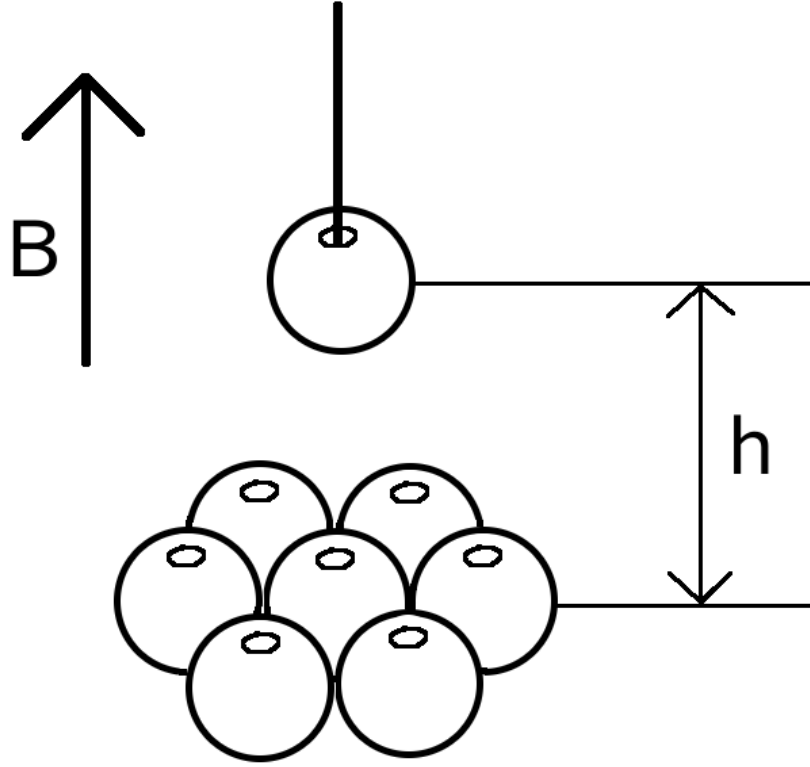
Figure 3.12: *One magnetine bead was suspended above a hexagon comprising seven beads, in a vertical magnetic field.*

behaving as point dipoles.

3.5.5 Measurements of the force between a bead and a layer

Having confirmed that our magnetine beads do act like point dipoles, we were able to measure the magnetic force between a bead and a collection of beads. We formed a close-packed hexagon shape of beads in the horizontal plane, and suspended another bead directly above the central bead in the hexagon (Figure 3.12). As well as measuring the dipole-dipole force experimentally, we calculated the force on the suspended bead by summing the contributions from each of the beads in the hexagon. This calculated force was in the vertical direction, as the horizontal component cancelled out due to symmetry. We were therefore able to directly compare the calculated force with our experimental measurements.

We denote the number of rings of beads in the hexagon by l (see Figure 3.13 for an illustration). A single bead was a hexagon with $l = 0$. A 7-bead hexagon,

Figure 3.13: *The magnetine beads formed a hexagon shape, with l rings of beads around a central bead.*

formed by placing a ring of beads around the central bead, had $l = 1$. We then added a second ring of beads around the edge of the 7-bead hexagon, forming a larger hexagon with $l = 2$ (19 beads). Adding a third ring around the $l = 2$ hexagon produced an even larger hexagon of 37 beads and $l = 3$. A hexagon of order l has a side length of $l + 1$ and a total of $3l(l + 1) + 1$ beads.
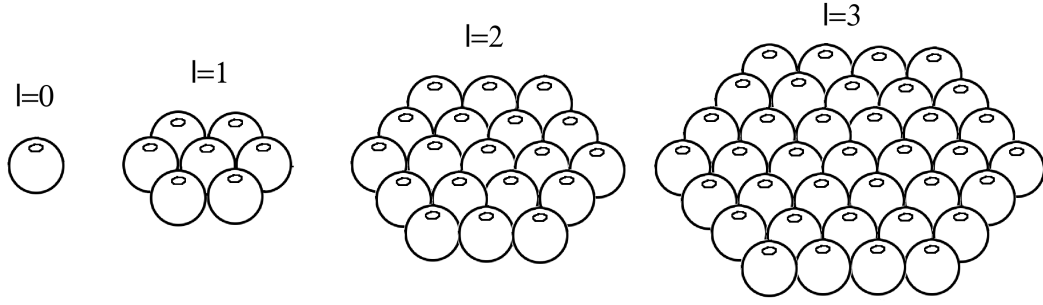
The field had radial components away from the axis, but these were not very large. At $z = 28.8$ cm, the radial magnetic field 3 mm (one bead diameter) from the axis was 1.43% of the vertical field. The largest hexagon we used was $l = 3$, so the beads at the edge of the hexagon were at most 3 bead diameters from the axis. At 9 mm from the axis, the radial magnetic field was 4.30% of the vertical field. We therefore assumed that the field is vertical and that radial forces were negligible.

Figure 3.14 shows the dipole-dipole force between the suspended bead and the $l = 1$ hexagon with 7 beads, plotted as a function of the vertical separation z. There was good agreement between the experimental measurements and the calculations. The forces were smaller than for two beads, demonstrating that magnetic cancellation occurred. The suspended bead was vertically repelled from the beads around the edge of the hexagon, and this repulsion partially balanced the attraction to the central bead.

Recall the equation for the vertical component of the magnetic dipole-dipole force between two particles in a vertical field:

$$F_v = \frac{3\mu_0 |\mathbf{m}|^2}{4\pi r^4} \cos\theta \, (3 - 5\cos^2\theta). \tag{3.76}$$

There is a critical angle $\theta_c = \cos^{-1}(-\sqrt{3/5}) = 140.8°$. At this angle, the factor
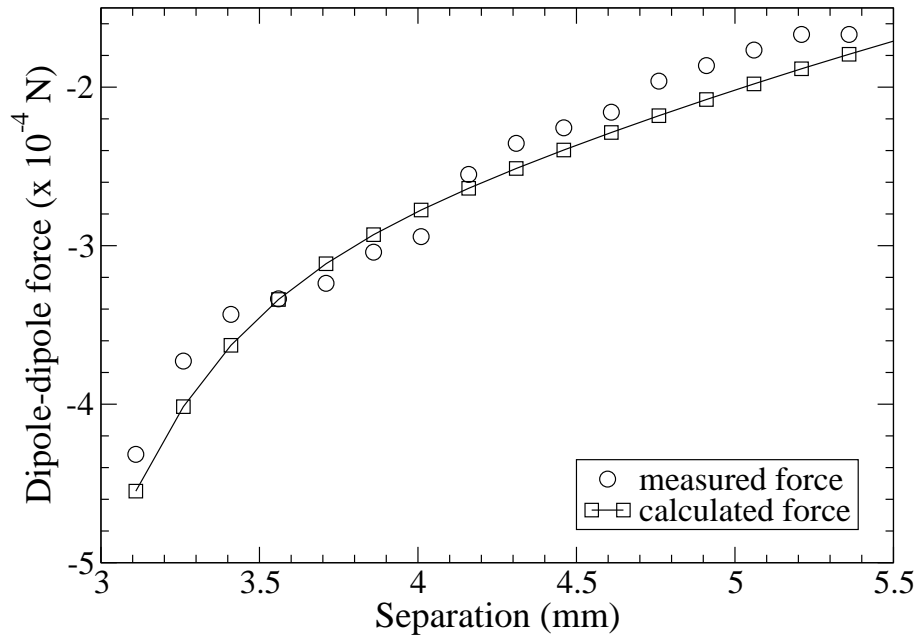
Figure 3.14: *Magnetic dipole-dipole force between a magnetine bead and a hexagon comprising seven beads, as a function of their separation. Bead diameter = 3.16 mm.*

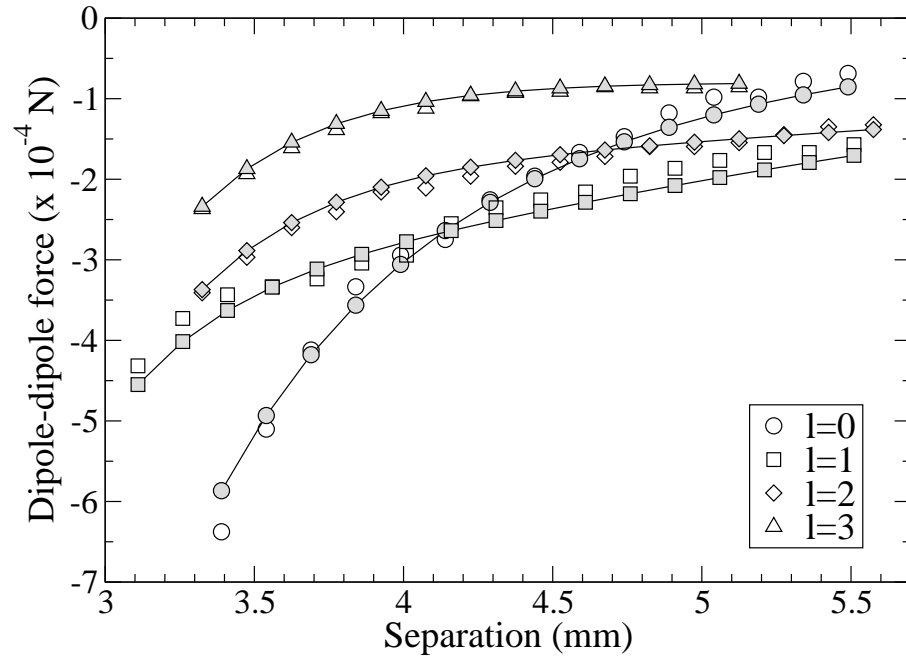**Figure 3.15:** *Magnetic dipole-dipole force between a magnetine bead and hexagons of different sizes, as a function of separation. Open symbols represent experimental measurements, and shaded symbols represent the calculated values. The hexagon with $l = 0$ was a single bead. Bead diameter = 3.16 mm.*

$\cos\theta(3 - 5\cos^2\theta)$ in Equation (3.76), and therefore the vertical component of the magnetic dipole-dipole force, is equal to zero.

The attraction of the top particle in the vertical direction to particles directly underneath (with $\theta > \theta_c$) is partially cancelled by the repulsion due to particles further away (with $\theta < \theta_c$). Although there are more of the latter, they are further away and thus have less of an influence. Magnetic dipole-dipole forces are proportional to r^{-4}, so influence drops off very quickly with distance.

Figure 3.15 shows the magnetic dipole force between a suspended bead and hexagons with l between 0 and 3, plotted against the vertical separation z. For all values of l, there was good agreement between the experiments and calculations. The shape of the curve changed as l increased, and the force on the dipole became smaller. This change happened because there were more beads at the edges of the hexagon at an angle greater than the critical angle $\theta_c = 140.8°$, at which the vertical component of the magnetic dipole-dipole force changed sign. The repulsion from these beads partially cancelled out the attraction of the suspended bead to the centre of the hexagon. The cancellation became more significant as the size of the hexagon increased. It is interesting to note that the magnetic force between a suspended bead and a hexagon dropped more slowly with increasing separation than the force between two beads.

3.5.6 Calculations of the force between a particle and a layer

In the last section we reported the results of experiments measuring the magnetic force between a magnetine bead suspended above a layer of beads arranged in a hexagonal lattice. We discovered that the magnetic force on the suspended bead due to a hexagon was attractive, but weaker than the force due to a single bead. The contributions to the magnetic force from the beads in the hexagon partially cancelled each other out, with the attraction to the central bead being partially balanced by repulsion from beads towards the edges of the hexagon. There was good agreement between our experimental measurements and calculations.

In this section we expand the calculations to see how the force changes with larger hexagons. We calculate the magnetic dipole-dipole force on a spherical particle
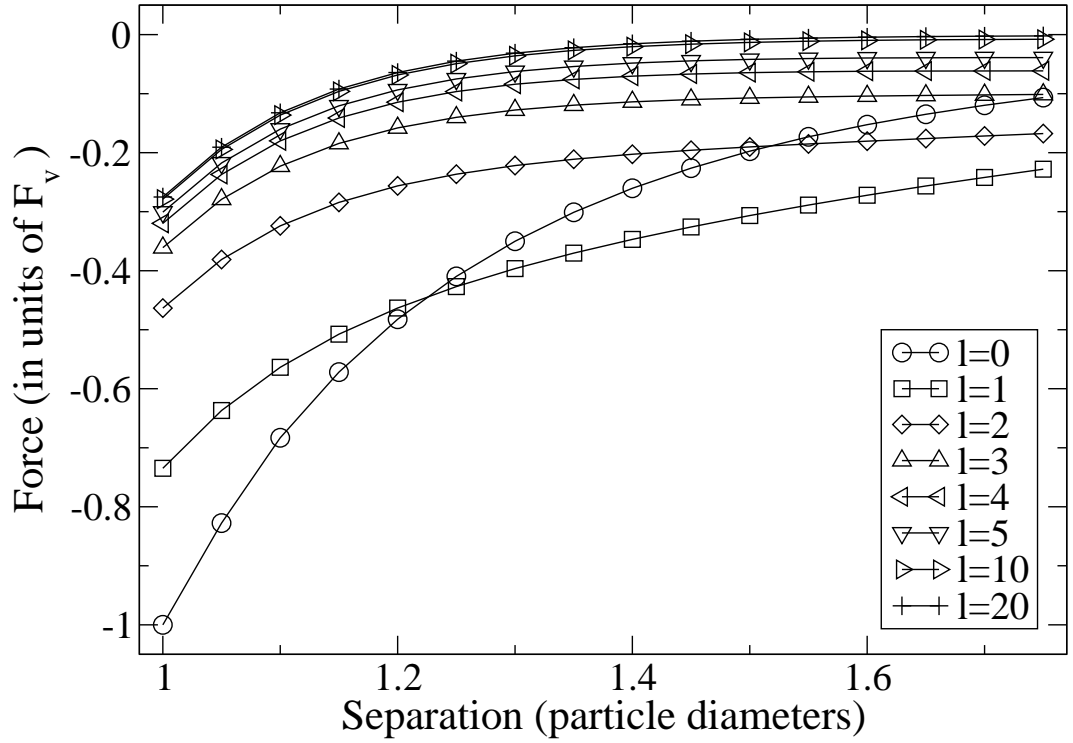
Figure 3.16: *The vertical magnetic force is plotted against separation, for hexagons with different values of l.*

positioned at a vertical distance h above a hexagonal layer of beads, by summing the forces due to each of the beads. All particles are perfect spheres of the same diameter, made of the same magnetizable material, and are assumed to act as point dipoles induced by and aligned with a uniform vertical magnetic field. The central sphere in the hexagon is at the origin, so the horizontal component of the magnetic force will cancel due to symmetry. We calculate the vertical force as a function of the separation h of the particle and the hexagon. As before, we denote the number of rings of dipoles in the hexagon by l.

Figure 3.16 shows the magnetic force plotted against the vertical separation of the particle and the hexagon. At a separation of one particle diameter, the particle and hexagon are touching. The magnetic force decays with separation, more slowly for a hexagon than the force between two particles. As l increases, the magnetic force decreases. This decrease happens because for larger hexagons there are more particles with an angle lower than the critical angle of $\theta_c = 140.8°$, at which the vertical component of the magnetic force changes sign. The repulsion due to these

particles with $\theta < \theta_c$ partially cancels out the attraction to the particle in the centre of the hexagon.

Figure 3.17 shows the magnetic force between a particle as a function of the hexagon size for a separation of one particle diameter. At this separation, the upper particle is resting on top of the central particle of the hexagon. The force decreases rapidly as a function of l, and saturates very quickly. When the hexagon is large, the addition of another layer makes very little difference to the force because the spheres on the outer layer are distant from the particle, so their contributions to the force will be very small. The force saturates at a value of -0.2746 F_v, just over a quarter of the force between two particles in contact. It is interesting to note that the magnetic force, though significantly lower than F_v, is finite. The system exhibits partial magnetic cancellation, unlike the case of a dipole above an infinite sheet, which experiences total magnetic cancellation (see Section 3.4.1).

Now we investigate the effect of varying the separation h of the top particle and the hexagon. Figure 3.18 shows how the magnetic force varies with the vertical separation of the particle and the hexagon. As the separation increases, the magnetic dipole-dipole force decreases rapidly. When the particle is far enough away from the lattice, the detail of the discrete particles cannot be resolved. The forces approach the continuum limit, in which the particle experiences the force due to an infinite plane of magnetizable material. As demonstrated earlier in this chapter (Section 3.4.1), the cancellation effect means that this force is zero.

3.6   Conclusion

We calculated the magnetic force between a point dipole positioned above an infinite horizontal sheet of magnetic material, in a vertical magnetic field. There is a critical angle $\theta_c = 140.8°$ at which the vertical component of the magnetic dipole-dipole force changes sign. The attraction of the dipole to material underneath at an angle θ greater than this critical angle was cancelled out by repulsion due to magnetic material farther away from the point dipole, with an angle θ less than the critical angle. The net force on the dipole due to the sheet was zero.
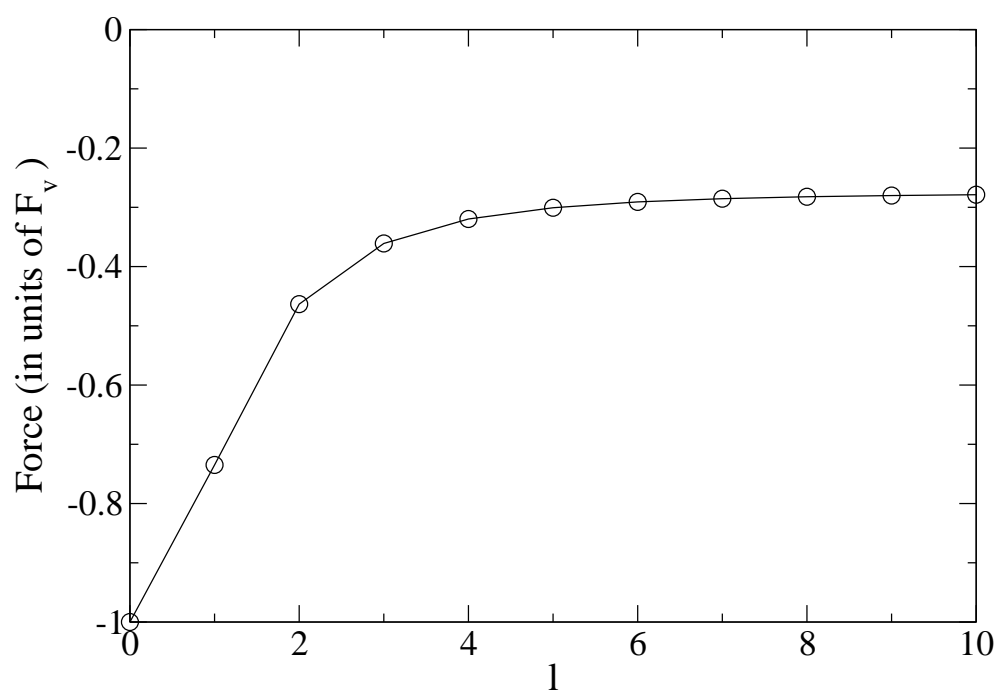
Figure 3.17: *The vertical magnetic force at a separation of one particle diameter is plotted as a function of l.*
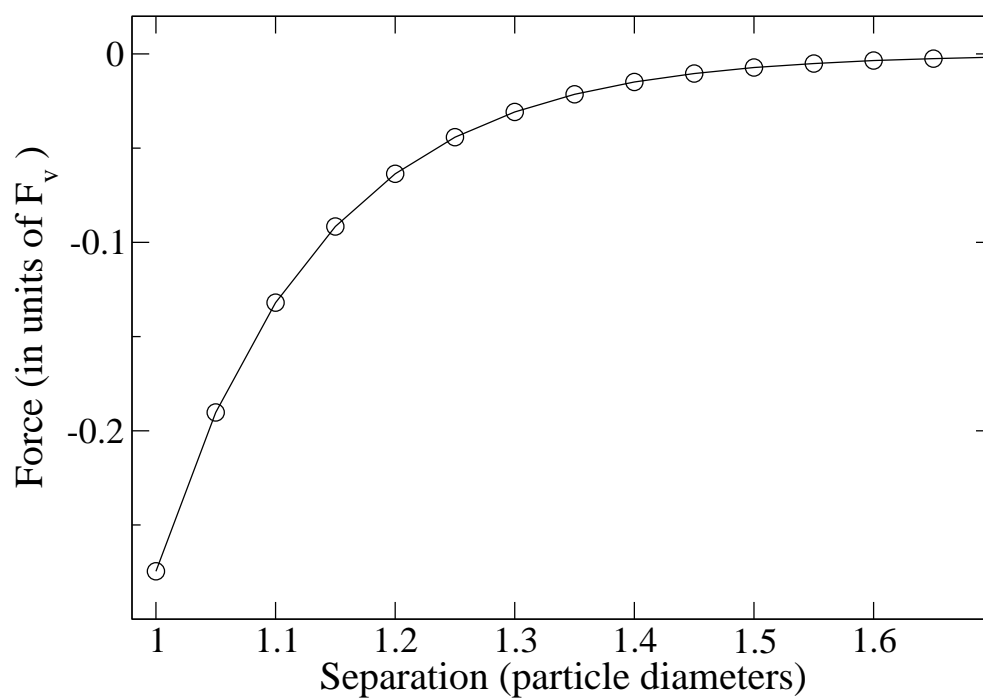
Figure 3.18: *The vertical magnetic force is plotted as a function of separation, for a large hexagon (l = 50).*

Experimental measurements of the force between two magnetine beads in a vertical magnetic field confirmed that the beads acted as point dipoles. We then measured the vertical magnetic force between a single bead suspended above a layer of beads arranged in a regular hexagonal lattice. The upper bead experienced an attraction to the hexagon, but not as strong as the attraction to a single bead. This difference was due to repulsion from beads towards the edges of the hexagon, which had an angle θ less than the critical angle θ_c. The magnetic cancellation was greater for larger hexagons. In all cases our experimental measurements of the force on the upper bead agreed well with calculations of the magnetic dipole-dipole forces.

We then extended our calculations to investigate the effect of increasing the size of the hexagon further. When the vertical separation of the dipole from the hexagon was one particle diameter (corresponding to the upper bead resting on top of the central part of the hexagon in our experiments), the force tended to -0.2746 F_v as the size of the hexagon was increased. This result demonstrated that there is partial magnetic cancellation, in contrast with the perfect magnetic cancellation observed in the case of a point dipole above a continuous sheet of magnetic material.

As the vertical separation of the particle and hexagon was increased, the magnetic force tended to zero. When the particle was far enough away from the hexagon, the detail of the discrete particles could not be resolved. The force approached the continuum limit, in which the particle experienced zero force due to an infinite plane of magnetizable material.

Chapter 4

Simulations of slope angles in two and three dimensions

4.1 Introduction

In this chapter we present the results of our two-dimensional molecular dynamics simulations. We measure the angle of repose of a granular pile in two dimensions and compare our data to previous work by Fazekas *et al.* [39, 62]. We offer an explanation of the puzzling discrepancy between the effect of cohesion on the repose angle of a granular pile in magnetic and wet systems, and conclude that wall friction is an important factor. The results of our two-dimensional simulations have recently been published [63].

We extend the simulations into three dimensions to investigate the effect of container width and wall friction on the repose angle and the dynamics of the pile. We measure the transverse magnetic force on the particles close to the container walls, and its effects on the velocity profile and distribution of particles in the pile. The details of our simulations technique have been described in Chapter 2.

4.2 Two-dimensional simulations

4.2.1 Literature review of simulations of two-dimensional slopes

Lee and Herrmann [51] report the results of two-dimensional molecular dynamics simulations including a static friction model. They measured the angle of repose of a granular pile. They found that the angle increases linearly with the friction coefficient. After an avalanche, it was found that the pile could be tilted through a small angle before another avalanche occurred.

In a later paper, Lee [64] investigated the effect of gravity on pile stability, using values of g ranging from half to nine times the acceleration due to gravity. A pile was formed with an angle of maximum stability, and then tilted until an avalanche occurred and the system came to rest at a lower angle of repose. The angle of maximum stability was independent of gravity. This result can be explained by considering the network of contacts between particles: assuming that increased gravity was not strong enough to alter the contact network, both the normal force and the shear force were proportional to g. The ratio of normal force to shear force was thus independent of gravity, as was the stability of the pile.

The angle just after an avalanche, however, was found to decrease with gravity. When an avalanche starts, the falling particles had a greater momentum in a stronger gravitational field. This increased momentum resulted in a less stable pile with a lower angle of repose.

Matuttis *et al.* [26] have investigated the forces in granular piles with a two-dimensional distinct element method simulation. The particles were placed in a regular hexagonal lattice, with a slope angle of 30°. Each particle in the bulk was in contact with six other particles, and a network of all the contacts between neighbouring particles was used to investigate the internal stresses. When the particles were spherical and of the same radius, the contact network was perfectly regular. However, even a low degree of polydispersity in the particle sizes destroyed the periodicity of the contact network; the lattice was still hexagonal, but some of the contacts between neighbouring particles were broken. The stress fluctuations were

substantial, and stress chains (paths through which large stresses acted) were quickly formed. For certain levels of polydispersity, there was a dip in the vertical stress measured at the bottom of the pile, a pressure minimum due to arching.

4.2.2   Literature review of repose angles of cohesive slopes

The angle of repose of a granular pile is a generally-used measure of the effect of cohesion. As the particles become more cohesive, the angle of a granular slope might be expected to increase. It is possible to define a cohesion strength R [11,39] as the ratio of the maximum cohesive force F_v between two particles in contact, and the particle weight. In the absence of cohesion ($R = 0$), the angle of repose is independent of the weight of the particles as frictional forces scale linearly with the particle's weight. When $R > 1$, the cohesive force is greater than the particle's weight and one particle can be suspended from another. As R increases from zero, the slope of a pile will be increasingly affected by cohesion, and one might expect the slope angle to approach $90°$ as R approaches a value of 1.

Forsyth *et al.* [11] have carried out a series of experiments investigating the influence of magnetic cohesion on repose angle. They poured steel ball-bearings into a narrow box to measure the angle of repose α_r in a uniform vertical magnetic field. They found that α_r increased slowly and linearly with the magnetic field strength. The increase in slope angle with cohesion was $d\alpha_r/dR = 0.5°$.

Fazekas *et al.* [39] used a two-dimensional molecular dynamics model to simulate the experiments of Forsyth *et al.*, treating the particles as point dipoles aligned with a uniform vertical magnetic field. The results showed a slow increase in angle of repose with magnetic field strength, at a rate of $0.5°$ per unit R. Even though the experiments were in three dimensions and the simulations were in two dimensions, there was good quantitative agreement in the rate of increase of α_r. However, the value of α_r in the absence of a magnetic field was substantially lower (19° rather than 31°) in the simulations. This discrepancy was attributed to the effects of friction between the particles and the front and back walls of the container.

The angle of repose of dry spheres is generally measured as about 23° (see [12] and references therein). The value of 31° obtained by Forsyth *et al.* is rather high,

and this can be attributed to the narrowness of the container (of width five particle diameters). Forsyth *et al.* found that the repose angle decreased when they used a wider container. A detailed experimental investigation of the influence of side walls on the repose angle has been carried out by Nowak *et al.* [13].

In contrast with magnetic systems, experiments on wet granular materials show a dramatic increase in angle of repose when a small quantity of liquid is added [12,14,15]. Liquid bridges have been observed to form between particles in contact, providing a cohesive force. It is, however, difficult to directly relate the quantity of liquid to the interparticle force. Albert *et al.* [12,14] measured the angle of repose of spherical glass particles with varying amounts of oil added. They fitted their data using a model based on the stability of a particle on the surface of a pile, treating the volume of the liquid bridges as an unknown parameter. They found that the slope angle approached 90° as $R \to 1$, and the rate of increase $d\alpha_r/dR$ was 58° per unit R.

The increase in α_r with R in magnetic systems is a very small effect; $d\alpha_r/dR$ is two orders of magnitude smaller than in wet granular systems. One would intuitively expect magnetic cohesion to have a more dramatic effect on the system, as occurs with liquid-bridge cohesion, but this appears not to be the case. To our knowledge, nowhere in the literature has anyone offered a satisfactory explanation of this discrepancy.

4.2.3   Angle of repose

Our simulation model, parameters, and geometry are described in detail in Chapter 2. The magnetic field was applied in the vertical direction. Figure 4.1 shows a snapshot of the simulation with no applied magnetic field.

We ran the simulation for values of the cohesion parameter R. Figure 4.2 shows our system with different values of R. The line on the diagram is our fit to the designated surface particles, which are shaded. In the absence of magnetic forces (Figure 4.2**a**), the slope was very smooth with mean deviation of less than one particle diameter. At $R = 5$ (Figure 4.2**b**), pyramid-like structures could be observed. These minimized the magnetic energy of the surface particles, while at the same time being
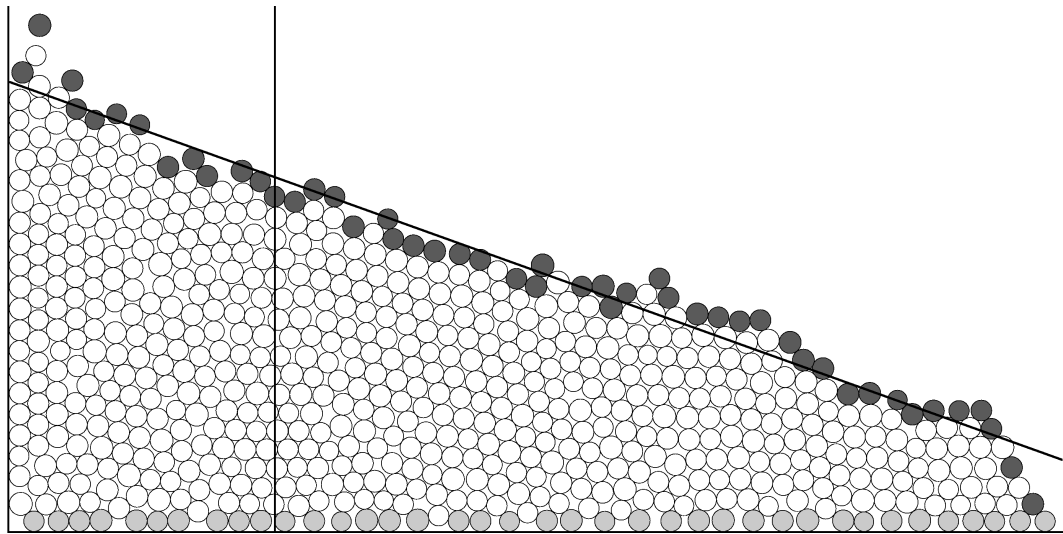
Figure 4.1: *A snapshot of a granular slope in the absence of a magnetic field. The diagonal line is a fit to the surface particles (darkly shaded). The lightly shaded particles adhered to the base of the container. The vertical line, a quarter of the container length from the left wall, was the position at which we evaluated the particles' velocities and magnetic forces as a function of depth in the pile, as discussed later.*

stable against gravity. At higher values of R (see Figure 4.2**c**, with $R = 24$) vertical columns of particles formed. The head-to-tail configuration of magnetic dipoles minimized their magnetic energy; this effect was much stronger than gravity when $R >> 1$.

Although Fazekas *et al.* [39] used values of R up to 24, we consider that with this much cohesion the slope is insufficiently smooth for a single angle to be an appropriate parameter to describe the system. With magnetic interactions of this strength it is clearly meaningless to describe the system by a single angle. The maximum slope angle is actually greater than 90°, as parts of the slope surface are overhanging. We therefore restricted our simulations to the range $0 \leq R \leq 10$.

We investigated the idea of vertical columns further by building up a column slowly until it collapsed. The simulation started with a single particle, fixed in position, and then another particle was gently placed another on top. The second particle was placed with a slight horizontal displacement, and oscillated above the fixed particle. The magnetic dipole-dipole interaction provided a restoring force.

We continued building until the column collapsed, and repeated this process for

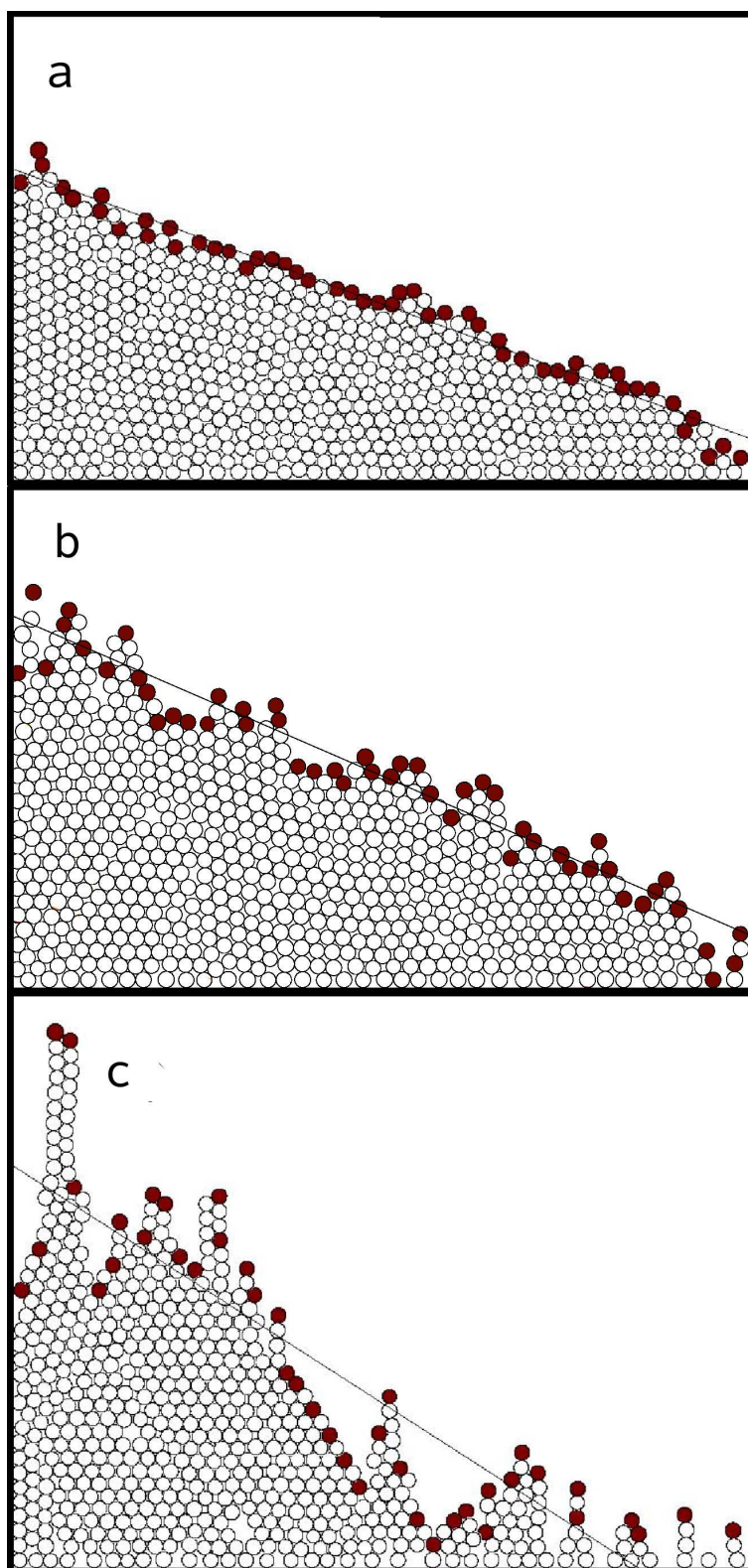**Figure 4.2:** *Simulation with* **a** *R=0* **b** *R = 5 and* **c** *R=24. The line on the diagram is a straight line fit to the surface particles (shaded). At high values of R, the slope cannot adequately be described by a straight line fit.*

values of the cohesion strength R between 0 and 10. The column failed at the base; the second particle slid off the first (fixed) particle, carrying the entire column with it. We found that the critical column height at which the column collapsed was $R + 1$ particles. The explanation for this is that in a column of height N particles, the force tending to make the column collapse was the weight of $N - 1$ particles, i.e. $(N - 1)mg$. The force maintaining the connection between the base particle and the one above it was approximately F_v. We consider the magnetic influence of other particles in the column to be negligible in comparison to that of nearest neighbours, as the magnetic dipole-dipole force decayed very quickly with distance. The next nearest neighbour to the base particle is the third particle in the column. It was twice as far away, and thus attracted the base particle with a force of $(1/2)^4 F_v = (1/16) F_v$.

At the critical column height, the magnetic force F_v was holding the column together, while the weight $(N - 1)mg$ of particles supported was tending to cause collapse. Equating these two forces, we obtain:

$$F_v = (N - 1)mg; \tag{4.1}$$

$$N = \frac{F_v}{mg} + 1 = R + 1. \tag{4.2}$$

These equations agree with our observations.

Figure 4.3 shows the roughness of the slope as a function of R. We define roughness as the mean distance, in particle diameters, of the surface particles from the line of best fit that describes the slope angle. The graph shows that the slope became less smooth at higher values of R. This increase in roughness is to be expected because the strong magnetic attraction in the vertical direction causes structures to form on the surface of the heap.

4.2.4 Comparison with previous simulation results

Firstly, we validated our model by repeating the simulations of Fazekas *et al.* [39] in a system with no front and back walls (see Figure 4.4). We ran the simulation for 180 seconds (simulated time), during which 12000 particles were introduced into the system. We used a range of values of the cohesion strength R between 0 and 10. Figure 4.5 shows the angle of repose as a function of the cohesion strength R.
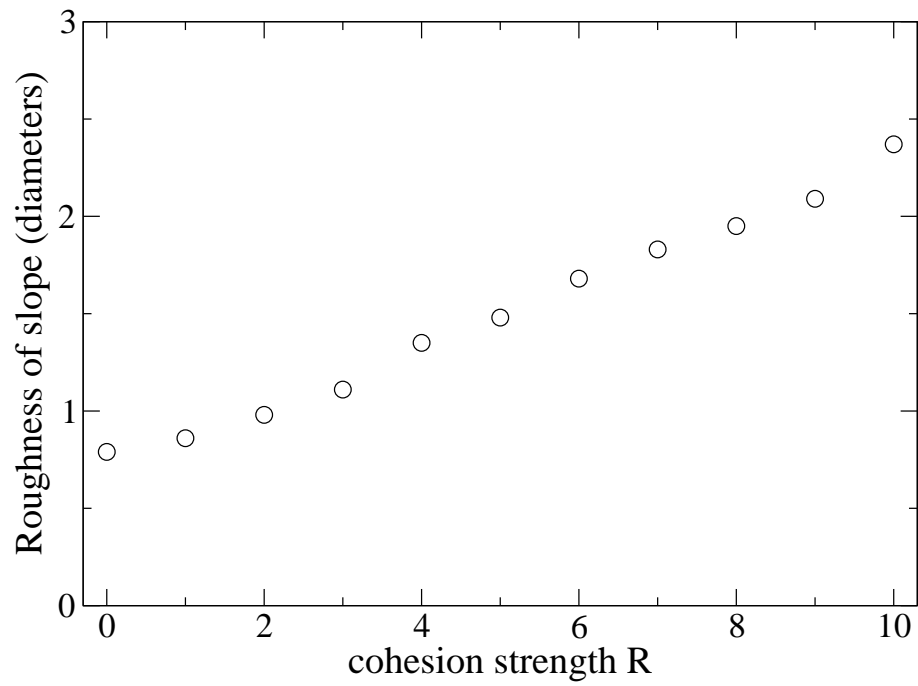
Figure 4.3: *Roughness of slope as a function of cohesion parameter R in a vertical magnetic field. Roughness is defined as the root mean square deviation of the surface particles from the line of best fit, in units of particle diameters.*
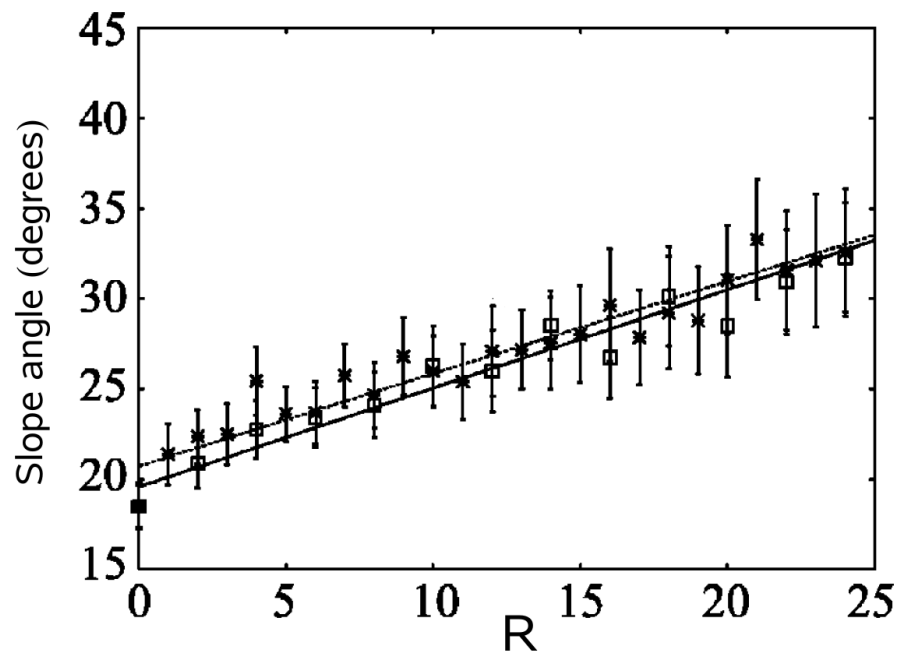

Figure 4.4: *Angle of repose as a function of cohesion parameter R in a vertical magnetic field, taken from Fazekas et al. [39]*

The angle increased slowly with cohesion, with an increase of only a few degrees even when the cohesive forces are ten times as great as the particle's weight. Our simulations show a linear dependence of the angle of repose on R, but with a non-linearity below $R = 2$. Our simulations yielded a value of $d\alpha_r/dR = 0.50°$ which is in excellent agreement with simulations of Fazekas *et al.* [39].

The effect of cohesion on α_r was weak: when $R = 1$, magnetic and gravitational forces were of the same magnitude, and one might expect the angle of repose to be substantially greater than in the case of zero cohesion. It has been suggested that the weak dependence of α_r on R is a result of the anisotropic nature of the cohesive force [11,39]. Due to this anisotropy, the field-induced magnetic dipole-dipole forces in the bulk of the pile partially cancel each other out. We explored the idea of magnetic cancellation in detail in Chapter 3. In Section 4.2.6 we will measure the cancellation effect in our simulations to determine whether it provides a sufficient explanation for the weak dependence of repose angle on magnetic cohesion.

4.2.5 Effect of varying simulation parameters

Figure 4.6 shows the angle of repose as a function of R, comparing Hertzian and linear contact models. The angles obtained using the Hertzian model were higher than those for the linear model, but only by a degree or two. The increase of α_r with R was the same for both models. The Hertzian model was in very good agreement with the results obtained by Fazekas *et al.* [39], who also used a Hertzian contact model. The remainder of the results presented in this chapter used the Hertzian model.

We also compared the repose angles obtained using different friction models. Figure 4.7 shows the angle of repose as a function of R for simulations with a viscous friction model and a static friction model. The static friction model required the tangential displacement over the duration of the contact to be stored, so was more computationally intensive than the simpler viscous friction model. The graph shows that the choice of friction model had no effect on the repose angle. We therefore used a viscous friction model (also used by [39]) rather than the more complicated static friction model.
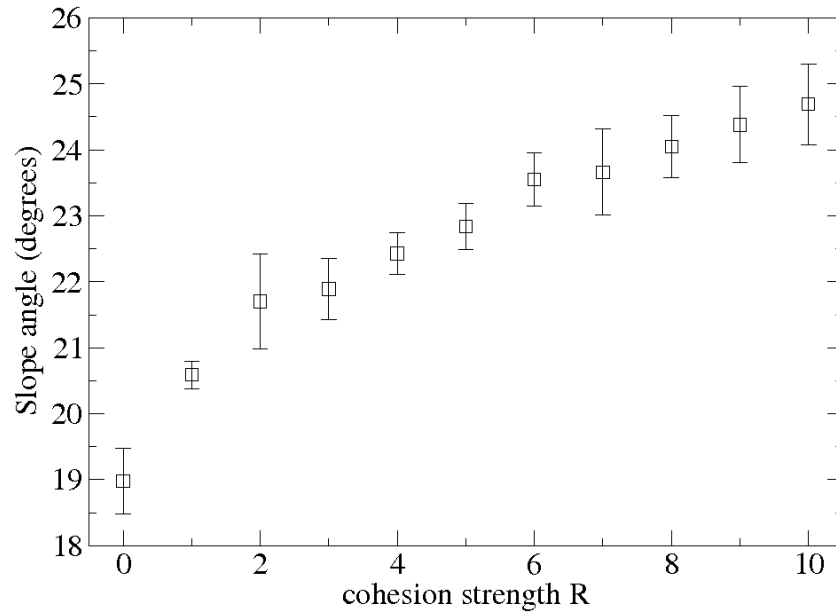
Figure 4.5: *Angle of repose as a function of cohesion strength R in a vertical magnetic field, in a container of length 50 particle diameters*
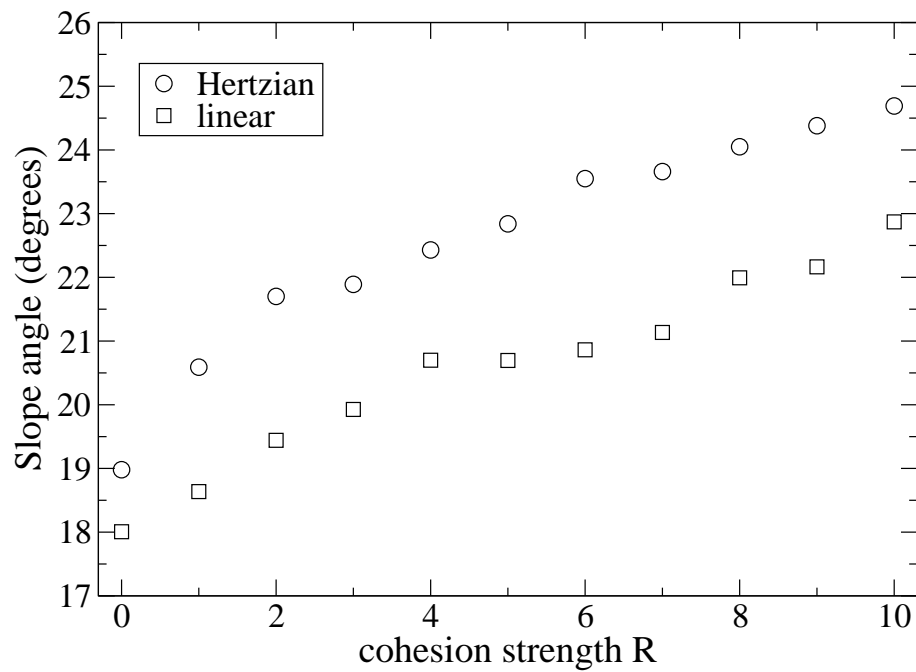

Figure 4.6: *Slope angle α_r as a function of cohesion strength R, using Hertzian and linear contact models*

We used a timestep of $\Delta t = 5 \times 10^{-6}$ seconds. This was small enough to ensure numerical stability. We ran simulations with a range of values of the timestep, and found that for the Hertzian model, simulations with timesteps smaller than $\Delta t = 4 \times 10^{-5}$ s were stable, but $\Delta t = 5 \times 10^{-5}$ s was unstable. For the linear model, we found that simulations with a timestep of 1.2×10^{-5} s were stable, but 1.3×10^{-5} s was unstable.

We ran the simulation with R between 0 and 10 for values of the coefficient of restitution e between 0.1 and 1 (elastic). Figure 4.8 shows the zero-field slope angle plotted against e. The coefficient of restitution had little effect on the angle of repose. We used $e = 0.95$ for the remainder of the simulations (in both two and three dimensions) reported in this chapter. We confirmed that the coefficient of restitution was correct by colliding two particles and measuring the particles' velocity before and after collision.

Figure 4.9 shows the zero-field slope angle plotted as a function of the coefficient of friction between particles. The slope angle was $13°$ in the absence of friction, and increased with μ. In the simulations reported in this chapter we used a value of $\mu = 0.5$.

4.2.6 Magnetic cancellation

The cohesion strength R overestimates the forces in the system. Because of the anisotropic nature of the magnetic dipole-dipole force, the average force between two particles in contact is less than the maximum cohesive force F_v. The force changes sign depending on the angle θ between $\mathbf{B}$ and $\mathbf{r}$, so the forces acting on a particle due to its surrounding particles can be either attractive or repulsive.

Chapter 3 explored the idea of magnetic cancellation in more depth. In this section we briefly describe the key results and measurements of magnetic forces in simulation.

In three dimensions, magnetic forces can cancel exactly. We calculated the net magnetic force on a point dipole above an infinite plane of magnetic material, in a uniform vertical magnetic field. The attraction of the dipole to material underneath was counteracted by repulsion from material to the sides. The forces cancelled
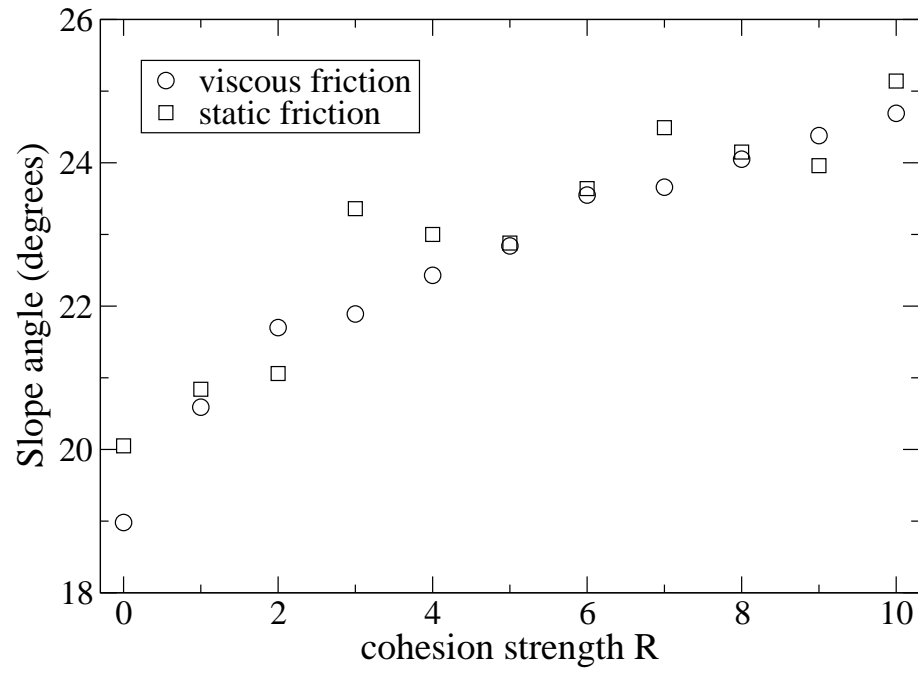
Figure 4.7: *Slope angle α_r as a function of cohesion strength R, using viscous and static friction models*
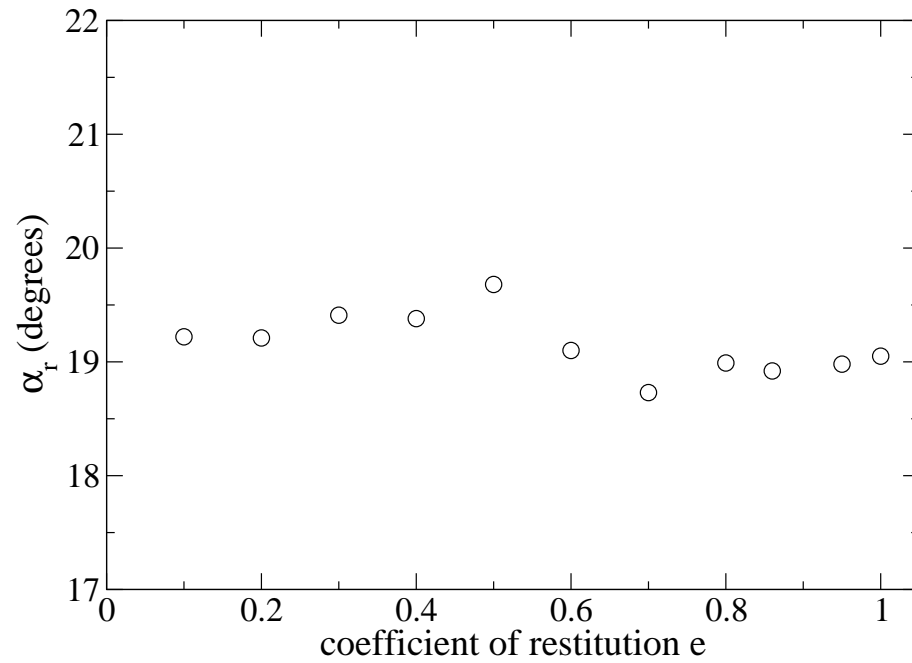

Figure 4.8: *The zero-field slope angle is independent of the coefficient of restitution.*

exactly and the dipole experienced no net force.

The analogous calculation in two dimensions (the net magnetic force on a point dipole due to an infinitely long line) demonstrated partial cancellation. The net force was non-zero but significantly less than F_v.

A dipole above an infinite layer of point dipoles arranged in a regular lattice also experienced partial cancellation, in both two and three dimensions. The magnetic dipole-dipole force is a relatively short-range force, decaying as $1/r^4$. Hence the force on a particle depends very sensitively on the arrangement of its neighbouring particles, but only weakly on the arrangement of particles further away.

The radial component of the force between two dipoles is $\mathbf{F}.\hat{\mathbf{r}}$. This is a scalar, with a negative sign for attraction and a positive sign for repulsion. The radial component $\mathbf{F}.\hat{\mathbf{r}}$ is given by Equation 3.40 in Chapter 3:

$$\mathbf{F}.\hat{\mathbf{r}} = F_r = \frac{3\mu_0|\mathbf{m}|^2}{4\pi r^4}(1 - 3\cos^2\theta). \tag{4.3}$$

We can express this in terms of F_v:

$$\mathbf{F}.\hat{\mathbf{r}} = F_v\frac{d^4}{2r^4}(1 - 3\cos^2\theta). \tag{4.4}$$

To estimate the magnetic force on a particle in the bulk of a pile, we calculated the sum of $\mathbf{F}.\hat{\mathbf{r}}$. A vectorial sum would be close to zero, even though the cohesive forces were always present and acted to oppose the particle's motion. For this reason, we used a sum of the radial components of the forces to give an estimate of the cohesion in the packing.

In our simulations, we measured the force $F_{\text{total}} = \sum_i \mathbf{F}_i.\hat{\mathbf{r}}_i$ on one particle due to all other particles in the same or neighbouring cells (i.e. all particles that were close enough to interact magnetically). F_{total} was spatially binned by neighbour cells, and averaged over an entire run.

Another estimate of the magnetic force was obtained by calculating $F_6 = \sum_{i=1}^{6} \mathbf{F}_i.\hat{\mathbf{r}}_i$. This measure is a theoretical approximation to the force on a particle in a granular bed; we made the assumption that particles had a regular hexagonal packing, and summed over a particle's six nearest neighbours.

By summing the contributions from all six neighbours, we obtained the net cohesive force $F_6 = 1.5F_v$. This was true for any orientation of the hexagon relative to

the magnetic field direction. Next, we added the contributions to the sum from the next-nearest neighbours. Consider another ring of particles added around the outside of our original hexagon. The total force $F_{18} = \sum_{i=1}^{18} \mathbf{F}_i.\hat{\mathbf{r}}_i$ including contributions from next-nearest neighbours was $F_{18} = 1.76 F_v$.

Figure 4.10 shows F_{total} plotted as a function of vertical position in the pile. The simulation results show that F_{total} was approximately constant in the bulk of the pile, and agrees well with our calculated value of $F_{18} = 1.76 F_v$.

We define another measure of the cohesive force, F_{net}, as the value of $(1/N) \sum_{i=1}^{N} \mathbf{F}_i.\hat{\mathbf{r}}_i$ where $\mathbf{F}_i$ is the magnetic force on one particle due to one other particle. F_{net} was spatially binned by neighbour cell, averaged over all N neighbouring particles, and time-averaged over an entire run.

Figure 4.11 is a snapshot of the simulation in progress. The particles are shaded differently depending on the value of F_{net}. Most of the particles in the bulk had forces in the range $0.25\,F_v < F_{\text{net}} < 0.5\,F_v$. Around the edges of the pile the net forces were a little higher, but still less than F_v.

Figure 4.12 shows F_{net} plotted against vertical position in pile. In the bulk of the pile, the magnetic forces were partially cancelled out, with F_{net} equal to about $0.4\,F_v$. At the top and bottom of the pile, the net magnetic forces were greater. This was true for values of R between 1 and 10.

F_{net} and F_{total} differ by a factor of about 4.5. This is the mean number of nearest neighbours. $F_{\text{net}} \approx 0.4\,F_v$ implies that the anisotropic nature of the dipole-dipole force makes the magnetic forces 2.5 times weaker than expected. Forsyth *et al.* [11] and Fazekas *et al.* [39] suggest that magnetic anisotropy could be an explanation for the discrepancy of factor 100 between the size of the effects of cohesion on magnetic systems and wet systems. Our calculations suggest that this is not the case, and in the next section we outline an alternative explanation for the weakness of the effect of magnetic cohesion.
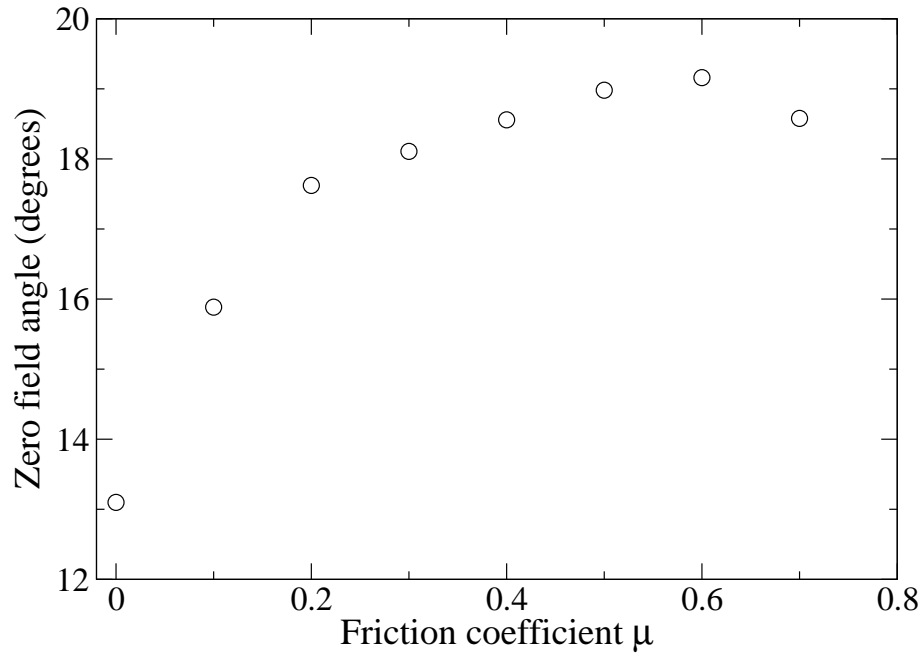
Figure 4.9: *The zero-field slope angle plotted as a function of the friction coefficient* μ
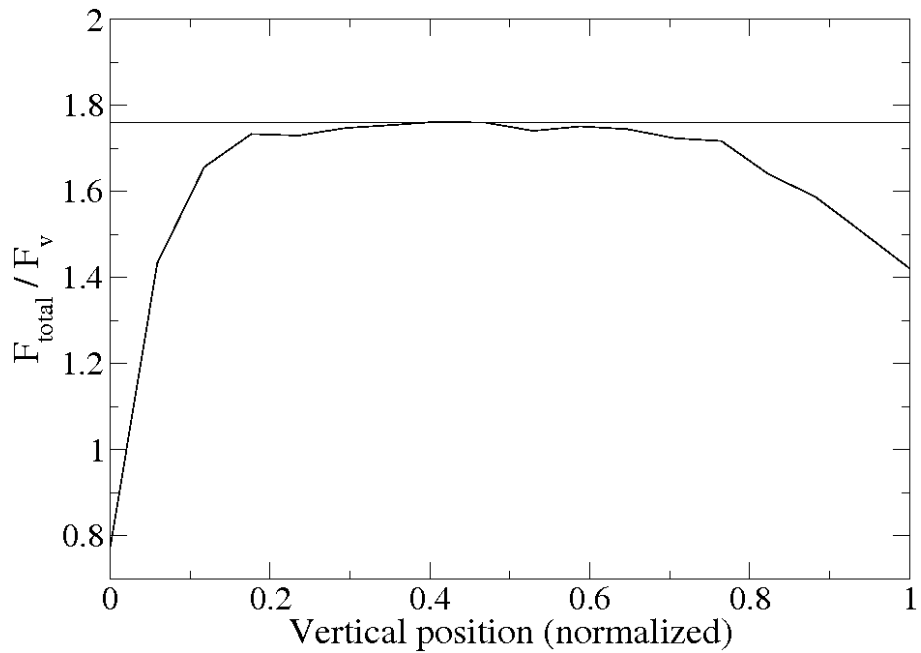
Figure 4.10: *Total radial magnetic force* $F_{\text{total}} = \sum \mathbf{F}_i.\hat{\mathbf{r}}_i$ *per particle as a function of vertical position in the pile, measured at a horizontal position a quarter of the container width away from the left wall. The horizontal line on the graph is* $F_{18} = 1.76 F_v$. *The particle positions are normalized so that the bottom of the pile is 0 and the top is 1.*
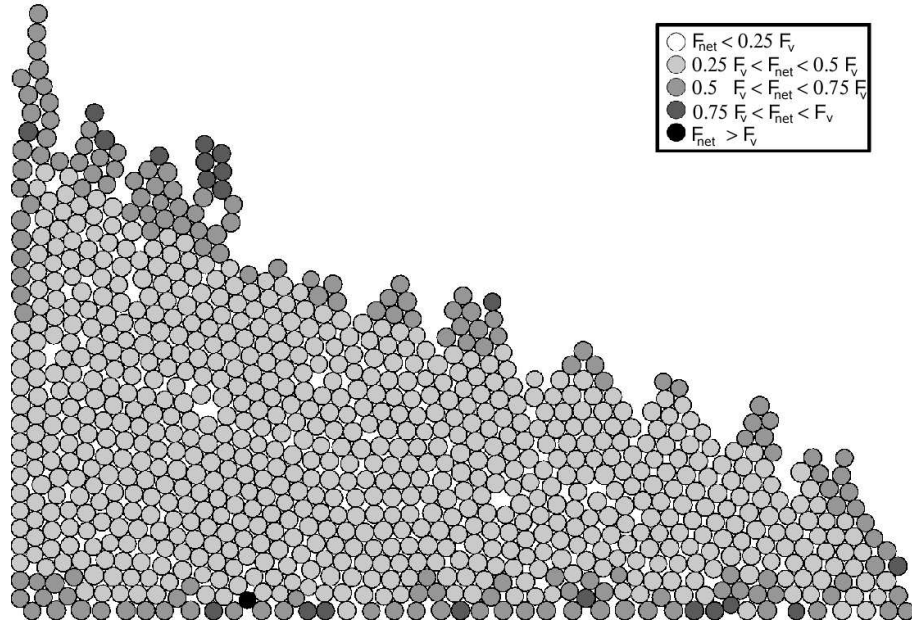
Figure 4.11: *Cancellation of magnetic forces at $R = 5$: lighter shading represents weaker net forces. The shading corresponds to forces that are averaged over a period of time.*
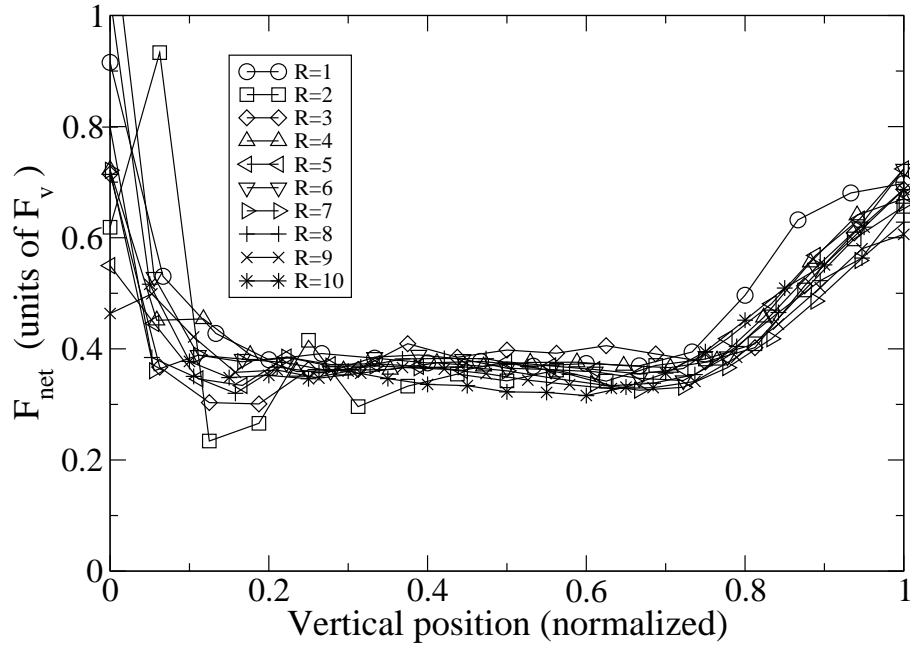
Figure 4.12: *Net magnetic force F_{net} as a function of vertical position in the pile*

4.2.7   Avalanche dynamics

Particles were added one by one to the left side of the system, and were removed from the system when they reached the right wall.

In the absence of a magnetic field, we observed shearing deep within the pile. In a magnetic field the surface of the pile was more rugged, and the size of surface irregularities increased with cohesion. Clusters of regularly-packed particles formed and moved as a block, both on the surface and in the bulk. Shear in the bulk occurred at the boundaries between clusters. The size of the clusters increased with cohesion, and contacts between neighbouring particles lasted for longer than in the absence of magnetic cohesion.

In steady fully-developed flows in three-dimensional piles, most of the motion occurs in a surface layer with a linear velocity profile into the pile and away from the surface. There is creep motion in the bulk that decays exponentially [65]. Crassous *et al.* [66] report an experiment with a continuously flowing pile of glass beads in a rectangular cell. They used particle tracking velocimetry to measure the velocity of particles on the surface of the pile, and dynamic light scattering in the bulk. The authors observed a rapidly flowing surface layer with a linear velocity profile, and creep motion in the bulk with a velocity that decayed exponentially with depth. The decay length was measured as one particle diameter. Another system that exhibits a predominantly exponential velocity profile is a collection of monodisperse spheres in a slowly-sheared three-dimensional Couette cell [67].

Aguirre *et al.* [68, 69] report that in two-dimensional experiments in a slowly tilted bed, the velocity profile was either purely exponential or a product of an exponential and a Gaussian. Renouf *et al.* [70], in two-dimensional rotating drum simulations, observed the same two phases of motion as in experiments in three dimensions. There was a rapidly flowing surface layer with a linear velocity profile, and the bulk had an exponential velocity profile with a decay length of three particle diameters.

Figure 4.13 shows the mean particle velocity in our simulations, plotted as a function of depth in the pile. The horizontal velocity was measured at a position a quarter of the container length away from the left wall. In the absence of a
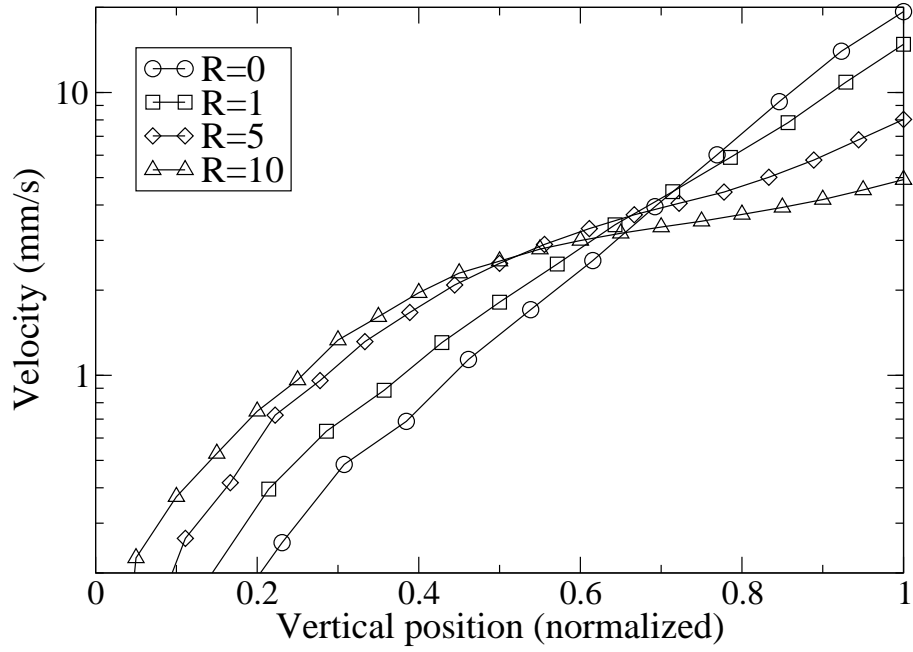
Figure 4.13: *The mean velocity per particle was plotted as a function of vertical position in the pile, measured at a horizontal position a quarter of the container length away from the left wall (the vertical line in Figure 4.1). The particle positions were normalized so that the bottom of the pile is 0 and the top is 1. An increase in cohesion strength R shifted the motion farther down into the bulk of the pile.*

magnetic field, the velocity decayed exponentially with depth. The rate at which we added particles was slow enough that there was no constantly-moving surface layer, and the zero-field velocity profile was approximately exponential. We calculated the decay length at zero field as 3.8 particle diameters. Experiments in three dimensions produced values of the decay length between 1 [65,66] and 3.4 [71] particle diameters. In two dimensional simulations, Renouf *et al.* [70] obtained a decay length of three particle diameters; this was quite close to our value of 3.8 diameters.

On average, the tendency to slip at any given depth was proportional to the weight of particles above that depth. The frictional force that opposed slip, however, was also proportional to the weight of particles above. Hence the weight cancelled out of the force balance equation, and slip could occur at any depth in the pile.

In the presence of a magnetic field the motion shifted farther down into the pile and the shape of the velocity profile changed, as can be seen in Figure 4.13. This shift happened because the interparticle cohesive forces in the bulk of the pile did

not depend upon depth. Near the surface of the pile, cohesive forces could readily support the weight of the particles above, resulting in less shear than in the absence of cohesion. Farther down in the pile the cohesive forces were less able to support the weight of the particles above, resulting in increased shear. It was this shear deep within the pile that prevented the angle of repose from increasing dramatically.

Restagno *et al.* [72] report a study of the dependence of cohesion on the normal force, and how this affects the failure of a granular pile. Their continuum analysis predicts that when the cohesive force is independent of the normal contact force between particles, the pile will fail at depth. The velocity profiles obtained from our simulations confirm this prediction. Restagno *et al.* also argue that when the cohesive force varies linearly with normal contact force, as in the case of liquid bridges, the pile is predicted to fail at the surface. Failure at the pile surface happens in the "granular regime" in the experiments of Tegzes *et al.* [17] with small amounts of liquid added to the grains. The dependence of cohesion on normal contact force explains the discrepancy between $d\alpha_r/dR$ in our simulations and in liquid bridge experiments, because, as previously noted, it is shear deep in the pile that prevents the angle of repose from increasing substantially.

4.2.8 Sliding block model

Consider a block of weight mg resting on a slope inclined at angle α to the horizontal (see Figure 4.14). There is a cohesive force F_c acting on the block directed perpendicularly into the slope's surface, and friction F_r acting up the slope. At the critical point when the block just begins to slide, Coulomb's criterion $F_r = \mu F_n$ applies, where μ is the coefficient of friction and F_n is the normal force. The normal force is equal to the sum of the cohesive force and component of the block's weight acting perpendicularly to the slope surface. The friction must be equal to the component of the block's weight acting in a direction parallel to the slope:

$$\mu(mg\cos\alpha + F_c) = mg\sin\alpha. \tag{4.5}$$

In the absence of a magnetic field, the cohesive force F_c is zero and the above
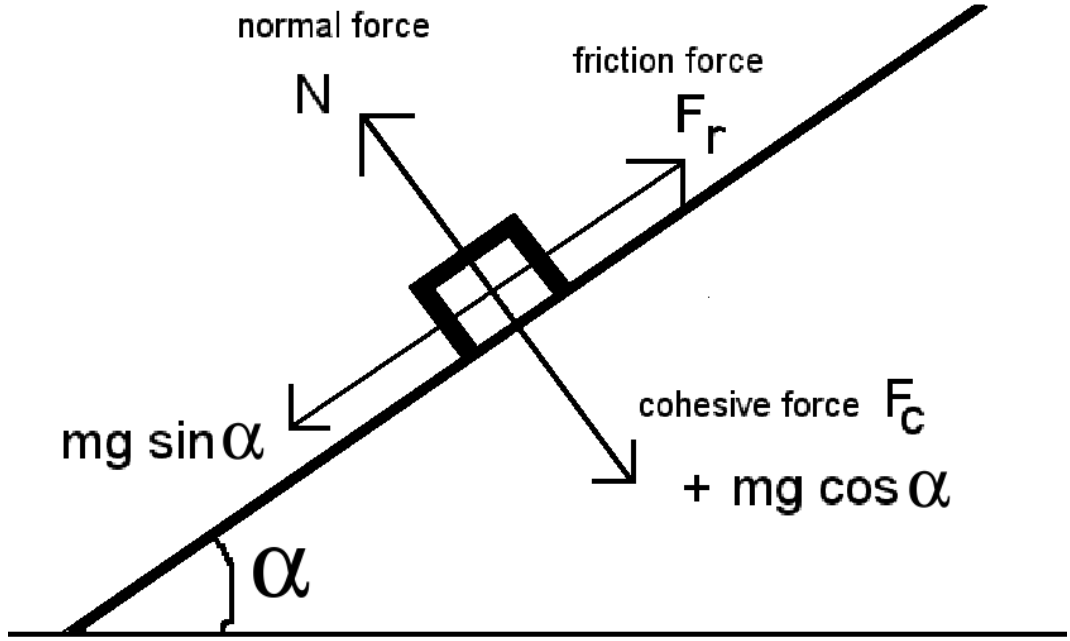
Figure 4.14: *The sliding block model*

equation reduces to $\mu = \tan \alpha$. Dividing through by mg, we obtain

$$\mu(\cos \alpha + \frac{F_c}{mg}) = \sin \alpha. \tag{4.6}$$

Consider a slip plane in the pile, supporting material above it with a weight mg. If the slip plane is deep in the pile, mg will be large and the cohesion term F_c/mg in the above equation will be small. Cohesion will not have a great effect and will be less likely to prevent shear from happening. Conversely, for a slip plane near the surface of the pile supporting a small weight mg, the cohesion term will be larger, so cohesion will be more likely to prevent shear at that point. The overall effect will be to shift the motion down farther into the bulk of the pile, as we have observed in our simulations.

4.2.9 Effect of changing the system size

We ran our simulations in containers of different sizes, with lengths from 40 particle diameters to 120 particle diameters. Figure 4.15 shows the repose angle α_r plotted as a function of R, comparing the different systems. In larger containers,
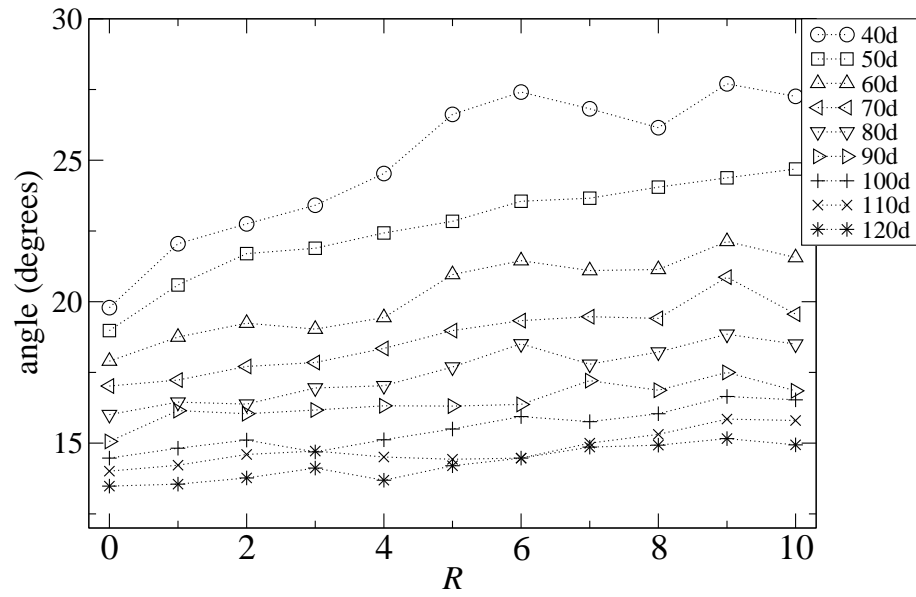
Figure 4.15: *Angle of repose as a function of the cohesion strength R for systems of different sizes*
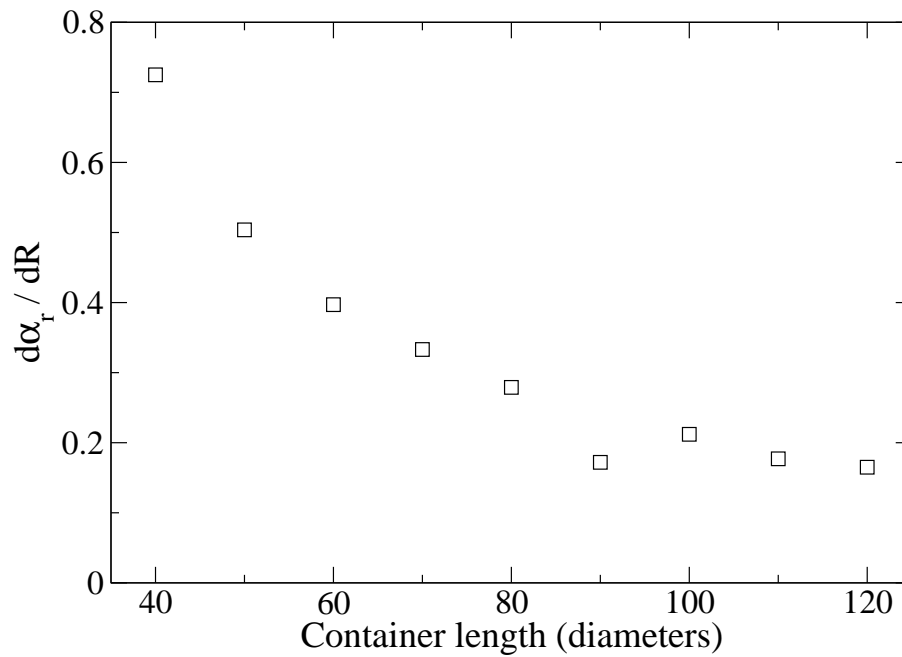
Figure 4.16: *Gradient $d\alpha_r/dR$ as a function of the system size*
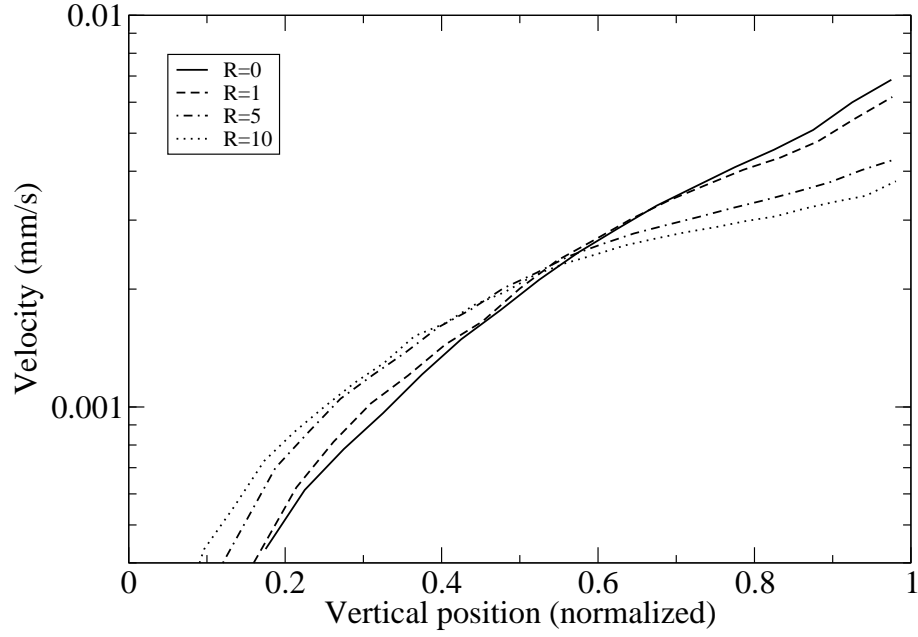
Figure 4.17: *The mean velocity per particle as a function of vertical position in the pile, measured at a horizontal position a quarter of the container length away from the left wall (the vertical line in Fig. 4.1). An increase in cohesion strength R shifted the motion farther down into the bulk of the pile.*

the slope angle is lower, and increases more slowly with cohesion.

Figure 4.16 shows the rate of increase $d\alpha_r/dR$ as a function of the system size. The gradient appears to decrease exponentially with container length.

Figure 4.17 shows the velocity profile in a larger system with a length of 100 particle diameters. It is similar in shape to Figure 4.13, though the change in profile shape with R is less pronounced.

4.2.10   Effect of friction with front and back walls

So far we have considered an idealized two-dimensional system. Any real physical system will be influenced by the container walls. It is well known that friction with confining walls can influence both the angle of repose and the velocity profile of avalanches in a narrow box [73, 74].

We introduced wall effects into our two-dimensional simulations by using two different friction models, as described in Chapter 2, Section 2.5.5. In the first model, a percentage, p, of each normal contact force was directed towards the front and

back walls. The frictional force depends upon the depth within the pile because a particle supports the weight of other particles resting on it. In the second model, a constant drag force proportional to the particle's weight was applied in the opposite direction to the particle's motion. In contrast with the first model, friction was independent of a particle's position in the pile.

Figure 4.18 shows the angle of repose α_r as a function of cohesion strength R for a range of values of p. The repose angle at zero field increases dramatically with p because the depth-dependent friction increasingly opposes motion further down in the pile. The variation of α_r with R is much greater for higher values of p. In fact, the gradient $d\alpha_r/dR$ increases linearly with p, as can be seen in Figure 4.19.

This behaviour can be understood by considering where the motion occurs in the pile. Figure 4.20 shows the mean particle velocity plotted as a function of depth. In the absence of front and back walls ($p = 0$), increasing the magnetic field shifts the motion further down into the pile, as explained in Section 4.2.7. However, if p is non-zero, the frictional forces with the walls oppose motion in the bulk, causing the velocity profile to change shape, and the motion to shift closer to the surface of the pile. Hence there is less motion in the bulk and α_r increases more quickly than in the absence of depth-dependent friction.

The effect of constant drag friction, however, is quite different. Fig. 4.21 shows the repose angle α_r as a function of R, for different values of the drag constant β. The angle in zero field is about 24° for $\beta = 0.1$, significantly higher than in the absence of front and back wall friction, and increases further for higher values of β. The repose angle α_r increases by only a small amount with cohesion. In fact, the gradient $d\alpha_r/dR = 0.5°$, the same as in the case with no front and back walls. Observing the simulations running, we can see that motion happens deep in the pile, not just near the surface.

The particle velocity profile as a function of depth in the pile was very similar to Figure 4.13, demonstrating that this implementation of friction with the front and back walls did not change where slip occurred. Shear still happenned deep within the pile, preventing the angle of repose from increasing dramatically with cohesion.
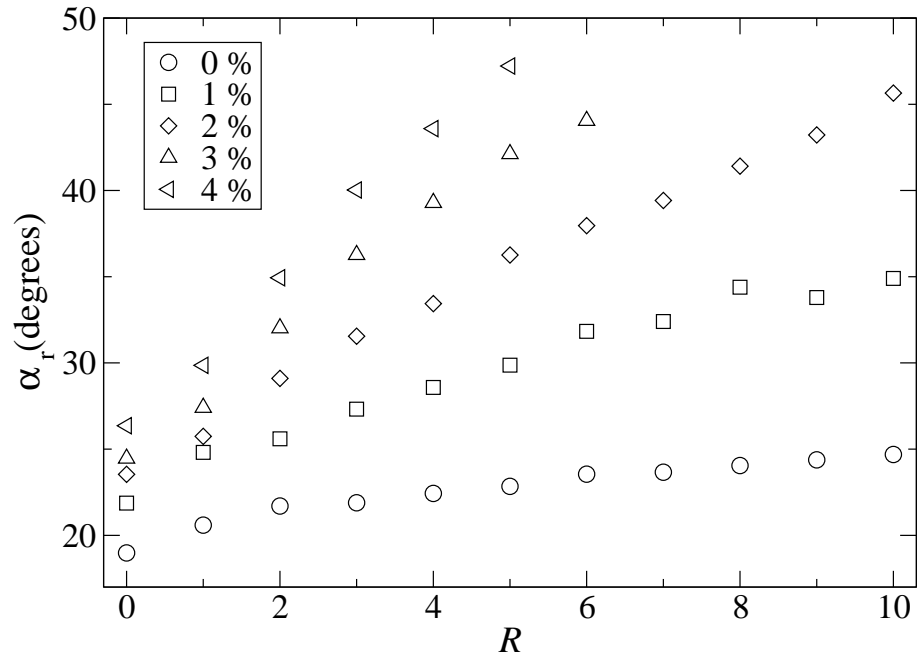
Figure 4.18: *Angle of repose as a function of cohesion strength R in a vertical magnetic field, in a container of length 50 particle diameters. Results are shown for different values of the friction percentage p.*
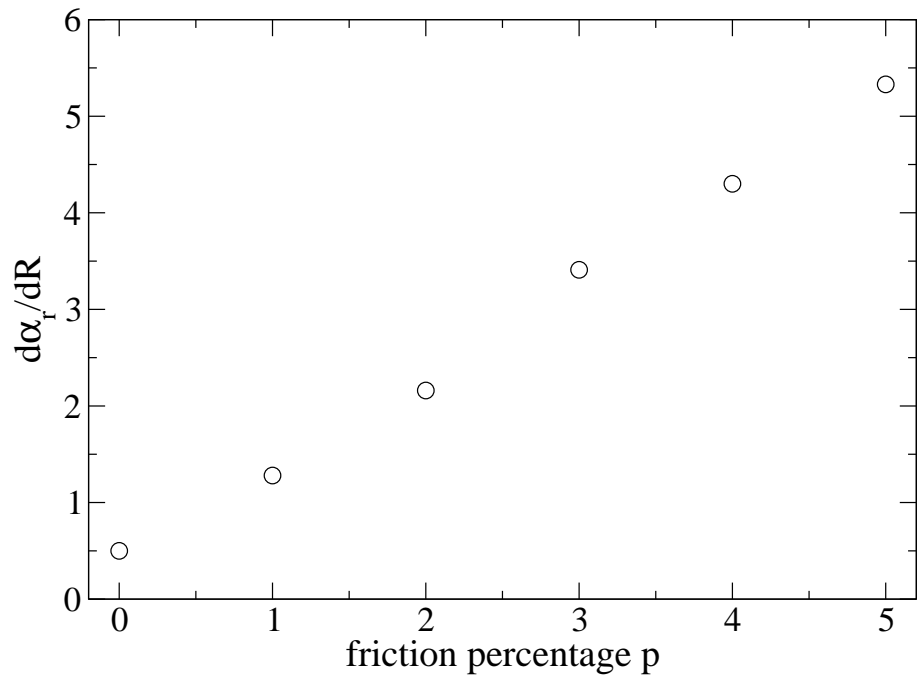
Figure 4.19: *Gradient $d\alpha_r/dR$ in a vertical magnetic field, in a container of length 50 particle diameters. Results are shown for different values of the friction percentage p.*
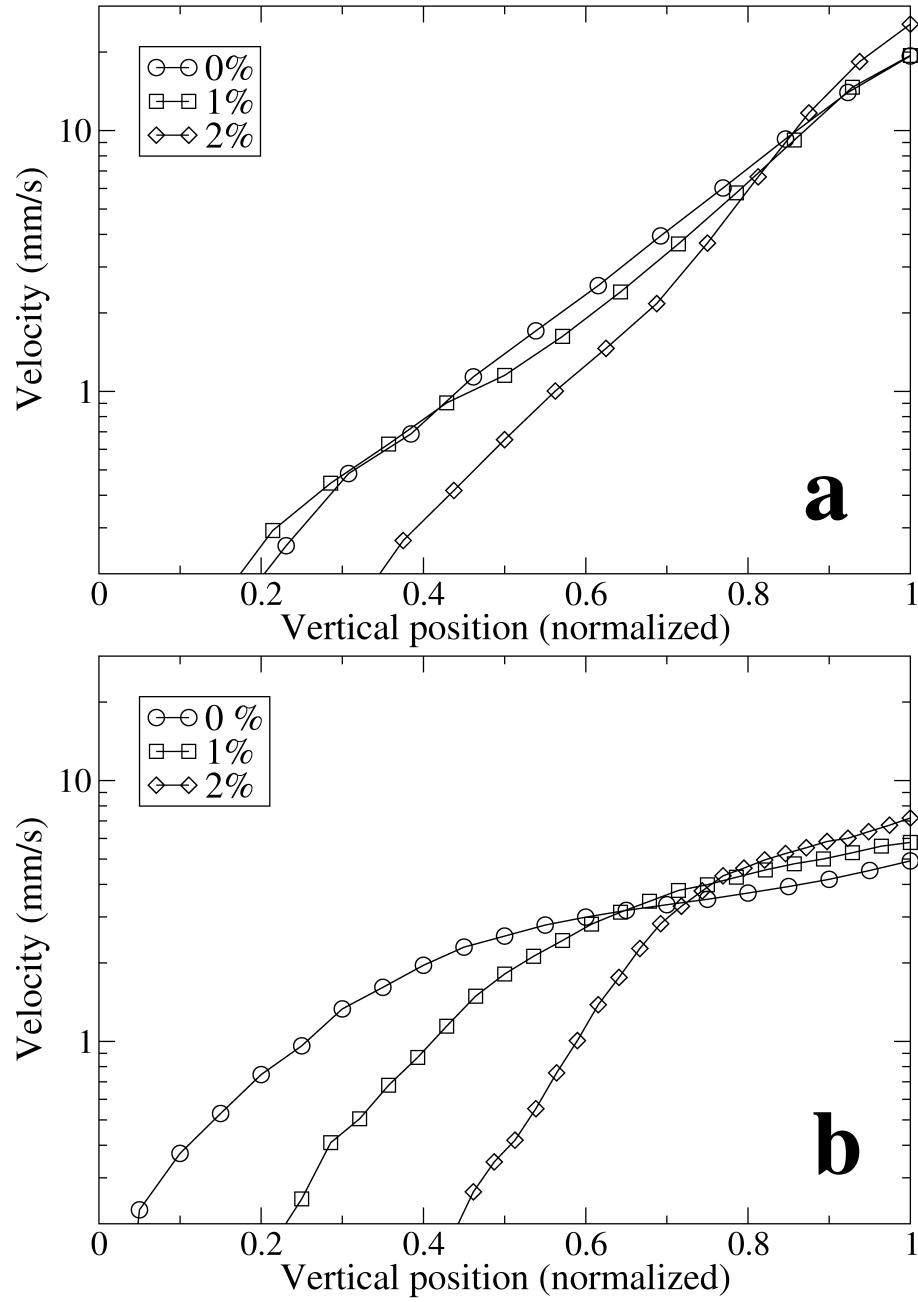
Figure 4.20: *The mean velocity per particle as a function of vertical position in the pile, measured at a horizontal position a quarter of the container length away from the left wall (the vertical line in Figure 4.1). The particle positions are normalized so that the bottom of the pile is 0 and the top is 1. Results are shown for* **a** *$R = 0$ and* **b** *$R = 10$, at different values of the friction percentage p.*
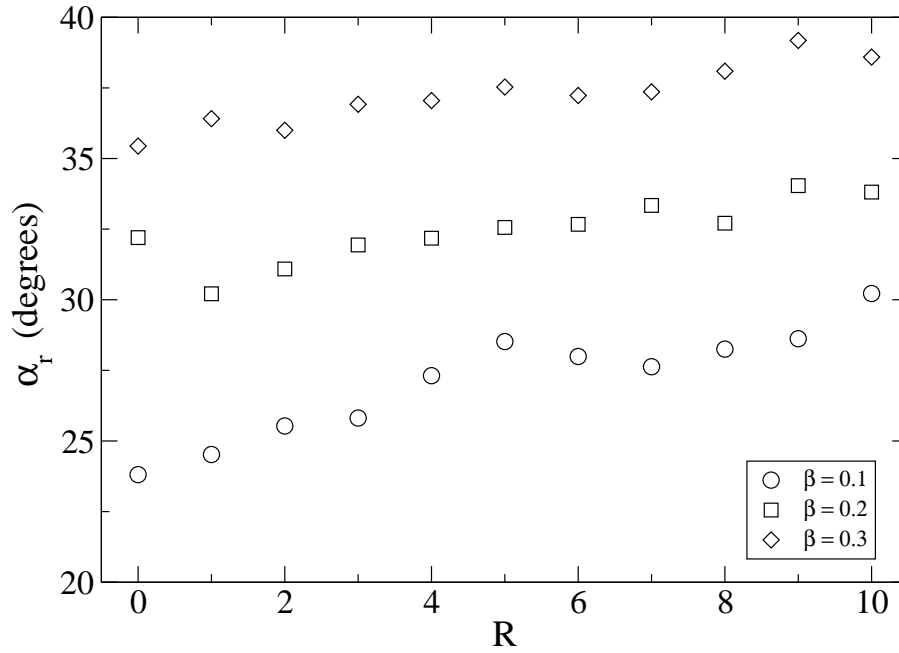
Figure 4.21: *Angle of repose as a function of cohesion strength R in a vertical magnetic field, in a container of length 50 particle diameters. Particles slide against the front and back walls of the container and are subject to a drag force βmg proportional to the particle weight. Results are shown for different values of the drag constant β.*

4.2.11 Application to three-dimensional systems

The shear deep in the bulk of the pile in the absence of front and back walls explains why the dependence of repose angle on magnetic cohesion is weak. The presence of depth-dependent wall friction, however, resulted in a much larger gradient $d\alpha_r/dR$. The inclusion of wall friction was an attempt to model the three-dimensional nature of many experimental geometries.

There is good agreement between $d\alpha_r/dR$ in idealized two-dimensional simulations (both our own and those of Fazekas *et al.* [39]), with the experiments of Forsyth *et al.* [11], despite the fact that the experiments are in three dimensions. However, when wall friction effects were included in the simulations, there was no longer any agreement. One possible explanation is that the simulations were carried out using weakly magnetic particles, for which the point dipole approximation is valid, whereas Forsyth *et al.* used iron spheres, which are ferromagnetic and have a susceptibility $\chi \gg 1$.

Another possible explanation for the apparent discrepancy is that the simulations

do not account for magnetic interactions in the third dimension, perpendicular to the front and back walls. We have estimated the magnetic force F_a on a particle close to the front or back wall of a three-dimensional container, due to other particles in the container, assuming that all particles are weakly magnetic. The horizontal component of the magnetic dipole-dipole force between two point dipoles of moment **m** and separated by **r** is given by

$$\mathbf{F_z} = -\frac{\partial E}{\partial z}\hat{\mathbf{z}} = \frac{3\mu_0|\mathbf{m}|^2}{4\pi|\mathbf{r}|^4}\sin\theta(1 - 5\cos^2\theta)\cos\phi\,\hat{\mathbf{z}}, \qquad (4.7)$$

where $\hat{\mathbf{z}}$ is a unit vector in the direction perpendicular to the wall and ϕ is the azimuthal angle. We calculate the contributions to the horizontal force F_a on a point dipole from all volume elements in the bulk, and integrate over the infinite half-space with $z > 0$ and $|\mathbf{r}| > d/2$. (The vertical component to the magnetic force cancels out due to symmetry.) We find that the dipole experiences an attractive force into the bulk of F_a=1.5 F_v.

Thus, particles close to the front and back walls of the container experienced a net attractive force pulling them towards the bulk of the pile and away from the walls. We speculate that this attraction will reduce the effect of wall friction on both the repose angle and its rate of increase with cohesion, and that the system will behave more like our idealized two-dimensional simulations. This may be the cause of the weakness of the effect of magnetic cohesion on the angle of repose observed experimentally.

Recent experiments on granular avalanches in confined geometries subject to electric fields demonstrated that electric cohesion and wall interactions can significantly influence the repose angle [75]. It would therefore be interesting to investigate whether magnetic systems exhibit similar behaviour, as suggested by our calculations in this section.

We investigate this idea with a series of three-dimensional simulations, described in the next section.

4.3   Three-dimensional simulations

4.3.1   Introduction

In this section we present the results of three-dimensional simulations of avalanching granular piles in a narrow container. The simulation method and parameters are described in Chapter 2. Collisions between particles and container walls were calculated in the same way as particle-particle collisions, with the walls treated as particles with an infinite mass and infinite radius.

We measured the angle of repose as a function of the cohesion strength R and the width of the container. We also measured the transverse (z-direction) magnetic force F_a acting on particles close to the front and back walls of the container, and the normal force F_w exerted (also in the z-direction) by particles in contact with these walls. Both of these forces were averaged over a period of 150 seconds, in each neighbour cell. We investigated how these forces vary with container width and cohesion.

We used a container with a horizontal length of 25 particle diameters. This was smaller than for our two-dimensional simulations (50 diameters) because three-dimensional simulations are more computationally intensive due to the greater number of degrees of freedom and the larger number of particles required. We varied the length of the container between three and ten particle diameters. The pile was formed in the same way as in our two-dimensional simulations. Particles were introduced into the system, one every 3000 time steps. Each new particle was released with zero velocity on the left side of the container, at a height just greater than that of the highest existing particle in the pile. Hence newly-introduced particles had zero momentum, and the low momentum obtained by falling from the starting position to the top of the pile did not cause any significant disturbance upon impact. Particles colliding with the base of the container became stuck, forming an uneven surface upon which the pile was constructed. Particles reaching the right side were removed from the system. To determine the angle of repose of the pile, the length of the container was divided into bins, and the highest particle in each bin identified. A least-squares straight line fit was applied to these particles.

4.3.2 Literature review of simulations of three-dimensional slopes

Zhou *et al.* [76–78] have studied the angle of repose of monosized spheres in simulations using a three-dimensional distinct element method. The simulation started by randomly generating spheres in the upper part of a container, and allowing them to settle under the influence of gravity, supported by a fixed plate. The ends of the plate were then removed to create two outlets, through which the spheres fell. The remaining spheres on the central plate formed a granular pile.

The authors incorporated a rolling friction model in the simulations: a torque was applied to each particle in such a direction as to oppose its rotation, proportional to the normal contact force with a coefficient of rolling friction. Two different formations of rolling friction were considered and compared: torque independent of relative angular velocity; and torque directly proportional to angular velocity. The former model was shown to be more physical in that it produced heaps of greater stability. The angle of repose of spherical particles depended strongly on the rolling friction coefficient, to such an extent that a stable heap could not be formed on a smooth horizontal plane in the absence of rolling friction. The angle of repose increased with friction (both rolling and sliding), and was found to decrease with particle size. The angle of repose decreased with container thickness until the thickness was about 20 particle diameters, at which point edge effects were negligible and the repose angle constant.

Li *et al.* [54] compared the results of three-dimensional discrete element simulations with experiments on piles of spherical particles (glass and steel). The simulations used Hertzian contacts, and the Mindlin-Deresiewicz model [47] in the tangential direction. The coefficient of friction was measured experimentally to enable simulations and experiments to be compared. Particles were glued to a board so that there was a multi-point contact between the board and a flat board underneath. The upper board was then pulled with a constant force F. From this and the normal force N (the weight of the upper board), the coefficient of friction μ could be calculated.

Two different geometrical arrangements were used. Firstly, particles were discharged into a narrow (5.5 particle diameters) rectangular cell, from either the centre or the side of the cell. There was good agreement between the angles of repose obtained through experiments and through simulations. With particles discharged from the centre of the container, the repose angle was 26.3° (experiment) and 26.9° (simulation). The corresponding angles for particles discharged at the side of the container were 26.4° (experiment) and 27.2° (simulation). Secondly, a conical pile was formed on a flat surface. The slope angle was lower than in a rectangular cell: 23.2° (experiment) and 22.7° (simulation). This is to be expected because in a conical pile the surface is less stable; each particle is slightly in front of its neighbours. See Section 1.4 in Chapter 1 for a more detailed explanation and diagram.

4.3.3 Forces in static granular beds

Before investigating the dynamics of avalanching, we first set out to understand the forces in a static granular bed in the container. We measured the force F_w exerted in the z-direction on the front and back walls. F_w is the time-average of the force exerted by one particle in contact with the wall. The bed was formed by creating particles in a regular grid and allowing them to fall under gravity. We took our measurements after the particles had settled and the kinetic and rotational energy had been dispersed by collisions.

Figure 4.22 shows the variation with R of the transverse magnetic force F_a and the normal force F_w exerted by particles on the front and back walls of a container of width three particle diameters. As the transverse magnetic force F_a increased, the particles were attracted inwards towards the bulk of the pile. Particles thus exerted a smaller force against the container walls and F_w was observed to decrease correspondingly. The sum of F_a and F_w was approximately constant.

Corresponding data for a container of width ten particle diameters are shown in Figure 4.23. F_a increased with R at the same rate as for a narrower container. F_w, however, decreased with R at a faster rate.
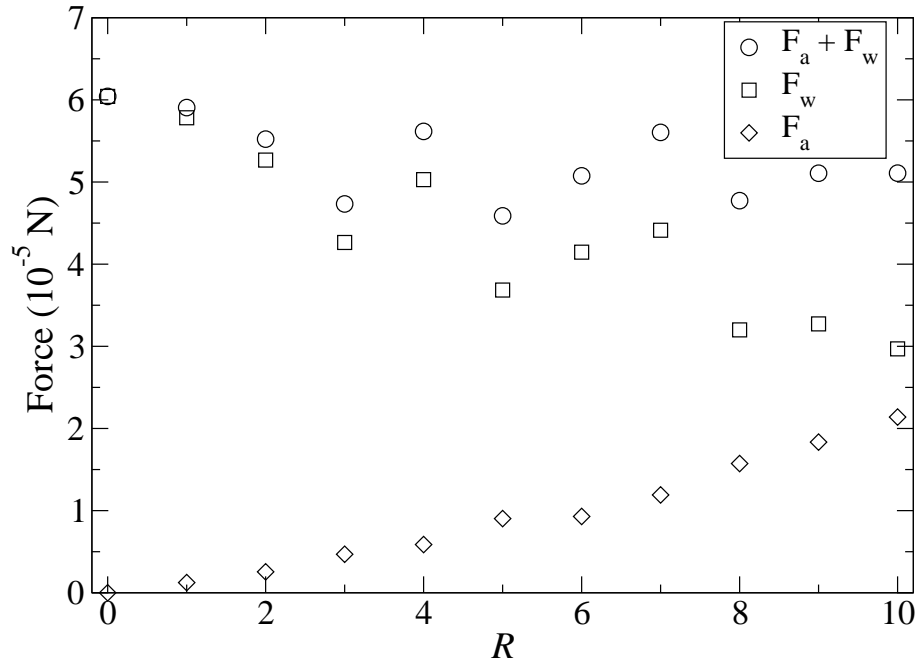
Figure 4.22: *Transverse magnetic force F_a and normal wall force F_w as a function of cohesion strength R for a static bed in a container of width three particle diameters*
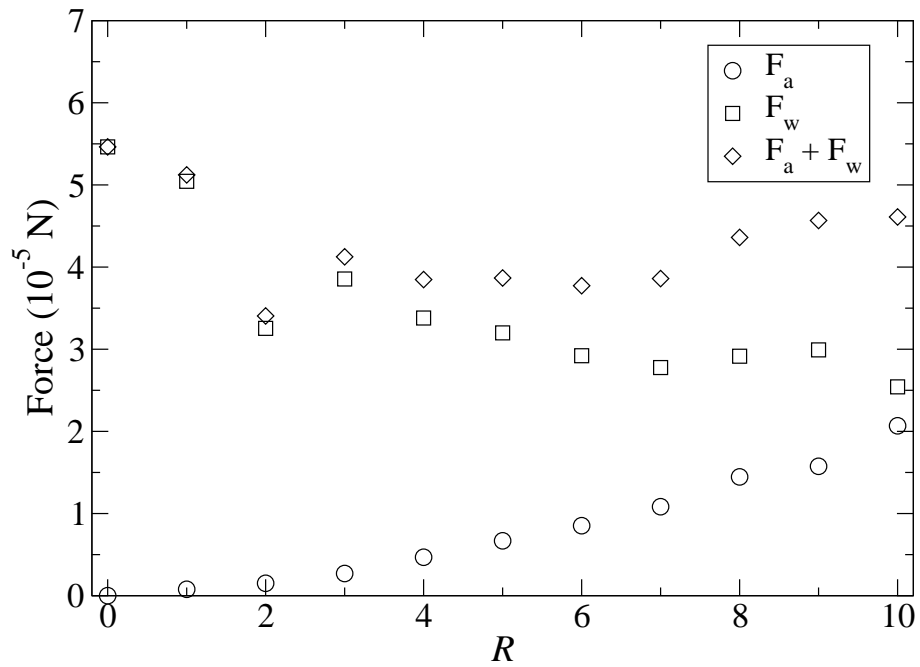
Figure 4.23: *Transverse magnetic force F_a and normal wall force F_w as a function of cohesion strength R for a static bed in a container of width ten particle diameters*

4.3.4 Angle of repose

Figure 4.24 shows the angle of repose α_r plotted against R for a container with a length of 25 particle diameters and a width of three particle diameters. The zero-field angle was just over $29°$, decreasing rapidly to a minimum of $26°$ at around $R = 1.5$, then increasing steadily.

We repeated the simulation for containers with widths of between three and ten particle diameters. Figure 4.25 shows α_r plotted as a function of R. All of the graphs have the same general shape as for a container of width three diameters; the angle decreased sharply to a minimum at about $R = 1.5$, and then increased steadily. For wider containers the repose angle was lower, and also the dip was more pronounced. In the widest container we used (ten particle diameters) the angle dropped by almost seven degrees between $R = 0$ and $R = 1.5$; for the narrowest container (three particle diameters) this drop was only three degrees.

The observed dip in α_r is counterintuitive; one would expect cohesion to cause the slope angle to increase rather than decrease. We are not aware of this effect being reported in the literature.

The observed decrease in α_r was related to the frictional interactions with the container walls. Figure 4.26 compares the slope angle as a function of R for systems with different values of the particle-wall friction coefficient μ_w. (The particle-particle friction coefficient was unchanged.) In the absence of wall friction ($\mu_w = 0$), α_r increased monotonically and no dip was observed. As the wall friction increased, the slope angle α_r also increased, and the dip became more significant.

4.3.5 Measurements of transverse magnetic force

We suggest that the initial decrease in α_r was due to the horizontal magnetic force F_a pulling the particles away from the front and back walls of the container, and thus decreasing the stabilizing effects of wall friction. As R increased further, cohesion caused the slope angle α_r to increase again. To investigate this possibility further, we measured F_a as a function of R for containers of different widths.

Figure 4.27 shows the transverse magnetic force F_a plotted against R for a con-
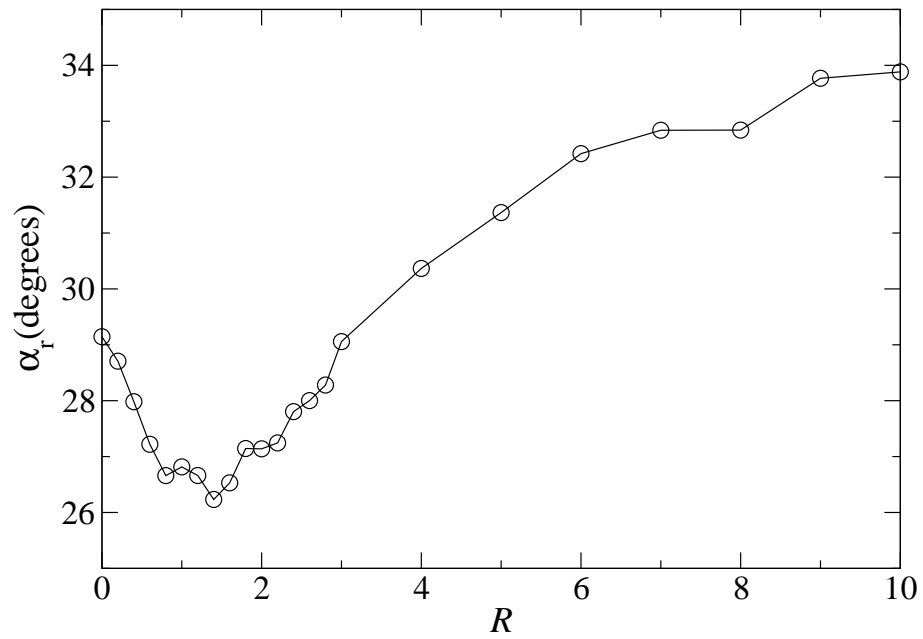
Figure 4.24: *The angle of repose of a granular pile in a container of width three particle diameters, as a function of the cohesion strength R*
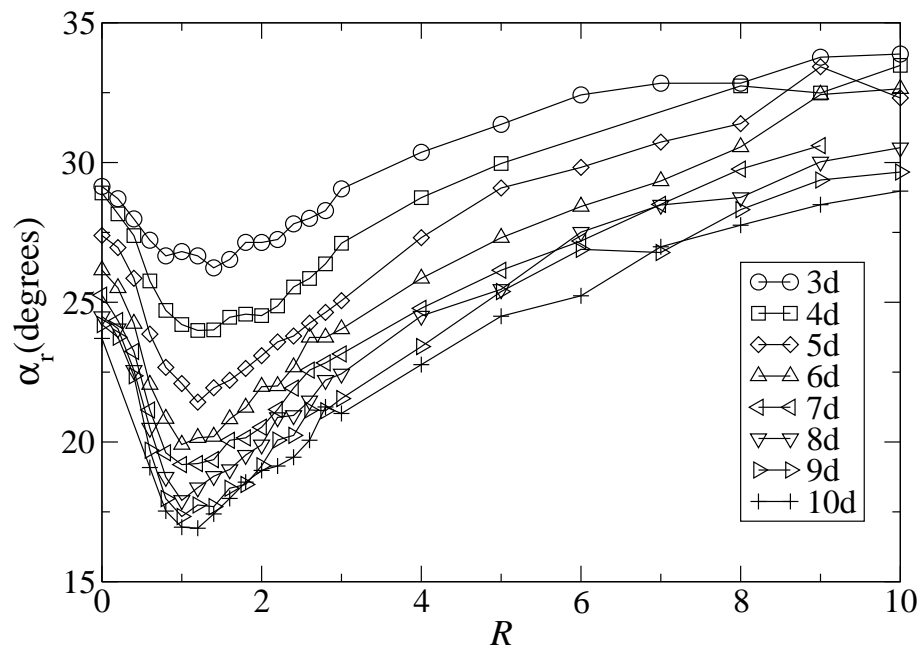
Figure 4.25: *The angle of repose of a granular pile as a function of the cohesion strength R, for different container widths*
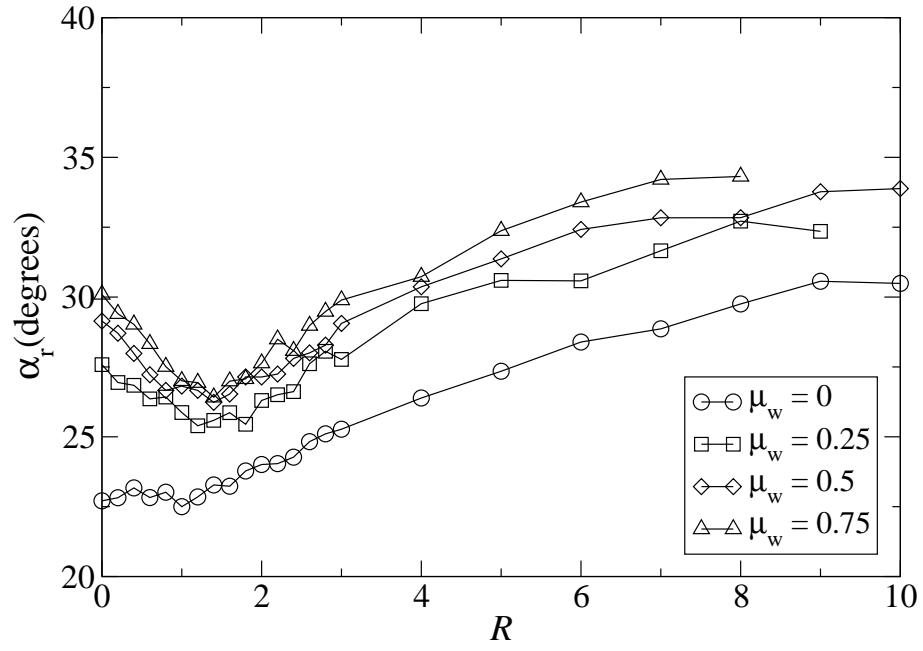
Figure 4.26: *Slope angle α_r as a function of the cohesion strength R for a container of width three particle diameters, for different values of the wall friction coefficient μ_w*
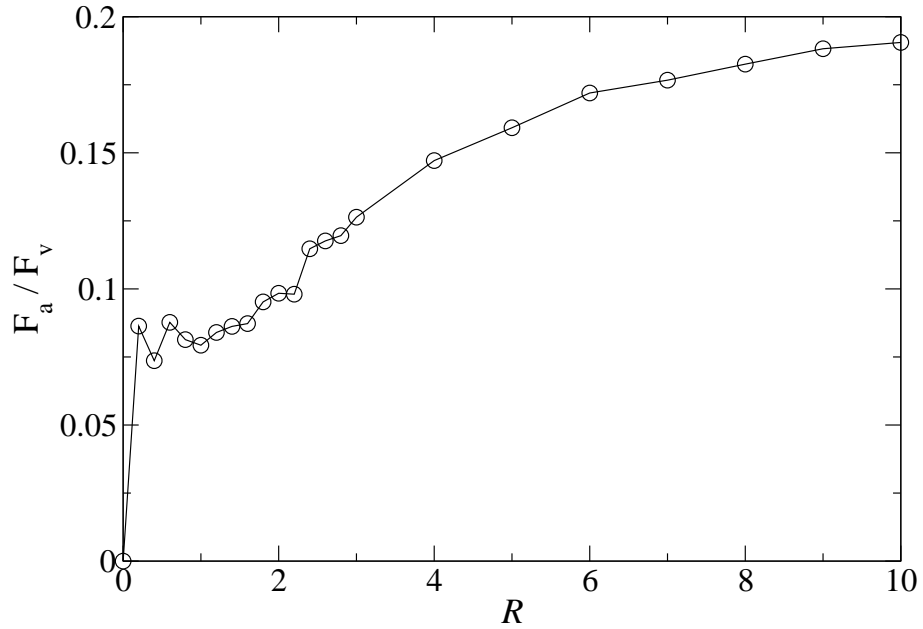
Figure 4.27: *F_a/F_v as a function of the cohesion strength R for a container of width three particle diameters*

tainer with a length of 25 particle diameters and a width of three particle diameters. F_a increased monotonically from 0.08 F_v at $R = 0$ to 0.19 F_v at $R = 10$. We took the time average of F_a over a run of 180 seconds simulated time, averaging over each neighbour cell close to the front and back walls of the container. A positive value of F_a signifies that the magnetic force was pulling the particles away from the container walls and towards the bulk.

The force F_a was smaller for wider containers (see Figures 4.28 and 4.29). In fact, when the container width was increased to six particle diameters or more, the force F_a was negative between $R = 0$ and about $R = 1.5$. The negative sign means that the magnetic force was pushing the particles outwards against the front and back walls of the container.

Our simple picture of the transverse magnetic force pulling particles away from the walls and into the bulk, thus reducing the effect of wall friction and lowering the angle of repose, is appropriate for narrow containers (less than six particle diameters). However, in wider containers the situation is a little more complicated. The transverse magnetic force depended sensitively on the local arrangement of nearest neighbours; particles at a greater distance had a much lesser effect. We suggest that the distribution of particles across the width of the container changed with R, and thus affected the value of F_a. To investigate this possibility further, we measured the volume fraction and velocity profiles across the width of the container. Our results are described in the next two sections.

4.3.6 Volume fraction profiles

Figure 4.30 shows the positions at which we measured the volume fraction and velocity profiles. We took a vertical slice a quarter of the container length from the left side. The vertical profile was measured in the centre of the container halfway between the front and back walls (Figure 4.30**a**). The transverse profile was measured both at the surface of the pile and in the bulk, halfway between the pile surface and the base (Figure 4.30**b**).

Figure 4.31 shows the time-averaged volume fraction of particles in the bulk of the pile, at a position a quarter of the container length from the left wall and halfway
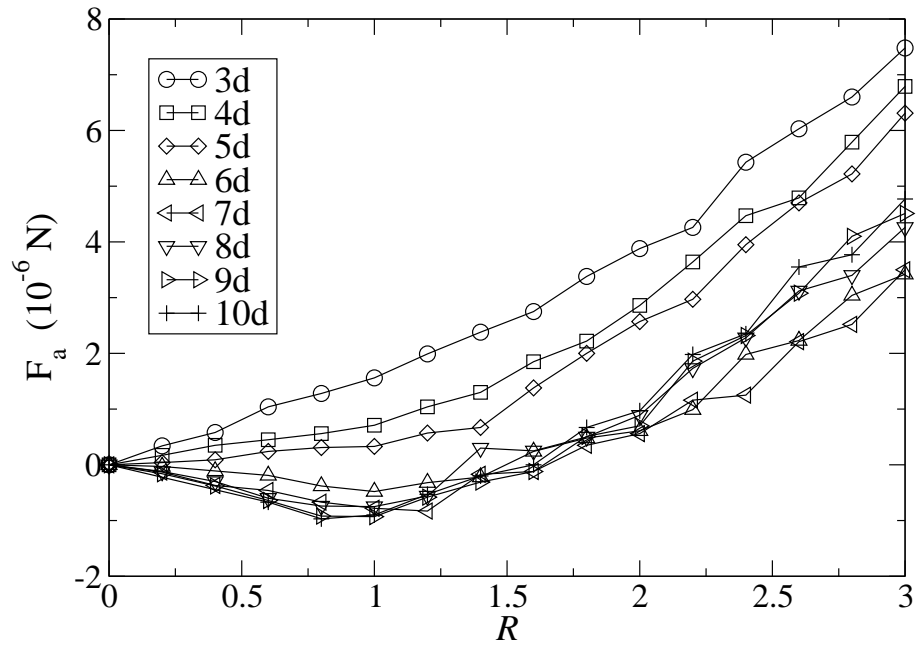
Figure 4.28: *F_a as a function of the cohesion strength R for containers of different widths*
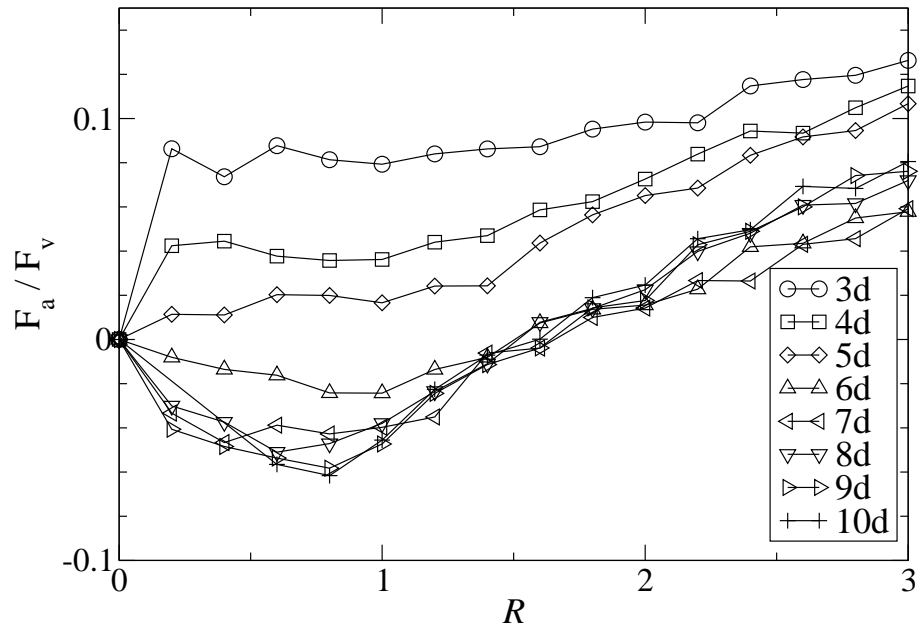
Figure 4.29: *F_a/F_v as a function of the cohesion strength R for containers of different widths*
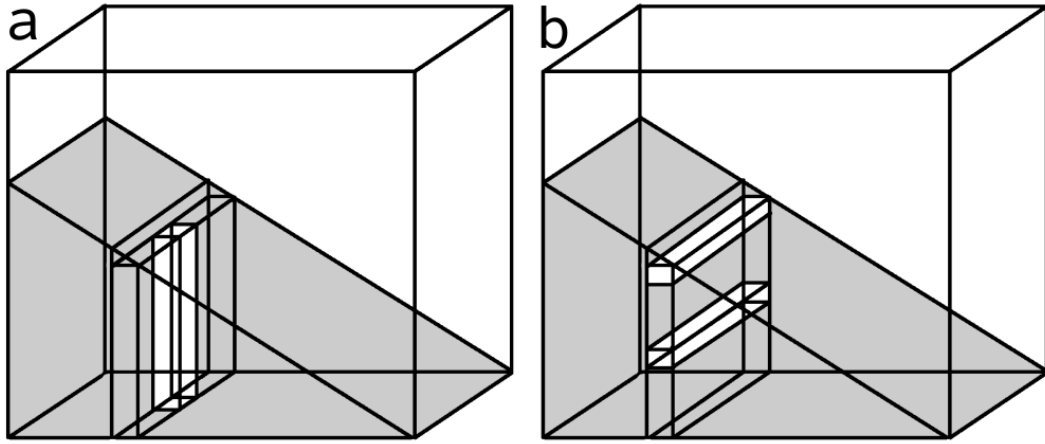
Figure 4.30: *We measured the volume fraction and velocity profile as a function of both transverse position and depth in the pile.* **a** *The vertical profile was measured at a position a quarter of the container length from the left side, in the centre of the container halfway between the front and back walls.* **b** *The transverse profile was measured at a position a quarter of the container length from the left side. We measured both at the surface of the pile and in the bulk, halfway between the pile surface and the base.*
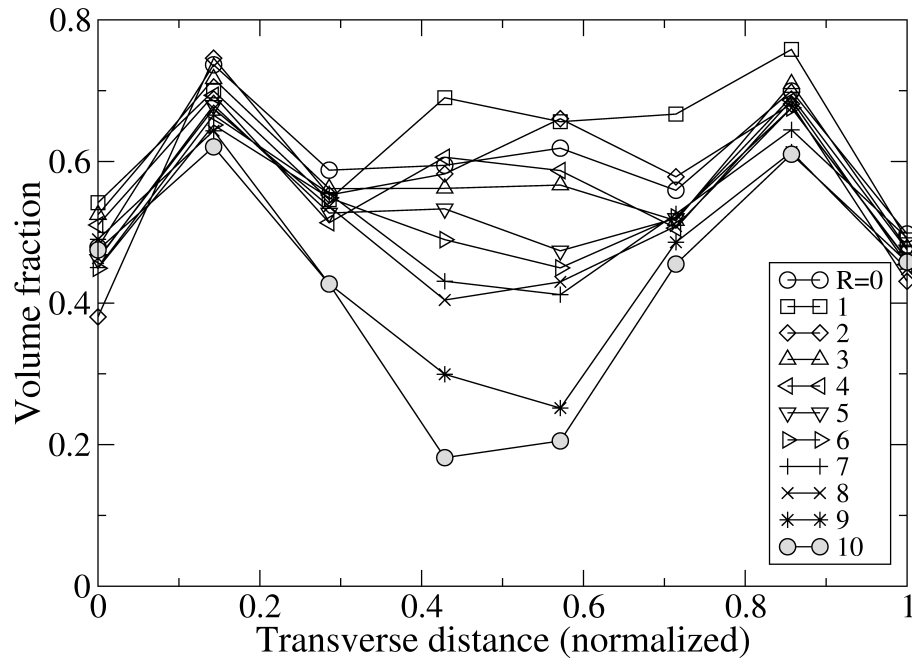
Figure 4.31: *Volume fraction in the bulk of the pile as a function of transverse position in a container of width ten particle diameters, for different values of cohesion strength R*

Figure 4.32: *Volume fraction at the surface of the pile as a function of transverse position in a container of width ten particle diameters, for different values of cohesion strength R*

between the surface and the base (see Figure 4.30). Figure 4.32 shows the equivalent data at the surface of the pile.

In the absence of a magnetic field the volume fraction at the surface of the pile had a convex profile, with particles being more concentrated in the centre than at the edges. This result was consistent with experiments and simulations reported by GDR MiDi [3] on granular flows down an inclined chute. As R increased from zero, the profile flattened. From about $R = 4$ two peaks emerged towards the edges of the container, with a pronounced dip in the centre.

The transverse magnetic interactions were affected by the volume fraction profile. The shape of the profile at low R resulted in a negative value of F_a. The outer particles were pushed outwards towards the edges of the container, resulting in the volume fraction evening out across the pile's width. This change in particle distribution caused a change in the transverse magnetic force, resulting in the force F_a changing sign and attracting the particles back towards the bulk. These particles pulled away from the edges and caused the two observed peaks. The change in shape of the volume fraction profile with R was more pronounced on the surface of the

pile than in the bulk; this difference was to be expected because particles closer to the surface are freer to move.

It should be noted that F_a did not change sign for containers narrower than six particle diameters; this was because the container is not wide enough to undergo the change in volume fraction profile described above.

4.3.7 Velocity profiles

In addition to volume fraction profiles, we measured the velocity profile as a function of depth and transverse position in the pile. Figure 4.33 shows the vertical velocity profile in a container of width three particle diameters, plotted for different values of R. The profile was measured at a horizontal position a quarter of the container length away from the left wall (see Figure 4.30**a**). The particle positions were normalized so that the bottom of the pile was 0 and the top was 1. In contrast with the velocity profiles in our two-dimensional simulations (see Figure 4.13), in which increasing cohesion caused the curve to change shape and the motion to shift farther down into the bed, the profiles for R=1 shows that the motion has shifted a little towards the surface of the pile.

Figure 4.34 shows the particle velocity plotted as a function of vertical position in a wider pile (container width ten particle diameters). Low values of R caused the motion to shift in the opposite direction. For R between 0.4 and 2.4, the velocity profiles were shifted upwards so that particle flow happened closer to the surface than for $R = 0$. Velocity profiles for $R = 5$ and above shifted the other way; particle flow happened deeper in the pile than for $R = 0$. These were the values of R that had repose angles greater than in zero field.

In order to investigate the effects of the front and back walls of the container, we measured the transverse velocity profiles in a container of width 10 particle diameters, both on the surface and in the bulk of the pile (see Figure 4.30**b**). Figure 4.35 shows the velocity of particles flowing at the surface of the pile. The transverse distance was normalized so that a particle touching the front wall was at distance 0 and a particle touching the back wall was at distance 1. In the absence of a magnetic field ($R = 0$) the profile was fairly flat, with velocity approximately constant across
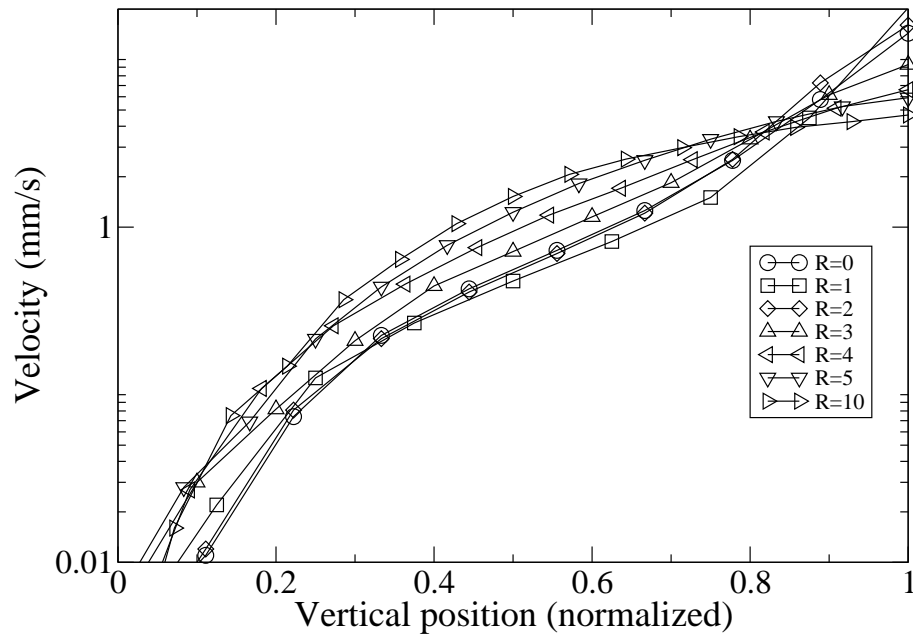
Figure 4.33: *Velocity profile as a function of vertical position in a container of width three particle diameters, for different values of cohesion strength R*
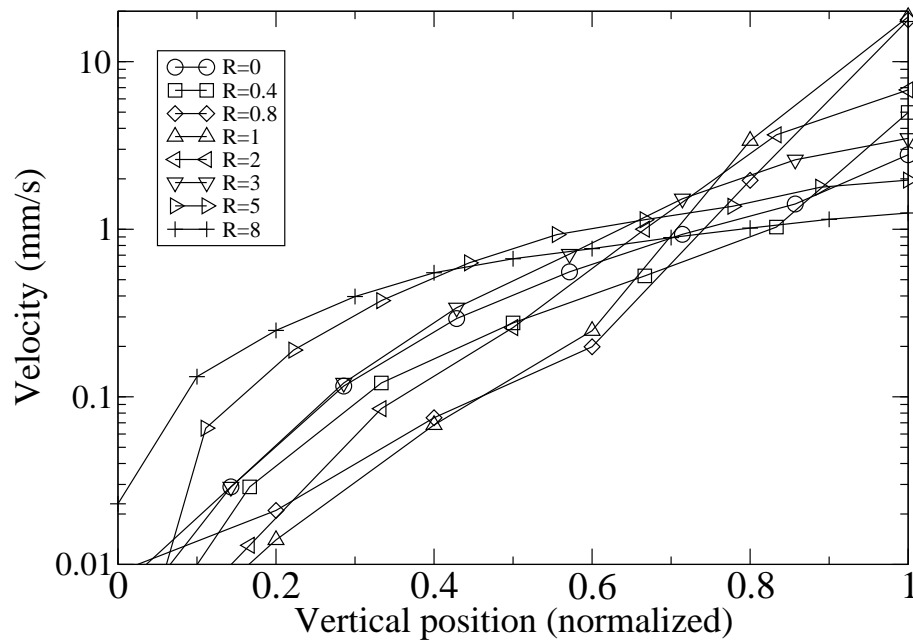
Figure 4.34: *Velocity profile as a function of vertical position in a container of width ten particle diameters, for different values of cohesion strength R*

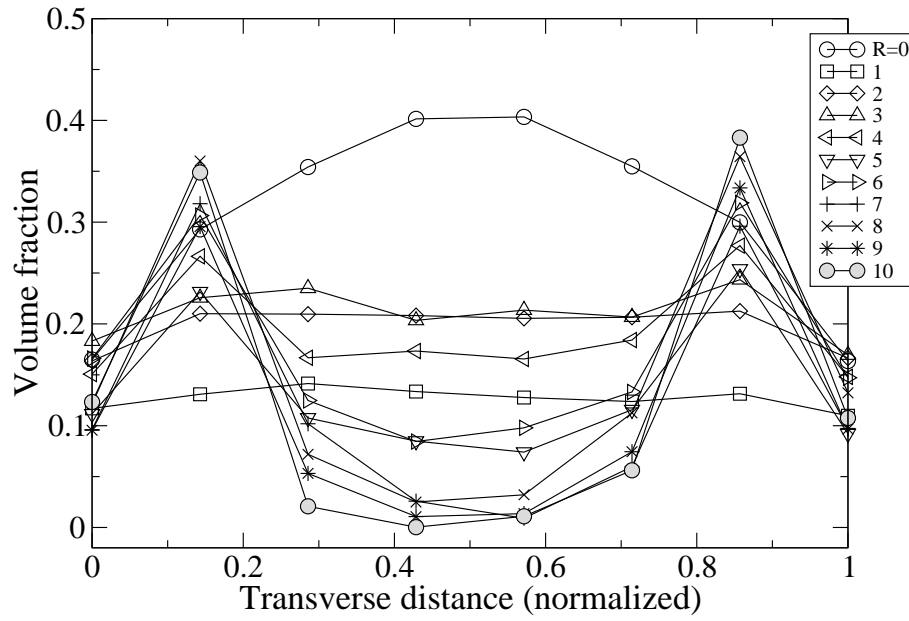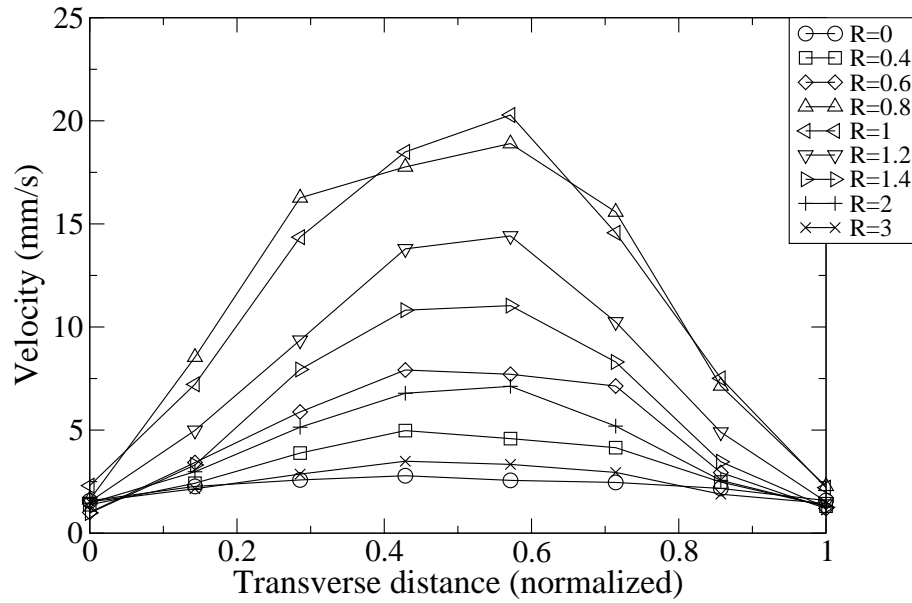**Figure 4.35:** *Transverse velocity profile of particles flowing at the surface of a pile in a container of width ten particle diameters, for different values of cohesion strength R*
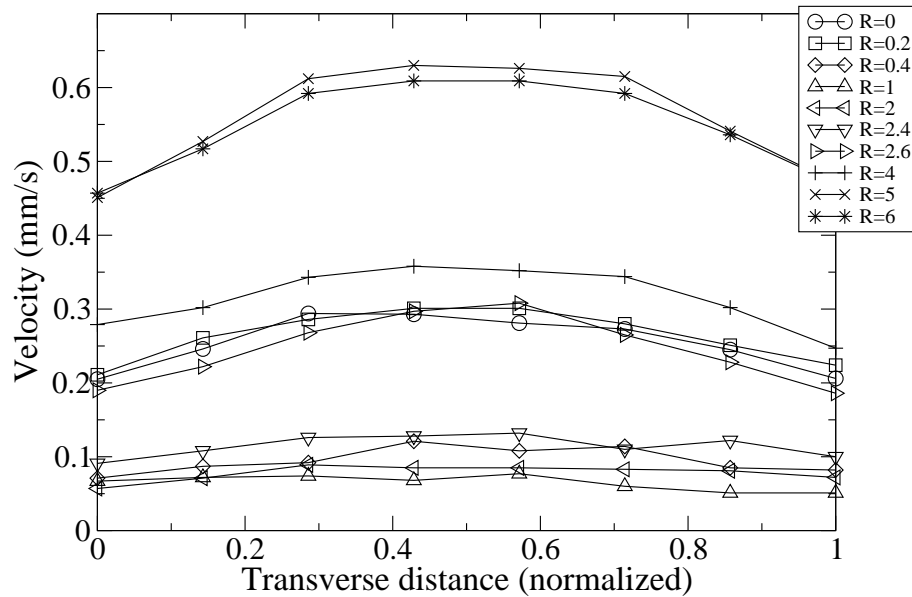
Figure 4.36: *Transverse velocity profile of particles flowing in the bulk of a pile in a container of width ten particle diameters, for different values of cohesion strength R*

the width of the pile (very slightly slower towards the walls). As R increased the velocity increased substantially and the profile changed shape. The particles were flowing much faster in the centre of the pile than towards the walls. The highest peak velocity and most curved profile occurred at $R = 1$. As the cohesion was increased further, the particle velocity decreased and the profile began to flatten. However, the profile was still curved and the velocity was greater in the centre than close to the container walls.

Figure 4.36 shows the velocity of particles flowing in the bulk of a pile plotted as a function of transverse distance across a container of width ten particle diameters. The velocity profile was measured halfway between the base and the surface of the pile. The lines fell into three distinct bands: a lower band (velocities ~ 0.1 mm/s, $0.4 \leq R \leq 2.4$); a middle band (velocities ~ 0.3 mm/s, $R \leq 0.2$ and $2.6 \leq R \leq 4$); and an upper band (velocities ~ 0.5 mm/s, $5 \leq R \leq 10$). Higher surface velocities generally correspond to lower bulk velocities. For the values of R in the lower band, the surface velocity was significantly greater than in the absence of cohesion, and the velocity profiles in Figure 4.35 were more curved.

For R between 0.4 and 2.4, the values of R in the lower band in Figure 4.36, the repose angles were lower than in zero field. Also, for this range of R the vertical velocity profiles in Figure 4.34 were shifted upwards so that particle flow happened closer to the surface than for $R = 0$. The upper band in Figure 4.36 with $R = 5$ and above corresponds to repose angles greater than in zero field. The vertical velocity profiles shifted in the opposite direction; particle flow happened deeper in the pile than for $R = 0$.

The shift in motion towards the surface of the pile observed in wide containers (6 particle diameters or greater) explains the decrease in slope angle at low values of R. In narrower containers, the shift in velocity profile was less significant. Hence the drop in α_r was smaller than for wider containers.

4.4   Conclusion

We used a two-dimensional molecular dynamics simulation to investigate the effect of magnetic cohesion on the repose angle of a granular pile. We found that the repose angle increased linearly with cohesion strength R. The effect was weak, even when magnetic forces were ten times as strong as gravity.

When a magnetic field was applied, the magnetic forces partially cancelled out deep in the pile. Motion happened by shearing deep within the pile, in addition to motion close to the surface. We showed that the slope angle had only a weak dependence on the magnetic field because shear deep in the pile prevented the angle of repose from increasing substantially.

We investigated the effect of different implementations of friction with the front and back walls of the container. The choice of friction model dramatically affected both the zero-field repose angle and its rate of increase with cohesion. Depth-dependent friction caused an increase in the zero-field repose angle and in the gradient $d\alpha_r/dR$. Depth-independent friction caused an increase in the zero-field repose angle, but $d\alpha_r/dR$ remained unchanged.

We discovered that in a three-dimensional container the angle of repose decreased with cohesion, reaching a minimum at about $R = 1.5$, and then steadily increased. This dip was more pronounced for greater container widths. We measured the transverse magnetic force F_a on particles near the front and back walls of the container.

We found that in containers with a width of at least six particle diameters, the force changed sign at about $R = 1.5$. Particles were pushed outwards towards the walls for $R < 1.5$, and as R increased beyond this value the particles were pulled towards the bulk and away from the walls. We suggest that this change in F_a was due to the rearrangement of particles in the pile; magnetic forces depend sensitively on the positions of neighbouring particles. We confirmed this idea by plotting the volume fraction profile across the width of the pile. The volume fraction profile changed shape as R increased: at $R = 0$ there was a greater concentration of particles in the centre of the container than near the front and back walls; as R increased the profile flattened due to particles being attracted to the walls; and as R increased further, two peaks were observed as F_a changed sign and pulled the

outer particles inwards towards the bulk. We also measured the velocity profile as a function of both transverse position and depth in the pile. The velocity was substantially greater towards the surface of the pile, in a middle region between the front and back walls. It was this motion that reduced pile stability and caused the drop in repose angle at low values of R.

Narrower containers (width less than six particle diameters), however, did not have sufficient space for a quickly moving middle region. The transverse magnetic force F_a was positive for all values of R. In this case the dip in slope angle was due to the transverse magnetic force pulling the particles away from the front and back walls, thus reducing the stabilizing effect of wall friction.

Chapter 5

Slope angles of fine bismuth grains

5.1   Introduction

This chapter presents a series of experiments on fine bismuth grains in a vertical magnetic field. We took a different approach to the simulations described in the previous chapter. Our experiments were conducted with non-spherical grains immersed in a liquid, with a much greater number of grains than used in our simulations.

The next chapter deals with the interactions between non-magnetic 'voids' in magnetic fluids. Understanding magnetic particles in non-magnetic liquid is a first step towards this.

It should be noted that our experiments with grains in fluids were not the same as liquid-bridge experiments. In our experiments, the grains were fully immersed in the liquid, and cohesion existed because of magnetic dipole-dipole interactions between the particles. In liquid bridge experiments, a small amount of interstitial liquid was added to dry particles (the volume of liquid was much less than the volume of the particles), and cohesion existed due to the liquid forming bridges between neighbouring particles.

In this chapter we first describe our experimental techniques, and then report the results of our angle of repose experiments. The angle of repose was measured using the draining crater method, in which the grains were allowed to drain from an upper chamber to a lower chamber and the angle of the resulting slope was measured. We also investigated the effect of varying the aperture size. We used bismuth grains

in different size ranges, both in air and in water. Bismuth was chosen for these experiments because it is strongly diamagnetic ($\chi = -1.65 \times 10^{-4}$).

5.2 Experimental details

In this section we describe the techniques used in our draining crater experiments. We used the 16.5T superconducting magnet described in detail in Chapter 3 Section 3.5.1, conducting the experiments at the central field position within the bore of the magnet. The magnetic field is vertical.

We characterized the strength of the magnetic cohesion by using the ratio R of the maximum magnetic dipole-dipole force F_v between two particles in contact, and the particle weight mg. The cohesion strength R is given by

$$R = \frac{\chi^2 B^2}{4\mu_0 \rho dg},\tag{5.1}$$

where χ is the magnetic susceptibility, B is the magnetic field strength, μ_0 is the permeability of free space, ρ is particle mass density, d is the particle diameter and g is acceleration due to gravity (see Chapter 3, Section 3.3.5). The angle of repose measurements were carried out at different field strengths, between $B = 0$ and $B = 14$T.

Our bismuth grains were non-spherical and highly variable in shape; the mean aspect ratio was 1.7, with a standard deviation of 0.3. Some particles were close to spherical and had an aspect ratio ≈ 1, but a few were very long and thin, with an aspect ratio of 3-4. As the grains were non-spherical, we defined the 'diameter' of a particular size range to be the mean of the mesh sizes of the two sieves used to separate out the grains in that size range.

The purpose of fully immersing the bismuth grains in water was to enable the results to be more easily compared to our experiments on non-magnetic particles in a paramagnetic fluid (described in Chapter 6). The susceptibility and density of the fluid have an effect on the value of the cohesion strength R. In addition to experiments on bismuth grains fully immersed in water, we measured the angle of repose of dry bismuth grains. This enabled us to investigate the effect of a liquid on the angle of repose.

The equation for cohesion strength R of particles in a fluid is given by

$$R = \frac{(\Delta\chi)^2 B^2}{4\mu_0 (\Delta\rho) d\tilde{g}}, \tag{5.2}$$

where $\Delta\chi$ is the difference in susceptibility between the grains and the fluid, and $\Delta\rho$ is the difference in density. The value of R in a fluid therefore depends on $(\Delta\chi)^2/\Delta\rho$. Water is slightly diamagnetic ($\chi = -9.0 \times 10^{-6}$), so $\Delta\chi$ for bismuth immersed in water is slightly smaller in magnitude than $\Delta\chi$ for dry bismuth. Also, $\Delta\rho$ for bismuth in water is lower than $\Delta\rho$ for bismuth in air. The presence of water subjects the bismuth particles to a buoyancy force, which is equal in magnitude to the weight of water displaced. This force is represented in Equation 5.2 by the use of $\Delta\rho$ instead of ρ.

The value of R for bismuth in water was very close to the value of R for bismuth in air; the two differ by only 0.2 %. The decrease in magnitude of $\Delta\chi$ due to the presence of water was almost cancelled out by the decrease in $\Delta\rho$, leading to very similar values of R for bismuth in air and in water.

We accounted for the fact that the upper and lower slopes were not exactly in the central field position by using the effective gravity $\tilde{g}$ instead of g in Equation 5.2. For more details about magnetization forces and effective gravity, see Appendix 1. The change in effective gravity $\tilde{g} - g$ was proportional to B^2. At $B = 14$ T, we calculated $\tilde{g} = 7.6$ ms^{-2} at the centre of the upper slope (1 cm above the cell's partition), and $\tilde{g} = 13.1$ ms^{-2} at the centre of the lower slope (1.5 cm below the cell's partition).

There are different geometrical configurations for draining crater experiments; these are described in Chapter 1, Section 1.4. In order to make best use of the limited space inside the 5 cm diameter magnet bore, we used a rectangular cell. There must be space in the magnet bore for a mirror and plumb line in addition to the cell. A rectangular cell had the advantage of being able to use almost the full width of the bore, whereas a cylindrical cell would need to be smaller to accommodate the mirror and plumb line.

In our experiments we used a specially designed rectangular cell of dimensions 6 cm $\times$ 4 cm $\times$ 1 cm. The cell contained an upper chamber with a small aperture to allow matter to drain, and a lower chamber to collect it (see Figure 5.1). At the
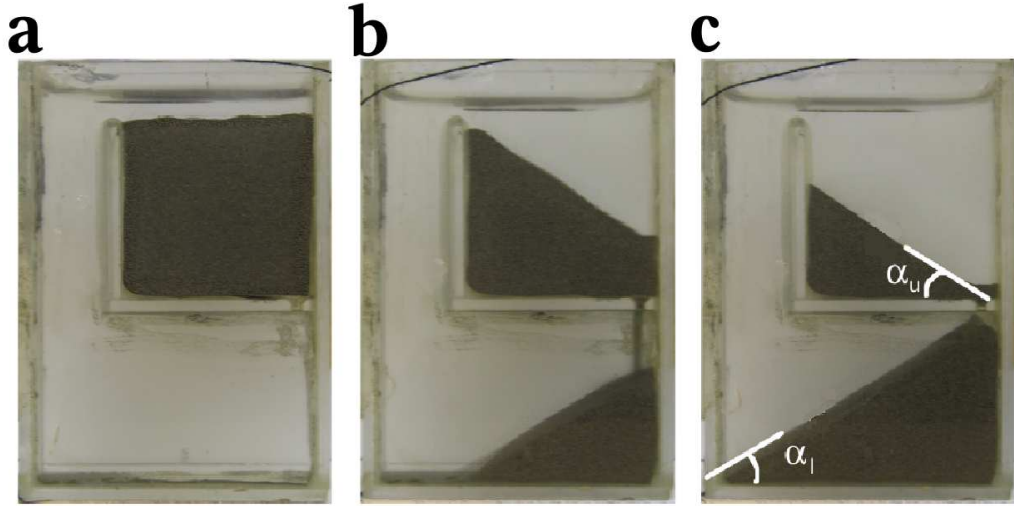
Figure 5.1: *Draining crater experiments:* **a** *the upper chamber was filled with bismuth powder to a bed depth of 2 cm* **b** *the wedge was partially raised, allowing bismuth to flow from the upper chamber to the lower chamber* **c** *the repose angles of both upper and lower slopes were measured.*

centre of the magnet the vertical field was fairly constant; it varied by 4.0% over a vertical distance of 6 cm (the height of the cell), and by 0.7% over a vertical distance of 2 cm (the depth of the bed).

When the draining crater experiment was carried out with the grains immersed in water, the flow of the grains caused an increase in the pressure beneath the aperture. To prevent this impeding the flow of matter through the aperture, the cell was designed with a small hole through the side of the upper chamber. The existence of the hole allowed the water to circulate without setting up large currents that could have affected the dynamics of slope formation.

The slope angle of the pile in both the upper and lower chambers of the cell can be measured. We define α_u to be the angle of the upper slope and α_l to be the angle of the lower slope. Measurements of α_u were found to be more consistent and repeatable, so most of the results presented in this chapter are measurements of the angle of the upper slope. However, we did measure α_l for the purpose of comparison.

A tapered wedge was placed in the upper chamber of the cell to block the hole. By raising and lowering the wedge, the size of the draining aperture could be varied in a controlled manner.
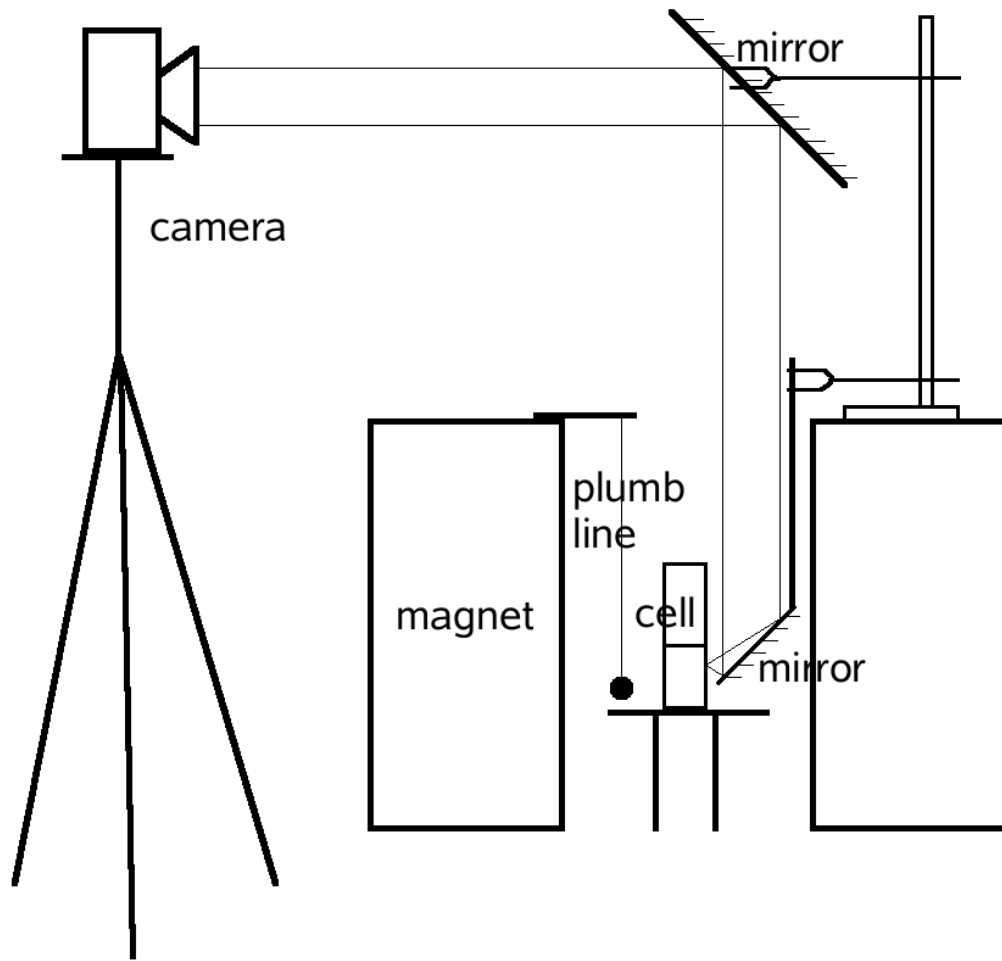
Figure 5.2: *Experimental set-up for angle of repose measurements in the bore of the 16.5 Tesla magnet*

Bismuth powder was poured into the upper chamber to a bed depth of 2 cm. The cell was then lowered into the bore of the magnet in a position such that the partition between the upper and lower chambers was at the central field point. The wedge was partially raised by rotating a long screw thread, and the bismuth powder was allowed to drain through the hole from the upper chamber to the lower.

A large mirror was placed at 45° to the vertical at the top of the magnet. A smaller mirror, also at 45°, was attached to an aluminium rod and lowered into the magnet bore. The vertical position of the small mirror could be adjusted to enable different parts of the cell to be photographed. The experimental arrangement is shown in Figure 5.2. A digital camera with powerful zoom was positioned at a great enough distance from the magnet so that the operation of the camera was not

affected by the high magnetic field. The camera was used to take photographs of both the upper and lower slopes when the powder had finished draining, enabling both α_u and α_l to be measured.

A piece of white paper was placed behind the cell to aid visibility by providing a contrasting background colour. A plumb line, consisting of a piece of (non-magnetic) lead on a long black thread, was also placed in the bore of the magnet. The plumb line could be seen in the photographs, providing a reference point for the angle measurements.

The photographs were analysed with an image manipulation program and the angle between the slope surface and the plumb line measured. Ten photographs were taken at each field strength. An accuracy of within a degree was readily achievable for the upper slope angle, and within two degrees for the lower slope angle. We therefore use error bars of 1° for α_u and 2° for α_l in all of the graphs in this chapter.

5.3 Results of draining-crater experiments

Firstly, we investigated the effect of the size of the draining aperture. We present our results and discuss the dynamics of particle flow and slope formation. We measured the angle of repose of the slope as a function of magnetic cohesion for different particle size ranges, both in air and fully immersed in water.

5.3.1 Aperture size

The size of the aperture through which the granular material drains can be expected to have a significant effect on the flow dynamics. A larger aperture will allow the grains to drain more quickly, causing currents to flow in the surrounding liquid, thus affecting the stability of the upper slope. Also, falling particles will impart momentum to the surface of the slope in the lower chamber of the cell as they land. This impact can flatten the top of the slope, resulting in a pile with a surface that is not straight.

To investigate the effect of aperture size on the flow dynamics and angle of repose, we carried out a preliminary experiment. A finely tapered piece of wood

		partially blocked	unblocked
upper slope	α_u	33.8°±0.3°	32.6°±0.4°
lower slope	α_l	31.5°±0.6°	
(upper portion)	α_2	31.3°±0.6°	26.6°±1.0°
(lower portion)	α_1	31.7°±0.7°	33.3°±0.7°

Table 5.1: *Angle of repose of 63-75 μm bismuth immersed in water, using the draining crater method, comparing results for a fully open and partially blocked aperture. The quoted errors are standard deviations of 10 measurements.*

was inserted into the cell to partially block the aperture. By raising and lowering the wedge the aperture size could be varied. The cell was filled with 63-75 μm bismuth fully immersed in water, up to a bed depth of 2 cm. We started with a fully-blocked aperture and slowly lifted the tapered wedge, enlarging the aperture until the grains just began to flow. Table 5.1 compares the resulting repose angles of both the upper and lower slopes with those obtained by allowing the grains to flow through a fully-open aperture.

The angle of repose of both upper and lower slopes was higher for a smaller aperture. Also, the lower slope surface was not straight for high flow rates. The time taken for the grains to flow from the upper chamber to the lower chamber was about 10 seconds when the aperture was fully open, but several minutes when the aperture was partially blocked.

The difference in the lower slope angle is easily explained: when the aperture was small, the grains flowed much more slowly and landed more gently on the surface of the lower slope. Thus the grains were less likely to disturb the slope and cause an avalanche.

As the lower heap grew in size, a series of avalanches could be observed. As material was added to the top of the heap, the slope became steeper until a critical angle was reached, at which point an avalanche occurred and the slope relaxed to a lower angle. This phenomenon offered an explanation as to why the measurements of the lower slope angle were less consistent and less repeatable than upper slope angle measurements: the lower slope angle varied with time as the heap is being
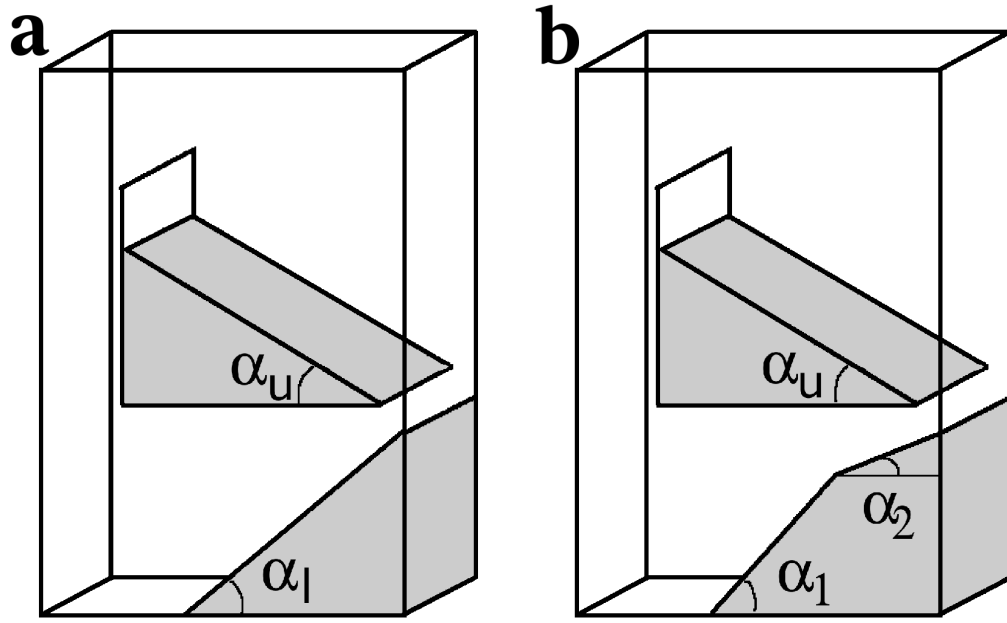
Figure 5.3: a *With a small aperture and low flow rate, the lower slope was a straight line.* **b** *However, at higher flow rates the falling grains could flatten the top of the lower slope.*

formed, whereas the upper slope angle did not.

When the draining aperture was fully unblocked, the upper portion of the lower slope had an angle of $\alpha_2 = 26.6° \pm 1.0°$, significantly less steep than the lower portion, which had an angle of $\alpha_1 = 33.3° \pm 0.7°$. This difference was much smaller for a partially-blocked aperture, where the corresponding slope angles were $\alpha_2 = 31.3° \pm 0.6°$ and $\alpha_1 = 31.7° \pm 0.7°$, which agreed within experimental error. See Figure 5.3 for an illustration.

There is another possible effect of aperture size: when immersed in water, a large aperture will permit a high flow rate of grains. A high flow rate through the draining aperture will cause currents in the water, which may affect the dynamics of particle motion. A current directed down the slope may act to decrease the angle. This effect is a possible explanation of why the upper slope angle α_u also decreased with increasing aperture size.

For the reasons detailed above, in this series of experiments we always used the minimum aperture size that allowed the material to drain, producing the highest possible angles. We used a wedge with a screw thread (see Figure 5.4), which allowed

Figure 5.4: *The draining aperture was closed with a wedge, which could be raised and lowered using a screw thread.*

the wedge to be raised gradually until the grains started to flow.

5.3.2   Effect of surrounding liquid

Figures 5.5 and 5.6 compare the upper slope angle α_u in air and in water, for bismuth in the size ranges 63-75 μm and 75-90 μm respectively. The graphs show good agreement between the repose angle in air and in water, demonstrating that the presence of water in the container had a negligible effect on the repose angle.

Ogale *et al.* [79] measured the angle of repose of steel spheres in a thin cell, immersed in various liquids. The boundaries of the pile were observed to be sharper when immersed in a liquid than in air, suggesting that the presence of a liquid decreased the effect of cohesion due to surface roughness. The repose angle was the same in air and in water.

5.3.3   Angle of repose

Figure 5.7 shows the angle of repose of the upper slope α_u for 63-75 μm bismuth immersed in water, plotted as a function of the cohesion strength R. The graph shows how the angle of repose increased with R. As the grains became more cohesive, they flowed less freely. The aperture had to be opened further for the particles to drain, and the process took longer. At values of R greater than about 0.25, the bismuth grains were so cohesive that they were unable to flow through the aperture.

At low values of R (up to about $R = 0.1$) the graph was approximately linear. After this point, α_u increased more slowly and the graph had negative curvature. We fitted a straight line to the first 8 data points (up to about $R = 0.08$), and found that the gradient was $d\alpha_u/dR = 277°$ per unit R. This was a very dramatic increase in angle with cohesion, greater than that observed in experiments with steel ball-bearings in magnetic fields [11], and in experiments with liquid bridges [12].

Figure 5.8 shows α_u plotted as a function of R for two different size ranges of bismuth in water. Both sets of data lay on the same curve, demonstrating that the size of the particles had little effect on the field-dependence of the angle of repose.

Figure 5.9 shows the angles of repose α_u and α_l of the upper and lower slopes
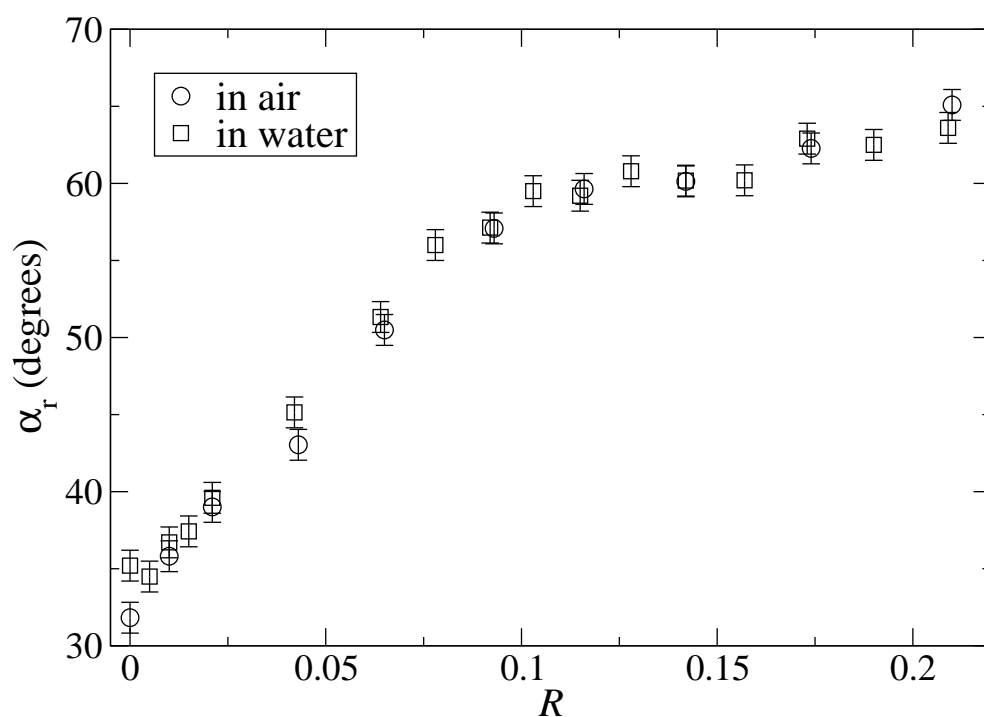
Figure 5.5: *Angle of repose of 63-75 µm bismuth in air and water, upper slope*
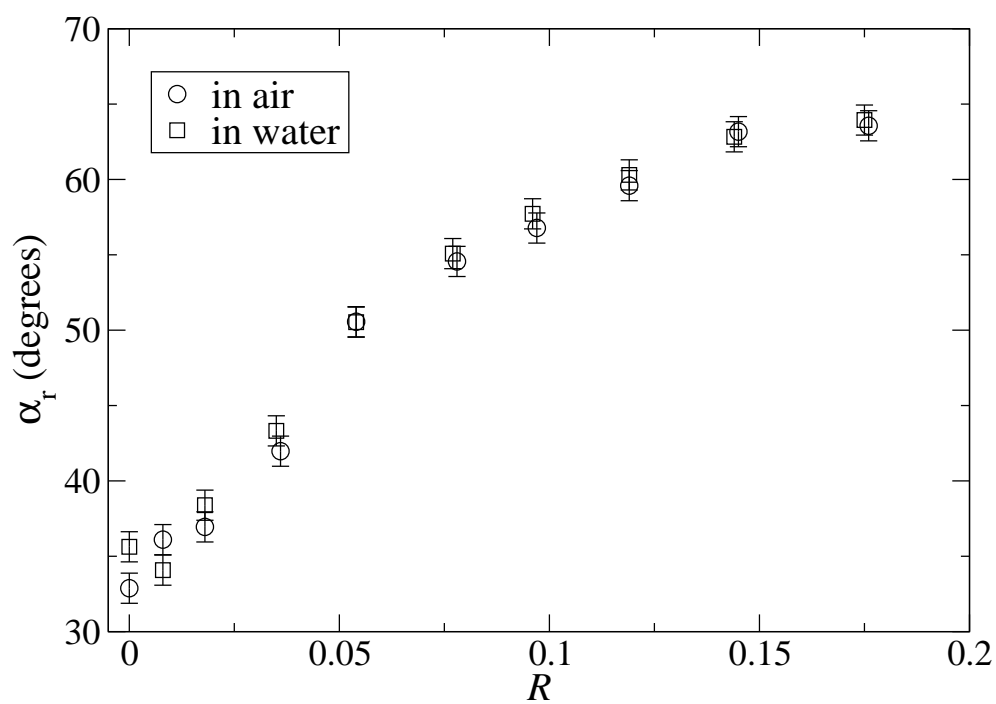
Figure 5.6: *Angle of repose of 75-90 µm bismuth in air and water, upper slope*
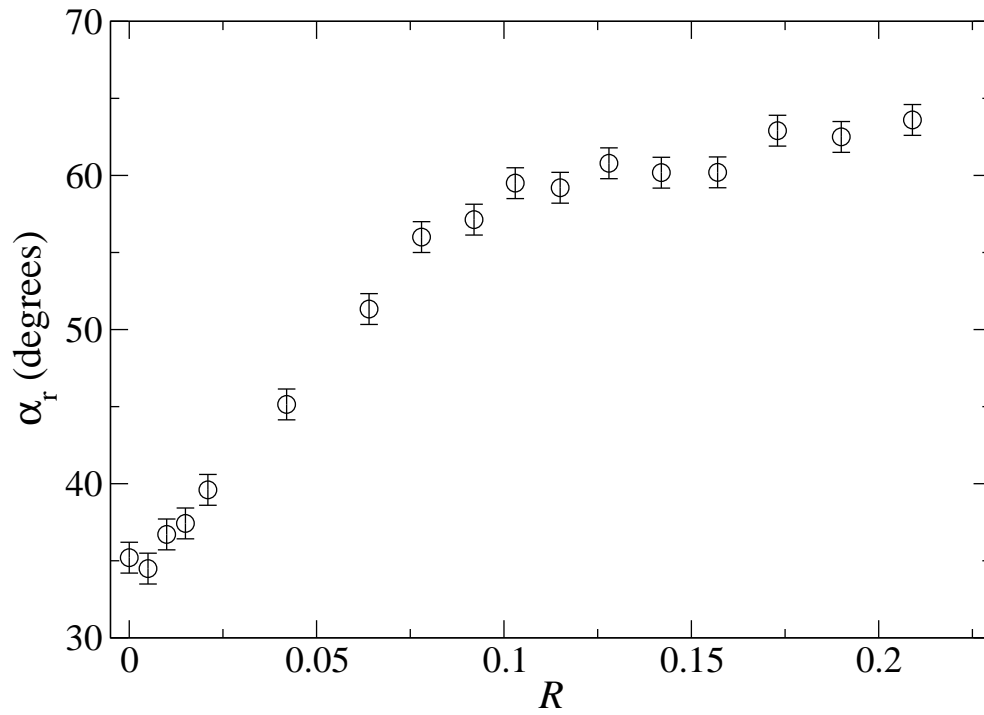
Figure 5.7: *Angle of repose of the upper slope α_u for fine bismuth powder in the size range 63-75 µm immersed in water, in a vertical magnetic field*
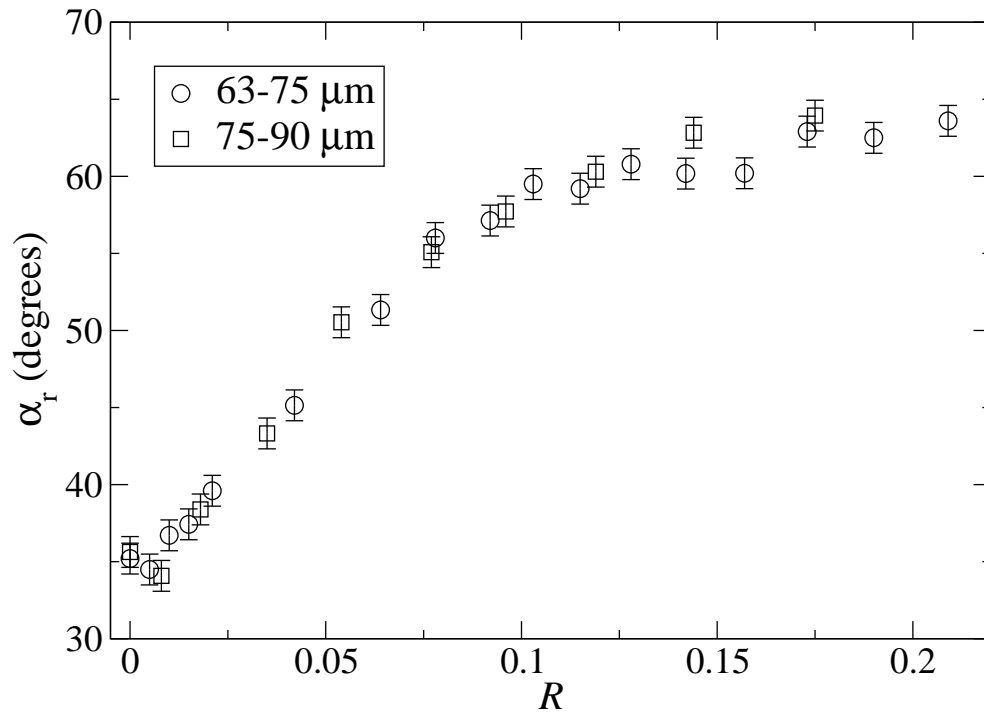
Figure 5.8: *Angle of repose of the upper slope α_u of fine bismuth powder fully immersed in water. Two size ranges were used: 63-75 µm and 75-90 µm*
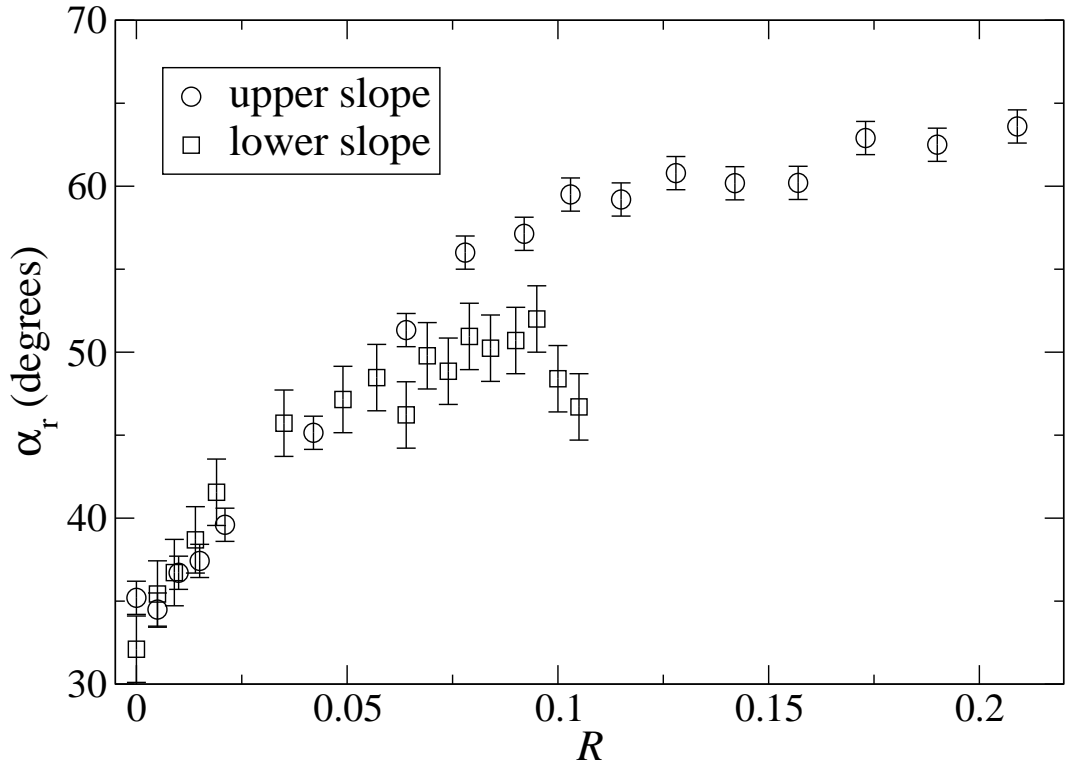
Figure 5.9: *Angles of repose of upper and lower slopes α_u and α_l of 63-75 μm bismuth fully immersed in water*

respectively, for 63-75 μm bismuth fully immersed in water. Both angles lay on the same curve for values of R less than about $R = 0.06$. After this point, the lower slope angle α_l did not increase significantly.

It is interesting to note that the noise on α_l was much greater than on α_u. At higher values of R, a smaller volume of bismuth drained through the aperture. Hence the top of the lower slope was a greater distance below the draining aperture, and the grains had farther to fall. Bismuth grains landing on the top of the heap had a greater impact velocity, which may have affected the stability of the lower heap and limited its maximum angle.

5.4   Conclusion

The observed increase in the repose angle with cohesion was a very large effect; from the linear part of the graph for the upper slope of 63-75 μm bismuth in water (Figure 5.7) we obtained a gradient of $d\alpha_r/dR = 277°$.

In the experiments of Albert *et al.* [12], in which cohesion between spheres was provided by an interstitial liquid, the angle of repose increased linearly with cohesion at a rate of $d\alpha_r/dR = 58°$. Forsyth *et al.* [11], in experiments with steel ball bearings in a vertical magnetic field, obtained a value of $d\alpha_r/dR = 0.5°$. In our two-dimensional simulations, and also those of Fazekas *et al.* [39], cohesion had a very small effect on angle of repose, resulting in a value of $d\alpha_r/dR = 0.5°$. This result agrees with Forsyth's value, despite the simulations being in two dimensions whereas the experiments are three-dimensional. We have explained why two-dimensional simulations produce low values of α_r and $d\alpha_r/dR$ in Chapter 4. Our value of $d\alpha_r/dR$ for bismuth was significantly higher than in all of the experiments mentioned.

A major difference between our experiments on bismuth and the experiments of Albert *et al.* and of Forsyth *et al.* was that our bismuth grains were highly non-spherical. Both of the groups mentioned used spherical particles. The particle shape has a significant influence on the angle of repose and its variation with cohesion.

Our bismuth grains were non-spherical and highly variable in shape; the mean aspect ratio was 1.7, with a standard deviation of 0.3. Some particles were close to spherical and had an aspect ratio $\approx$1, but a few were very long and thin, with an aspect ratio of 3-4.

We have observed bismuth draining in our rectangular cell. We used a microscope with a mirror at a 45° angle to the vertical, in order to observe the draining process. Motion was observed in the top few layers of grains only. The bismuth grains on the surface tumbled over one another, but the irregular shape of the grains, particularly those with high aspect ratios, impeded motion deeper in the bulk. This observation explains why the zero-field repose angle was high (35° for 63-75 μm bismuth in water); this was much steeper than the 23° typically observed for spherical particles (see [12] and references therein).

We should also question whether non-spherical particles can behave like point dipoles. Let us assume that we can use the concept of 'magnetic charge', in an analogy to electric charge, though magnetic 'monopoles' have not been observed to exist in reality. Magnetic 'charge' has a tendency to concentrate at sharp edges and irregularities on the surface of the particles [80–84]. These areas will interact more

strongly with one another, increasing the effect of magnetic cohesion. This effect is described in more detail in the next chapter.

Chapter 6

Slope angles of non-magnetic voids in a paramagnetic liquid

6.1 Introduction

In the previous chapter, we measured the angle of repose as a function of cohesion for non-spherical bismuth grains in water. The increase in slope angle with cohesion was a very large effect, and we attributed this to the non-spherical shape of the particles.

We would like to do the same experiment with spherical bismuth. Unfortunately, spherical bismuth could not be obtained in sizes smaller than a millimetre. Instead, we took a different approach by using non-magnetic 'voids' in a magnetic liquid. This allowed us to use a variety of differently shaped particles.

When surrounded by a magnetic liquid, non-magnetic particles experience a magnetic dipole-dipole interaction. Although the particles themselves are not magnetic, they interact analogously to dipolar spheres in free space, with an induced dipole moment equal to the moment of the magnetic liquid displaced. They effectively act as 'voids' in a magnetic medium, and are almost exactly equivalent to magnetic particles in a non-magnetic medium.

The paramagnetic liquid used in these experiments was an aqueous solution of manganese chloride, a paramagnetic salt. The magnetic susceptibility of the solution could be altered by varying the concentration. Firstly we confirmed that non-

magnetic voids do behave like magnetic particles, by measuring the angle of repose of diamagnetic bismuth grains in a manganese chloride solution. We then measured the repose angle as a function of cohesion for various non-magnetic particles: spherical glass; non-spherical crushed glass; and rod-shaped polymethyl-methacrylate (PMMA) particles formed by cutting optic fibres into short lengths.

6.1.1 Magnetic interactions of voids

The force between two magnetic dipoles induced by a uniform magnetic field in free space is given by Equations 3.42 and 3.43 in Chapter 3. The forces $F_\parallel$ parallel to and $F_\perp$ perpendicular to the magnetic field are given by

$$F_\parallel = \frac{3\mu_0 |\mathbf{m}|^2}{4\pi r^4} \sin\theta \left(1 - 5\cos^2\theta\right); \tag{6.1}$$

$$F_\perp = \frac{3\mu_0 |\mathbf{m}|^2}{4\pi r^4} \cos\theta \left(3 - 5\cos^2\theta\right), \tag{6.2}$$

where $\mathbf{m}$ is the magnetic moment, r is the separation of the two dipoles, and θ is the angle between $\mathbf{r}$ and the magnetic field. Now consider two homogeneous magnetic spheres in free space, subject to a uniform vertical magnetic field $\mathbf{B}$. The maximum cohesive force F_v between the two spheres is obtained when the particles are in contact and aligned with the field so that $\mathbf{r}$ is parallel to $\mathbf{B}$:

$$F_v = -\frac{\pi \chi^2 B^2 a^2}{6\mu_0}, \tag{6.3}$$

where χ is the magnetic susceptibility and a is the sphere's diameter.

When considering cohesion between holes in a magnetic liquid, Equation 6.3 must be modified to account for the susceptibility of the surrounding liquid. In place of the susceptibility χ we use the difference $\Delta\chi$ between the susceptibilities of the magnetic liquid and the non-magnetic particles. The susceptibility $\Delta\chi$ should be inserted into Equation 6.3 with a minus sign, given that the particles are diamagnetic compared to the liquid. However, $\Delta\chi$ is squared, so the sign has no effect on the cohesion. Thus, diamagnetic and paramagnetic particles experience the same dipole-dipole interactions.

The interparticle force to weight ratio R for magnetic particles is given by

$$R = \frac{\chi^2 B^2}{4\mu_0 d\rho g}. \tag{6.4}$$

In calculating the values of cohesion strength R for voids in a magnetic liquid, we use a modified version of the above equation: the susceptibility χ is replaced by the difference $\Delta\chi$ in susceptibility between the magnetic liquid and the particles; the density ρ is replaced by the difference in the density $\Delta\rho$; and gravity g is replaced by effective gravity $\tilde{g}$. Although the field at the centre of the magnet is close to uniform over a small volume, there is a field gradient. We must therefore account for the magnetization force on the grains using effective gravity (see Appendix A). The above equation, modified to account for the magnetic liquid, becomes

$$R = \frac{(\Delta\chi)^2 B^2}{4\mu_0 d(\Delta\rho)\tilde{g}}. \tag{6.5}$$

6.2 Equivalence of particles and non-magnetic voids

In this section we offer evidence to support our argument that non-magnetic voids in a magnetic liquid are equivalent to magnetic particles of the same susceptibility in the limit of low χ.

6.2.1 Laplace equation

Recall that, in Chapter 3, we solved the Laplace equation for the magnetic scalar potential. We applied the solution to a sphere of magnetic susceptibility χ_{in} in a medium with magnetic susceptibility χ_{out}. The field due to the sphere was given by

$$\mathbf{H}_S = -\frac{H_0 V}{4\pi r^3}(\chi_{\text{out}} - \chi_{\text{in}})(3\cos\theta\,\widehat{\mathbf{r}} - \widehat{\mathbf{d}}). \tag{6.6}$$

Now let us assume that the sphere is a non-magnetic void ($\chi_{\text{in}}=0$) in a magnetic medium of susceptibility $\chi_{\text{out}} = \chi$. The above equation reduces to

$$\mathbf{H}_S = -\frac{\chi H_0 V}{4\pi r^3}(3\cos\theta\,\widehat{\mathbf{r}} - \widehat{\mathbf{d}}). \tag{6.7}$$

The magnetic moment of the sphere is given by $\mathbf{m} = \chi V \mathbf{H}_0$. The magnetic field due to the sphere is therefore

$$\mathbf{H}_S = \frac{|\mathbf{m}|}{4\pi r^3}\left(\widehat{\mathbf{d}} - 3\cos\theta\,\widehat{\mathbf{r}}\right). \tag{6.8}$$

This magnetic field is the same as the field due to a magnetic sphere in free space (Equation 3.36 in Chapter 3), except for a change of sign. We have therefore demonstrated that the magnetic field due to a non-magnetic sphere in a magnetic medium is the same as the magnetic field due to a magnetic sphere in a non-magnetic medium. The change of sign happens because the susceptibility of the sphere is negative compared to its surroundings.

The only assumptions made in this analysis are that the magnetic field is uniform, and the susceptibility of the surrounding medium is small ($\chi \ll 1$). The field at the centre of the magnet varies by 0.42% over the height of the granular bed, and 4.0% over the height of the cell. The susceptibility of the most concentrated manganese chloride solution used in these experiments was 4.72×10^{-4}, therefore our assumptions are justified.

6.2.2 Literature review on measurements of dipole-dipole forces between non-magnetic voids

Fujita and Mamiya [56] measured the magnetic dipole-dipole force between two non-magnetic objects in a magnetic liquid. The liquid was water-based, containing various concentrations of magnetite. A brass sphere was fixed in the centre of a cylinder filled with the magnetite solution, and the cylinder placed in a vertical uniform field produced by a solenoid. A second brass sphere in the cylinder was suspended from a wire attached to a strain gauge. The two spheres were initially in contact, and the upper sphere was raised until the contact was broken. The vertical force required to overcome the dipole-dipole attraction was measured, as a function of field strengths.

A magnetic surface charge model was used to calculate the force between two non-magnetic spheres in a magnetic medium. The two spheres were touching, and aligned with a uniform magnetic field. Magnetic charges were assumed to accumulate on the surfaces of the two spheres. The force between the spheres was calculated by evaluating the integral of the magnetic charge densities over the surfaces, using a Monte Carlo method.

The authors also calculated the force between two vertically-touching spheres by

assuming that they acted as point dipoles. The force is given by Equation (6.3).

Fujita and Mamiya found very good agreement between all three sets of results. The experimental measurements of the force between two brass spheres, the surface charge model, and the dipole model all agreed to within a few percent. This agreement is evidence that non-magnetic voids in a magnetic liquid behave like point dipoles.

Takayama *et al.* [85] measured the dipole-dipole interactions between two paramagnetic palladium cylinders suspended from threads in a vertical magnetic field. The distance between the cylinders was measured as a function of the magnetic field strength. The separation of the two cylinders was found to increase with field, due to the repulsive magnetic dipole-dipole force between them. The experimental data were used to calculate the force between the two cylinders.

The experiment was repeated with non-magnetic gold cylinders in a paramagnetic liquid (aqueous manganese chloride solution). The gold cylinders acted as non-magnetic voids in the paramagnetic solution, and the dipole-dipole interaction resulted in a repulsion between the two cylinders. Again, the separation of the two cylinders increased with magnetic field strength. In both cases order-of-magnitude agreement between experimental results and calculated values of the repulsive dipole-dipole force was obtained.

These papers provide evidence that two non-magnetic objects in a magnetic liquid behave in the same way as two magnetic objects. The question is whether this similarity extends to a situation in which there are more than two particles. In experiments, there will be edge effects at the boundaries of the container, given that the surrounding fluid does not extend to infinity. However, dipole-dipole interactions reduce rapidly with distance ($1/r^4$ dependence), so when the size of the container is large in comparison to the size of the particles, these effects should be negligible away from the container boundaries.

6.3   Experimental details

In this section we report a series of experiments using various granular materials in manganese chloride solution. The experimental details are given in Chapter 5. The angle of repose was measured using the draining crater method. Most of the results reported in this chapter are the repose angle of the slope in the upper chamber of the cell. However, for our polymethyl-methacrylate (PMMA) rods we also plot the lower repose angle for comparison.

Firstly, we verified that non-magnetic voids behave like particles. We used 63-75 μm bismuth in 0.95 M manganese chloride solution. The concentration was chosen such that the value of $\Delta\chi$ for bismuth in manganese chloride solution was double that of bismuth in water. We therefore expect that using half the value of B will result in the same slope angle.

The slope angle was then measured using non-magnetic grains of different shapes in manganese chloride solution. The following materials were used: spherical glass particles in the size range 125-150 μm, immersed in 0.71 and 1.75 molar manganese chloride solutions; non-spherical glass, consisting of sheet glass crushed with a hammer and sieved into the size range 125-150 μm, immersed in 1.75 M and 3 M manganese chloride solutions; and rod-shaped particles made by chopping 265 μm diameter PMMA optical fibres by hand into half-millimetre lengths, immersed in 0.1 M manganese chloride solution. The reason for using different concentrations of manganese chloride for different particles was that the size of the effect of magnetic cohesion on the angle of repose varied depending on the shape of the particle. We therefore needed a different range of R to produce a reasonable increase in slope angle.

We examined a sample of each of our granular materials under a microscope (see Figure 6.1). Each sample was photographed, and from the pictures the aspect ratio of each particle was measured. A rectangle was drawn around the outside of each particle, and the aspect ratio measured. The rectangle was oriented to give the largest possible aspect ratio, judging by eye. Over a hundred particles of each type were characterized in this way. It should be noted that any two-dimensional measure of particle shape is necessarily a projection of the three-dimensional shape,

Figure 6.1: *A photograph taken through a microscope, showing* **a** *bismuth grains,* **b** *non-spherical crushed glass, and* **c** *polymethyl-methacrylate (PMMA) rods formed from optic fibres cut into short lengths*

and is thus just an indication of the shape rather than a full description.

Aspect ratio is only one of several different ways in which particle shape can be quantified. Another measure is 'circularity', defined as the ratio of the radius of the largest possible circle that is fully contained within the shape to the radius of the smallest possible circle that fully contains the shape. The circularity of a circle is, by definition, 1. Particles that deviate from being circular have a circularity of less than 1. We measured the aspect ratio rather than the circularity because it is much easier to measure, and enabled us to examine a large number (>100) of particles of each granular material.

Our bismuth grains were not homogeneous in shape; the mean aspect ratio was 1.7 and the distribution had a high standard deviation. Some particles were close to spherical and had an aspect ratio ≈ 1, but a few were very long and thin, with an aspect ratio of 3-4 (see Figure 6.1**a**). The glass spheres had an aspect ratio of 1, as expected. The crushed glass was slightly more elongated, with a mean aspect ratio of 1.4. The particles were angular in shape, and had sharp corners(see Figure 6.1**b**). The PMMA rods were uniform in diameter, but had a distribution of lengths, with a mean aspect ratio of 2.0 (see Figure 6.1**c**).

It is more difficult to define the size of non-spherical particles. For the spherical glass, non-spherical glass and bismuth grains used in these experiments, the quoted size ranges were the sizes of the sieves with which we separated the required size range of the material. For the PMMA rods, however, we used $d = 300$ μm when calculating the value of R. This value is the diameter of a sphere of the same volume as our rod-shaped particles. A sieve of mesh size 300 μm would allow our

rods of diameter 265 μm to pass through in one orientation, but not the other, so we considered it a reasonable value to use for d.

We measured the density of our grains by partially filling a measuring cylinder with water, and then adding a known weight of grains. The water level rose by an amount equal to the volume of the grains added to the measuring cylinder. Using this volume and the weight of the particles, we calculated the density.

We measured the magnetic susceptibility of our spherical glass, crushed glass and PMMA rods by levitating them above the magnet bore in manganese chloride solution. See Appendix A for more information about levitation. We recorded the height on the z axis at which the grains levitated, and looked up the value of BdB/dz at this position, using the profile plotted in Figure 3.8 in Chapter 3. We then used the levitation condition, Equation A.16 in Appendix A, to calculate the value of χ. We repeated this procedure several times using different concentrations of manganese chloride solution to obtain a mean value of χ.

concentration (moles/litre)	density ρ (kgm^{-3})	magnetic susceptibility χ
0 (water)	1000	- 9.0×10^{-6}
0.1	1008	+ 8.94×10^{-6}
0.71	1058	+ 1.14×10^{-4}
0.95	1076	+ 1.56×10^{-4}
1.75	1136	+ 2.85×10^{-4}
3	1223	+ 4.72 ×10^{-4}

Table 6.1: *Table comparing the density and magnetic susceptibility of various concentrations of paramagnetic manganese chloride solution used in our angle of repose experiments*

Tables 6.1 and 6.2 list the properties of the particles and solutions used in our experiments.

material	size (μm)	aspect ratio	density (kgm^{-3})	susceptibility
spherical glass	125 - 150	1.0 ± 0.0	2500	- 4.48×10^{-5}
non-spherical glass	125 - 150	1.4 ± 0.1	2400	- 8.97×10^{-5}
bismuth	63 - 75	1.7 ± 0.3	9800	- 1.65×10^{-4}
PMMA rods	500 ×265∅	2.0 ± 0.2	1190	- 2.73×10^{-5}

Table 6.2: *Table comparing the size, aspect ratio, density and magnetic susceptibility of the granular materials used in our angle of repose experiments*

6.4 Angle of repose measurements in draining-crater experiments

This section describes and discusses the angle of repose measurements for bismuth grains, spherical glass, non-spherical crushed glass, and PMMA rod-shaped particles fully immersed in manganese chloride solution.

6.4.1 Bismuth in manganese chloride solution

Bismuth particles in manganese chloride are diamagnetic voids in a paramagnetic fluid. We tuned the concentration of the manganese chloride solution so that it had the same magnetic susceptibility as bismuth, but with the opposite sign. One would therefore expect the bismuth grains to be four times more cohesive in manganese chloride than in water, because R increases with $\Delta\chi^2$. We measured the angle of repose of bismuth in manganese chloride using the same values of R that we used for bismuth in water (see Figure 5.5 in Chapter 5). These correspond to using magnetic field strengths half as great as those used for bismuth in water. All of the values of R plotted in this chapter were corrected to account for the susceptibility and density of the surrounding liquid.

Figure 6.2 shows the angle of repose of 63-75 μm bismuth in water and in 0.95 M MnCl$_2$, plotted as a function of R. The error bars are 1°. The two sets of data were close together, demonstrating that non-magnetic voids did behave like magnetic particles. The slope angle α_r increased linearly with R up to about $R = 0.1$, and
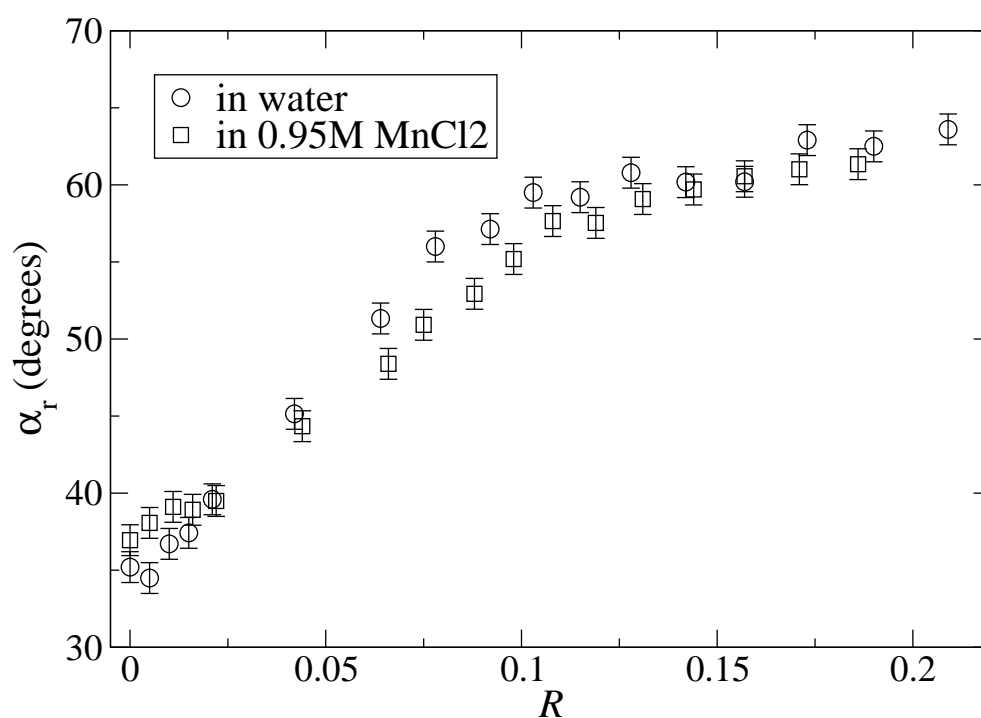
Figure 6.2: *Angle of repose of 63-75 μm bismuth in water and in 0.95 M MnCl₂*
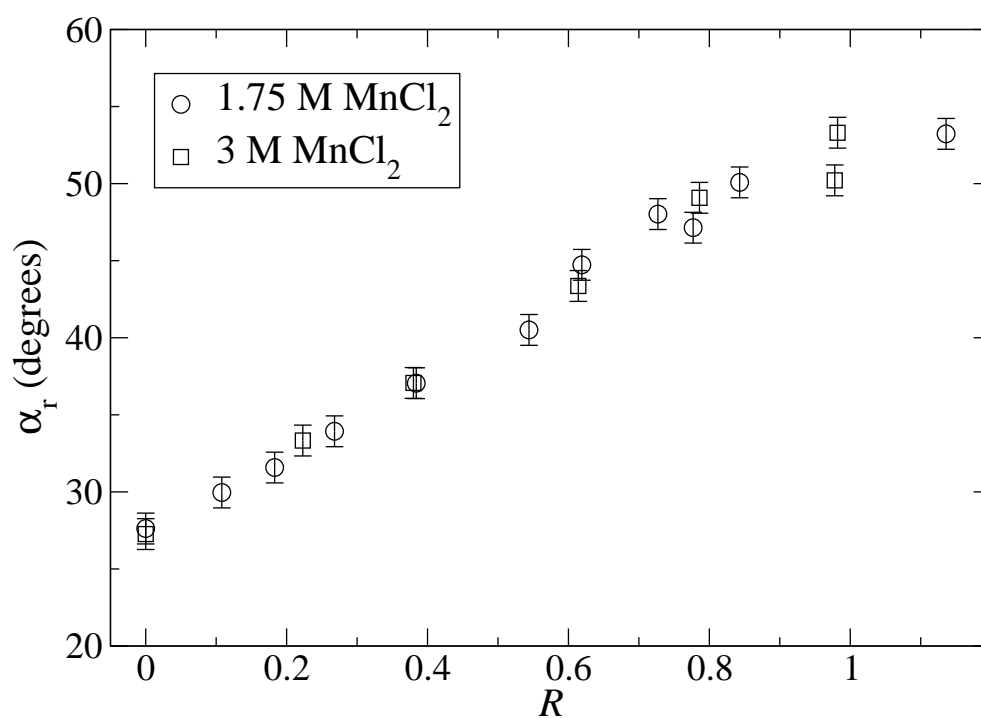
Figure 6.3: *Angle of repose of 125-150 μm spherical glass in MnCl₂*

then exhibited negative curvature. In the linear part of the graph, the gradient was $d\alpha_r/dR = 255.9°$ for bismuth in water, and $d\alpha_r/dR = 190.5°$ for bismuth in manganese chloride solution. We expected these gradients to be the same. The difference was due to scatter on the data.

6.4.2   Spherical glass in manganese chloride solution

Figure 6.3 shows the angle of repose of 125-150 μm spherical glass plotted as a function of cohesion, in two different concentrations of manganese chloride solution. The slope angle α_r increased linearly with R, at a rate of $d\alpha_r/dR = 24.9°$ for the 1.75 M concentration of manganese chloride, and $d\alpha_r/dR = 25.3°$ for the 3 M concentration. The error bars are 1°. The two sets of data lay on the same graph. The zero-field angle α_r was 27°, a little higher than the usual reported value of 23° for spherical particles (see [12] and references therein). We attributed this difference to the effect of confining geometry; it is well known that repose angles tend to be higher in narrow cells than in conical piles on a flat surface.

Our value of $d\alpha_r/dR \approx 25°$ was substantially lower than that obtained for bismuth grains in the previous chapter. This difference was due to the particle shape.

We used a range of the cohesion strength from zero up to $R = 1$. At this point one particle can be vertically suspended from another. The repose angle at $R = 1$ was around 50°, significantly higher than in the absence of a magnetic field. The angle was not approaching 90° as suggested by Albert *et al.* [12, 14], but at $R = 1$ the average cohesive force between to grains will be less than the maximum cohesive force F_v.

6.4.3   Non-spherical crushed glass in manganese chloride solution

Figure 6.4 shows the angle of repose of 125-150 μm non-spherical crushed glass plotted as a function of R, in two different concentrations of manganese chloride solution. We observe that α_r increased linearly with R, at a rate of $d\alpha_r/dR = 51.5°$ in the 1.75 M solution, and $d\alpha_r/dR = 78.6°$ in the 0.71 M solution. The error
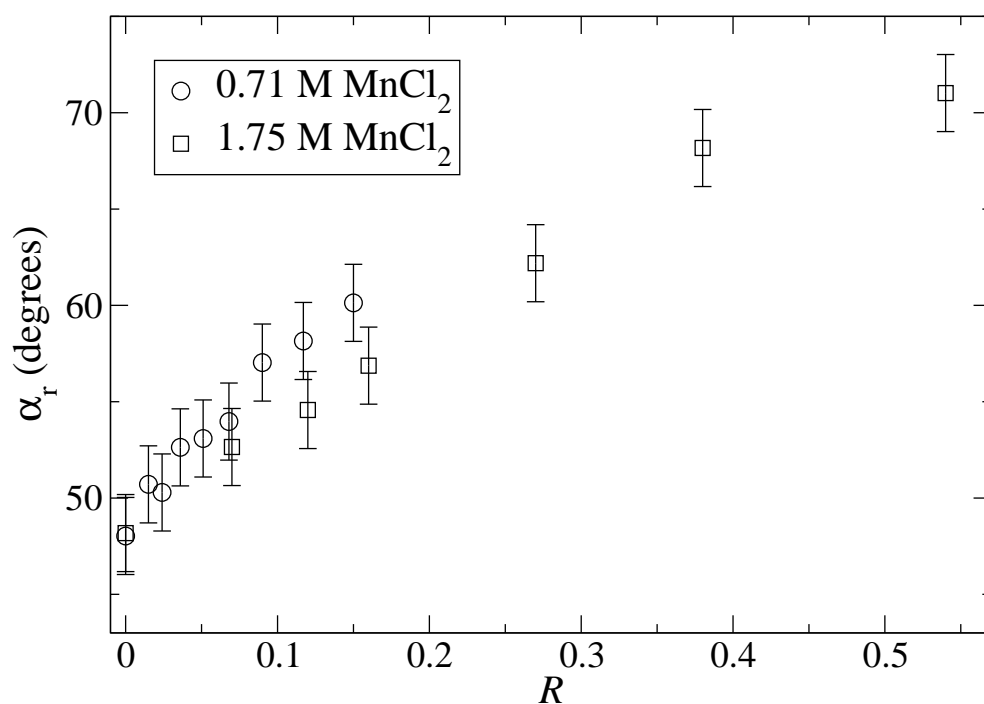
Figure 6.4: *Angle of repose of 125-150 μm non-spherical glass in different concentrations of MnCl₂*
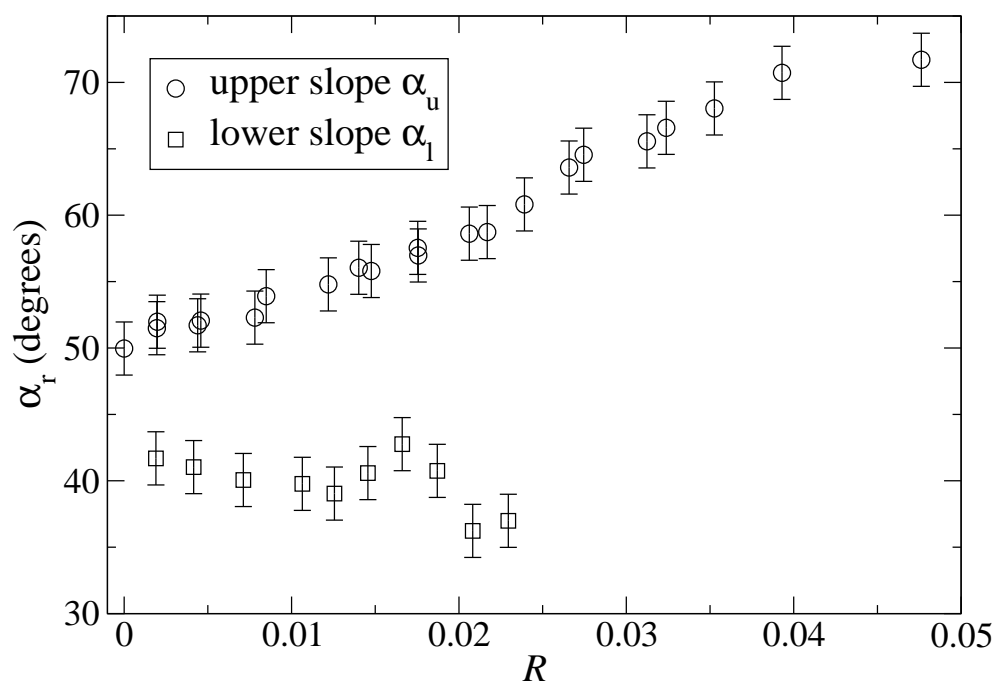
Figure 6.5: *Angle of repose of optic fibre rods in 0.1 M MnCl₂*

bars were 2°, larger than for bismuth grains because the standard deviation of the measurements was higher. The two sets of data do not appear to lie exactly on the same curve, unlike the results for spherical particles. However, they were still quite close together. We expected these gradients to be the same. The difference was due to scatter on the data.

6.4.4 PMMA rod-shaped particles in manganese chloride solution

In this experiment we used field strengths from zero up to $B = 8.5$ T. The cell was positioned in the bore of the magnet such that the partition between the upper and lower chambers was at the central field position.

Figure 6.5 shows the angle of repose of 500 μm PMMA rods in 0.1 M manganese chloride solution. We measured both the upper and lower angles of repose. The upper angle α_u increased linearly with R, at a rate of $d\alpha_r/dR = 498.9°$. The error bars were 2°. The increase in repose angle with cohesion was a very strong effect; even more so than for bismuth grains. The strength of the effect was due to the the elongated shape of the particles. We discuss particle shape in more detail in the next section.

The slope angle α_l in the lower chamber of the cell decreased with cohesion. We account for this result as follows: due to the high slope angle in the upper chamber, only a small volume of granular material drained through the aperture, resulting in a small pile in the lower chamber. As the magnetic cohesion was increased, grains draining through the aperture had a larger distance to fall to the top of the pile. The falling grains thus imparted a greater momentum, flattening the pile and resulting in a smaller slope angle in the lower chamber of the cell.

The zero-field angle of 50° was rather high, again because of the particle shape.

6.5 Discussion of the effect of particle shape

The zero-field repose angle for spherical glass was 27°. This value was a little higher than the usual reported value of about 23°. The discrepancy may be due to

the effects of confining geometry. For non-spherical crushed glass, the zero-field angle was higher at 48°, and for the PMMA rods the zero-field angle was 50°. The more aspherical the particles, the higher the zero-field repose angle. This correlation is to be expected, because irregularities in non-spherical particles resulted in a greater coefficient of friction between the particles, and therefore the pile could support a steeper slope.

material	liquid	aspect ratio	α_r at zero field	$d\alpha_r/dR$
spherical glass	1.75 M MnCl$_2$	1.0 ± 0.0	27°	24.9°
spherical glass	3 M MnCl$_2$	1.0 ± 0.0	27°	25.3°
non-spherical glass	1.75 M MnCl$_2$	1.4 ± 0.1	48°	51.5°
non-spherical glass	0.71 M MnCl$_2$	1.4 ± 0.1	48°	78.6°
bismuth	0.95 M MnCl$_2$	1.7 ± 0.3	37°	190.5°
bismuth	water	1.7 ± 0.3	35°	255.9°
PMMA rods	0.1 M MnCl$_2$	2.0 ± 0.2	50°	498.9°

Table 6.3: *Table comparing the aspect ratios, zero-field repose angle α_0 and gradient $d\alpha_r/dR$ of different materials*

Table 6.3 compares the aspect ratios, zero-field repose angles and gradient $d\alpha_r/dR$ of different materials. As the particles became less spherical (as quantified by the aspect ratio), both α_r at zero field and the gradient $d\alpha_r/dR$ increased. Crushed glass had a higher zero-field repose angle than bismuth, even though bismuth had a higher aspect ratio. This difference can be attributed to the fact that the crushed glass had sharp corners, which increased the inter-grain friction.

Figures 6.6 and 6.7 show the gradient $d\alpha_r/dR$ plotted as a function of particle aspect ratio. $d\alpha_r/dR$ appears to increase exponentially with aspect ratio, though more experiments with particles with larger aspect ratios are necessary to confirm whether this relationship holds over a greater range.
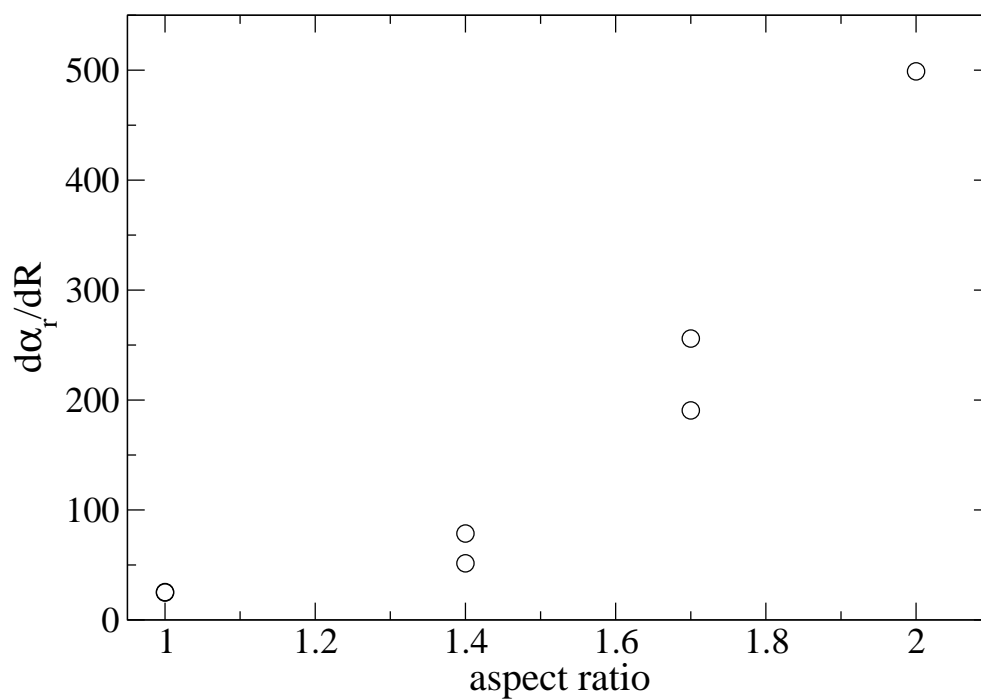
Figure 6.6: *Gradient $d\alpha_r/dR$ as a function of aspect ratio of different shapes of particle*
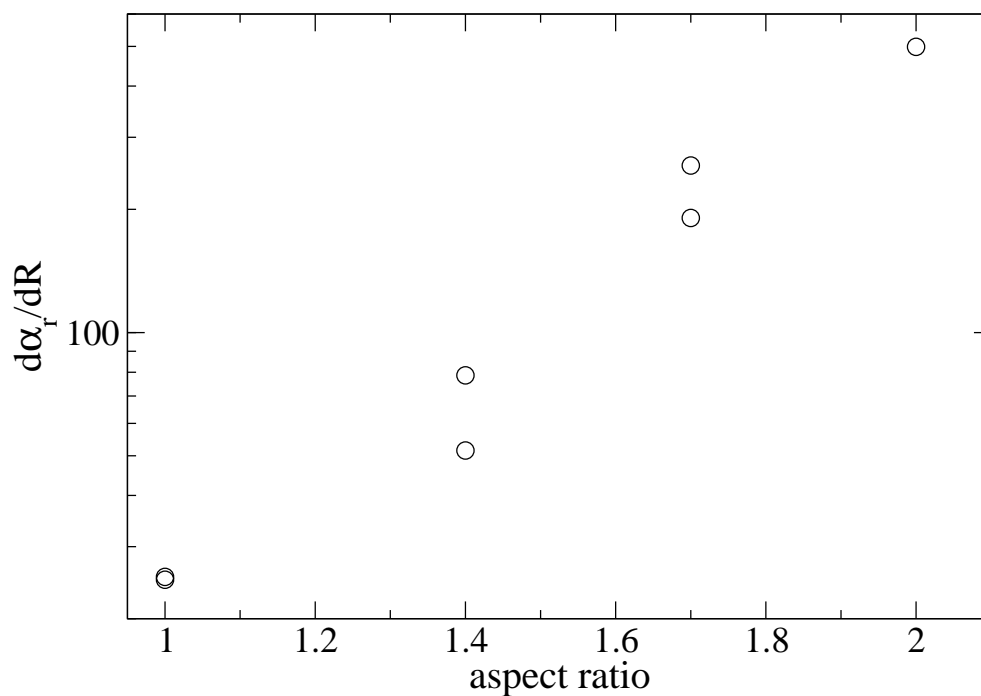
Figure 6.7: *Gradient $d\alpha_r/dR$ as a function of aspect ratio of different shapes of particle, plotted on a logarithmic scale*

6.5.1 Effect of particle shape on magnetic moment

Another important consideration is that for non-spherical particles, we must question the assumption that the magnetic moment of each particle is equivalent to that of a point dipole.

Tejedor *et al.* [86] calculated the magnetic field due to uniformly magnetized ellipsoids. They calculated the potential by summing the potentials due to two uniformly charged ellipsoids with opposite charge densities and centres slightly shifted relative to each another. For a prolate ellipsoid magnetized along the major axis, the magnetic field on the axis close to the ellipsoid was stronger than for a dipole. The field strength was greater for larger aspect ratios. The field approached that of a point dipole at a distance far from the ellipsoid. Ellipsoids with larger aspect ratios had stronger fields on the axis close to the surface of the ellipsoid.

However, when an oblate ellipsoid was magnetized along the minor axis, the magnetic field on the axis was weaker than for a point dipole. The field approached the dipolar limit much more slowly for larger aspect ratios.

Our bismuth grains and PMMA rods were prolate. The magnetic dipole-dipole forces are short-range, therefore in a granular pile it is reasonable to expect that the magnetic fields close to the grain surface will dominate behaviour. The strength of the magnetic field at the ends of the particle increased with aspect ratio, and this increased field could be expected to increase the cohesion.

Kobayashi and co-workers used the concept of 'magnetic charge' to investigate the effect of the shape of an object in a magnetic field. They calculated the surface magnetic 'charge distribution' on cylinders, in a magnetic field either parallel or perpendicular to the axis of the cylinder [80–84,87]. They found that the magnetic surface 'charge' had a minimum value at the centre of the end surfaces of the cylinder, increased almost linearly away from the centre and then increased suddenly towards the edges, theoretically approaching infinity. The magnetic surface 'charge density' on the end surfaces was greater for higher values of the permittivity and higher aspect ratios.

Because the magnetic surface 'charge' was concentrated at the edges and irregularities of non-spherical particles, the interparticle cohesion was increased. This

concentration of 'charge' resulted in a greater increase in the angle of repose with cohesion than would be expected for spherical particles. Our cohesion parameter R was calculated using the cohesive force F_v between two spheres, and therefore did not account for particle shape.

6.6   Conclusion

We have demonstrated that a collection of non-magnetic particles in a paramagnetic solution behaved the same way as a collection of magnetic particles, by comparing the angle of repose of bismuth grains in water and in manganese chloride. We investigated the dependence of the angle of repose on cohesion for non-magnetic particles of different shapes in a paramagnetic manganese chloride solution. The rate of increase $d\alpha_r/dR$ of angle with cohesion was found to increase dramatically with the particle aspect ratio. The relationship appears to be exponential, though a greater range of aspect ratios is needed to test this hypothesis.

Magnetic 'charge' has a tendency to concentrate at the edges and irregularities of non-spherical particles. The magnetic field close to the ends of an elongated particle will be stronger. Also, elongated particles interlock in the bulk so that motion is confined to particles on the surface.

Chapter 7

Slope angles of bismuth grains in a horizontal magnetic field

7.1 Introduction

In this chapter we investigated the effects of magnetic field direction. We measured the slope angle of diamagnetic bismuth grains fully immersed in water, using the rotating drum method in the horizontal field of a 7T MRI scanner.

7.2 Experimental details

7.2.1 7T scanner

The 7T MRI scanner used in these experiments is the first of its kind in Europe. It is used for magnetic resonance imaging of the brain and whole body. The high field strength results in higher quality images, and enables brain activity to be observed in real time.

Our experiments were carried out in the centre of the magnet, on the axis. The field at this position was very uniform, and directed along the axis of the magnet. Over an axial distance of 5 cm, the magnetic field varied by 0.0002%. Over a radial distance of 5 cm, the magnetic field varied by 0.00007%.
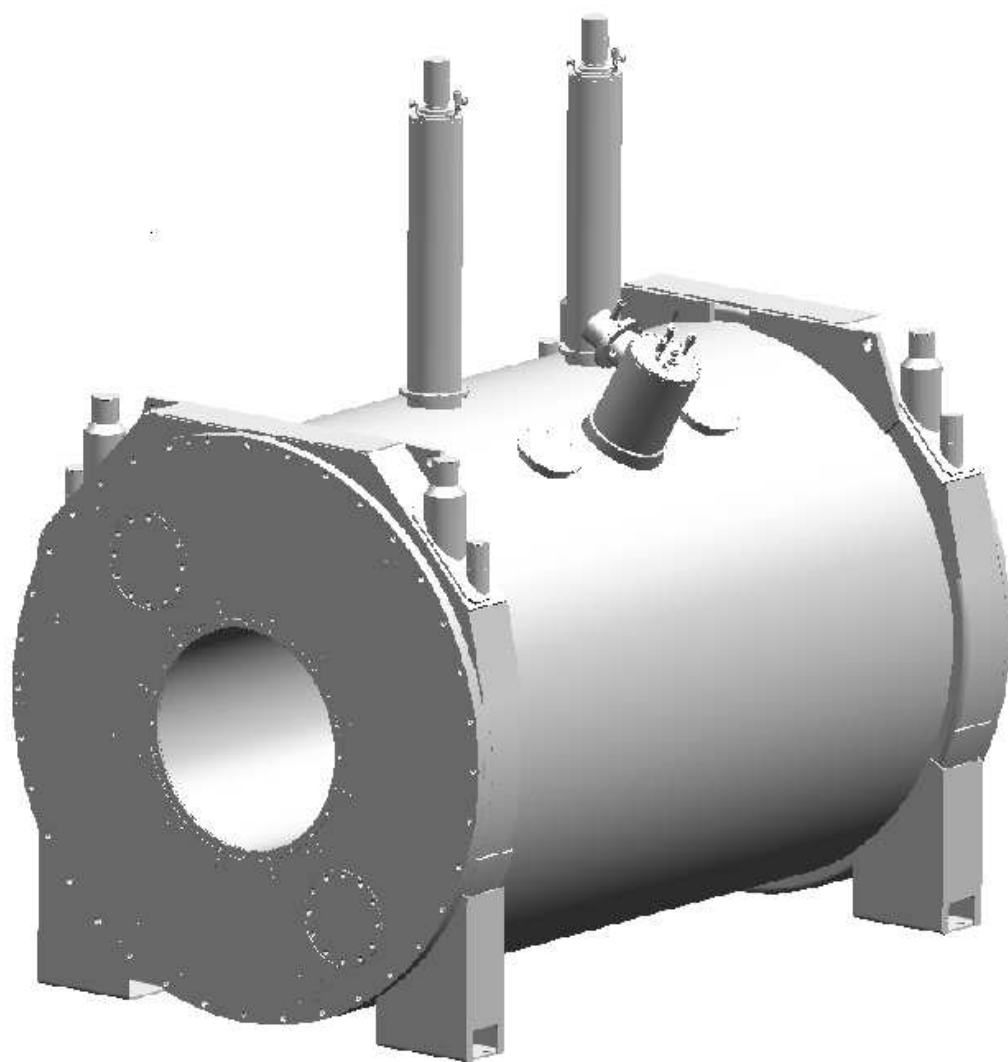
Figure 7.1: *Phillips 7T MRI scanner*
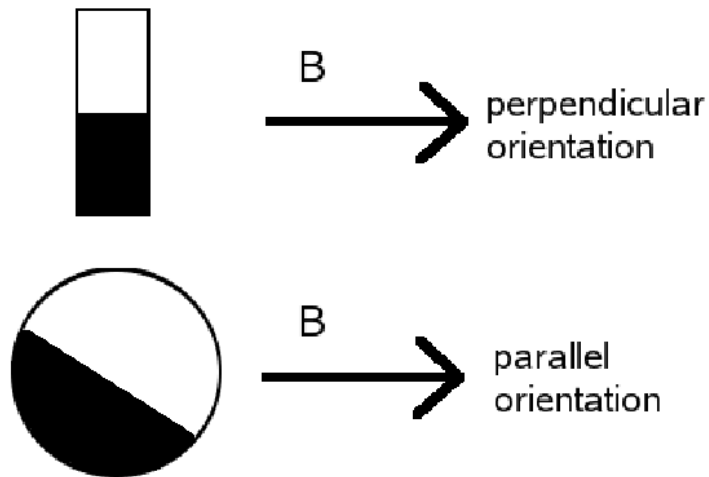
Figure 7.2: *Perpendicular and parallel orientations of the rotating drum*

7.2.2   Rotating drum experimental details

In this investigation we used the rotating drum method. The experiment was adapted for use in high magnetic fields by constructing the apparatus almost entirely from non-magnetic materials. The field direction was along the horizontal axis of the magnet, and the magnet bore was large enough to accommodate the apparatus in different orientations; the axis of the rotating drum could be either parallel or perpendicular to the magnetic field.

Six sets of data were obtained: two at zero field (rotating clockwise and anti-clockwise); two in a magnetic field of 7T with the plane of the drum perpendicular to the field direction; and two at 7T with the plane of the drum parallel to the field direction (see Figure 7.2).

The container used in this series of experiments was a perspex drum (Figure 7.3), of inner diameter 5 cm and inner width 1.4 cm. The drum was partially filled with grains (A) immersed in a liquid (B), via a small hole in the side of the drum. The drum was then sealed with a rubber bung (C). A pin was inserted into the centre of the bung, forcing liquid out and ensuring that no air bubbles remained. The drum had three threaded holes (D) with which it could be attached to the apparatus. The drum was roughened on the inside of its curved surface to prevent the entire heap slipping against the internal surface of the container.
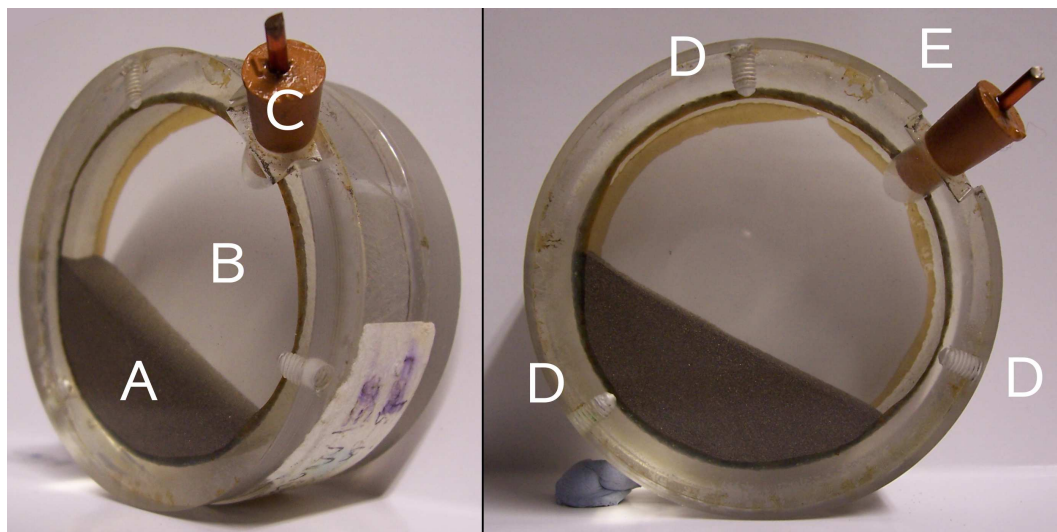
Figure 7.3: *Container used in rotating drum experiments*
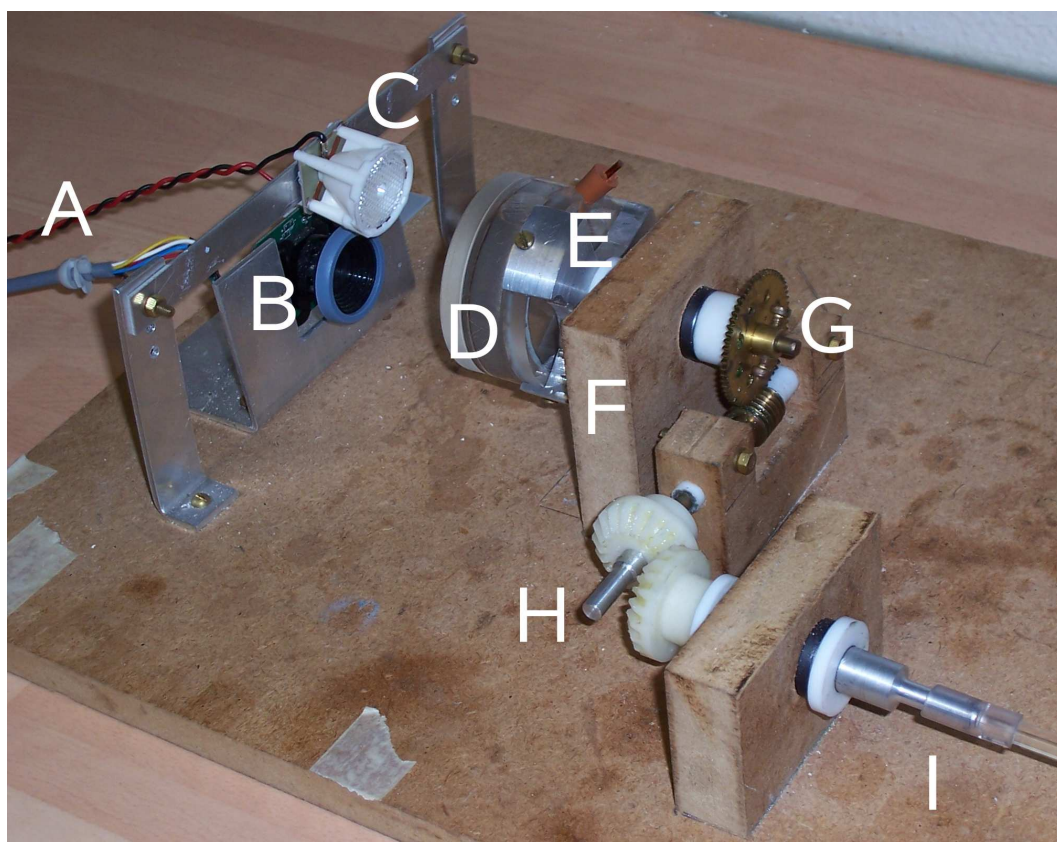
Figure 7.4: *Drum, camera and part of the rotation mechanism*

The method of image analysis used in this series of experiments required the images to have a very good contrast between the granular material in the drum and the background. To facilitate this, a sheet of black or white paper (E) was inserted behind the drum.

Figure 7.4 shows the apparatus that was inserted into the centre of the magnet. The rotating drum (D) was mounted on a flat and heavy MDF platform, and images were captured using a modified webcam (B). A white-light LED (C) with a diffuser lens was used to illuminate the drum. The camera and the LED were connected to a laptop computer and a power supply respectively with long cables (A), enabling the laptop and power supply to be positioned at a distance from the magnet.

Still images were extracted from the video files at a rate of one frame every second. Preliminary experiments showed negligible difference between the same set of data analysed using this frame rate and a higher frame rate.

The drum was fixed in an aluminium holder (E) secured by three bronze screws. A shaft attached to the holder passed through a bearing mounted in a section of MDF (F), connecting to a 60:1 worm gear (G) and an input shaft (H). A pair of bevel gears was used to connect a second shaft (I) in a direction perpendicular to the first. Either shaft H or shaft I was coupled to the input, depending on which orientation was required. The platform with the drum attached was checked with a spirit level before each run, to ensure that it was horizontal.

The platform was positioned carefully in the magnet so that the drum was exactly at the centre (positioned accurately to within a few millimetres). The platform was oriented such that the surface of the drum was either perpendicular or parallel to the field direction. The magnetic field was almost constant over the volume of the drum. Magnetization forces due to field gradients were negligible.

The long shaft (5 metres) connecting the motor to the drum was necessary because the motor contained ferromagnetic components which had to be kept well clear of the magnet. The shaft consisted of several 6 millimetre diameter perspex rods, connected securely with segments of plastic tubing. This was necessary to eliminate the possibility of slipping between consecutive sections of the shaft. The shaft was well supported along its length by wooden supports that were carefully
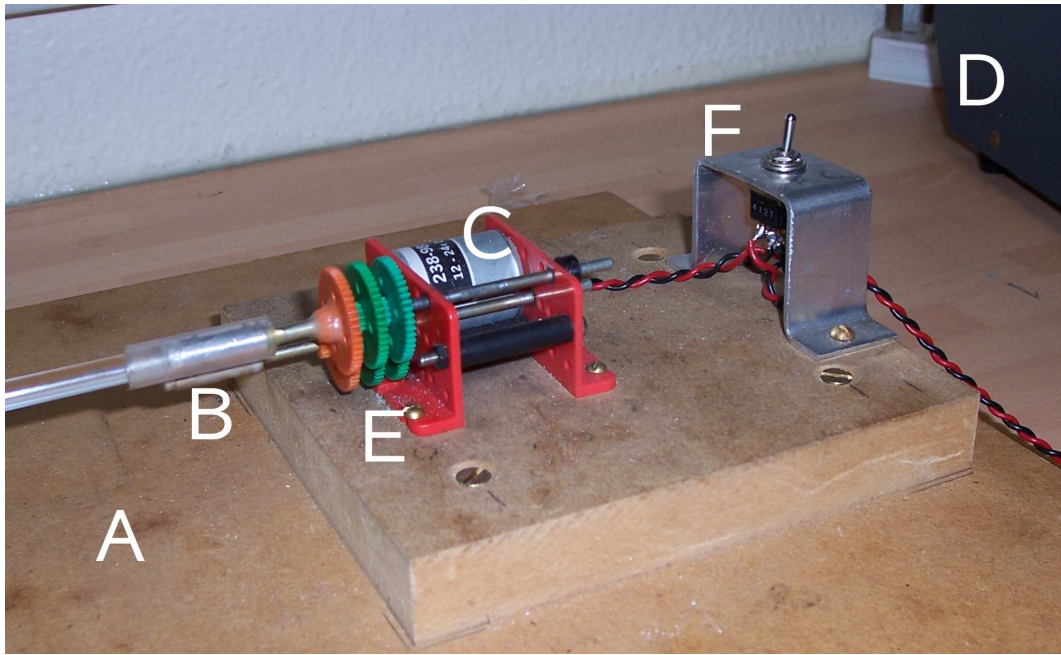
Figure 7.5: *Motor and gearbox*

positioned at the same height to ensure that the shaft was straight, thereby reducing extra torques. The supports had Teflon inserts to facilitate smooth rotation. Before starting each run, the shaft was rotated by hand to ensure that the surface of the slope was perpendicular to the face of the drum.

The platform on which the drum was mounted was positioned in the centre of the magnet. A second MDF platform (A) was positioned on the horizontal axis of the magnet 5 metres away from the first platform (see Figure 7.5). The two platforms were coupled with a 5 m shaft (B) parallel to the axis of the magnet. A d.c. motor (C) was powered by a variable-voltage power supply (D). The rotation speed was reduced by a system of gears (E) attached to the motor, and also by the worm gear at the other end of the shaft. Six gears of ratio 4:1 were used, which together with the 60:1 worm gear gave a total gear ratio of $60 \times 4^6 = 245\,760$.

The experiment was carried out with rotation in both the clockwise and anti-clockwise directions. A switch (F) was used to reverse the electrical contacts on the motor. Although the platform itself was horizontal, there may be a small systematic error in camera alignment. Any alignment error could be detected by comparing the data obtained by rotating in both directions.
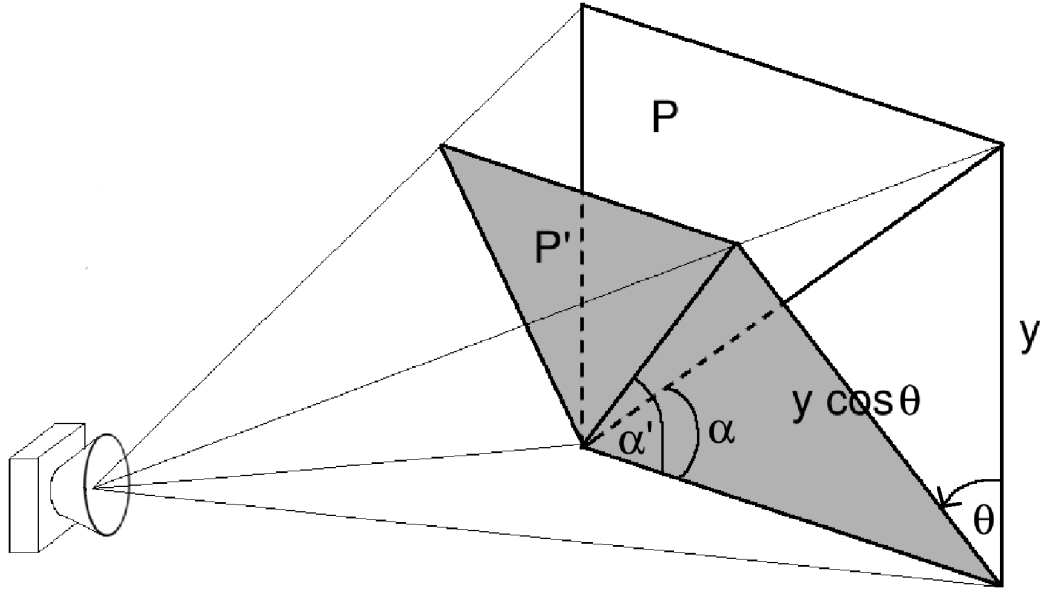
Figure 7.6: *Camera angle calibration*

7.2.3 Effect of rotation speed

The speed of rotation is important: too fast, and the system does not have sufficient time to reach equilibrium after one avalanche before the next one starts, and the motion is continuous; too slow, and the capture of a statistically significant number of data takes an impractically long time. To find an optimum rotation speed between these two extremes, short runs were carried out in zero field at a range of rotation speeds. As the drum rotated faster, α_r increased and α_m decreased until the two angles were the same and the system reached a dynamic equilibrium. At this point, the granular material was avalanching continuously, such that the rate of increase of the slope angle due to the rotation of the container was equal to the rate of decrease of the slope angle due to avalanching.

Our experiments used a time period of about 40 minutes for one complete revolution. The angles α_m and α_r did not depend on the rotation speed in this regime. One image was captured every second, and each experimental run lasted 80 minutes.

7.2.4 Analysis of slope angles in the rotating drum

The camera was fixed in position, angled slightly upwards rather than directly facing the front surface of the drum. This arrangement was used to eliminate the possibility of a double image, i.e. both the front and back surfaces of the slope being visible. However, the camera angle introduced a distortion of the image (see Figure 7.6). The plane of the surface of the drum (labelled on the diagram as P) was vertical. It was not perpendicular to the camera's line of sight, but tilted through an angle θ. Imagine a plane P', perpendicular to the line of sight of the camera, at an angle θ to P. Horizontal and vertical lines in plane P will be projected onto plane P' as horizontal and vertical lines, but any angles in between will be distorted by varying amounts, with the greatest distortion at $45°$.

Consider a right-angled triangle on the surface of the drum in plane P, with height y and width x. The angle between the triangle's hypotenuse and the horizontal is $\alpha = \arctan(y/x)$. Now imagine that the triangle in plane P is projected onto plane P'. The camera will observe a right-angled triangle in plane P', with width x' and height y'. The angle between this triangle's hypotenuse and the horizontal is $\alpha' = \arctan(y'/x')$.

The two planes P and P' intersect at line x, therefore $x' = x$. The angle between P and P' is θ, therefore the height y' of the triangle in plane P' is $y' = y \cos \theta$. Thus $\tan \alpha = \cos \theta \tan \alpha'$.

There was another distortion in the image: when the camera was set to maximum resolution (640x480 pixels), there was a change in the aspect ratio of the captured image. The aspect ratio was $\tan \alpha = y/x$. The change can be expressed as a constant factor a multiplying the ratio of $\tan \alpha$ and $\tan \alpha'$, such that $\tan \alpha = a \tan \alpha'$.

These two distortions can be taken together as a single constant so that $\tan \alpha = c \tan \alpha'$, where $c = \cos \theta + a$.

We have quantified and compensated for these errors by measuring a set of known angles and comparing these to the angle detected by the camera. The value of c was calculated by fitting the tangent $\tan \alpha'$ of the measured repose angle α' and the tangent $\tan \alpha$ of the true repose angle α. We obtained the value $c = 0.977$. This value was used to modify all subsequent measured angles to compensate for errors

introduced by both the camera angle and the change in aspect ratio.

The image analysis was carried out by a program written in MATLAB (mathematical software developed by The MathWorks). Firstly the captured video was extracted to create a series of bitmap images. Each of these bitmap files was read by the program, and converted into a black and white image. The image was analysed as an array of bits, one for each pixel, with 1 representing white and 0 black. The program read down each of a selected range of columns until the pixels changed from white to black, then stored the position of these pixels. To calculate the slope angle, a straight line fit was applied.

To ensure that the slope was being measured correctly, the mean deviation of the pixels from the straight line was calculated for each image. Thus any problems with the image processing were easily visible (for example, a grain sticking to the inside surface of the drum), because the deviation increases from its steady value of about one pixel. The calculated slope was superimposed onto the original picture, to check that the program was functioning correctly.

We plotted the slope angle as a function of time. As the drum rotated, the slope angle slowly increased until an avalanche occurs and the granular material came to rest at a lower angle. This behaviour resulted in a series of maxima and minima in the slope angle. An algorithm was employed to locate these maxima and minima: firstly the data points were split into intervals containing 5 points. If the highest point in an interval of 5 points was higher than the highest point of the two adjacent 5-point intervals, that point was designated as a maximum. Similarly, if the lowest point in an interval of 5 points was lower than the lowest point of the two adjacent intervals, it was designated as a minimum. Checking these calculated maxima and minima alongside the data demonstrated that this algorithm is reasonably reliable, although occasionally noise in the data was recognized as an avalanche. To ensure that the avalanches were determined correctly, all of the data were checked by hand and any avalanche smaller than $0.2°$ was excluded from the statistical analysis.

The distributions of maximum angle of stability α_m, angle of repose α_r and avalanche size $\Delta\alpha$ (defined as the difference between the angle just before an avalanche and the angle just after) were plotted for each run.

7.2.5   Draining crater measurements

To investigate whether the method of measuring the slope angle has a significant effect, we carried out some draining-crater experiments in the horizontal magnetic field. The same cell was used as for our experiments in a vertical magnetic field, described in Chapters 5 and 6. We measured the slope angles in both the upper and lower chambers of our cell in the 7T MRI scanner, in both perpendicular and parallel orientations. Still images were captured using the webcam. A plumb line (consisting of a lead weight suspended on a cotton thread) was photographed along with the cell. The photographs were analysed using an image manipulation program, and the slope angle was measured using the plumb line as a reference point.

7.3   Preliminary measurements

A piece of card, placed against a contrasting background, was fixed to the front surface of the drum and rotated slowly. Video images were captured, and the angle was plotted as a function of time (see Figure 7.7). The graph shows slight noise on the upward slope, well below 0.1 degrees.

We now present the results of our rotating drum experiments. Figure 7.8 is a typical graph showing how the measured angle evolved with time. The sample was 63-75 μm bismuth in water, in the absence of a magnetic field. The slope angle became steeper as the drum was slowly rotated, reaching a maximum angle α_m. An avalanche then occurred, resulting in a drop in angle to the angle of repose α_r.

When the distributions of α_m, α_r and $\Delta\alpha$ were plotted, they were all found to be approximately Gaussian. Figure 7.9 is a typical example: this is the distribution of the avalanche size $\Delta\alpha$ for 63-75 μm bismuth in water at zero field.

7.4   Slope angle of bismuth in a horizontal magnetic field

Table 7.4 shows the slope angles for 63-75 μm and 75-90 μm bismuth immersed in water. The table lists the maximum angle of stability α_m and the repose angle
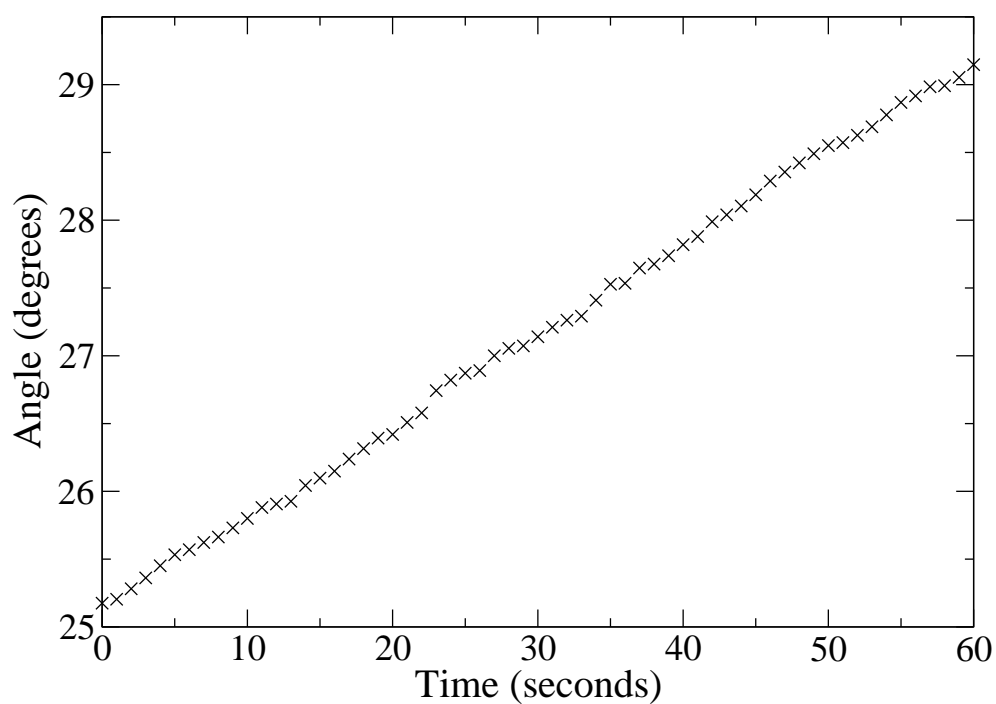
Figure 7.7: *A graph showing the increase in angle of a rotating piece of card as a function of time, used to test the image analysis program*
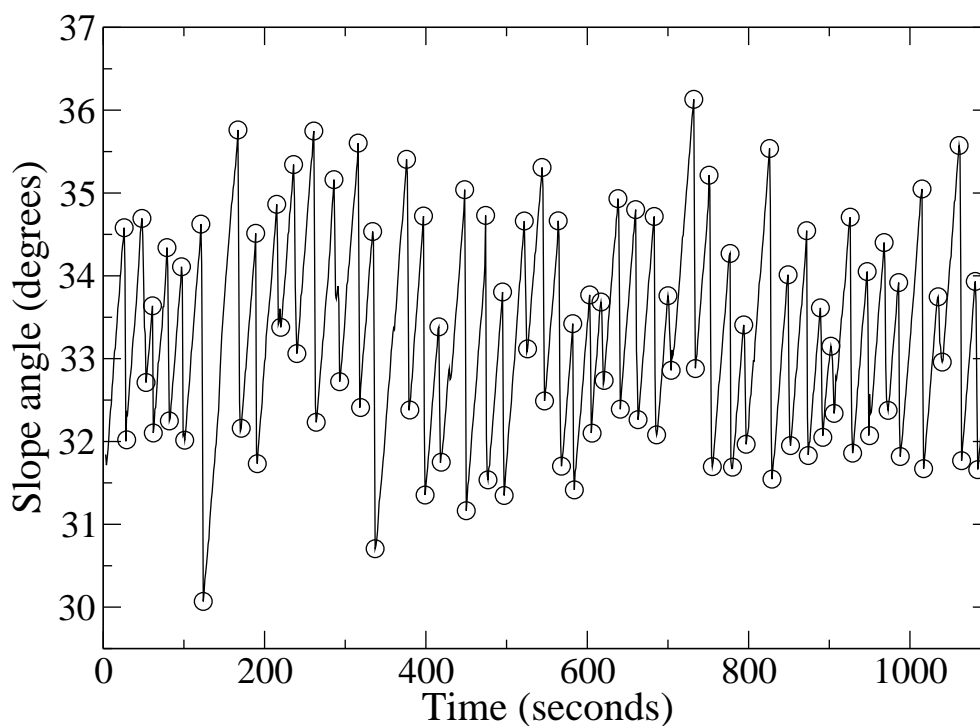
Figure 7.8: *A typical section of a graph showing how angle varies with time. The sample is 63-75 μm bismuth immersed in water, in zero applied field. The circles mark the maxima and minima.*
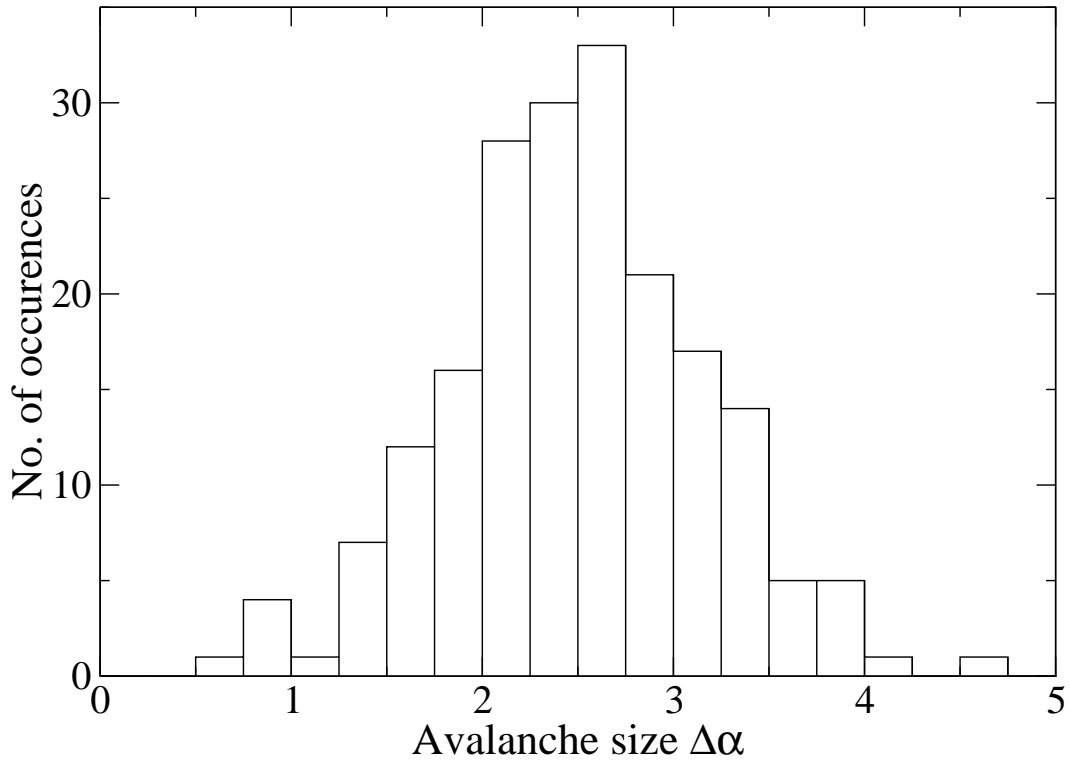
Figure 7.9: *Statistical distribution of the avalanche size $\Delta\alpha$ for 63-75 μm bismuth in water*

α_r. We compare the angles in the 7T horizontal field in both orientations (the axis of the drum parallel to and perpendicular to the magnetic field), and in zero field.

Comparing the angles obtained in the clockwise and anticlockwise runs, we find that the results agree to within about a degree.

There is very little difference between the slope angle in zero field and with the magnetic field in the perpendicular orientation. The angle is slightly higher with the magnetic field, but only by a degree or two. With the magnetic field in the parallel orientation, however, we observe a significantly higher slope angle (around 10° higher). The cohesion strength and rate of increase of R with slope angle were $R = 0.040$ and $d\alpha_r/dR = 299°$ for the 63-75 μm size range, and $R = 0.033$ and $d\alpha_r/dR = 292°$ for the 75-90 μm size range respectively. The values of $d\alpha_r/dR$ agree reasonably well with the value of $d\alpha_r/dR = 277°$ obtained by draining crater experiments with 63-75 μm bismuth in a vertical field.

The size range of the bismuth grains has a small effect. The 63-75 μm has a slightly higher angle in the parallel orientation of the magnetic field. This is

	clockwise			anticlockwise			
	α_m	α_r	$\Delta\alpha$	α_m	α_r	$\Delta\alpha$	mean α
63-75 μm							
zero field	34.6±0.6	32.1±0.4	2.4±0.7	33.6±0.8	31.1±0.6	2.5±1.0	32.8
7T ⊥	36.5±0.9	34.0±1.3	2.5±1.2	35.8±0.7	32.8±1.0	3.0±1.1	34.8
7T ∥	45.5±0.6	44.4±0.6	1.1±0.5	45.3±0.7	44.1±0.7	1.2±0.6	44.8
75-90 μm							
zero field	35.1±0.8	33.0±0.6	2.1±1.0	34.8±0.7	31.7±0.6	3.1±0.9	33.7
7T ⊥	36.8±0.9	33.7±1.0	3.1±1.2	35.5±1.0	32.7±1.0	2.8±1.1	34.7
7T ∥	44.5±0.9	43.7±0.9	0.8±0.5	43.0±0.8	42.1±0.8	0.9±0.5	43.3

Table 7.1: *Angle of repose of 63-75 μm and 75-90 μm bismuth immersed in water, using the rotating drum method. We compare zero-field repose angle with the angle in a horizontal field, in two orientations. The quoted errors are the standard deviations; typically, several hundred avalanches were observed for each run. The cohesion strength was $R = 0.040$ for 63-75 μm and $R = 0.033$ for 75-90 μm.*

because the cohesion strength R is inversely proportional to the particle diameter, so smaller particles are more cohesive than larger particles at the same magnetic field.

Table 7.2 compares the slope angles obtained using the draining crater and rotating drum methods, in a horizontal field. We include the zero-field angle for reference, and also the slope angle obtained in a vertical field (as reported in Chapter 5). The slope angles α_m and α_r in the table are averages of the angles obtained in the clockwise and anticlockwise runs in the rotating drum experiments. The quoted errors for the slope angles obtained by the draining crater method are the standard errors of four measurements.

In both orientations of the horizontal field, we found that the slope angles obtained using the rotating drum and draining crater methods were in good agreement, varying only by a degree or two. This slight discrepancy was probably due to the difference in experimental geometry.

The slope angles in a horizontal field in the parallel orientation were signifi-

| | rotating drum | | draining crater | |
	α_m	α_r	α_u	α_l
zero field	34.1	31.6	35.2 ± 0.2	32.1 ± 0.6
7T $\perp$	36.2	33.4	34.8 ± 0.5	32.6 ± 0.3
7T $\parallel$	45.4	44.3	47.0 ± 1.1	46.0 ± 0.5
7T vertical			45.1 ± 0.4	47.7 ± 0.5

Table 7.2: *Slope angle of 63-75 µm bismuth immersed in water, comparing the draining crater and rotating drum methods. We compare the angle in zero field, in a horizontal 7T field in two orientations, and also in a vertical 7T field. In the magnetic field the cohesion strength is $R = 0.0398$.*

cantly (about 10°) higher than in the absence of a magnetic field. There was good agreement between these and the slope angles in a vertical field.

However, the slope angles in a horizontal field in the perpendicular orientation were not very different from the zero-field slope angles. In the presence of the field the angles α_m and α_r were only a degree or two higher than in zero field.

7.5   Discussion and conclusion

We measured the angle of repose of bismuth grains fully immersed in water, with a magnetic field applied in various orientations, using both the rotating drum and the draining crater methods. When the field was applied vertically, or horizontally in the orientation parallel to the plane of the drum, the bismuth grains experienced a dramatic increase in the angle of repose. However, when a magnetic field was applied in the direction perpendicular to the plane of the drum, little effect was observed.

We explain this effect by considering that the magnetic dipole-dipole force is anisotropic; particles attract in the direction of the magnetic field and repel in the direction perpendicular to the field. When the magnetic field is applied parallel to the plane of the drum, whether horizontal or vertical, a component of the attraction in the direction of the field will be directed towards the surface of the pile. This
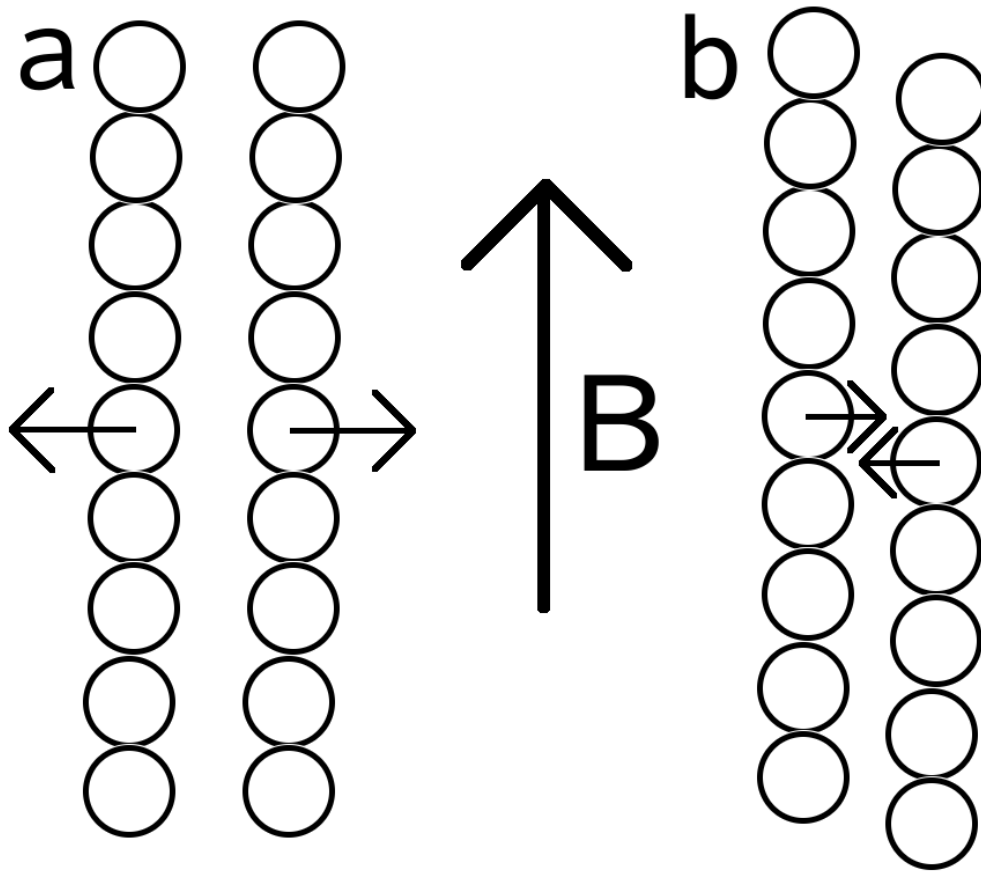
Figure 7.10: *Two chains of dipolar spheres aligned with an external magnetic field* **B** *will either* **a** *repel or* **b** *attract weakly.*

attraction will tend to increase the stability of particles on the surface, resulting in a higher angle of repose.

With the magnetic field perpendicular to the plane of the drum, the grains will attract in a direction that has no component directed towards the surface of the pile.

Consider two chains of particles aligned end-to-end in the direction of the magnetic field (see Figure 7.10**a**). The two chains will repel each other. If the two chains are touching, a particle in one chain will experience a repulsive force of $-0.5F_v$ in the direction perpendicular to the magnetic field, due to its nearest neighbour in the other chain. For simplicity we ignore the magnetic force due to other particles in the chain.

If one chain is displaced by a distance of half a particle diameter in the direction of

the field (Figure 7.10**b**), the two chains will attract weakly. However, this attraction is much weaker than the force F_v between two particles aligned in the direction of the magnetic field. We can calculate the force on a particle in the direction perpendicular to **B**, due to the particle's two nearest neighbours in the other chain. Using the equation

$$F_\perp = \frac{3\mu_0|\mathbf{m}|^2}{4\pi r^4} \sin\theta(1 - 5\cos^2\theta), \tag{7.1}$$

with $\theta = 60°$ and assuming that the chains are touching ($r = d$ is the particle diameter), we obtain the force $-3\sqrt{3}\mu_0|\mathbf{m}|^2/32\pi d^4$. This is approximately equal to $0.217\ F_v$. In a granular pile, this force is not sufficiently strong to cause the angle of repose to increase.

Appendix B presents the results of angle of repose experiments with non-magnetic voids in a horizontal magnetic field. As yet those results are not fully understood.

Chapter 8

Conclusions

In Chapter 1 we provided a general introduction to granular dynamics, cohesion, and angle of repose measurements. We reviewed the literature on the influence of cohesion on granular slopes and the separation of binary mixtures, and the effect of particle shape on angles of repose.

Chapter 2 described our two- and three-dimensional molecular dynamics simulation techniques. We also reviewed the literature on different simulation models.

Chapter 3 presented analytical and numerical calculations of magnetic dipole-dipole forces. The dipole-dipole force is highly anisotropic; dipoles attract in the direction parallel to the magnetic field, and repel in the direction perpendicular to the field. We discussed the concept of magnetic cancellation, in which the magnetic attraction due to some material in one area of space is fully or partially cancelled out by the magnetic repulsion due to other material. We directly measured the magnetic dipole-dipole force between magnetine beads, both between two individual beads and between one bead and a layer of beads arranged in a regular lattice. Our experimental measurements of the magnetic force agreed well with our theoretical calculations.

In Chapter 4 we presented the results of two- and three-dimensional simulations, investigating the effect of magnetic cohesion on the angle of repose and dynamics of a granular pile. In two dimensions, the angle of repose α_r increased very slowly with R, at a rate of $d\alpha_r/dR = 0.5°$. This was over two orders of magnitude smaller than observed in experiments with cohesion due to liquid bridges between particles. Mag-

netic anisotropy has been suggested as a reason for this difference [11, 39], but we argue that, although magnetic cancellation exists, it is not a large enough effect to explain the discrepancy. We offer an alternative explanation. The two-dimensional nature of our simulations allowed the particles to shear deep in the pile, thus preventing α_r from increasing dramatically. The addition of a magnetic field caused the motion to shift farther down into the pile. While the normal contact forces increased with depth, the cohesion did not. Hence at the surface of the pile the cohesion was relatively more important. When we included depth-dependent frictional effects of walls in our simulation, we obtained much higher values of $d\alpha_r/dR$.

We also carried out three-dimensional simulations measuring the angle of repose of a granular pile in a narrow box. We found that the angle of repose decreased as we increased the cohesion, contrary to our expectations. As R was increased further, the slope became steeper again. We measured the transverse magnetic force on particles close to the front and back walls of the container, and discovered that the particles were generally attracted towards the bulk of the pile and away from the walls. However, in wide containers (at least seven particle diameters), the transverse magnetic force had the opposite sign for low values of R. This magnetic force caused a change in the volume fraction distribution of the heap, with particles pulling towards the walls and leaving a lower particle density in the centre. This change in volume fraction distribution led to an increased particle velocity, thus reducing the stability of the pile and resulting in a drop in the angle of repose.

Chapter 5 described our angle-of-repose experiments on fine bismuth grains in a vertical magnetic field, using the draining-crater method. We first described the 16.5T superconducting magnet and our experimental method. We measured the angle of repose as a function of the magnetic field, and found a dramatic increase of $d\alpha_r/dR = 277°$. This value was much greater than has been reported in liquid-bridge cohesion experiments, in which the angle of repose approached 90° at $R = 1$ [12, 14]. The slope angle approaching 90° intuitively makes sense, because at $R = 1$, one grain can be suspended from another. We argue that the discrepancy between our value of $d\alpha_r/dR$ and that of Albert *et al.* was due to the particle shape. The liquid-bridge experiments used spherical particles, but our bismuth grains were non-spherical, and

some grains were non-convex.

In Chapter 6 we extended our experiments to investigate further the effect of particle shape. Due to the lack of availability of fine bismuth grains of varying shape, we took a different approach by using the non-magnetic 'voids' in a magnetic solution. Non-magnetic particles immersed in a weakly magnetic fluid in a field have induced magnetic dipole moments, and they interact in exactly the same way as magnetic particles with the same moment. The advantage of the technique was that it enabled us to use a variety of differently shaped grains. Spherical glass particles showed an increase in repose angle with cohesion of $d\alpha_r/dR = 25°$, much lower than for the non-spherical bismuth grains. For non-spherical crushed glass, we obtained $d\alpha_r/dR = 51.5°$ and $d\alpha_r/dR = 78.6°$, greater than for spherical glass but less than for bismuth. We also used rod-shaped particles, which experienced a much stronger effect, with $d\alpha_r/dR = 498.9°$. Plotting $d\alpha_r/dR$ against particle aspect ratio revealed a strong correlation; $d\alpha_r/dR$ appears to increase exponentially with aspect ratio, though more data are needed to verify this relationship.

The cohesion parameter R as a measure of cohesion was based on the assumption that the grains act as point dipoles. This assumption is valid for spherical particles, but must be questioned for different particle shapes. Kobayashi *et al.* [80–83] have developed a 'magnetic surface charge' model. When a non-spherical object was placed in a uniform magnetic field, the 'surface charge' was concentrated along the edges and sharp corners. This concentration of 'charge' resulted in a particles interacting more strongly than would be expected for point dipoles.

We suggested that in granular piles consisting of particles with larger aspect ratios, avalanches will occur closer to the surface. We observed avalanches in zero magnetic field under a microscope, and found that motion occurred only at the surface of the pile.

Chapter 7 investigated the effect of the direction of the magnetic field. We measured the angle of repose of bismuth in the horizontal magnetic field of a 7T MRI scanner. Firstly we described our experimental method, in which a drum was partially filled with bismuth grains and slowly rotated in the magnetic field. When the horizontal field was aligned parallel to the plane of the drum the slope angle

increased as much as for a vertical field of the same magnitude. However, when the magnetic field was aligned perpendicularly to the plane of the drum, no change in slope angle was observed. We explain this effect by considering that, when the magnetic field is parallel to the plane of the drum, whether horizontal or vertical a component of the attraction in the direction of the field will be directed towards the surface of the pile. This increased the stability and resulted in a higher angle of repose. With the magnetic field perpendicular to the plane of the drum there was no such component. Chains of particles aligned with the field will be either repelled or weakly attracted to one another, and this attraction was not sufficiently strong to cause the angle of repose to increase.

Appendix A describes the principles behind diamagnetic levitation, and review some of the literature on this topic.

Appendix B presents some preliminary experimental measurements of the angle of repose of non-magnetic voids in magnetic solutions, in a horizontal magnetic field. Contrary to our expectations, the magnetic field did not cause the slope angle to increase. These results are not yet fully understood, but we have included them for completeness.

8.1 Further work

In this section we pose some unanswered questions and describe a few possible avenues for future research.

• Why do non-magnetic voids in a rotating drum appear not to respond to a horizontal field parallel to the plane of the drum? The experimental results described in Appendix B are puzzling, and we do not currently have an explanation.

• Does the exponential relationship between the particle aspect ratio and $d\alpha_r/dR$ hold over a greater range? It would be interesting to measure the angle of repose of particles with larger aspect ratios to find out whether this is the case.

• What would happen to non-spherical cohesive particles in simulation? Modelling non-spherical cohesive particles in simulation is challenging because of the assumption that the particles behave as point dipoles; this assumption is only valid

for spheres. Composite particles consisting of several point dipoles joined together are one possible option.

- What would happen in simulations if the magnetic field were applied horizontally?

- Can we reproduce experimentally the dependence of the angle of repose on R observed in three-dimensional simulations?

Appendix A

Magnetic levitation

A.1 Introduction

There has been much recent interest in the field of diamagnetic levitation, since Andre Geim's experiment with the levitating frog (for which he received an IgNobel prize in 2000, with Michael Berry) [88].

All materials exhibit diamagnetism, but usually the weak diamagnetic effects are masked by other magnetic properties. However, the weak magnetism of purely diamagnetic materials can be exploited in unique and innovative ways. When placed in an inhomogeneous magnetic field, a diamagnetic object experiences a magnetization force, directed away from the region of highest field strength. Although the susceptibility is very small (typically diamagnetic susceptibilities are of the order of $\chi = -10^{-5}$ where χ is the magnetic susceptibility per unit volume), in a very strong field with a very large field gradient the magnetization force can be strong enough to balance the object's weight, causing it to levitate.

The 16.5T superconducting magnet at Nottingham has a high enough magnetic field strength to levitate water (see Section 3.4.1 in Chapter 3 for more details about the magnet). Many objects with high water contents can also be levitated. Figure A.1 is a photograph of a levitating strawberry.
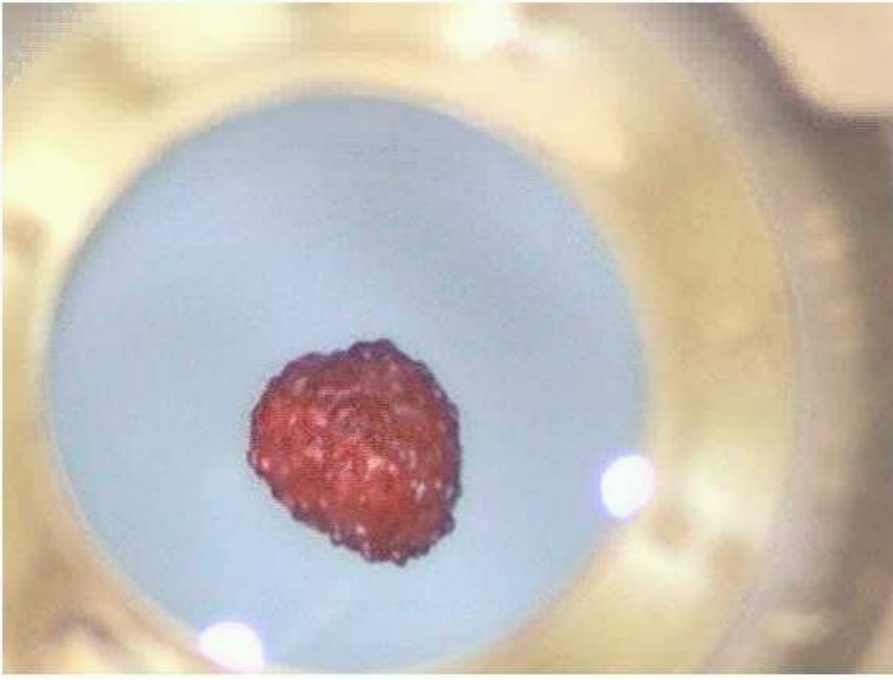
Figure A.1: *A strawberry levitating. The strawberry is diamagnetic due to its high water content.*

A.2 Earnshaw's theorem

Earnshaw's theorem [89] states that a body cannot be held in a stable equilibrium position by a combination of magnetostatic, electrostatic and gravitational forces. This seems to preclude the possibility of stable levitation. However, stable levitation can be achieved for diamagnetic objects, because the magnetic moment of the object is induced rather than permanent, and the susceptibility is negative.

We begin with two of Maxwell's laws: $\nabla \cdot B = 0$ and $\nabla \times H = J + \frac{\partial D}{\partial t}$. For a uniformly magnetized object, and in the absence of any time-dependent fields or currents we can assume $\nabla \cdot H = 0$ and $\nabla \times H = 0$. The magnetic field H can be expressed as $H = -\nabla \psi_M$ where ψ_M is the magnetic scalar potential (because of the vector identity $\nabla \times (\nabla \psi_M) = 0$). Taking the divergence of H, we obtain:

$$\nabla \cdot H = \nabla \cdot (-\nabla \psi_M) = 0; \tag{A.1}$$

$$\nabla^2 \psi_M = 0. \tag{A.2}$$

The Laplacian of a magnetostatic potential (or any sum of magnetic potentials) is zero. The same applies for electrostatic potentials: $\nabla \times E = -\frac{\partial B}{\partial t} = 0$ in the absence

of time-dependent fields, therefore E can be expressed in terms of an electric scalar potential $E = -\nabla\psi_E$ (because $\nabla \times (-\nabla\psi_E) = 0$). Therefore

$$\nabla \cdot E = -\nabla^2\psi_E = \frac{\rho}{\epsilon_0}, \qquad (A.3)$$

and in a region of space with no electric charges ($\rho = 0$), we obtain

$$\nabla^2\psi_E = 0. \qquad (A.4)$$

Thus the Laplacian of any sum of electrostatic and magnetostatic potentials is zero, and there cannot be a minimum in the potential energy. For a fixed dipole of moment M, the magnetic energy in a field B is $U = -M \cdot B$. For magnetostatic fields, $\nabla^2 B = 0$. Since U is proportional to B, this implies that $\nabla^2 U = 0$ and a potential well cannot exist. Therefore stable levitation is not possible.

However, Earnshaw's theorem applies only to materials with fixed magnetic dipole moments (ferromagnets, or saturated paramagnets). Diamagnetic materials and paramagnetic materials below their saturation field have magnetic moments that are not fixed, but vary with the strength of the surrounding magnetic field. This provides a loophole for diamagnetic materials. Paramagnetic materials cannot be levitated (except when surrounded by a more paramagnetic fluid, which forces them to act as effective diamagnets) because that would require a field maximum in free space. Field maxima only occur at the sources of the field, i.e. the magnet itself, and so cannot be in free space.

Because diamagnetic materials have a magnetic moment $M = \chi V B/\mu_0$ that is proportional to the field strength, the energy $U = -M \cdot B$ is proportional to $-\chi B^2$, and the condition $\nabla^2 U > 0$ for existence of a potential well becomes $-\chi\nabla^2 B^2 > 0$. This condition can be satisfied only if $\chi < 0$, i.e. for diamagnetic materials. Levitation of diamagnetic substances (graphite and bismuth) was first achieved by Braunbeck in 1939 [90, 91].

A.3   Stability criteria

For stable levitation, it is not sufficient to satisfy $\nabla^2 B^2 > 0$; in addition it is necessary for the energy surface to have positive curvature and thus provide a

confining potential in every direction [92]. Thus the condition is

$$\frac{\partial^2 B^2}{\partial x^2} \, , \, \frac{\partial^2 B^2}{\partial y^2} \text{ and } \frac{\partial^2 B^2}{\partial z^2} \text{ all } > 0. \tag{A.5}$$

The magnetic field can be expanded about the levitation position:

$$B_z = B_0 + \frac{\partial B_z}{\partial z} z + \frac{1}{2} \frac{\partial^2 B_z}{\partial z^2} z^2 - \frac{1}{4} \frac{\partial^2 B_z}{\partial z^2} r^2 + \dots \, ; \tag{A.6}$$

$$B_r = -\frac{1}{2} \frac{\partial B_z}{\partial z} r - \frac{1}{2} \frac{\partial^2 B_z}{\partial z^2} rz + \dots \, , \tag{A.7}$$

where B_z is the component of the field in the vertical direction, and B_r the horizontal component. The magnetic energy is proportional to $B^2 = B_z^2 + B_r^2$. Grouping coefficients together and neglecting any terms of higher orders than quadratic produces

$$B^2 = B_0^2 + 2B_0 \frac{\partial B_z}{\partial z} z + \left[\left(\frac{\partial B_z}{\partial z} \right)^2 + B_0 \frac{\partial^2 B_z}{\partial z^2} \right] z^2 + \frac{1}{4} \left[\left(\frac{\partial B_z}{\partial z} \right)^2 - 2B_0 \frac{\partial^2 B_z}{\partial z^2} \right] r^2. \tag{A.8}$$

A potential well exists only if condition (A.5) holds; this means that the coefficients of z^2 and r^2 must both be positive. These are the horizontal and vertical stability conditions:

$$K_h = \left(\frac{\partial B_z}{\partial z} \right)^2 - 2B_0 \frac{\partial^2 B_z}{\partial z^2} > 0; \tag{A.9}$$

$$K_v = \left(\frac{\partial B_z}{\partial z} \right)^2 + B_0 \frac{\partial^2 B_z}{\partial z^2} > 0. \tag{A.10}$$

In addition to these conditions, the vertical magnetization force must be balanced by the levitating object's weight. The magnetization energy is $U = -M \cdot B$ where the magnetic moment is $m = \chi V B / \mu_0$. The magnetization force F_m is given by

$$F_m = -\frac{\partial U}{\partial z} = \frac{\chi V}{\mu_0} B \frac{\partial B}{\partial z}. \tag{A.11}$$

F_m must be balanced by the gravitational force $F_g = -\rho V g$, where ρ is density, V volume and g acceleration due to gravity. This leads to the condition $F_m + F_g = 0$, which can be expressed as

$$\frac{\chi V}{\mu_0} B \frac{\partial B}{\partial z} - \rho V g = 0. \tag{A.12}$$

Rearranging, we obtain the levitation condition

$$B\frac{\partial B}{\partial z} - \frac{\mu_0\rho g}{\chi} = 0. \tag{A.13}$$

In a superconducting levitation magnet, a paramagnetic material can be vertically stable (on the axis, the field strength is greatest at the centre of the magnet), but not horizontally stable (the field strength is greatest at the outer edges of the bore, next to the coils). It is interesting to note that the force of gravity is essential for vertical stability of a diamagnetic object; without gravity, there would be no force to balance its repulsion from the region of high field strength in the centre of the magnet.

A.4 Effective gravity

Objects can experience a magnetization force if the levitation condition is not satisfied. We define an 'effective gravity' $\tilde{g}$ as the combination of the acceleration due to gravity and the acceleration produced by the magnetization force. The effective gravity $\tilde{g}$ is given by

$$\tilde{g} = g - \frac{\chi}{\mu_0\rho}B\frac{\partial B}{\partial z}. \tag{A.14}$$

Levitating objects have an effective gravity of zero. Note that the effective gravity can be greater than $g = 9.81 \text{ ms}^{-2}$ if a diamagnetic object is placed below the centre of the magnet, where $B\partial B/\partial z$ is positive.

Brooks and Cothern [93] report a series of experiments involving granular dynamics on a larger scale, using millimetre-scale diamagnetic particles made of a composite of graphite and epoxy. The particles exhibit non-uniformity in that they all have slightly differing values of χ/ρ, and thus levitate at slightly different positions in the magnet bore. The radial field gradient provides a force pushing the particles towards the axis, so a 'nucleus' of particles forms. As the magnetic field strength is gradually lowered, the particles fall into and out of the nucleus. The centre is in a pseudo-solid state, but the surface is dynamic with particles entering and leaving the nucleus.

A.5   Levitation of permanent magnets

Geim *et al.* [94] levitated a small permanent NdFeB magnet beneath a solenoid, using a diamagnetic bismuth cylinder for stabilization. The presence of the diamagnetic cylinder shifts the horizontal stability function, resulting in a stable region (where both K_v and K_h are positive) at the bottom of the solenoid. It is possible to achieve the same effect using a stronger field (provided by a superconducting magnet) and a weaker diamagnet (human fingers, which contain diamagnetic water).

Cansiz and Hull [95,96] carried out a similar experiment, using bismuth plates to stabilize the levitation of a permanent magnet beneath a ferrite ring magnet. The use of magnetic bearings stabilized by diamagnets has applications in engineering; superconductive bearings have little practical use because of the necessity of cooling and the presence of hysteresis. The small permanent magnet was spun at high speeds, and then allowed to slow down. The experiment was conducted in vacuum to eliminate deceleration due to air resistance. It was found that the rotational losses were frequency-dependent, and thus were attributed to eddy currents.

A.6   Magneto-Archimedes effect

If an object is immersed in a fluid, it experiences a magnetic buoyancy force due to the difference in magnetization force acting on the object and on the surrounding fluid. This is analogous to Archimedes buoyancy, in which there is a difference in gravitational force (due to the difference in density) acting on the object and on the surrounding fluid. Hence the two forces are considered as an 'effective buoyancy' comprising both gravitational and magnetic forces.

The magneto-Archimedes effect increases the range of materials to which the technique of magnetic levitation can be applied. If the surrounding fluid is paramagnetic, it experiences a magnetization force directed towards the centre of the magnet, where the field strength is greatest. The object is pushed upwards as the fluid moves downwards to displace it. Non-magnetic particles with high densities, and even paramagnetic materials, can be levitated [97,98].

The condition for levitation of an object in a magnetic field B is given by

$$B\frac{\partial B}{\partial z} - \frac{\mu_0 \rho g}{\chi} = 0, \tag{A.15}$$

where ρ and χ are the object's density and susceptibility respectively. When the object is immersed in a liquid, the above equation must be modified to account for the susceptibility of the liquid and the buoyancy force. We therefore use the differences $\Delta\chi$ and $\Delta\rho$ between the susceptibility and density of the object and surrounding magnetic fluid in place of χ and ρ:

$$B\frac{\partial B}{\partial z} - \frac{\mu_0 \Delta\rho g}{\Delta\chi} = 0. \tag{A.16}$$

A.6.1 Literature review of the magneto-Archimedes effect and non-magnetic voids

Catherall *et al.* [97,98] report the results of experiments using cryogenic oxygen gas, in which dense diamagnetic objects were levitated. At a fixed pressure, the density of a gas is inversely proportional to its temperature (Boyle's law); also the paramagnetic susceptibility is inversely proportional to temperature (Curie's law). These two factors mean that the susceptibility of oxygen gas at low temperatures (90K) was about ten times greater than its susceptibility at room temperature, significantly enhancing the effect of magnetic buoyancy.

Using liquid instead of gaseous oxygen provides even greater buoyancy, sufficient to levitate very dense diamagnetic materials. Catherall *et al.* have succeeded in levitating a range of materials, including lead and gold. See Figure A.2.

Surrounding a granular mixture with a paramagnetic fluid increases the range of materials which can be levitated, through the magneto-Archimedes effect. Kitazawa *et al.* [99] have levitated a droplet of paramagnetic copper sulphate solution, surrounded by pressurized oxygen gas. Although the droplet is paramagnetic, it is less paramagnetic than the surrounding gas, and can therefore be levitated.

The same authors have succeeded in separating a mixture of two diamagnetic salts (NaCl and KCl) by the magneto-Archimedes effect. Pressurized oxygen gas was used to enhance the magnetization force on the particles. The slightly different

Figure A.2: *Various objects were levitated above the bore of the 17T superconducting magnet in paramagnetic liquid oxygen. Figure taken from Catherall et al. [97].*

susceptibilities and densities of the two salts resulted in their levitating at different heights in the magnetic field.

Ikezoe *et al.* [100] report the results of experiments levitating different kinds of glass. The glass particles have similar densities but different susceptibilities due to the presence of different impurities. When placed in an inhomogeneous magnetic field, the particles separated into layers, levitating at different heights.

Techniques for separation by density have existed for some time, but this innovative method of separating granular materials of similar densities extends the range of materials that can be separated. The use of a paramagnetic fluid enhances the

magnetization force, and thus allows denser materials to be levitated, and in weaker magnetic fields.

The first direct observations of the patterns produced by magnetic holes when subject to an external field were carried out by Skjeltorp in 1983 [101]. Micrometre-scale polystyrene spheres were surrounded by a paramagnetic manganese chloride solution and confined between two glass plates, with a low concentration of slightly larger spheres used as spacers.

With the magnetic field parallel to the plane of the particles, chains were formed along the field direction. As the magnetic field was reduced, the chains were observed to break up as a result of thermal motion. With the magnetic field in a direction perpendicular to the plane of the particles, a hexagonal lattice was formed. The magnetic holes repel each other in the plane, and so arrange themselves into the minimum energy configuration.

In this experiment edge effects were a useful property rather than a problem; the polystyrene spheres positioned themselves midway between the two glass plates, because of the repulsion caused by the magnetic surface charge on the boundaries.

Jones *et al.* [102,103] have observed the same kind of ordering in 12 μm monodisperse polystyrene spheres in a thin layer of ferrofluid confined between two glass plates. With the magnetic field parallel to the plane of the particles, chains are observed. With the field perpendicular to the plane of the particles, a hexagonal lattice pattern is formed. Photographs of the hexagonal pattern were taken at different magnetic field strengths, and the fast Fourier transform of the images calculated. This provided a direct measurement of the degree of order present in the pattern, as a function of the magnetic field strength. The main peak in the intensity profile resulted from nearest-neighbour interactions. At higher field strengths a second peak (corresponding to next-nearest-neighbour interactions) was visible, demonstrating that the system was becoming more ordered.

Appendix B

Slope angles of non-magnetic voids in a paramagnetic liquid, in a horizontal field

B.1   Introduction

In this appendix we present angle of repose measurements of non-magnetic particles in magnetic liquids. We used both the draining crater and the rotating drum techniques. A horizontal magnetic field of 7T was applied in two orientations; perpendicular to and parallel to the plane of the drum. The experimental method was described in Chapter 7.

The rotating drum experiments in Chapter 7 used a time period of about 40 minutes for one complete revolution. However, a few of the experiments reported in this apendix used strong solutions of manganese chloride, which had a high viscosity. The system took much longer to settle after each avalanche (up to several minutes), so we used a much slower rotation speed (500 minutes for one rotation). We captured one image every ten seconds, and each experimental run lasted approximately 12 hours. Several hundred avalanches were observed in each run.

B.2   Slope angles of bismuth grains in manganese chloride solution

	clockwise			anticlockwise			
	α_m	α_r	$\Delta\alpha$	α_m	α_r	$\Delta\alpha$	mean α
zero field	34.3±0.4	33.5±0.5	2.0±0.8	34.5±0.5	33.2±0.5	1.3±0.5	33.9
7T ⊥	38.7±0.4	37.6±0.4	1.2±0.5	36.7±0.4	35.6±0.4	1.1±0.5	37.1
7T ∥	44.0±0.7	43.4±0.6	1.0±0.7	44.1±0.5	43.3±0.5	0.8±0.5	43.7

Table B.1: *Repose angle of 63-75 μm bismuth in 0.95 molar manganese chloride solution, in zero field and two orientations of a horizontal magnetic field of 7T. In the magnetic field the cohesion strength was $R = 0.170$.*

Table B.1 presents the results of rotating drum experiments with 63-75 μm bismuth in 0.95 molar manganese chloride solution. As for bismuth in water, the horizontal magnetic field in the perpendicular orientation did not produce any significant change in the slope angle.

When the horizontal magnetic field was applied in the parallel direction, both α_m and α_r were about 10° higher than in zero field. However, the value of $\Delta\chi$ for bismuth in manganese chloride solution was twice that for bismuth in water. This means that the cohesion strength R was four times as great ($R = 0.170$ for bismuth in manganese chloride solution, and $R = 0.0398$ for bismuth in water), so we would expect to obtain higher slope angles. The angles for bismuth in manganese chloride solution were, in fact, very close to those measured for bismuth in water. This is a puzzling result.

Table B.2 compares the slope angles obtained using the two experimental methods (draining crater and rotating drum). The angles obtained using both methods were in good agreement.

In a vertical magnetic field, the magnetic susceptibility of the manganese chloride solution increased the upper slope angle α_r (61.3° compared with the 45.1° obtained for bismuth in water). In the magnetic field the cohesion strength was $R = 0.170$. The magnetic fluid augmented the effect of magnetic cohesion on slope angle in

	rotating drum		draining crater	
	α_m	α_r	α_u	α_l
zero field	34.4	33.4	37.0 ± 0.3	33.2 ± 0.7
7T $\perp$	37.7	36.6	34.4 ± 0.4	34.7 ± 0.3
7T $\parallel$	44.1	43.4	46.2 ± 0.3	48.0 ± 1.7
7T vertical			61.3 ± 0.5	45.3 ± 1.5

Table B.2: *Slope angle of 63-75 μm bismuth immersed in 0.95 M manganese chloride solution, comparing the draining crater and rotating drum methods. We measured the slope angle in zero field, in a horizontal 7T field in two orientations, and also in a vertical 7T field. In the 7T field the cohesion strength was R = 0.170.*

a vertical magnetic field, as expected, but appeared to have no effect when the magnetic field was applied horizontally. The reasons for this are unclear.

B.3 Slope angles of non-magnetic glass spheres in manganese chloride solution

We measured the slope angle of spherical glass particles in the size range 250-300 μm immersed in 1.75 molar manganese chloride solution, and also 200-400 μm immersed in 4.75 molar manganese chloride solution. The stronger concentration of manganese chloride was used because the cohesive force scales as susceptibility squared (see Equation 6.5), so a high value of R should be expected to produce a more dramatic and hence easily measurable effect. We also used the lower concentration of manganese chloride to investigate the effect of viscosity on the slope angle.

The data in Table B.3 show a very small change in α_m and α_r in the presence of a magnetic field. The angles are slightly lower in the perpendicular orientation, and slightly higher in the parallel orientation, but both differ from the zero-field results only by about a degree. The errors quoted in the table are the standard deviations of the data.

	clockwise			anticlockwise			
	α_m	α_r	$\Delta\alpha$	α_m	α_r	$\Delta\alpha$	mean α
250-300 μm spherical glass in 1.75 M MnCl$_2$ solution							
zero field	25.5±0.2	24.8±0.2	0.7±0.3	25.9±0.3	25.4±0.2	0.7±0.2	25.4
7T $\perp$	24.9±0.3	24.2±0.2	0.7±0.3	25.0±0.2	24.3±0.2	0.7±0.3	24.6
7T $\parallel$	25.5±0.2	24.9±0.2	0.7±0.3	25.1±0.2	24.6±0.2	0.6±0.2	25.0
200-400 μm spherical glass in 4.75 M MnCl$_2$ solution							
zero field	25.9±0.2	25.3±0.2	0.5±0.2	25.4±0.2	24.9±0.2	0.5±0.2	25.4
7T$\perp$	25.2±0.2	24.5±0.2	0.7±0.3	25.1±0.2	24.3±0.2	0.7±0.3	24.8
7T $\parallel$	26.8±0.2	26.3±0.2	0.5±0.2	26.5± 0.2	26.1±0.2	0.5±0.2	26.4

Table B.3: *Slope angle of spherical glass immersed in two different concentrations of manganese chloride solution, measured using the rotating drum method. We compare the zero-field slope angle with the angle in a horizontal magnetic field, in two orientations. In the 7T magnetic field, $R = 0.288$ for the 1.75 M concentration and $R = 1.596$ for the 4.75 M concentration of the manganese chloride solution.*

These results are puzzling; we expected values of $R = 0.288$ and $R = 1.596$ to have a much more dramatic effect on the angle of repose, given that higher angles were observed for these values of R in a vertical magnetic field.

Table B.4 compares the slope angle of 125-150 μm spherical glass immersed in 1.75 M manganese chloride solution in zero field, in a horizontal 7T field in two orientations, and also in a vertical 7T field, measured using the draining crater method. In the 7T field the cohesion strength was $R = 0.576$. Although a vertical magnetic field caused a dramatic increase in slope angle, when applied horizontally the magnetic field had no effect.

When plotting the slope angle against time, we noted that the increase in slope angle before an avalanche is not as smooth as for bismuth grains (see Figure 7.8 in Chapter 7). For spherical particles we observed the existence of subsidiary avalanches between the major avalanches. We suggest a reason for this phenomenon: the granular material undergoes a series of small rearrangements as the drum is rotated between major avalanches. These rearrangements allow the particles to form

	draining crater	
	α_u	α_l
zero field	27.0 ± 0.4	25.9 ± 0.7
7T $\perp$	28.3 ± 0.8	28.1 ± 1.0
7T $\parallel$	27.9 ± 0.5	27.0 ± 0.9
7T vertical	50.1 ± 0.6	

Table B.4: *Slope angle of 125-150 µm spherical glass immersed in 1.75 M manganese chloride solution, measured using the draining crater method. We compare the slope angle in zero field, in a horizontal 7T field in two orientations, and also in a vertical 7T field. In the 7T field the cohesion strength was $R = 0.576$.*

a more stable and energetically favourable configuration. The rearrangements may induce movements of grains on the surface of the heap, causing subsidiary avalanches in between the main avalanches. Similar small rearrangements of grains before a major avalanche have been observed by Aguirre *et al.* [68, 69] in packings of two-dimensional disks, and by Scheller *et al.* [104] in a granular monolayer of spheres on an inclined plane.

Effect of viscosity

Samadani and Kudrolli [16] report a series of experiments in which grains were poured into a silo. The grains were fully immersed in water-glycerol mixtures of various viscosities. The liquid viscosity was found to have no systematic effect on angle of repose.

Ogale *et al.* [79] also found that the angle of repose was independent of viscosity for particles dropped into a cell filled with fluid, at least for cells that were wide enough for the effects of friction against the cell walls to be neglected. However, when the cell was thin, the repose angle was found to increase with viscosity. The boundaries of the pile were observed to be sharper in fluid than in air, suggesting that the presence of fluid decreased the effect of cohesion due to surface roughness.

We used two different concentrations of manganese chloride solution, to vary the value of cohesion strength R and also to investigate the effect of viscosity on

the avalanche dynamics. We used spherical glass particles in the size range 200-400 μm immersed in 4.75 molar manganese chloride solution, and 250-300 μm glass immersed in 1.75 M manganese chloride solution. 4.75 M is just below the maximum possible concentration that can be dissolved in water at room temperature.

The cohesive force scaled with susceptibility squared (Equation 6.5), and we initially expected a high value of R to have a more substantial effect. For the 4.75 M concentration the value of R was calculated to be 1.596. The cohesive dipole-dipole force between two vertically touching particles in a vertical magnetic field was therefore twice as great as the gravitational force, so the angle of repose could be expected to vary significantly from the zero-field value.

Manganese chloride solution is very viscous; at room temperature, 4.75 molar concentration was 4.4 times as viscous as water. Preliminary experiments at zero field indicated that, when the drum was being continuously rotated, the system took a considerable time (2-3 minutes) to settle completely after an avalanche. We therefore used a very slow rotation speed (one rotation every 500 minutes), and captured one frame every 10 seconds.

To investigate the effect of fluid viscosity on α_r, α_m and the avalanche dynamics, we repeated the experiment for 200-400 μm glass in air and in water, in zero magnetic field. We then compared this to our zero-field results for glass in 1.75 M and 4.75 M manganese chloride solution. See Table B.5.

	clockwise			anticlockwise			
	α_m	α_r	$\Delta\alpha$	α_m	α_r	$\Delta\alpha$	mean α
4.75 M	25.9±0.2	25.3±0.2	0.5±0.2	25.4±0.2	24.9±0.2	0.5±0.2	25.4
1.75 M	25.9±0.3	25.0±0.2	0.8±0.3	25.8±0.3	25.1±0.2	0.7±0.3	25.5
water	25.4±0.3	24.8±0.2	0.7±0.3	24.7±0.2	24.2±0.2	0.5±0.2	24.8
air	27.7±0.7	24.2±0.4	3.4±1.1	27.8±0.9	24.1±0.6	3.7±1.5	26.0

Table B.5: *Mean angle of maximum stability, angle of repose and avalanche size of spherical glass in different concentrations of manganese chloride solution, water and air, at zero magnetic field*

The data in Table B.5 show that both α_m and α_r were very slightly greater for

glass in manganese chloride than for glass in water. The highest concentration of manganese chloride solution used in these experiments was 4.4 times as viscous as water at room temperature, hence the flow of grains within the fluid was much more strongly damped. An increase in damping will lead to a higher maximum angle α_m because the grains will take longer to begin avalanching once a critical point is reached. During this response time the drum continues rotating, increasing α_m. Once started, an avalanche in a more viscous medium will stop sooner, leading to an increased repose angle α_r.

This argument could lead one to expect that glass in air (which is a very low-viscosity fluid) would have even lower values of α_m and α_r. Although α_r was indeed lower, the angle of maximum stability α_m was in fact a couple of degrees higher for glass in air than for glass in water or manganese chloride. Viscosity of the surrounding fluid was not the only factor affecting avalanche dynamics here; the state of the fluid also had an effect. The presence of a gas rather than a liquid will have a dramatic influence on the particle dynamics, and frictional properties in particular. A liquid effectively 'smooths out' surface roughness by forming a boundary layer around the particles, thus reducing the effective coefficient of friction, resulting in a lower angle.

There was also a dramatic difference between the size of avalanches in liquid and in gas: the mean $\Delta\alpha$ in air was 3.6°, whereas in water or manganese chloride the mean avalanche size was less than 1°. This again demonstrated the significance of the role played by damping in avalanche dynamics.

A study by du Pont *et al.* [105] investigated the avalanching of glass beads in a rotating drum. The authors report that avalanches of glass beads in air were large ($\Delta\alpha \approx 3°$) and happened quickly ($t \approx 1$ s). However, avalanches of glass beads fully immersed in water were smaller ($\Delta\alpha < 1°$) and were of longer duration (≈ 1 minute). These results agree with our findings.

	clockwise			anticlockwise			
	α_m	α_r	$\Delta\alpha$	α_m	α_r	$\Delta\alpha$	mean α
7T $\perp$	37.8±0.6	35.1±0.6	2.7±1.0	37.4±0.5	34.7±0.7	2.7±0.9	36.2
7T $\parallel$	38.7±0.4	37.6±0.4	1.2±0.5	36.7±0.4	35.6±0.4	1.1±0.5	37.1
zero field	37.3±0.4	35.3±0.5	2.0±0.8	37.6±0.6	35.4±0.6	2.2±1.0	36.4

Table B.6: *Slope angle of 250-300 μm non-spherical crushed glass immersed in 1.75 M manganese chloride solution, using the rotating drum method. We compare zero-field repose angle with the angle in a horizontal field, in two orientations. In the 7T field the cohesion strength was $R = 0.401$. The quoted errors are the standard deviations.*

B.4   Slope angles of non-spherical crushed glass in manganese chloride solution

Table B.6 compares the slope angles of 250-300 μm non-spherical crushed glass in 1.75 M manganese chloride solution in zero field and in a horizontal field in both orientations, measured using the rotating drum method. In the 7T field the cohesion strength was $R = 0.401$. Adding a horizontal magnetic field appeared to have no effect on the slope angle.

	draining crater	
	α_u	α_l
zero field	44.7 ± 1.0	38.5 ± 1.1
7T $\perp$	47.6 ± 2.1	35.6 ± 2.1
7T $\parallel$	47.5 ± 2.3	39.4 ± 0.8

Table B.7: *Slope angle of 125-150 μm non-spherical crushed glass immersed in 1.75 M manganese chloride solution, measured using the draining crater method. We compare the slope angle in zero field and in a horizontal 7T field in two orientations. In the magnetic field the cohesion strength was $R = 0.803$.*

Table B.7 compares the slope angle of 125-150 μm non-spherical crushed glass immersed in 1.75 M manganese chloride solution for a horizontal 7T field in two orientations. In the magnetic field the cohesion strength was $R = 0.803$. The slope

angle did not appear to increase due to the horizontal field. In a vertical magnetic field the slope angle increased dramatically, exceeding 70° at field strength of $B = 4.5$ T.

B.5 Slope angles of PMMA rod-shaped particles in manganese chloride solution

	clockwise			anticlockwise			
	α_m	α_r	$\Delta\alpha$	α_m	α_r	$\Delta\alpha$	mean α
zero field	36.7±0.7	35.4±0.5	1.3±0.8	37.2±0.8	34.3±0.5	2.9±1.1	35.9
7T ⊥	39.5±0.7	37.5±0.6	1.9±1.1	39.8±0.6	37.5±0.6	2.3±0.9	38.6
7T ∥	35.7±0.6	34.5±0.5	1.3±0.8	36.5±0.7	34.7±0.5	1.9±0.9	35.4

Table B.8: *Slope angle of 500 μm PMMA rods immersed in 0.1 M manganese chloride solution, measured using the rotating drum method. We compare zero-field repose angle with the angle in a horizontal field, in two orientations. In the 7T field the cohesion strength was $R = 0.0239$. The quoted errors are the standard deviations.*

Table B.8 compares the slope angles in zero field and in a horizontal field in both orientations, measured using the rotating drum method. In the 7T field the cohesion strength was $R = 0.0239$. Adding a horizontal magnetic field appeared to have no effect on the slope angle.

Table B.9 compares the slope angles of 500 μm length PMMA rods immersed in 0.1 M manganese chloride solution, obtained using the draining crater and rotating drum methods. The angles measured using the draining crater method were significantly higher than in the rotating drum. The reason for this is unclear. In the 7T field the cohesion strength was $R = 0.0239$. The horizontal magnetic field did not appear to have any effect on the slope angle, although a vertical magnetic field of the same magnitude caused the slope angle to increase substantially.

	rotating drum		draining crater	
	α_m	α_r	α_u	α_l
zero field	37.0	34.9	50.0 ± 0.3	38.9 ± 0.9
7T $\perp$	39.7	37.5	46.3 ± 1.1	35.1 ± 1.6
7T $\parallel$	36.1	34.6	46.5 ± 0.0	42.5 ± 0.9
7T vertical			60.8 ± 0.7	37.0 ± 1.9

Table B.9: *Slope angle of 500 μm length PMMA rods immersed in 0.1 M manganese chloride solution, comparing the draining crater and rotating drum methods. We measured the slope angle in zero field, in a horizontal 7T field in two orientations, and also in a vertical 7T field. In the 7T field the cohesion strength was $R = 0.0239$.*

B.6   Conclusion

We have measured the slope angle of various materials in a 7T horizontal magnetic field, using both the rotating drum and the draining crater method. The results are puzzling. For spherical and non-spherical glass and PMMA rods in manganese chloride solution, the magnetic field did not appear to have any effect on the slope angle. However, in a vertical magnetic field of the same magnitude, the slope angle was found to increase significantly.

All of the literature on the subject of magnetic holes assumes that the dipole-dipole interactions between magnetic holes are equivalent to interactions between point dipoles of the same moment. Direct measurements of the interparticle force provide evidence that this assumption is valid for two particles [56, 106].

Of course, the assumption that magnetic holes behave just like point dipoles is only valid in certain circumstances. Although the individual magnetic holes are small compared to the dimensions of the container, in bulk the magnetic holes fill a large proportion of the drum. When the holes are in direct contact with the sides of the drum, edge effects will not be negligible.

It is debateable whether the magnetic holes model is applicable in a case where the holes take up a greater volume fraction than the magnetic fluid. There will be an effective surface charge along the faces of the drum, which may have had a

significant influence on the results.

In Chapter 7 we described the results of angle of repose measurements on bismuth grains in water, in the presence of a horizontal magnetic field. The slope angle was found to increase substantially when a horizontal magnetic field was applied parallel to the plane of the drum. In fact, the angle was the same as that measured in a vertical magnetic field of the same magnitude. However, a horizontal magnetic field applied perpendicularly to the plane of the drum had no effect on the slope angle, as in the case of non-magnetic particles in manganese chloride solution.

We repeated the experiment with bismuth grains in paramagnetic manganese chloride solution (see Chapter 7). The presence of the magnetic fluid increased the cohesion between grains, resulting in a cohesion strength R four times as great as for bismuth in water. The slope angles measured for bismuth in manganese chloride were the same as for bismuth in water, despite the increased cohesion.

The results seem to suggest that the cohesion between non-magnetic voids in a magnetic solution did not have any effect on the slope angle in a horizontal field, although there was an effect in a vertical magnetic field. The slope angle of magnetic bismuth particles in a non-magnetic liquid, however, was influenced by a horizontal field in one orientation but not the other. As yet these phenomena are not fully understood.

References

[1] A. Fingerle, K. Roeller, K. Huang, and S. Herminghaus. Phase transitions far from equilibrium in wet granular matter. *New Journal of Physics*, 10, MAY 2008.

[2] O. Pouliquen and F. Chevoir. Dense flows of dry granular material. *Comptes Rendus Physique*, 3(2):163–175, MAR 2002.

[3] GDR MiDi. On dense granular flows. *European Physical Journal E*, 14(4):341–365, AUG 2004.

[4] R. Pfister and M. Schneebeli. Snow accumulation on boards of different sizes and shapes. *Hydrological Processes*, 13(14-15):2345–2355, OCT 1999.

[5] R. L. Brown and J. C. Richards. *Principles of powder mechanics : essays on the packing and flow of powders and bulk solids*. Pergamon, Oxford, 1970.

[6] R. M. Nedderman. *Statics and kinematics of granular materials*. Cambridge University Press, 1992.

[7] J. M. Lian and S. S. Shima. Powder assembly simulation by particle dynamics method. *International Journal for Numerical Methods in Engineering*, 37(5):763–775, MAR 1994.

[8] J. M. Valverde, A. Castellanos, A. Ramos, and P. K. Watson. Avalanches in fine, cohesive powders. *Physical Review E*, 62(5, Part B):6851–6860, NOV 2000.

[9] M. A. S. Quintanilla, J. M. Valverde, and A. Castellanos. The transitional behaviour of avalanches in cohesive granular materials. *Journal of Statistical Mechanics - Theory and Experiment*, JUL 2006.

[10] F. Peters and E. Lemaire. Cohesion induced by a rotating magnetic field in a granular material. *Physical Review E*, 69(6, Part 1), JUN 2004.

[11] A. J. Forsyth, S. R. Hutton, M. J. Rhodes, and C. F. Osborne. Effect of applied interparticle force on the static and dynamic angles of repose of spherical granular material. *Physical Review E*, 6303(3, Part 1), MAR 2001.

[12] R. Albert, I. Albert, D. Hornbaker, P. Schiffer, and A. L. Barabasi. Maximum angle of stability in wet and dry spherical granular media. *Physical Review E*, 56(6):R6271–R6274, DEC 1997.

[13] S. Nowak, A. Samadani, and A. Kudrolli. Maximum angle of stability of a wet granular pile. *Nature Physics*, 1(1):50–52, OCT 2005.

[14] D. J. Hornbaker, R. Albert, I. Albert, A. L. Barabasi, and P. Schiffer. What keeps sandcastles standing? *Nature*, 387(6635):765, JUN 1997.

[15] P. Tegzes, R. Albert, M. Paskvan, A. L. Barabasi, T. Vicsek, and P. Schiffer. Liquid-induced transitions in granular media. *Physical Review E*, 60(5, Part B):5823–5826, NOV 1999.

[16] A. Samadani and A. Kudrolli. Angle of repose and segregation in cohesive granular matter. *Physical Review E*, 64(5, Part 1), NOV 2001.

[17] P. Tegzes, T. Vicsek, and P. Schiffer. Development of correlations in the dynamics of wet granular avalanches. *Physical Review E*, 67(5, Part 1), MAY 2003.

[18] P. Tegzes, T. Vicsek, and P. Schiffer. Avalanche dynamics in wet granular materials. *Physical Review Letters*, 89(9), AUG 2002.

[19] A. T. Catherall, P. López-Alcaraz, P. Sanchez, M. R. Swift, and P. J. King. Separation of binary granular mixtures under vibration and differential magnetic levitation force. *Physical Review E*, 71(2, Part 1), FEB 2005.

[20] S. R. Hutton, A. J. Forsyth, M. J. Rhodes, and C. F. Osborne. Effect of interparticle force on mixing and segregation of dry granular materials. *Physical Review E*, 70(3, Part 1), SEP 2004.

[21] A. Samadani, A. Pradhan, and A. Kudrolli. Size segregation of granular matter in silo discharges. *Physical Review E*, 60(6, Part B):7203–7209, DEC 1999.

[22] A. Samadani and A. Kudrolli. Segregation transitions in wet granular matter. *Physical Review Letters*, 85(24):5102–5105, DEC 2000.

[23] H. M. Li and J. J. McCarthy. Phase diagrams for cohesive particle mixing and segregation. *Physical Review E*, 71(2, Part 1), FEB 2005.

[24] D. A. Robinson and S. P. Friedman. Observations of the effects of particle shape and particle size distribution on avalanching of granular media. *Physica A - Statistical Mechanics and its Applications*, 311(1-2):97–110, AUG 2002.

[25] S. A. M. El Shourbagy, S. Morita, and H. G. Matuttis. Simulation of the dependence of the bulk-stress-strain relations of granular materials on the particle shape. *Journal of the Physical Society of Japan*, 75(10), OCT 2006.

[26] H. G. Matuttis, S. Luding, and H. J. Herrmann. Discrete element simulations of dense packings and heaps made of spherical and non-spherical particles. *Powder Technology*, 109(1-3):278–292, APR 2000.

[27] Paul W. Cleary. The effect of particle shape on simple shear flows. *Powder Technology*, 179(3):144–163, JAN 2008.

[28] C. S. Campbell. Boundary interactions for 2-dimensional granular flows .1. flat boundaries, asymmetric stresses and couple-stresses. *Journal of Fluid Mechanics*, 247:111–136, FEB 1993.

[29] T. Poschel and V. Buchholtz. Molecular-dynamics of arbitrarily-shaped granular particles. *Journal de Physique I*, 5(11):1431–1455, NOV 1995.

[30] V. Buchholtz, T. Poschel, and H. J. Tillemans. Simulation of rotating drum experiments using noncircular particles. *Physica A*, 216(3):199–212, JUN 1995.

[31] T. Poschel and V. Buchholtz. Static friction phenomena in granular-materials - coulomb law versus particle geometry. *Physical Review Letters*, 71(24):3963–3966, DEC 1993.

[32] P. A. Langston, M. A. Al-Awamleh, F. Y. Fraige, and B. N. Asmar. Distinct element modelling of non-spherical frictionless particle flow. *Chemical Engineering Science*, 59(2):425–435, JAN 2004.

[33] J. T. Lia, P. A. Langston, C. Webb, and T. Dyakowski. Flow of sphero-disc particles in rectangular hoppers - a DEM and experimental comparison in 3D. *Chemical Engineering Science*, 59(24):5917–5929, DEC 2004.

[34] F. Alonso-Marroquin. Spheropolygons: A new method to simulate conservative and dissipative interactions between 2D complex-shaped rigid bodies. *EPL*, 83(1), 2008.

[35] T. Poeschel and T. Schwager. *Computational Granular Dynamics*. Springer, Berlin, 2004.

[36] P. A. Cundall and O. D. L. Strack. Discrete numerical-model for granular assemblies. *Geotechnique*, 29(1):47–65, 1979.

[37] H. J. Herrmann and S. Luding. Modeling granular media on the computer. *Continuum Mechanics and Thermodynamics*, 10(4):189–231, AUG 1998.

[38] H. P. Zhu, Z. Y. Zhou, R. Y. Yang, and A. B. Yu. Discrete particle simulation of particulate systems: A review of major applications and findings. *Chemical Engineering Science*, 63(23):5728–5770, DEC 2008.

[39] S. Fazekas, J. Kertesz, and D. E. Wolf. Piling and avalanches of magnetized particles. *Physical Review E*, 71(6, Part 1), JUN 2005.

[40] D. Zhang and W. J. Whiten. The calculation of contact forces between particles using spring and damping models. *Powder Technology*, 88(1):59–64, JUL 1996.

[41] C. Briggs and R. Bearman. The Assessment of Rock Breakage and Damage in Crushing Machinery. In *Proc. EXPLO '95*, 1995.

[42] B. K. Mishra and C. V. R. Murty. On the determination of contact parameters for realistic DEM simulations of ball mills. *Powder Technology*, 115(3):290–297, APR 2001.

[43] K. S. Liddell and M. H. Moys. The effects of mill speed and filling on the behavior of the load in a rotary grinding mill. *Journal of the South African Institute of Mining and Metallurgy*, 88(2):49–57, FEB 1988.

[44] S. Yuu, T. Abe, T. Saitoh, and T. Umekage. Three-dimensional numerical simulation of the motion of particles discharging from a rectangular hopper using distinct element method and comparison with experimental data (effects of time steps and material properties). *Advanced Powder Technology*, 6(4):259–269, 1995.

[45] S. Ji and H. H. Shen. Effect of contact force models on granular flow dynamics. *Journal of Engineering Mechanics-ASCE*, 132(11):1252–1259, NOV 2006.

[46] O. R. Walton and R. L. Braun. Viscosity, antigranulocytes-temperature, and stress calculations for shearing assemblies of inelastic, frictional disks. *Journal of Rheology*, 30(5):949–980, OCT 1986.

[47] R. D. Mindlin and H. Deresiewicz. Elastic spheres in contact under varying oblique forces. *Journal of Applied Mechanics - Transactions of the ASME*, 20(3):327–344, 1953.

[48] G. Kuwabara and K. Kono. Restitution coefficient in a collision between 2 spheres. *Japanese Journal of Applied Physics Part 1*, 26(8):1230–1233, AUG 1987.

[49] A. B. Stevens and C. M. Hrenya. Comparison of soft-sphere models to measurements of collision properties during normal impacts. *Powder Technology*, 154(2-3):99–109, JUL 2005.

[50] C. Thornton. Coefficient of restitution for collinear collisions of elastic perfectly plastic spheres. *Journal of Applied Mechanics - Transactions of the ASME*, 64(2):383–386, JUN 1997.

[51] J. Lee and H. J. Herrmann. Angle of repose and angle of marginal stability - molecular-dynamics of granular particles. *Journal of Physics A - Mathematical and General*, 26(2):373–383, JAN 1993.

[52] S. Fazekas, J. Kertesz, and D. E. Wolf. Two-dimensional array of magnetic particles: The role of an interaction cutoff. *Physical Review E*, 68(4, Part 1), OCT 2003.

[53] C. S. Campbell. Granular shear flows at the elastic limit. *Journal of Fluid Mechanics*, 465:261–291, AUG 2002.

[54] Y. J. Li, Y. Xu, and C. Thornton. A comparison of discrete element simulations and experiments for 'sandpiles' composed of spherical particles. *Powder Technology*, 160(3):219–228, DEC 2005.

[55] J. D. Jackson. *Classical Electrodynamics*. John Wiley and Sons, 3rd edition edition, 1998.

[56] T. Fujita and M. Mamiya. Interaction forces between nonmagnetic particles in the magnetized magnetic fluid. *Journal of Magnetism and Magnetic Materials*, 65(2-3):207–210, MAR 1987.

[57] B. I. Bleaney and Bleaney. B. *Electricity and Magnetism*. Oxford University Press, 3rd edition edition, 1989.

[58] M. L. Boas. *Mathematical Methods in the Physical Sciences*. John Wiley and sons, 2nd edition edition, 1983.

[59] P. Lorrain, D. P. Corson, and F. Lorrain. *Electromagnetic Fields and Waves.* W. H. Freeman and Company, 3rd edition edition, 1988.

[60] I. S. Grant and W. R. Phillips. *Electromagnetism.* John Wiley and sons, 2nd edition edition, 1990.

[61] R. E. Rosensweig. *Ferrohydrodynamics.* Dover Publications, Inc., 1985.

[62] S. Fazekas, J. Kertesz, and D. E. Wolf. Computer simulations of magnetic grains. In Hoogendoorn, S. P. and Luding, S. and Bovy, P. H. L. and Kchreckenberg, M. and Wolf, D. E., editor, *Traffic and Granular Flow '03*, pages 489–501, 2005. 5th International Conference on Traffic and Granular Flow, Delft, NETHERLANDS, 2003.

[63] K. Taylor, P. J. King, and M. R. Swift. Influence of magnetic cohesion on the stability of granular slopes. *Physical Review E*, 78(3, Part 1), SEP 2008.

[64] J. Lee. Avalanches in (1+1)-dimensional piles - a molecular-dynamics study. *Journal de Physique I*, 3(10):2017–2027, OCT 1993.

[65] T. S. Komatsu, S. Inagaki, N. Nakagawa, and S. Nasuno. Creep motion in a granular pile exhibiting steady surface flow. *Physical Review Letters*, 86(9):1757–1760, FEB 2001.

[66] J. Crassous, J. F. Metayer, P. Richard, and C. Laroche. Experimental study of a creeping granular flow at very low velocity. *Journal of Statistical Mechanics - Theory and Experiment*, MAR 2008.

[67] D. M. Mueth, G. F. Debregeas, G. S. Karczmar, P. J. Eng, S. R. Nagel, and H. M. Jaeger. Signatures of granular microstructure in dense shear flows. *Nature*, 406(6794):385–389, JUL 2000.

[68] M. A. Aguirre, A. Calvo, I. Ippolito, A. Medus, and M. Mancuso. Rearrangements in a two-dimensional packing of disks. *Physical Review E*, 73(4, Part 1), APR 2006.

[69] M. A. Aguirre, A. Medus, M. Mancuso, A. Calvo, and I. Ippolito. Effect of spontaneous rearrangements in the disorder of packing of discs. *Physica A-Statistical Mechanics and its Applications*, 371(1):29–32, NOV 1 2006.

[70] M. Renouf, D. Bonamy, F. Dubois, and P. Alart. Numerical simulation of two-dimensional steady granular flows in rotating drum: On surface flow rheology. *Physics of Fluids*, 17(10), OCT 2005.

[71] B. A. Socie, P. Umbanhowar, R. M. Lueptow, N. Jain, and J. M. Ottino. Creeping motion in granular flow. *Physical Review E*, 71(3, Part 1), MAR 2005.

[72] F. Restagno, L. Bocquet, and E. Charlaix. Where does a cohesive granular heap break? *European Physical Journal E*, 14(2):177–183, JUN 2004.

[73] N. Taberlet, P. Richard, and R. Delannay. The effect of sidewall friction on dense granular flows. *Computers & Mathematics with Applications*, 55(2):230–234, JAN 2008.

[74] S. C. du Pont, P. Gondret, B. Perrin, and M. Rabaud. Wall effects on granular heap stability. *Europhysics Letters*, 61(4):492–498, FEB 2003.

[75] J. F. Metayer, A. Valance and P. Richard. private communication, 2008.

[76] Y. C. Zhou, B. D. Wright, R. Y. Yang, B. H. Xu, and A. B. Yu. Rolling friction in the dynamic simulation of sandpile formation. *Physica A - Statistical Mechanics and its Applications*, 269(2-4):536–553, JUL 1999.

[77] Y. C. Zhou, B. H. Xu, A. B. Yu, and P. Zulli. Numerical investigation of the angle of repose of monosized spheres. *Physical Review E*, 6402(2, Part 1), AUG 2001.

[78] Y. C. Zhou, B. H. Xu, A. B. Yu, and P. Zulli. An experimental and numerical study of the angle of repose of coarse spheres. *Powder Technology*, 125(1):45–54, MAY 2002.

[79] S. B. Ogale, R. N. Bathe, R. J. Choudhary, S. N. Kale, A. S. Ogale, A. G. Banpurkar, and A. V. Limaye. Boundary effects on the stability of thin submerged granular piles. *Physica A - Statistical Mechanics and its Applications*, 354:49–58, AUG 2005.

[80] M. Kobayashi and N. Takachio. Surface magnetic charge distribution of cylindrical cores. *Trans IEEE Japan*, 106(A):111–117, MAR 1986.

[81] M. Kobayashi and Y. Ishikawa. Surface magnetic charge-distributions and demagnetizing factors of circular-cylinders. *IEEE Transactions on Magnetics*, 28(3):1810–1814, MAY 1992.

[82] M. Kobayashi, Y. Ishikawa, and S. Kato. Magnetizing characteristics of circular cylinders in perpendicularly applied magnetic field. *IEEE Transactions on Magnetics*, 32(1):254–258, JAN 1996.

[83] M. Kobayashi and H. Iijima. Surface magnetic charge distributions of cylindrical tubes. *IEEE Transactions on Magnetics*, 32(1):270–273, JAN 1996.

[84] K. Ozaki and M. Kobayashi. Surface magnetic charge distribution of a long, thin cylinder and its edge singularity. *IEEE Transactions on Magnetics*, 34(4, Part 2):2185–2191, JUL 1998. 7th Joint Magnetism and Magnetic Materials / International Magnetics Conference, SAN FRANCISCO, CALIFORNIA, JAN 06-09, 1998.

[85] T. Takayama, Y. Ikezoe, H. Uetake, N. Hirota, and K. Kitazawa. Interactions among magnetic dipoles induced in feeble magnetic substances under high magnetic fields. *Physica B - Condensed Matter*, 346:272–276, APR 2004.

[86] M. Tejedor, H. Rubio, L. Elbaile, and R. Iglesias. External fields created by uniformly magnetized ellipsoids and spheroids. *Magnetics, IEEE Transactions on*, 31(1):830–836, JAN 1995.

[87] S. Kato and M. Kobayashi. Magnetic charge densities around edges of circular cylinders. *Magnetics, IEEE Transactions on*, 32(3):1880–1887, MAY 1996.

[88] A. K. Geim and M. Berry. Ignobel prize press release. IgNobel Prize Press Release, 2001.

[89] S. Earnshaw. On the nature of the molecular forces which regulate the constitution of the luminiferous ether. *Transactions of the Cambridge Philosophical Society*, 7:97, 1842.

[90] W. Braunbeck. Freischwebende korper im elektrischen und magnetischen feld (freely suspended bodies in electric and magnetic fields). *Zeitschrift für Physik*, 112:753, 1939.

[91] W. Braunbeck. Freies schweben diamagnetischer korper im magnetfeld (free floating of diamagnetic bodies in a magnetic field). *Zeitschrift für Physik*, 112:764, 1939.

[92] M. D. Simon and A. K. Geim. Diamagnetic levitation: Flying frogs and floating magnets (invited). *Journal of Applied Physics*, 87(9, Part 3):6200–6204, MAY 2000.

[93] J. S. Brooks and J. A. Cothern. Diamagnetism and magnetic force: a new laboratory for granular materials and chaotic/deterministic dynamics. *Physica B-Condensed Matter*, 294:721–728, JAN 2001.

[94] A. K. Geim, M. D. Simon, M. I. Boamfa, and L. O. Heflinger. Magnet levitation at your fingertips. *Nature*, 400(6742):323–324, JUL 1999.

[95] A. Cansiz and J. R. Hull. Stable load-carrying and rotational loss characteristics of diamagnetic bearings. *IEEE Transactions on Magnetics*, 40(3):1636–1641, MAY 2004.

[96] J. R. Hull and A. Cansiz. Vertical and lateral forces between a permanent magnet and a high-temperature superconductor. *Journal of Applied Physics*, 86(11):6396–6404, DEC 1999.

[97] A. T. Catherall, L. Eaves, P. J. King, and S. R. Booth. Floating gold in cryogenic oxygen. *Nature*, 422(6932):579, APR 2003.

[98] A. T. Catherall, P. López-Alcaraz, K. A. Benedict, P. J. King, and L. Eaves. Cryogenically enhanced magneto-Archimedes levitation. *New Journal of Physics*, 7, MAY 2005.

[99] K. Kitazawa, Y. Ikezoe, H. Uetake, and N. Hirota. Magnetic field effects on water, air and powders. *Physica B-Condensed Matter*, 294:709–714, JAN 2001.

[100] Y. Ikezoe, T. Kaihatsu, S. Sakae, H. Uetake, N. Hirota, and K. Kitazawa. Separation of feeble magnetic particles with magneto-Archimedes levitation. *Energy Conversion and Management*, 43(3):417–425, FEB 2002.

[101] A. T. Skjeltorp. One-dimensional and two-dimensional crystallization of magnetic holes. *Physical Review Letters*, 51(25):2306–2309, 1983.

[102] B. A. Jones, J. A. Searle, and K. O'Grady. Magnetic measurements of self-organisation. *Journal of Magnetism and Magnetic Materials*, 290(Part 1 Sp. Iss. SI):131–133, APR 2005.

[103] B. A. Jones and K. O'Grady. Magnetically induced self-organization. *Journal of Applied Physics*, 97(10, Part 3), MAY 2005.

[104] T. Scheller, C. Huss, G. Lumay, N. Vandewalle, and S. Dorbolo. Precursors to avalanches in a granular monolayer. *Physical Review E*, 74(3, Part 1), SEP 2006.

[105] S. C. du Pont, P. Gondret, B. Perrin, and M Rabaud. Granular avalanches in fluids. *Physical Review Letters*, 90(4), JAN 2003.

[106] T. Takayama, Y. Ikezoe, H. Uetake, N. Hirota, and K. Kitazawa. Self-organization of nonmagnetic spheres by magnetic field. *Applied Physics Letters*, 86(23), JUN 2005.